AINA JOHANNA REICH

Single charge carrier–defect complexes in CdSe and CdS nanowires observed by photoluminescence spectroscopy.

DISSERTATION ZUR ERLANGUNG DES DOKTORGRADES DER FAKULTÄT
FÜR MATHEMATIK UND NATURWISSENSCHAFTEN

UNIVERSITÄT HAMBURG, HAMBURG, FREIGEGEBEN ZUR
VERÖFFENTLICHUNG AM 28.06.2019, GUTACHTER: PROF.
ALF MEWS, DR. TOBIAS VOSSMEYER, DATUM DER
DISPUTATION: 28.06.2019

If you don’t aim for the center
it’s a waste of the art

—Dessa *Fighting Fish*

Für Oma Christel.

Single charge carrier–defect complexes in CdSe and CdS nanowires observed by photoluminescence spectroscopy.

Aina Johanna Reich

Zusammenfassung

Im Rahmen dieser Arbeit wurden die optischen Eigenschaften von CdSe und CdS Quantennanodrähten und nicht größenquantisierte Nanodrähte untersucht und verglichen.

Für ein gutes Verständnis der Nanodrahtlumineszenz wird die Lumineszenz makroskopischer CdS-Kristalle tiefgehend besprochen. Die unterschiedlichen Typen der Lumineszenzbänder wird kategorisiert und katalogisiert für spätere Bezugnahme. Diese Besprechung wird mit Arbeiten über die Lumineszenz von makroskopischen CdSe-Kristallen in Kontrast gesetzt.

Die Messungen, die im Rahmen dieser Arbeit durchgeführt wurden, haben einen Fokus auf Nanodrähte gelegt, die mittels nasschemischer Methoden hergestellt wurden. Mehrere Proben von Drähten aus unterschiedlichen Synthesedurchläufen wurden präpariert, sowohl für die Analyse der CdSe-Quantennanodrähte, als auch der CdS-Nanodrähte. Zusätzlich wurden einzelne CdS-Nanodrähte mittels optischer Lithografie kontaktiert, sowie nicht größenquantisierte CdSe-Nanodrähte direkt auf Substraten synthetisiert. Die Proben wurden in einem im Arbeitskreis aufgebauten Konfokalmikroskop analysiert, bei Probentemperaturen im Bereich von 5 K bis 7 K.

Die Messungen an den CdSe-Quantennanodrähten zeigten, dass für einzelne Nanodrähte die individuellen Lumineszenzbänder starkes, unabhängiges Blinken aufwiesen. Das blinkende Lumineszenzsignal wurde spektral aufgespalten, dabei wurde die höchstmögliche Zeitauflösung gewählt, bei der das Signal-Rausch-Verhältnis noch eine Auswertung der Spektren zuließ. Gleichzeitig wurden Lumineszenzintensitätsspuren mit der *time-tagged time-resolved*-Methode (englisch für [mit] einem Zeitwert markiert und zeitaufgelöst) aufgenommen, was die messzeitaufgelöste Analyse der Lumineszenzzerfälle ermöglichte. Diese beiden kombinierten Datensätze wurden hauptsächlich für die Charakterisierung der Nanodrahteigenschaften herangezogen. In den Spektrenzeitspuren konnten drei unterschiedliche Gruppen an Signalen identifiziert werden: eine hochenergetische Signalgruppe, eine bandkantennahe Signalgruppe, sowie die Fallenemission. Die hochenergetischen Signale bilden die Gruppe mit der niedrigsten Intensität, ihr Ursprung ist wahrscheinlich die Rekombination von freien und schwach gebundenen Exzitonen. Die bandkantennahe Emissionsgruppe stellt häufig die das Spektrum dominierende Emission dar. Teil dieser Gruppe sind schmale, alternierend blinkende Emissionslinien, die zusätzlich eine gruppenübergreifende Intensitätsdynamik zeigen. Diese Emission befindet sich energetisch direkt unter den hochenergetischen Banden. Ihr Ursprung ist wahrscheinlich die Rekombination von partiell gebundenen *free–to–bound*-Ladungsträgerkomplexen (*free–to–bound*: englisch für frei-zu-gebunden). Die dritte Gruppe ist die Fallenemission, welche ein charakteristisches Muster von breitem Emissionsband mit zwei oder mehr Phononrepliken zeigt. Der Ursprung dieser Gruppe an Emissionslinien ist aller Wahrscheinlichkeit nach die Rekombination von Donor-Akzeptor-Paaren. Alle drei dieser Gruppen können in relativ breiten Energiebereichen beobachtet werden. Diese Energiebereiche passen in die von Berechnungen vorhergesagten Werte für unterschiedliche Komplexe zwischen Defekten und Ladungsträgern und bestätigen den starken Einfluss der Defektumgebung auf die Emissionslinien. Das Verhalten der einzelnen Lumineszenzbanden lässt bei beiden Systemen darauf schließen, dass einzelne Signale von einzelnen Defekten herrühren. Weiterhin wurde beobachtet, dass die Nanodrahtlumineszenz entweder vom Blinken der bandkantennahen Emission oder der Fallenemission dominiert wird. Beide Arten folgen einem inversen Potenzgesetz und haben höchstwahrscheinlich ihren Ursprung in der Ionisation der beteiligten Defektstellen und der Ladungsträgerwanderung in Oberflächenzustände. Zusätzlich konnten parallel Prozesse beobachtet werden, in denen Intensitätsfluktuationen nicht von Lebensdauerfluktuationen begleitet wurden, und umgekehrt. Dies unterstreicht die Komplexität der elektronischen Prozesse der angeregten Quantennanodrähte.

Bei der Untersuchung der Lumineszenz der nichtquantisierten CdS Nanodrähte konnte, wie zuvor für die CdSe Quantennanodrähte, starke Parallelen zu der Emission makroskopischer Kristalle beobachtet werden. Dabei war die Lumineszenz signifikant empfindlicher in Anbetracht unterschiedlicher Anregungsleistungen, und Defektsignale konnten seltener beobachtet werden. Hyperspektrale, konfokale Bildgebung, sowie ortsaufgelöste Floureszenzlebensdauermessungen wurde benutzt um die Defektsignale aufzufinden und zu identifizieren. Es wurden Signale in den Energiebereichen und mit den Eigenschaften der Rekombination gebundener Exzitonen, partiell gebundener Ladungsträgerpaare, sowie von Donor-Akzeptor-Paaren gefunden. Für ein System ohne Größenquantisierung unerwartet wurden starke Variationen in der Emissionsenergie sowie Lumineszenzblinken einzelner Banden beobachtet.

Die durchgeführten Messungen zeigen, dass sowohl CdSe Quantennanodrähte, sowie CdS Nanodrähte signifikant komplexere Systeme sind, als zuvor angenommen. Die Lumineszenzspektra und -dynamiken spiegeln diese Komplexität der elektronischen Eigenschaften und Prozesse auf der Ebene einzelner Defekte wieder.

Abstract

This work investigates and compares the optical properties of CdSe and CdS quantum nanowires and bulk nanowires.

To properly understand the luminescence of the nanowires, an indepth review of the luminescence of bulk CdS is done. The different types of luminescence bands are categorised and catalogued as a further reference point. This review is contrasted with the works that reviewed the CdSe bulk luminescence.

The measurements done in this work centre on nanowires produced via wet chemistry. Multiple samples from different synthesis batches were prepared for single wire analysis for both CdSe quantum nanowires and CdS bulk nanowires. In addition, single CdS nanowires were contacted via optical lithography and bulk CdSe nanowires were synthesised in an on-substrate synthesis. The samples were then analysed with a home-built confocal setup at sample temperatures between 5 K to 7 K.

The measurements on the CdSe quantum nanowires showed strong blinking of a multitude of individual luminescence bands for single quantum nanowires. The blinking was spectrally resolved at the highest time resolution possible while retaining acceptable signal–to–noise ratios in the spectra. At the same time a time-tagged time-resolved intensity trace was recorded for luminescence decay time analysis. These two simultaneous measurements were the main type of data collected for the analysis of the CdSe quantum nanowires. In the spectral traces, with the reference of the bulk spectroscopy data, three types of individually blinking groups of luminescence bands could be identified: a group of high energy bands, the near band edge emission and the trap emission. The high energy group is the least intense group, with its origin most likely due to free and weakly bound excitons. The near band edge emission is often the dominating group of alternating sharp emission lines that also show a simultaneous emission dynamic. They are situated just at lower energies of the high energy emission. Their origin is most likely

strong exciton complexes or free–to–bound recombinations. The third signal group is the trap emission, which consists of broad zero-phonon lines and two or more phonon replicas. The origin of these lines are most likely donor–acceptor pair recombinations. All of the three types of lines can be observed within a broad energy range. Previously performed calculations confirm the assignments of the different charge carrier–defect complexes to these lines, as well as the strong influence of the defect environment. The behaviour of the individual luminescence bands is best described under the assumption that each line can be associated with a specific defect site in the wire volume. Also, the nanowire blinking is usually dominated either by near band–edge blinking or trap signal blinking. Both types follow power law behaviour and are likely due to trap ionisation and surface processes. In addition some processes that influence decay time but not intensity or intensity but not luminescence decay time can be observed, showing that the quantum nanowires are much more complex system than single nanocrystals.

For CdS bulk nanowires, as for CdSe quantum nanowires, observation of emission lines with strong resemblance to the bulk emission can be made, but with much stronger sensitivity to the excitation power and much less frequent. Hyperspectral imaging and fluorescence lifetime imaging were used to observe and characterise these defect-related lines. Signals in the energy regions of bound exciton lines, free–to–bound emission and of donor–acceptor pair emission could all be identified. Unexpected for a bulk system these lines showed strong variations in energy and also luminescence blinking.

The studies showed that CdSe quantum nanowires, but also CdS bulk wires are much more complex systems than previously thought. The luminescence spectra mirror this complexity and the electronic properties on the level of single defect processes.

Contents

Glossary

AFM atomic force microscope. 50–52, 61, 63, 132

APD avalanche photo diode. 49, 58–60, 67

CCD charge-coupled device. 49, 58, 60, 67, 136

CLSM confocal laser scanning microscopy. 49

CW continuous wave. 48, 55, 56

DAP donor–acceptor pair,. 38, 43, 45, 46, 75, 84, 87, 90, 93–98, 104, 106–113, 127, 132, 138, 140, 141, 143, 144, 153, 155

DCET diffusion-controlled electron transfer. 23, 25, 27

DOS density of states. 19

DPSS diode-pumped solid state. 55, 56

EL electroluminescence. 34

FFT fast Fourier transform. 132, 133

FLID fluorescence lifetime–intensity diagram. 28, 105, 106, 114, 115, 156

FLIM fluorescence lifetime image. 141, 144

HE high energy. 77–84, 86, 95, 98, 99, 106–108, 110, 112, 115–117, 121, 146, 147, 151–156

HPLC high performance liquid chromatography. 60, 62

HSI hyperspectral imaging. 136–141, 143, 144, 154

IR infrared. 41, 44, 56, 120

IRF instrument response function. 71, 81

ISC intersystem crossing. 21

LED light emitting diode. 15

LO longitudinal optical. 37–39, 43, 65, 66, 94, 116, 138, 140, 143, 145, 146

MRC multiple recombination centres. 26, 156

NBE near band–edge. 30, 65–67, 75–77, 80, 86, 88, 89, 93, 98–108, 110–118, 122, 124, 129, 130, 132, 134, 135, 151–157

OPO optical parametric oscillator. 56, 57

PL photoluminescence. 33–36, 40

pmma poly(methyl methacrylate). 62

pr photoreflectance. 34, 42

qnw quantum nanowire. 16, 46, 65–67, 73, 76, 77, 95, 151–153, 157

sem scanning electron microscope. 50, 62, 135

shg second harmonic generation. 56, 57

sls solution–liquid–solid. 52, 53

sted stimulated emission depletion. 49

stm scanning tunnelling microscope. 50

storm stochastic optical reconstruction microscopy. 20

t trap. 66, 75, 76, 84–100, 102–108, 110–119, 122, 124, 130, 134, 146, 148, 149, 151–157

tcspc time correlated single photon counting. 57–59, 67, 68, 71, 113, 141

tem transmission electron microscope. 50, 60, 61, 129, 130

top trioctylphosphine. 62, 63

tttr time-tagged, time-resolved. 28, 59, 67–70, 72, 73, 80, 81, 86, 88, 91, 102, 105, 114–117, 132, 152

uv ultraviolet. 36, 63

vb valence band. 17, 34, 42, 45

vis visible. 63

vls vapour–liquid–solid. 52

1

Introduction

Light is one commodity that was once a luxury and is now so cheaply available that it's affordability is not even questioned. From the time when the cost of fuel limited the available hours of light in the evening to Thomas Edison's much more affordable light bulb to today's light emitting diodes (LEDs) based light sources, the availability of light became a given in the industrialised world.[1]

At the same time, light is responsible for one of the great failures of classical physics, as its wave–particle duality necessitated the advent of quantum mechanics.[2]

Directly tied to the properties of light is the interaction of matter with it. From the elastic scattering of light to inelastic processes of absorption, excitation and relaxation, light from the radio wave region to X-rays are regularly used to analyse different properties of matter. The illustration of the electromagnetic spectrum in figure 1.1[2] shows the broad range of regions and the material properties that can be probed using light from the respective wavelength regions. The visible region is the one that can be used to excite electronic transitions. This means that the absorption and emission in this spectral region will depend on the electronic properties of the material.

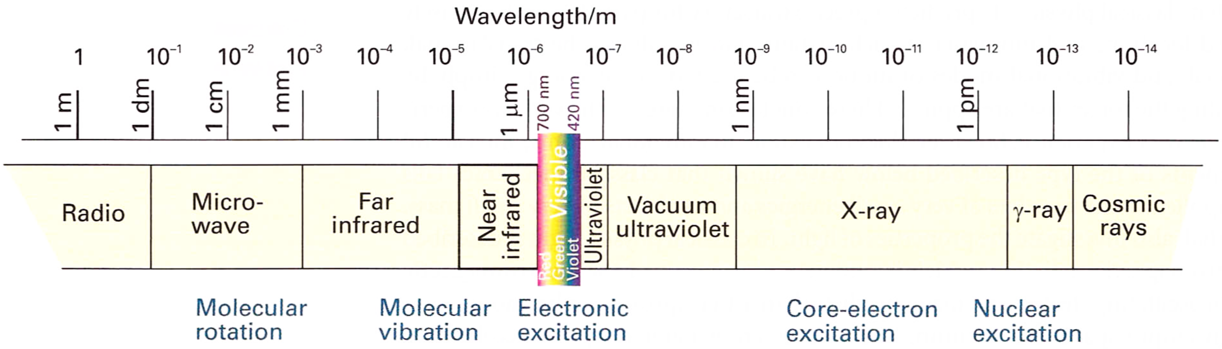

Figure 1.1: The electromagnetic spectrum: The light wavelengths with the corresponding radiation names and the transitions that can be excited with radiation in that energy range.[2]

For II-VI semiconductors the analysis of the visible absorbed and especially the emitted light has been used to characterise their electronic structure, band gap, and doping levels since it was technically feasible to do so.[3, 4] The thorough low-temperature analysis of the luminescence of CdS and CdSe made it possible to verify models of their electronic structure and to identify the defect types present in the materials.[5–11]

Subsequently, with the rising interest in semiconductor nanostructures in the 1990s, the size-dependent electronic properties also showed in the absorption and emission of nanocrystals and quantum nanowires (QNWs).[12–15]

The properties of the luminescence of nanocrystals and nanowires goes both ways – the emitted light contains informations about the structure itself, it shows where its properties deviate from the bulk material and in the end it can say something about the potential of the material for applications. As the investigation of semiconductor nanostructures has helped to tailor the properties of these materials they can be refined into building blocks and be used, for example for quantum dot light emitting diodes[16, 17] or in photodetectors.[18]

As the shape of QNWs makes them easy to contact while retaining the size tunability of their electronic properties, they make for an interesting subject of study. As has been shown before[19, 20] the low temperature luminescence of these nanostructures show complex spectra and dynamics that are not easily described. Especially the photoluminescence intermittency that can typically be observed for such nanoscale systems is an aspect that might influence the performance of nanocrystals and nanowires as light emitting building blocks. Based on the two earlier works above, this work will analyse the CdSe QNW dynamics in detail and compare the CdSe QNW low temperature luminescence to the low temperature photoluminescence of CdS bulk nanowires with the goal to get a better understanding of the systems' electronic properties and the origin of and mechanism behind the photoluminescence blinking.

1.1 *General properties of CdS and CdSe*

Cadmium selenide and cadmium sulphide are both semiconductor materials from the group of II–VI semiconductors. These materials crystallise in ionic crystals with the cation (cadmium) holding a +2 charge and the anion (selenide or sulphide) holding a −2 charge. The different degrees of ionisation between different anions and cations – sulphur has a larger electronegativity than selenium and the degree of ionisation in CdS can therefore be expected to be higher than in CdSe – are one main difference influencing the electronic properties. In addition, ion size will influence the crystal structure and therefore also the electronic properties.

In the case of CdSe and CdS, in addition of similar binding conditions the elements contributing as anionic binding partners are as chemically close as same group elements can be – sulphur (a nonmetal) is a period three elements, while selenium (a metalloid) can be found in period four.

Both CdSe and CdS can crystallise in two crystal structures that are stable at room temperature and under ambient pressure: the hexagonal wurtzite structure and the cubic zincblende. For CdS the hexagonal wurtzite structure is the more stable and therefore common one. For CdSe under ambient conditions the cubic zincblende structure is more stable.[21]

The two crystal lattices are shown in figure 1.2. Both types are very similar in that both anions and cations are arranged in the same sublattice

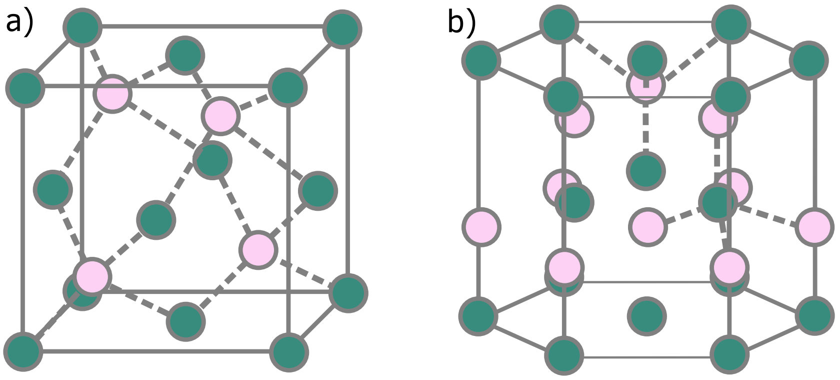

Figure 1.2: Main crystal modifications of CdSe and CdS under ambient conditions. One type of ions is coloured green while the oppositely charged type is coloured light pink. a) The cubic zincblende structure. b) The hexagonal wurtzite structure. In either structure each ion is located in the tetrahedron volume defined by four of the oppositely charged ions.

– as cubic close-packed spheres in zincblende and as hexagonal close-packed spheres in wurtzite. The ion sub-lattices are now arranged so that each ion is surrounded by four ions of the opposite charge that sit at the edges of a tetrahedron. In CdSe the energetic difference between the two crystal structures is so small that CdSe QNWs can be observed to crystallise in both systems with frequent changes occurring along the axis of growth.[22]

The room temperature band gaps of the CdSe zincblende and CdS wurtzite crystal are 1.7 eV and 2.25 eV, respectively, placing them energetically in the spectrum of visible light. This makes both materials interesting for applications that require emitters in visible, as well as for those that require absorption of visible light. As shown in figure 1.3 the two materials are quite similar in absolute band gap width, as well as in relative potential location of valence and conduction band to the vacuum level and subsequently the H_2/H_2O reduction level, which also makes the material interesting for the catalytic reduction of hydrogen from water.[23]

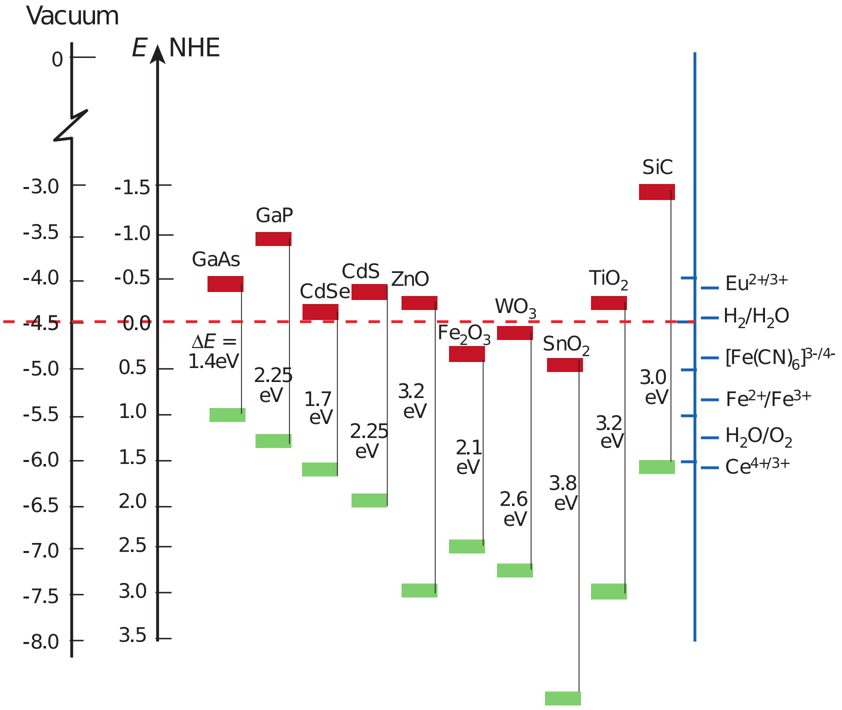

Figure 1.3: The band gaps and relative potential positions of different semiconductors.[23]

One thing that is of relevance for both materials is the band splitting of the valence band (VB) for both lattices at the Γ point. This splitting is shown in figure 1.4. Based on a) the zincblende lattice considering spin-orbit coupling results in b) the splitting of the zincblende valence band into two subbands. Adding an additional hexagonal crystal field yields c) the threefold split wurtzite VB.[24] This splitting has been experimentally confirmed through photoreflectance measurements both for CdSe[26] and CdS bulk crystals.[25] For applications such as luminescence measurements it means that for each valence band an excitonic line – A, B, and, C – could in principle be observed.

1.2 *The influence of the nanoscale*

The special properties that make nanostructures such an interesting field of study arise for a large part from the fact that their size directly influences their electronic properties. This dependence of properties on a system's size can be illustrated with the fundamental quantum mechanical model of a particle in a box. Any model in quantum mechanics is

Figure 1.4: The valence band splitting in CdS crystals.[25]

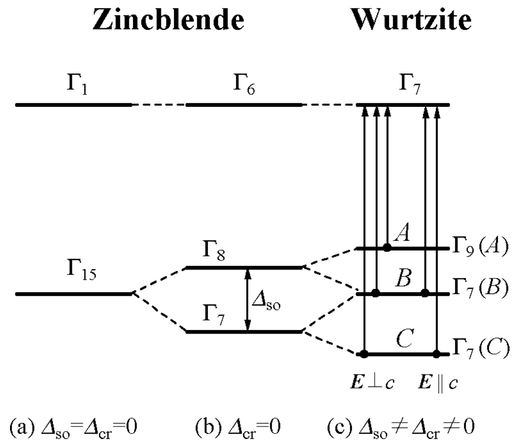

based on the Schrödinger equation, as shown in equation 1.1

$$\hat{H}\psi = E\psi \tag{1.1}$$

The equation associates the energy of a quantum mechanical system with the wave function ψ and the Hamiltonian $\hat{H}$. For the solution of this equation the system potential energy has to be considered. In the easiest case of the particle–in–a–box this is the infinite square-well potential with a potential energy of zero in the well. Substitution with a suitable wave function yields the following relationship for the energy states of the system:[27]

$$E_n = \frac{n^2h^2}{8mL} \tag{1.2}$$

In equation 1.2 n is the system quantum number which is defined as a positive integer and describes the possible energy states, h is the Planck constant, m is the particle mass and L is the potential well length. This equation shows that a larger potential well will decrease the system energy, while a smaller box will increase it. This fundamental principle of quantum mechanics can be directly observed in nanoparticles through changes in their absorption edge and emission energies to higher energies for smaller sizes.

As a semiconductor crystal is a much more complex system than the one-dimensional particle in a box, the size dependence will be directly related to the nanostructure's electronic properties. The most general factor in this case is that the electron and hole that form an exciton in an excited semiconductor have an optimum distance to each other. The electron and hole with the respective effective masses m_e^* and m_h^* will have a reduced size μ:

$$\mu = \frac{m_e^* m_h^*}{m_e^* + m_h^*} \tag{1.3}$$

Treating the exciton analogous to a hydrogen atom, it will have the following Bohr radius:

$$a_0 = \frac{4\pi\varepsilon\varepsilon_0\hbar^2}{\mu e^2} \tag{1.4}$$

In equation 1.4 ε is the material dielectric constant, ε_0 is the vacuum dielectric constant, $\hbar$ is the reduced Planck constant and e is the electron charge. This simplification can be made for Wannier-Mott excitons, which are prevalent in most semiconductors. The values are typically in the range of several nanometres, for example 3.0 nm for CdS and 5.4 nm for CdSe.[12] That means, that any system smaller than the exciton diameter will strongly increase the energy of the excited semiconductor.

A good approximation for the description of the introduction of quantum confinement to a bulk material is starting with the model of the free electron. In this description of a solid with N free electrons those electrons in this electron gas are assumed to not interact, neither with each other, nor with the atoms composing the crystal. The interactions that actually do influence the electrons can be considered by exchanging the free electron mass with the effective electron mass. In this model each electron's energy is equal to its kinetic energy:[28]

$$E = {}^{1}\!/\!{}_{2} m\mathbf{v}^2 \tag{1.5}$$

and its linear momentum

$$\mathbf{p} = m\mathbf{v} = \frac{h}{2\pi}\mathbf{k} \tag{1.6}$$

with the electron wave vector $\mathbf{k}$. For a bulk solid it is assumed that the electrons are not influenced by the solid surface, which assumes an infinite solid with a spatial expansion $d \longrightarrow \infty$ and $\Delta k_{x,y,z} = {}^{2\pi}\!/\!{}_{d_{x,y,z}} \longrightarrow 0$ throughout. Such a solid possesses a large number of very close energetic states, as the density of states (dos) of a three-dimension system is

$$DOS = \frac{\mathrm{d}N(E)}{\mathrm{d}E} = \frac{\mathrm{d}N(k)}{\mathrm{d}k} \propto \sqrt{E} \tag{1.7}$$

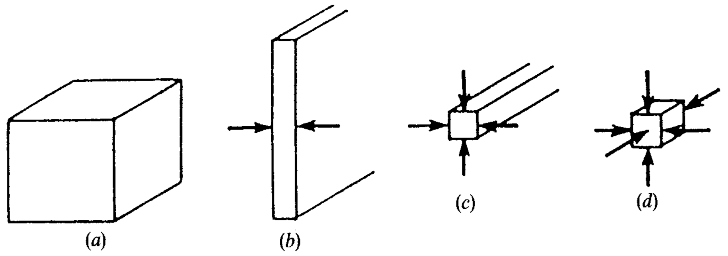

Figure 1.5: Illustration of systems with different degrees of confinement. a) A bulk solid with no confinement b) A two-dimensional system with confinement in one dimension. c) A one-dimensional system, which is confined in two dimensions d) A system whose size is confined in all three dimensions.[12]

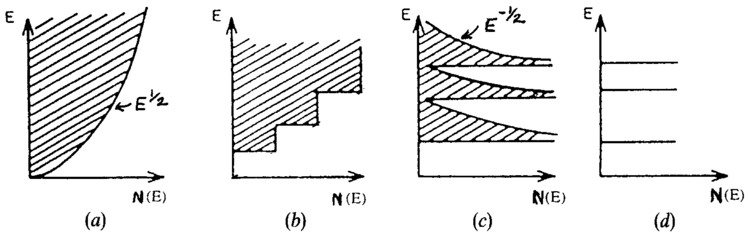

Figure 1.6: The density of states for the systems shown above: a) The bulks solid dos with an increase of $\sqrt{E}$. b) The two-dimensional system dos with discrete steps. c) The dos of a one-dimensional system with the characteristic Van Hove singularities. d) The completely confined system shows only discrete energy levels.[12]

Figure 1.5a through d shows solids with different degrees of confinement: a shows a bulk solid, b one-dimensional confinement (e.g. a nanosheet), c shows confinement in two dimensions (e.g. a quantum nanowire), and d shows three-dimensional confinement (e.g. a quantum dot). This respective dos are shown in figure 1.6a through d. The dos in figure 1.6a is the relationship shown by equation 1.7. Confinement is introduced by treating one or more dimensions analogous to the particle in a box, resulting in discrete wave vectors and energies for the electrons in the respective dimensions, respective equation 1.2. This leads from the continuous dos in figure 1.6a to the steps in figure 1.6b. The case of two-dimensional confinement leads to the Van Hove singularities shown in figure 1.6c and a confinement in all dimensions finally leads to the discrete levels in figure 1.6d.[12]

In addition to the increasing discretisation an increase in confinement will also lead to an increase in energy gap between levels, which in turn will increase a semiconductor nanostructure band gap.

1.3 The blinking of CdSe nanowires

1.3.1 From quantum jumps to power law: fluorescence intermittency in single emitters

The advances in single molecule spectroscopy since the late 1980s have revealed that the constant luminescence of the material ensemble of a fluorophore is not so constant at the single emitter level. The single atom studies by Cohen-Tannoudji & Dalibard record binary bright and dark periods for the luminescence and describe it with a simple three level model. This clear-cut switch of the atoms between not only a ground state and an excited state, but also a third, metastable dark state is a direct expression of a fundamental principle of quantum physics – the quantum jump as proposed in the very beginning stages of quantum physics.[30]

This fluorescence intermittency – or fluorescence blinking – was further observed for larger systems, such as single pentacene molecules[31, 32] that were placed in a larger crystalline matrix and later for isolated dye molecules[33] and isolated molecules of green fluorescent protein[34]. Finally, luminescence blinking was also discovered in semiconductor nanocrystals, namely CdSe quantum dots.[13] The phenomenon was quickly also observed for related material systems, such as CdS nanocrystals[35] and systems of higher dimensionality – such as CdSe nanowires.[36, 37]

For all above mentioned systems the fluorescence intensity over time can be roughly described as follows: the emission intensity changes in a random pattern between a high intensity *ON* state and a low intensity *OFF* state. These two states appear binary. As the changes between states appear as random, so do the dwell times in one or the other state. The most astonishing aspect about this observation is that it can be made for so many, so different systems. This makes it both intriguing and almost mysterious, even if, or especially because of the usefulness of blinking systems for such things as statistics-based hyper-resolution microscopy techniques, such as stochastic optical reconstruction microscopy (storm).[38–40]

While in a single molecule a model considering a triplet state can be an easy explanation for the occurrence of *ON* and *OFF* states and the sudden changes between the two, a nanocrystal is a much more complex system. Consequently, there is a strong motivation to analyse and find the origin of the nanostructure luminescence blinking.

Statistical analysis of luminescence blinking

While the blinking events and their duration are seemingly random, for the above described triplet system the duration distribution of both *ON* and *OFF* events are very well defined. As the system is defined as a ground state, an emissive, unstable excited state and a metastable triplet state the transition between these states can be defined and rate constants can be assigned for each transition. These rate constants are defined by the properties of the states themselves and the resulting probabilities of the transitions between them.

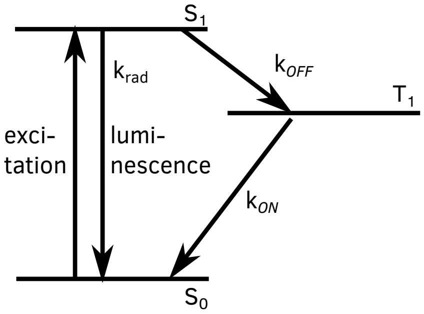

Figure 1.7: The energy diagram showing the triplet transition of a system. While the transition from the ground state S_0 to the excited singlet state S_1 is allowed and happens quickly, the transition to the triplet state T_1 is forbidden and therefore happens significantly slower.

For any such system an energy level diagram as shown in figure 1.7 applies. The system's ground state is the singlet state S_0. Excitation lifts the system into the S_1 excited singlet state. This excited state can either relax back to the singlet ground state directly via emission of light. The other possible relaxation path is to the triplet state T_1. This pathway is nominally forbidden, as it constitutes a form of intersystem crossing (isc). This means that it happens at a much slower rate than the radiative relaxation into the ground state. On the other hand, when a system does relax into the triplet state, the only available path back into the singlet ground state also involves a change of multiplicity and is slow as well, making the triplet state metastable.

In terms of single molecule fluorescence intermittency the system is in its *ON* state when the excitation and relaxation between the singlet states takes place. The moment the system crosses to the triplet state – with the probability for this process governed by the rate constant k_{OFF} – it will stay there for a certain time and not relax. The dwelling time in this state can itself be expressed through the rate constant k_{On} which is the main factor determining the probability for the return to the *ON* state. These probabilities are expressed by the following equation[41]:

$$N_{On/Off}(\tau) = \exp\left(-k_{On/Off} \cdot \tau\right) \tag{1.8}$$

The probability N off the system staying either in the *ON* or the *OFF* shows an exponential dependence on the time τ and the respective rate constant k. This means, the longer the system remains in either state, the probability for it remaining there decreases exponentially, with a larger rate constant decreasing the slope and increasing the probability for a stay.

To characterise ans compare such blinking systems the two transition probabilities would be an important reference number. As a probability can not be measured directly, the probability density $P$of the transition has to be determined instead. It is defined as the first deviation of the probability[41]:

$$P_{On/Off}(\tau) = \frac{\mathrm{d}N}{\mathrm{d}\tau} = k_{On/Off} \cdot \exp -k_{On/Off} \cdot \tau \tag{1.9}$$

In nanocrystals the model of a triplet state can of course not be directly applied. As their data processing yielded exponential probability densities Efros & Rosen developed more fitting description of the processes that could lead to blinking in nanocrystals.[14] They assigned the *On* state to the plain nanocrystal, in which under illumination continuously excitons are created – these recombine, sending out a photon. The *Off* state in contrast is associated with the nanocrystal being ionised, either thermally or via an Auger process. In this state any created exciton would transfer its energy on recombination to the extra charge, which could then relax via emission of vibrational energy. The partner charge carrier would to have be trapped outside of the crystal – in the outside medium or on the crystal surface – and the return of the charge to the crystal volume would neutralise it and again switch the crystal from the *Off* state into the *On* state. The ionisation and neutralisation of the crystal can be directly compared to the intersystem crossing processes that are present in molecular emitters and would therefore also yield the same mathematical description of the blinking statistics.

The exponential relationship would still imply a quite simple system and in fact, the blinking of many single molecules[42–44] as well as the nanocrystal luminescence fluctuations do not follow it. As the works by Shimizu *et al.*[45] and Kuno *et al.*[15, 46] showed, the statistical analysis of nanocrystal blinking does not yield an exponential *ON* or *OFF* time histogram, but rather a distribution that follows a power law relationship:

$$P_{On/Off}(\tau) \propto \tau^{-m} \tag{1.10}$$

According to this relationship the probability density of *On* and *Off* states is proportional to their duration times to the negative power of the constant m, which describes the individual blinking system – e.g. the nanocrystal – and is often found to be around 1.5.[15] In simple words the power law behaviour describes a system that does not only possess a single rate constant for the *On–Off* transitions and a single rate constant for the transition back, but rather a distribution of rates. This means that the binary blinking has to be explained by a mechanism that is much less binary in nature. The following chapter will give an overview over the main mechanisms that have been discussed for the power law blinking of nanocrystals and how well they match to the observed behaviours.

1.3.2 *Proposed models for quantum dot blinking*

After it was observed that the behaviour of the luminescence intensity fluctuations of nanocrystals – and other emitters – was too complex to be explained within the framework of simple singlet–triplet intersystem crossing several different models were developed and discussed to explain the experimental findings. The main point of these models was to find a way to explain a range of rate constants for the *On–Off* transition. To achieve this it has to be assumed that either a range of states are present or that a single state fluctuates in some way. [47] The models that have been discussed over the years are the following:

Multiple traps – multiple transitions

Verberk *et al.* have proposed a model that explains the power law behaviour by proposing a distribution of surface states.[48] Based on the observation of blinking of CdS quantum dots at 1.2 K their mechanism behind the luminescence intensity fluctuations assumes that one half of the charge carrier pair will tunnel from the excited nanocrystal to a surface trap. A thermal ionisation is ruled out because of the power law exponents insensitivity to temperature changes. In the charged nanocrystal the fast Auger recombination dominates and for a return to the emissive state a return of the charge is necessary, just as proposed before by Efros & Rosen.[14]

Now, the power law distribution depends on the availability of a uniform distribution on the surface of or in the matrix around the nanocrystal. As trapping probability is strongly dependent on the distance of the exciton wave function to the traps outside of the crystal volume, the probability density for the recovery time from the dark state of the crystal is itself an inverse power law.

To further explain the long *On* times and *On* time power law behaviour of nanocrystal with a capping shell Verberk *et al.* additionally propose that charged crystals can still emit, but only if the the hole is also trapped just outside the core and with a Coulomb blockade preventing far away trapping.[48] Without this modification the *On* times distribution would be expected to be exponential, which is not observed. In this model a *grey* luminescence state is proposed. Truly neutral nanocrystals will blink much faster than those with a localised hole, which makes their fluctuations often hard to resolve and the recorded intensities therefore appear in between dark and bright.

The model is simple but efficient at explaining the observed fluctuations, the value of the power law exponent and the temperature independence, but does neglect other observed phenomena, such as spectral diffusion and the observed[49] insensitivity of the statistics to the nanocrystal environment.

The spatial diffusion model

As a variation on the take of Verberk *et al.* on the multiple trap model and the need for a mechanism to explain the long *On* times Margolin *et al.* have proposed that an ejected charge carrier can perform a random walk on the surface of the nanocrystal for a crystal without a capping shell.[50] Their model always yields an exponent $m = 1.5$. While exponents close to this value are commonly reported, the exact value is not often found and strong deviations are common[15, 47, 48, 51], which this model cannot explain.

The fluctuating barrier model

This model, proposed by Kuno *et al.*[15, 52], is an extension of the multiple trap model that, like the Coulomb blockade addendum by Verberk *et al.* is a means to explain the power law behaviour of the *On* state distribution.

As the experimentally observed time scales of the luminescence blinking correspond to low tunnelling probabilities – with 10×10^{-10} to 10×10^{-16} attempts per successful event[15] – the sensitivity of the system for barrier fluctuations is large. The two possible mechanisms, as shown in figure 1.8, can contribute the entire observed dynamic range of event durations with a fluctuation of less than ±25 %, if a barrier height of 4 eV is assumed. The influence of the barrier width in this case even goes beyond the observed range. The observed variation in tunnelling barrier width and height could already be caused by small configuration changes in the organic ligand shell. It also favours actually a smaller number of charge carrier traps in the nanocrystal environment, as larger numbers would cause an average of different observed transitions and dampen rate fluctuations to individual sites.[15]

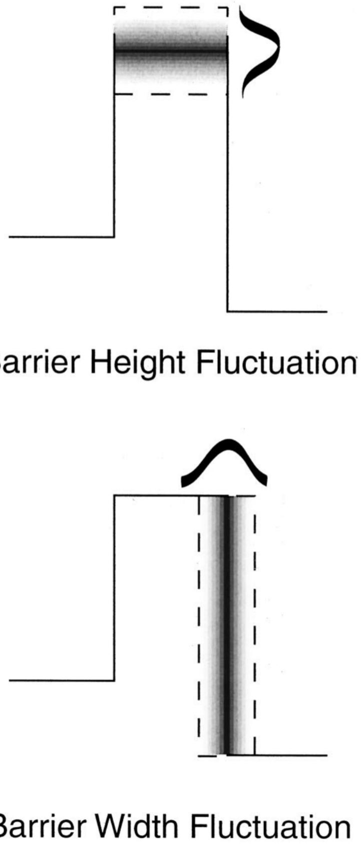

Figure 1.8: Illustration of the tunnel barrier fluctuations as described by Kuno *et al.*.[15] The barrier is imagined to either fluctuate in height or width, influencing tunnelling probability.

While this model is a valid alternative to that of multiple traps, it also suffers from the flaw of the dependence on environmental changes that would influence the blinking statistics. The study by Pelton *et al.* showed that statistics are preserved even between nanocrystals in solution and those fixed on a solid substrate, which ultimately has to considered, in addition to the differences in blinking statistics on submillisecond timescales.[49, 53]

The spectral diffusion model

Instead of a fluctuating tunnelling barrier, the spectral diffusion model assumes that the every energetic state of the crystal will exhibit diffusion within a potential well and that states can overlap.[45, 54, 55] This idea, first proposed by Shimizu *et al.*, could be described by Tang & Marcus in the diffusion-controlled electron transfer (dcet) model[54, 55] by basing it upon the Marcus model, which Marcus developed back in the 1950s to describe electron transfer between molecules.[56] The model puts the two states – charged nanocrystal and neutral nanocrystal – onto a collective reaction coordinate Q with two intersecting parabolas representing their free energies. Transition between these two states can only happen at a point of resonance Q_c, the point of intersection.[51, 54, 55]

The model is shown schematically in figure 1.9. The switch between the bright and the dark state is shown in form of a simple energy diagram in figure 1.9a. The nanocrystal is excited from its ground state $|G\rangle$ to its excited state $|L^\star\rangle$. From this state the nanocrystal can either relax back to $|G\rangle$ via emission of a photon or transition to $|D\rangle$, the ground state of the dark crystal. When in this state the crystal will be excited into the dark excited state $|D^\star\rangle$, out of which the system will relax non-radiatively. The transitions between the bright excited state and the dark ground state are assigned the rate constants γ_L and γ_D.

Now the power law behaviour for the transitions between the states $|L^\star\rangle$ and $|D\rangle$ arises from the transition model as shown in figure 1.9b. Each state is represented as a parabola on the reaction coordinate Q. For the system to cross over from the light to the dark state – and vice versa – it has to reach the crossing point of the parabolas and therefore has

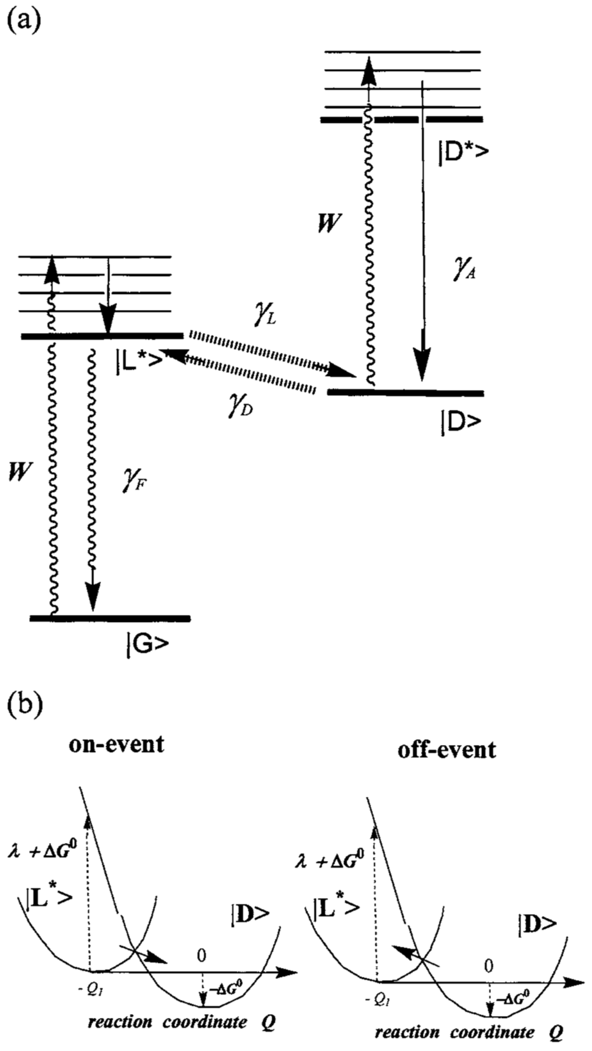

Figure 1.9: The model of spectral diffusion illustrated.[54] a) A system that is excited from a ground state $|G\rangle$ into its excited state $|L^\star\rangle$ can either radiatively relax or transition to a dark state $|D\rangle$, which can in turn be excited into a dark excited state $|D^\star\rangle$, which will always relax through a nonradiative pathway. b) For the transition from the bright to the dark state the excited bright state and dark ground state are each described as two parabolas on a reaction coordinate Q. Two cross from one to the other state the system has to move over the crossing point of both parabolas.

to move along the reaction coordinate Q. The potential on which the system can move is defined as follows for $|L^\star\rangle$:

$$U_1 = \kappa_E \frac{(Q + Q_1)^2}{2} \tag{1.11}$$

In this relationship κ_E is the curvature of the parabola. The respective definition for the energy of $|D\rangle$ is:

$$U_2 = \Delta G^0 \frac{\kappa_E Q^2}{2} \tag{1.12}$$

with ΔG° being the free energy gap for electron transfer and the reorganisation energy for electron transfer λ being defined as:

$$\lambda = \frac{\kappa_E Q_1^2}{2} \tag{1.13}$$

The same κ is assumed for both parabolas as a simplification. The crossing between the two parabolas can only happen at the point Q_c, which is defined as:

$$Q_c = \frac{\Delta G^0 - \lambda}{\sqrt{2\kappa_E \lambda}} \tag{1.14}$$

In practice these parabolas can potentially represent different processes by which the nanocrystal reaches its *Off* state, as long as a fluctuation of both bright and dark state are permitted.[53] Originally the DCET model assumes a phonon-assisted diffusion to the potential intersections – at which e.g. a ionisation of the crystal happens – which yields power law exponents of $m = -0.5$ for dynamics with submillisecond state duration below a parabola-dependent critical time t_c and of $m = 1.5$ for states state with longer duration.[55]

Usually submillisecond are not within the temporal resolution of blinking analysis, as even if these measurement speeds are supported by the instrumentation, the signal–to–noise ratio will often not suffice to resolve dynamics on these fast time scales. Nonetheless, investigation by Pelton *et al.* show that if these time scales can be accessed the smaller exponents can be confirmed.[53]

What can not be strictly explained within this model is the deviation from these exact values, especially as the exponent can reach values of $m > -2$ in some cases. One possibility is to assume anomalous diffusion in a non-Debye dielectric medium[53, 55]. By and large this model for the luminescence blinking is quite robust and fits easily with the experimental results while still being vague in terms of what kind of actual physical processes are described.

The fluctuating non-radiative rate model

An alternative model for the nanocrystal blinking assumes that ionisation and neutralisation are not the two processes that switch the crystal between the binary *On* and *Off* state, but that a fluctuation of the rate of the competing non-radiative rates cause the intensity dynamics. This model was proposed by Frantsuzov & Marcus

The exact mechanism of radiative and nonradiative recombinations is dependent on the existence of an energetic band of surface states. This kind of band is predicted in the calculations by Pokrant & Whaley[58] and caused by the overlap of nanocrystal surface dangling bonds. It is predicted to consist of at least 200 states and infrared absorption spectroscopy of nanocrystal ensembles has shown that it can span well over 100 meV, depending on the nanocrystal radius. In this model the bright and dark phases can be schematically drawn as shown in figure 1.10. The

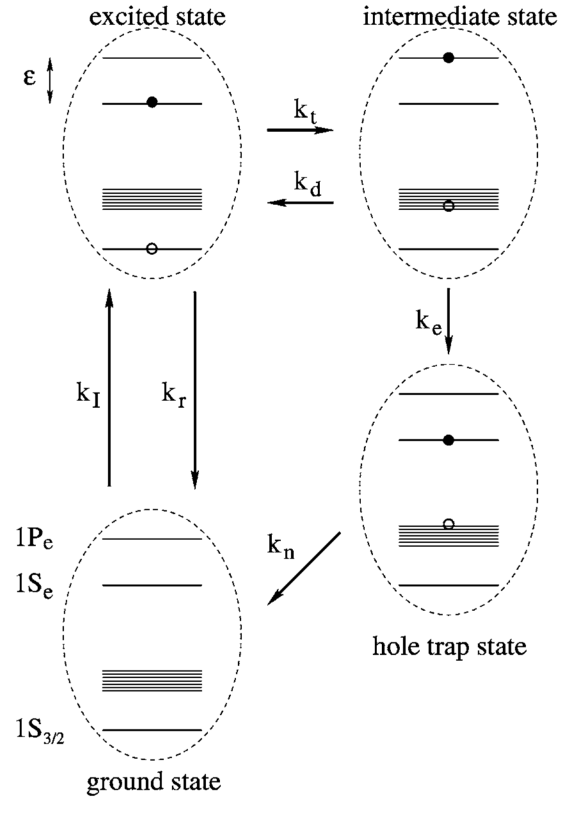

Figure 1.10: The processes described with the fluctuating nonradiative rate model.[57] Rates for the transition to and from the excited state, both the the ground state and intermediate state are assumed to fluctuate.

nanocrystal is excited with light into its excited state: An electron–hole pair is generated. The charge carrier pair can either recombine radiatively or the hole can be trapped into the surface bands through and Auger process, transferring the energy difference to the electron. The electron is in turn elevated to the first excited electron state in the conduction band – from $1S_e$ to $1P_e$.

From this intermediate state the nanocrystal can either return to the excited state or transition to the hole trap state. The electron and hole can relax from this state back to the ground state via a nonradiative pathway. Excitations that occur while the system is in the trapped state will lead to Auger recombination of the newly generated charge carrier pairs. All the above processes can be described by straightforward rate relationships.

For the observed binary intensity dynamics of the nanocrystal an additional selection criterion for the transition has to be considered. The model therefore assumes that the energetic gap between the states $1S_e$ and $1P_e$ is not static but varies due to electron–phonon interactions. The Gauss distribution of the possible energy gaps and the statistic diffusion of this value directly influences the radiative recombination rate and the trapping rate to the intermediate state. When the energy diffuses above a certain value, the nonradiative rate dominates and the other way round below that value. This leads to the seemingly binary behaviour.

While numerically, this model leaves open questions – for examples as to how to explain the dynamic range of the fluorescence intermittency, the differences in cut off and any exponent different from $m = -1.5$ – but it does for one explain the variations in relaxation rate as observed by Schlegel *et al.* for the radiative rate and consequently the non-radiative rate.[59] It is also a sensible starting point for the explanation of non-binary dynamic behaviour of the nanocrystal fluorescence intensity.

One way to translate this rather abstract model into a concrete blinking mechanism is the multiple recombination centres (mrc) model.[60] In this model multiple defect states are proposed that have two states – an inactive on and an active one. In their active state they can localise holes. The localised charge carriers will recombine with the mirror charge carrier non-radiatively, while a free charge carrier pair will recombine radiatively. The defects will fluctuate between their active and inactive state with a specific rate and as there are multiple defects there is a distribution of rates. This model can explain non-binary intensity distribution and can be used to model the luminescence dynamics with good results.

Statistic analysis and subsequent modelling of the blinking of different emitters – from molecules over quantum dots to nanowires – have shown that the different observed blinking behaviours can be explained by adjusting the number and distribution of recombination centres.[61] This makes this fairly descriptive model one of the most universal ones, even though it does not take the role of charging for the luminescence blinking into account.

1.3.3 *Specialities: truncated On-times, grey states and strange intensity behaviours*

Not expanded on in the above descriptions are observations and descriptions that go beyond a simple power law *On–Off* behaviour. This includes differences in behaviour between *On* and *Off* times, intermediate intensity states and fluctuations that deviate from a simple intensity–lifetime relationship. While these observations necessitate the introduction of specific constraints on every description of the nanocrystal blinking, if regularly observed they can in fact help to specify or rule out certain mechanisms of the fluorescence intermittency.

Truncated *On* time probability distributions

Already in their observation of the power law behaviour of the *On* and *Off* time distribution Shimizu *et al.* also observed that this behaviour did not extend to long intervals for the *On* times.[45] This so-called truncated power law behaviour instead shows a change to an exponential behaviour at a specific point, the fall-off time $\tau_{\text{fall-off}}$. An example, as shown in the study of Peterson & Nesbitt[62], can be seen in figure 1.11. The plot, shown with logarithmic x and y axis, shows the in this representation expected straight line that represents the power law distribution of the *Off* times. The *On* times on the other hand deviate from the straight line after the fall-off time by curving down. This form of distribution represents a reduction in probability for long *On* times with the the probability reducing the longer the on times, in comparison to a pure power law behaviour. In comparison, long *Off* times are more probable to occur, due to the continued power law behaviour.

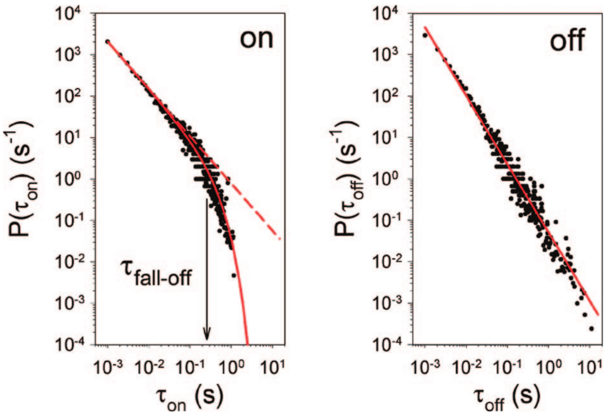

Figure 1.11: The truncated probability distributions for the *On* state, as observed by Peterson & Nesbitt.[62] The truncation is due to a lower probability for long on times, which results in an exponential probability density after a fall-off time.

This observed behaviour fits well into the dcet model of Tang & Marcus, which already predicts the truncated power law for *On* times.[55] As the dcet model only describes the nanocrystal mathematically in terms of energetic states and its movements on the reaction coordinate between the *On* and *Off* states, the actual process behind the behaviour still has to be deducted from the luminescence behaviour and within the frame of the nanocrystal as a semiconductor crystal.

While the behaviour has been repeatedly and reliably observed, different studies show different dependence on different experimental conditions. Shimizu *et al.* see a temperature dependence of the fall-off point on sample temperature, as well as laser power. They attribute the truncation to saturation effects that block radiative channels above certain temperatures and number of generated charge carriers as the reason for the truncation.[45] In contrast, Knappenberger *et al.* only see a dependence on excitation wavelength at room temperature. They particularly see a 200 meV threshold (above the nanocrystal band gap energy) for the observation of the probability density truncation. The excess energy leads to the population of conduction band states that are more likely to relax non-radiatively.[63] In comparison, Peterson & Nesbitt report a wavelength and, in disagreement with Knappenberger *et al.*, also a power dependence. of the truncation and fall-off time. Their proposed model is an Auger process, caused by the formation of biexcitons.[62]

The above models for the behaviour of the *On* time probability densities for long *On* intervals are, dependent on the specific observations, plausible. As it cannot be said with certainty as to why the different *On* time behaviours have been observed none of the models can be excluded with certainty when discussing it.

Multiple *On* states and inconsistent lifetime dependencies.

As was already implied in the conclusions of the study by Verberk *et al.*, a binary *On–Off / neutral nanocrystal–charged nanocrystal* system is not necessarily the correct description of nanocrystal blinking. This was further confirmed by Zhang *et al.* who could show that the recorded *On* levels would span a range of intensities, in effect bridging the intensity gap between the previously assumed discrete *Off* and *On* states with an often more or less continuous distribution of states.[64] This is also the result of the statistic analysis of nanocrystal blinking by Margolin *et al.*[65]

What Zhang *et al.* also show is the clear dependence of the luminescence decay rate on the luminescence intensity. This can be clearly seen in a fluorescence lifetime–intensity diagram (FLID) – recording the luminescence blinking with time-tagged, time-resolved (TTTR) mode will yield both an intensity value and a luminescence decay for every bin, which can be plotted as a function of each other. Three of these FLIDs, as shown by Zhang *et al.*[64], are plotted in figure 1.12. The three figures 1.12a–c show FLID plots of three representative nanocrystals. The plots show that, while nanocrystals with apparent binary intensity distributions exist (fig. 1.12a), they also show intensity states in between the *Off* and *On* intensity level. The dependence of luminescence lifetime on intensity is also always present, but the increase of lifetime with increasing intensity depends on each individual nanocrystal.

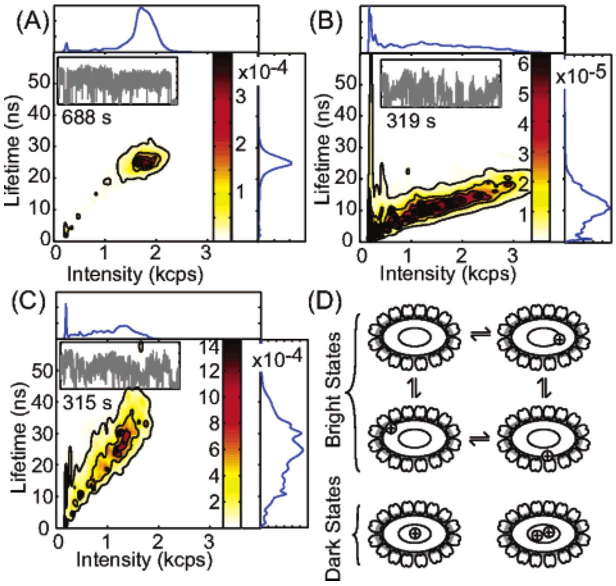

Figure 1.12: Different intensity–lifetime distributions with (A) an almost binary *On–Off* behaviour and, (B) and (C), continuous intensity–lifetime distributions.As origin of the continuous distributions bright charged nanocrystals are postulated.[64]

This observation is explained by Zhang *et al.* by a model with is shown schematically in figure 1.12d. To explain the many different *On* intensity levels they propose a changing *On* state. This is realised by assuming that in most cases the *On* state is in fact a charged but still emitting nanocrystal. Emission is suggested to take place in the smaller band gap nanocrystal core. While the nanocrystal is charged there is always a chance for non-radiative Auger recombination, which is always faster than the competing radiative recombination of the exciton. As the excess positive charge – as proposed by Zhang *et al.* – can be present anywhere in the nanocrystal or its shell the probability for Auger recombination also depends on the location of the charge relative to the nanocrystal core. The closer the charge, the higher the likelihood for non-radiative recombination and the quicker the measured luminescence decay. In the extreme case of one or more charges being present in the core the excited nanocrystal will always relax through the Auger route.[64]

This mechanism is also confirmed by the observations made by Malko *et al.*.[66] They see an increase of the number of *On* states with increasing excitation powers for nanocrystals with thin shells. This fits with an increased ionisation rate due to larger numbers of photo-generated excitons in the nanocrystal. At the same time, an increasing shell thickness of the nanocrystal will decrease the number of states and eliminate the power dependence. This can be related to the increased volume of the nanostructure in which additional charges' wave functions would be much less likely to overlap with that of a generated exciton. Therefore the quantum yield of the charged crystal and that of the neutral crystal would at a certain volume of the system be the same and an additional charge would not influence the crystal anymore. This is also in agreement with the blinking suppression that happens in so-called giant quantum dots.[66]

In quantum dots with thick shells Galland *et al.* also observe the related phenomenon of lifetime blinking without intensity blinking. They argue that in a negatively charged nanocrystal the Auger recombination for the negative trion is strongly suppressed. Due to the CdSe–CdS core–shell electronic structure the hole would be localised in the core, while the electrons would be delocalised in the shell, strongly lowering the likelihood of the Auger process.[67]

Galland *et al.* also show in a second study that the opposite process is possible – intensity blinking without a change in luminescence lifetime, by electrochemically shifting the potential and charge of surface states. In some configurations the surface states will catch hot electrons after excitation, while in other they can not easily cross over in to these states and will recombine normally. The first process, the b type blinking does not influence the radiative rate but only the number of excitons available for recombination. The conventional a type blinking on the other hand derives its intensity variations directly from the competition between radiative and non-radiative recombinations, meaning a lower intensity is correlated to a higher incidence of faster non-radiative decays along the remaining radiative decays.[68]

1.3.4 *Luminescence intermittency of semiconductor nanowires*

Like semiconductor nanocrystals the luminescence of semiconductor nanowires also shows luminescence intermittency. The system is usually treated as a special case of single nanocrystal luminescence[47], which is understandable as the general observations regarding for example blinking statistics are quite similar, as is of course the system itself. The relevant studies in the past have all investigated CdSe nanowires with diameters usually within the regime of strong quantum confinement. One big difference between the nanocrystal and nanowire studies is that the growth of nanowires from solution does not as easily allow for the growth of a protective shell, which is a standard for nanocrystals from solution and, as elaborated above, can strongly influence the optical properties and the fluorescence blinking.

As nanowires have two confined and one bulk-like dimension to them, a spatially resolved investigation of blinking is possible with fluorescence microscopy and this already reveals a difference to the nanocrystal blinking. In fact, the general luminescence intensity has been reported to be heterogeneous along the length of the nanowire. Protasenko *et al.* correlate disorder in the nanocrystal with nanowire spatial and temporal intensity fluctuations, due to carrier and exciton localisation at different points of the potential landscape.[36]

In contrast Glennon *et al.* have reported a synchronous blinking of the whole length of single nanowires for a minority of their wires.[69]

They explain the phenomenon by considering the highly emissive state of the wire as a state that is achieved by filling the wire's surface traps over time, increasing the recombination probability through direct radiative recombination for the delocalised charge carrier pairs.

The above two different blinking mechanisms already show that the nanowire blinking has to be considered as a different process – or rather multiple processes – from quantum dot blinking. Interestingly, when looking at blinking statistics the power law probability density can be observed for these different processes as well. The main difference to the quantum dot luminescence blinking is that a truncation of the *On* probability density can be observed earlier than for the nanocrystals, showing that long *On* times are even less likely than in nanocrystals, which might have to do with the lack of a protective shell, as this might increase the probability for certain ionisation processes.[36, 47, 69]

The intensity of the CdSe nanowire luminescence has been shown to directly react to manipulation of the local or global carrier concentrations. While there is some disagreement on the exact underlying mechanisms, intensity variations as responses to both and electric field[37, 70] as well as the injection of charges into the wires[71, 72] could be observed. The experiments by Schäfer *et al.* show that the removal of electrons from the system quenches the wires while injection of electrons can enhance the luminescence for a short time. This implies that a luminescence intensity fluctuation due to charge trapping and Auger processes is very likely. The involvement of trap states in the CdSe nanowire luminescence processes also play a crucial rule in the model of Vietmeyer *et al.* that aim to explain the luminescence decay curves. The third degree exponential decay curves and the very fast decays of the nanowire luminescence are integrated into a model that proposes both electron and hole traps to explain the multitude of quick, nonradiative decays.[73, 74] All these above mentioned studies indicate that for both the *On* phases of the nanowire as well as the *Off* phases the involvement of traps states have to be considered.

Lastly, our single wire studies at low temperature have shown that the individual luminescence bands also show individual blinking.[75] Here the radiative processes, especially of the low energy trap-related emission signal shows very distinct and apparently binary blinking. The higher energy near band–edge (nbe) emission shows independent dynamics that happen on independent time-scales. This is a further level of complexity added to the luminescence dynamics that have to be further analysed and quantified.

1.4 Nonradiative transitions: Possible mechanisms

The study of bulk semiconductors – namely their luminescence – usually involves the study of the measurable processes. The radiative recombination pathways of photo-generated electron–hole pairs are therefore discussed in great detail, as is shown for CdS specifically in chapter 6.1. That said, in many semiconductors the non-radiative recombinations dominate.[76] This has also been shown for nano-crystalline structures, especially those without a well-passivated surface. In the case of CdSe nanowires the room temperature quantum yield is reported as below 1 %[77] for those wires showing relatively strong luminescence. While in the investigation of the optical properties of nanocrystals Auger processes have been cited as the likely cause of the intermittency[13] there are several other mechanisms that have to be considered.

The relative contribution of non-radiative recombinations in comparison to the radiative ones are temperature dependent – as is again observed in the measurements of CdS nanowires in this work. Energetically there are two possible explanations for this behaviour – the saturation of involved defect states and the potentially necessary activation energy onto the non-radiative recombination pathway.

The first option is only valid for the recombination of charge carrier pairs of which at least one component is localised at a defect. Depending on the sample temperature the thermal energy can excite charge carriers into the defect states, if these are energetically close enough to the valence or conduction band. This prevents the recombination through the now occupied defect states.

The second type of mechanism is a much more general description that can be true for different kinds of non-radiative recombination pathways and can also occur in combination with the previously mentioned quenching of specific recombination pathways. This process describes the transition from the excited state that can recombine radiatively to the non-radiative pathway. The temperature dependence of the probability of the non-radiative pathway lies in this model in the fact that the system has to be excited to a certain point at which the non-radiative pathways are accessible. This can as a more specific example be the excitation of an electron across an energy barrier to access for example surface states.

Different mechanisms can be assumed for the non-radiative pathways of excited system to its ground state. The proposed mechanisms[76] are as follows:

Multiple-phonon emission This process has the lowest probability but is possible in principle. The exited state relaxes via the emission of a cascade of phonons, without occupying any intermediate states between excited state and ground state. There is no indication that this mechanism plays any role for the non-radiative recombinations for nanocrystals and nanowires.

Surface band recombination at external and internal surfaces The orbitals of the dangling bonds at the surface of a semiconductor overlap to form a continuous energy band that can be accessed by charge carriers in close proximity to this band. The same can happen at the surface of inclusions of foreign matter or defects areas within the semiconductor volume (internal surface). Charge carrier pairs can recombine through this continuous band through phonon emission. This mechanism might well play a role for semiconductor nanostructures due to the large surface–to–volume ratio.

Auger mechanism The Auger mechanism has been discussed as the main non-radiative recombination pathway for nanocrystals for decades.[51] It is a three body collision of one charge carrier pair with an access charge carrier. In this collision the recombination energy of the charge carrier pair is transferred to the excess charge which experiences an interband excitation and relaxes again through the emission of phonons. The process is temperature dependent, as higher samples temperatures lead to higher charge carrier concentrations and therefore a higher likelihood of Auger processes.

Independent of the exact recombination mechanism the number of radiative versus non-radiative decays will not only influence the luminescence intensity, but also the measured luminescence lifetime. While, of course, only radiative decays can be observed through the emission of photons, the measured rate is directly dependent on both the non-radiative and radiative rate. This is due to the dependence of the population of the excited state on the rates of both processes. This is expressed in equation 1.15.

$$\frac{\mathrm{d}N}{\mathrm{d}t} = -(k_{rad} + k_{nrad}) \cdot N \tag{1.15}$$

In this equation N is the population of the excited state, while k_{rad} and k_{nrad} are the recombination rates through the competing radiative and non-radiative pathway, respectively. As this equation shows, changes in one of the depopulation rates will influence the total change in population, meaning that an increasing non-radiative rate will depopulate the excited state faster, thus less luminescence is measured. The measured decay in this case will therefore be quicker.

The above is true for competing recombination rates. Changes in luminescence intensity without any change in decay time that can sometimes be observed for nanocrystals[68] need instead to be described differently. This is done by differentiating the non-radiative recombination of hot and cold charge carriers. Hot charge carriers are those electrons and holes that have been excited into the valence and conduction band and have yet to relax to the band edge. These already excited charge carriers can now either relax to the band edge or transition to a non-radiative pathway. At this point the transitions to this non-radiative pathway does not compete with a radiative recombination, but with the non-radiative relaxation to the band edge and does therefore not influence the recombination lifetime.

2

The CdS and CdSe bulk luminescence

The luminescence of solids, and therefore also the luminescence of semiconductors, has been an object of scientific research for a long time. As progress in science helped the advent of more and more sophisticated technologies in the first half of the 20th century – from the TV screen[78] to sophisticated instruments[79] – the push for new materials and application also catalysed academic interest in the underlying mechanism of the utilized properties. Different properties of the materials influenced the properties of their luminescence, as explained by Spedding in 1939.[3] Position and width of the signal lines and bands were known to be an indicator about a material's composition, structure, and purity and consequently its electronic properties. With technological progress the accessible data also steadily improved. Cooling the samples revealed more complex spectra with sharper bands and signals that were not visible at all in room temperature measurements.

2.1 *The luminescence of cadmium sulphide*

One of the first studies of the cadmium sulphide PL by Kröger[80] shows an impressive example of the benefits of low-temperature measurements. An intense edge emission, not visible in room temperature spectra, dominates the long wavelength side of the PL signal at –180 °C (93.15 K). The spectrum in figure 2.1 shows the – according to Kröger – mostly unchanged short wavelength side of the spectrum at 480 nm to 490 nm and the very intense additional bands between 510 nm to 540 nm.

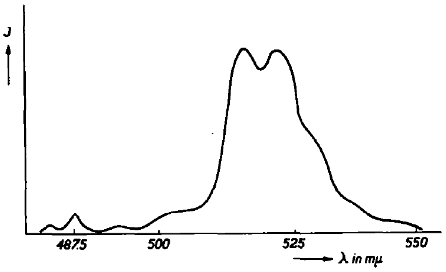

Figure 2.1: The photoluminescence (PL) spectrum of a CdS single crystal at –180 °C, as recorded by Kröger[80]

The strong influence of sample temperature, even in the low temperature range, is nicely visible in the spectra Furlong & Ravilious show in their 1955 study. The two spectra in figure 2.2 show marked difference in the resolution and strength of especially the signals on the high energy side of the spectrum. The upper spectrum a, recorded at 4 K sample temperature, shows many very defined lines in the blue spectral region which blur to broad signals at 77 K sample temperature (lower spectrum b).

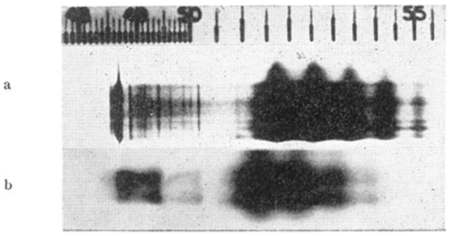

Figure 2.2: Spectra of the luminescence of CdS at a) 4 K; b) 77 K. The top wavelength scale is in units of 100 Å[5]

These advancements in the analysis of the CdS luminescence ties in with the previously found and mechanistically described relationship between the PL and the conductivity. A study by Gudden & Pohl found a dependence of greenockite crystals' conductivity on light illumination as early as 1920. Both illumination intensity as well as light wavelength – in a manner directly related to the absorption spectrum – influenced the sample resistance.[81] Broser *et al.* later on used these and their own experimental findings to expand the energy band model of solids. They postulated both doping levels and charge carrier trap sites that would influence luminescence and conductivity in different ways.[4] While this model would be heavily modified and expanded, these concepts are still important aspects to many models of the current state of research.

In the following decades, the luminescence of CdS wurtzite crystals was analysed with different methods. The PL[9] and electroluminescence (EL) measurements were combined with Zeeman effect measurements and the selective introduction of defects into the material.[7]

Roughly, the low temperature signals can be divided into three groups. The high energy, narrow lines originate from the free excitons as well as bound exciton complexes. The edge emission or green bands can be linked to processes where at least one charge carrier is localized at a defect side. And lastly, highly doped crystals also emit very broad red fluorescence bands.

2.1.1 Excitons in wurtzite CdS

In the high energy section of the spectrum a number of bands were identified early as a reoccurring feature in all spectra.[82] Photoreflectance (PR) measurements matched the PL measurements in so far that two absorption signals could be correlated to two lines in the fluorescence spectra. A third band was also observed at even higher energies, but no corresponding PL signal. [5, 82]

The observation of three absorption signals corresponds to the CdS band structure at $\vec{k} = 0$. The valence band splits into three spin-degenerate states, as explained in chapter 1.1. The bands are denoted A, B, and C with decreasing energy. The A band has Γ_9 symmetry, while the B and C band have Γ_7 symmetry. This is reflected in the selective excitation with the polarization direction of the incident light. While the B and C band excitation is polarization independent, the A band selectively interacts with light with the polarization direction $E \perp c$.

The C exciton typically shows a comparatively broad photoreflectance signal for the exciton ground state $n = 1$ and no signal for the $n = 2$ excited state. Thomas & Hopfield point out that this is an indication for short exciton lifetimes. They propose that C excitons spontaneously auto-ionize to form a free hole in one of the other two valence bands and a free electron. They also estimate that the excited state of the B exciton would be more stable than the C exciton ground state.[82] This would easily explain the absence of fluorescence peaks related to the C valence band.

Values for the band gap, exciton binding energies, and hence the expected fluorescence signal energies vary from measurement to measurement[21]. Fairly current values have been measured through photoreflectance spectroscopy by Imada *et al.* in 2002.[25] The values for the band gap energies and exciton energies at $T = 0\,\mathrm{K}$ according to Imada *et al.* obtained with the analytical expression for band gap temperature dependence by Pässler[83] are listed in table 2.1. The the temperature dependence of the exciton energies are particularly small in the low temperature region up to $T = 10\,\mathrm{K}$.

VB	$E_g(0)$ (eV)	$E_X(0)$ (eV)	G (meV)
A	2.573	2.546	27
B	2.599	2.567	31
C	2.659	2.629	30

Table 2.1: Band gap energies of wurtzite CdS, as measured by PR.[25]

$$E(T) \cong E(0) - (\alpha\Theta_p/2)\left[\left(1 + \left({}^{2T}\!/_{\Theta_p}\right)^p\right)^{\frac{1}{p}} - 1\right] \tag{2.1}$$

Employing equation 2.1 the decrease in exciton energy results in $\Delta E = 0.01\,\mathrm{meV}$ for both the A exciton and the B exciton, or a shift of $\Delta\lambda = 0.04\,\mathrm{nm}$ to longer wavelengths for the luminescence signals. This makes measurements carried out in this temperature range easily comparable.

The experimental values used in most works for comparisons are those by Thomas & Hopfield in 1959. Their photoreflectance and fluorescence measurements at 4.2 K sample temperature yielded exciton energies of $E_X^A = 2.5537\,\text{eV}$, $E_X^B = 2.5686\,\text{eV}$, as well as $E_X^C = 2.630\,\text{eV}$.[8, 82]

The investigations of pure wurtzite CdS luminescence usually show the occurrence of several very narrow bands close to the exciton signals. The signals have varying strengths and require a low enough sample temperature and a high enough setup spectral resolution to be resolved. Detailed investigations of each band have been carried out over the years[8–10, 84–87], showing that these bands can be associated with both the A and the B exciton being bound to different defects. This part of the spectrum is relatively complex. The following section will outline the all main observed lines, their positions and means of identification, grouped by their origin.

2.1.2 The near band edge emission

Reviewing the literature on near–band edge emission of CdS can yield information on an overwhelming amount of signals. The spectra change depending on the crystals that were investigated in the respective studies and the experimental conditions; the signal intensities, absolute wavelength and energy values, as well as the multiplicity of lines can change and complicate comparison.

Nonetheless, these signals – all very narrow lines with widths of usually less than 1 meV – all arise from processes that involve states with a relatively small energetic benefit in comparison to the free exciton. In the work of Thomas & Hopfield[9] the signals denominated I_1 and I_2 are shown to originate from an A band exciton bound to a neutral acceptor and an A band exciton bound to a neutral donor, respectively. These two lines are found in most luminescence and absorption spectra of pure CdS crystals and were described before they could be further identified.[8] With more in-depth investigations of the high-energy side of the spectra further signals could also be assigned to interactions of excitons with neutral defects. In their 1962 report Thomas & Hopfield already expand the previously used nomenclature to account for B valence band excitons, as well as defects situated at different energetic depths below the exciton energy.

The signal I_1 was found by Thomas & Hopfield at an emission energy of 2.535 95 eV (488.85 nm).[8, 9] This is equivalent of an energy difference of 17.7 meV to their exciton A fluorescence band at 2.5537 eV. This energy difference is the binding energy of the exciton to the neutral defect. Lovergine *et al.* measure a binding energy of 17.2 meV in 1992,[86] thus showing the reproducible occurrence of this line in the CdS PL spectra.

Thomas & Hopfield only observe the I_1 line for excitation with light that is polarized $E \perp c$, analogous to the A exciton line.[9] The I_1 line, as observed by Thomas & Hopfield, is further quenched by illumination with infra-red light. This behaviour is easily explained with the ionization of the neutral defect sites.

Another means of identification of the lines is their behaviour in a magnetic field. The I_1 line shows a linear Zeeman effect typical for a system with one unpaired charge carrier. By investigating the thermalisation effects of the split absorption signal – an intensity difference between lines dependent on magnetic field orientation – they assign the line to a complex with two holes and one electron. This configuration is synonymous with an exciton bound to a neutral acceptor.

Besides the electronic properties of the defects, it is of interest to know their exact chemical identification. Usually, the investigated CdS crystals in all aforementioned studies were described as the pure material, with great care taken in the preparation process to achieve such a crystal. Nonetheless, these spectra of different pure crystals were reported to markedly differ. Irradiation experiments by Randolph *et al.* show that the I_1 band quenches under gamma ray irradiation while a new band emerges.[88] Energy threshold experiments clarify that the change in fluorescence is due to the displacement of sulphur atoms. Interstitial sulphur would act as an acceptor an can thus be considered a possibility for the identity of the defect.

Sample temperatures above 140 K anneal the defects and the fluorescence returns to a near initial state. The annealing behaviour of the I_1 band is identical to the annealing behaviour of the edge emission, or green fluorescence, which will be described further down. This indicates that one kind of defect can be the origin of different fluorescence bands through different interactions of the charge carriers with said defect. Annealing is also possible at temperatures as low as 4.2 K by illumination of the sample with ultraviolet (uv) light.[88] The annealing behaviour is insofar of additional interest when the mobility of the defects plays a role, as it might in the spectroscopy of nanostructures.

Another finding by Handelman & Thomas is the quenching of the I_1 emission after treatment of the crystals with cadmium vapour.[87] This points into the direction of cadmium vacancies as the responsible defect, but in general fits with the the idea of an excess of sulphur. In general, the pristine n-type crystals in the study did not show the I_1 line. The pl line could be induced by heat-treating the crystals in a vacuum (low Cd pressure) atmosphere, which would also reduce the amount of free charge carriers.

This relatively straightforward description of the I_1 line is complicated by the observation of Henry *et al.* of two I_1 lines. They see these lines at energies of 2.5362 eV (488.86 nm) and 2.5364 eV (488.82 nm) and name them I_{1a} and I_{1b}, respectively.[10, 85] These lines all show a weaker companion line at lower energies. Henry *et al.* assign this second line to a dopant with a naturally abundant isotope. The intensity ratio suggests only very few possible dopants and of those only lithium can be successfully introduced into the crystal. Doping with lithium enriched with the less abundant Li_6 increases the intensity of the associated line of the I_{1a} signal. The conclusion to these findings is that apparently dopants will be incorporated in crystals that are assumed to be pure. As the I_{1b} signal is not influenced by the Li_6 doping, but responds to addition of sodium to the crystal. Two additional neutral acceptor lines can be found in crystals with added phosphorus.[85]

The aforementioned I_1-type lines all arise from the recombination of bound A excitons and show the dependence on excitation polarization. In CdS absorption spectra Thomas & Hopfield identify several I_1 like bands that are active for $E \parallel c$ instead of $E \perp c$.[9] These bands can be assigned to B excitons bound to neutral acceptors. The bands are not visible in the emission spectra.

The second characteristic defect-related emission in the high energy region of the CdS luminescence spectrum is the I_2 emission which, as the counterpart to the I_1 emission, is generated by the recombination of excitons bound to neutral donor sites. These lines appear much closer to the exciton lines, implying a smaller binding energy of the exciton–defect complex. Both the I_2 and I_{2B} line were identified and characterized by Thomas & Hopfield[9] by employing absorption and emission spectroscopy and Zeeman effect measurements. They see the I_2 line at 486.715 nm (2.5471 eV), or at an energetic distance of 6.6 meV. A similar value of 6.3 meV is also reported by Lovergine *et al.*[86].

The exact I_2 line energy – like the I_1 line energy – is dependent on the defect's chemical identity. Figure 2.3 shows the energy distribution of the signals from excitons bound to different neutral donors and acceptors. They are distributed in a certain energy region with small variations, dependent on the exact dopant.

For both, I_1 and I_2 lines, phonon replicas could be observed.[9] Bands that arise from contributions from optical as well acoustic phonons are shown in figure 2.4. While the image shows nine replicas, they all are fairly low in absolute intensity and the coupling strength is small. The most prominent replica is the longitudinal optical (LO) phonon replica of the I_1 band, which has a higher intensity of about one order of magnitude in comparison to the other replicas.

Also, all the lines described above are attributed to the recombination of bound A excitons. Thomas & Hopfield also describe several lines they attribute to bound B excitons, due to how they react to selective polarization of excitation light. These I_{1B} and I_{2B} lines are listed with all other unique signals in tables 2.3 to 2.6.

In conclusion, the excitonic region of the CdS fluorescence will usually show two main signals related to the recombination of excitons bound to neutral acceptors and donors, respectively. In detail, the chemical identity of the defects will determine the exact signal energy. These slight shifts in energy – dependent on exact sample composition and structure – will sometimes lead to reports of lines that are declared as separate signals. Reynolds & Litton for example reported a line they named I_5 at 486.914 nm (2.545 92 ev) which would equate to an energy difference of 6.4 meV to the A band exciton fluorescence.[89] This band fits right into the series of different I_2 bands, as reported in later years, both in spectral position and opto-magnetic properties.[21]

Lifetimes of the bound excitons were measured by Henry & Nassau to be $\tau_{I_1} = (1.03 \pm 0.10)$ ns and $\tau_{I_2} = (0.5 \pm 0.1)$ ns. [84] These values fit into earlier reports by Collins, who measured the lifetime for the near band–edge component of the spectrum as $\tau_{\mathrm{NBE}} < 10$ ns.[6] These values imply that the radiative decay of the free excitons would have to be even faster for it to occur at all.

In addition to these two intense main signals, several other signals have been reported near the band–edge energy. They have been observed between 2.4306 eV (510.10 nm) and 2.4472 eV (506.64 nm). These signals are usually much lower in intensity than the I_1 and I_2 lines and show strong temperature dependence. The lines can be intensified by application of strain to the crystal, They are named I_{I} through I_{VII} and are associated with dislocations in the crystal lattice.[90, 91] Zeeman effect measurements suggest several different kinds of complexes as possible signal origins, including both excitons bound to deep neutral defects and charged complexes. As these lines are comparatively low in intensity, especially at temperatures higher than liquid helium temperature, they are fairly hard to observe. An overview over these bands can be found in table 2.2.

In the same spectral region the I_6 and I_7 lines were observed by Reynolds & Litton. The I_6 signal showed a zero-field split into two lines.[89] Further investigations of these lines by Smeaton show a strong sample dependence of the signal strength and position, as well as a an indication that these deeper states arise from the relaxation from the I_2 state.[92] The state is assigned to a deeply bound exciton. The exact ground state and chemical identity of the impurities is still unclear.

In addition to neutral defects, there have also been reports of a signal that has to arise from the recombination of an exciton bound to an ionised defect. Thomas & Hopfield see this line – named I_3 – in absorption spectra but not in the fluorescence signal of their samples. The line is narrow and situated at a wavelength of 486.17 nm (2.5499 eV).[9] They identify the defect as an ionised donor via Zeeman measurements. Later, Reynolds & Litton observe this signal in fluorescence spectra as a zero-field doublet at 468.166 nm (2.549 84 eV) and 486.225 nm (2.549 53 eV).

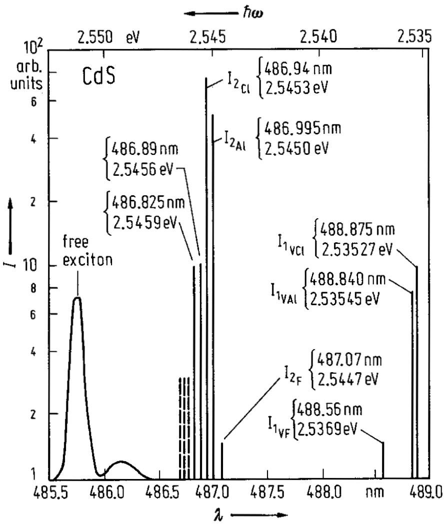

Figure 2.3: Impurity lines in the photoluminescence of bulk crystal CdS.[21]

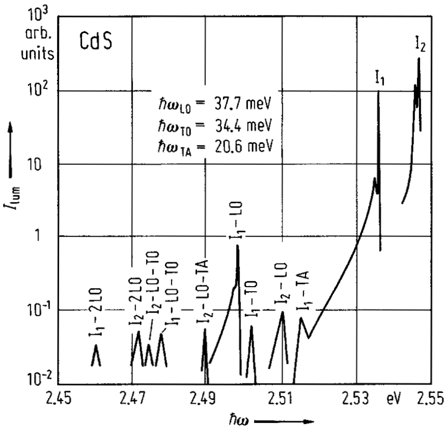

Figure 2.4: Phonon replicas of the I_1 and I_2 bands as observed by Thomas & Hopfield.[9]

Signal	E (eV)	λ (nm)
I_{I}	2.4472	506.64
I_{IIa}	2.4455	506.99
I_{IIb}	2.4452	507.05
I_{III}	2.4401	508.11
I_{IV}	2.4377	508.61
I_{V}	2.4330	509.59
I_{VI}	2.4315	509.91
I_{VII}	2.4306	510.10

Table 2.2: Lines associated with deeply bound excitons.[90] Data was collected at 1.6 K.

2.1.3 The green bands

One of the most striking features of the CdS low temperature fluorescence is a group of signals called *green emission* or *edge emission*, due to its proximity to the band edge energy. This describes usually one or two broad signals with equidistant LO phonon replicas. These signals – if observed – often dominate the emission spectrum, making the crystal seem green to the eye.[7, 89] In both, figure 2.1 and figure 2.2, the green bands are eye-catching, broad signals, starting between 510 nm to 520 nm.

Experiments by Collins in 1959 characterize the green emission fairly thoroughly, by looking at the luminescence after electron beam irradiation.[6] The results, for one, show a distinct lifetime difference between the blue near band–edge emission and the green emission, with the green emission arising from a much more stable complex. Treatment with sulphur vapour quenches the green bands in their experiment, while electron bombardment reintroduces the signal. An evident conclusion drawn from these results are sulphur vacancies as the defect responsible for these bands.

These results are supported by Randolph *et al.*, who also show that the I_1 and green emission react the same to the same treatments, suggesting the involvement of the same defects in the emission mechanisms.[88] The same is suggested by the observation by Handelman & Thomas that cadmium vapour quenches both I_1 and green luminescence. Both signals are always observed together, albeit with different relative intensities, depending on each individual sample.[87]

The exact energy of the *green emission* has also been shown to vary from crystal to crystal. Different authors report a slight shift of the zero–phonon line from sample to sample, as well as two different zero–phonon bands.[87, 93] These bands can also occur together. They are denominated X band ($\lambda \approx 514\,\mathrm{nm}$) and Y band ($\lambda \approx 518\,\mathrm{nm}$).

Maeda assigns the lower energy X band by investigating it's thermal quenching to a donor–acceptor pair, (DAP), meaning an electron and a hole, localized at defects functioning as acceptors and donors, respectively.[93] Colbow concludes from time- and temperature-dependent measurements that the higher energy X band can be assigned to the recombination of a free charge carrier with a bound one, while the lower energy Y band is due to a donor–acceptor pair recombination.[94] He proposes a model with a shallow donor and a deep acceptor and therefore assigns a bound electron and a free hole as the free–to–bound transition. This leaves the question why a bound–to–bound transition shows a very similar signal to the free–to–bound lines.

In general, the occurrence of a donor–acceptor pair signal implies for one a sufficient amount of defects, so that two localized charge carriers can compensate each other.[76] The energy and signal shape of these signals are dependent on the specific binding energy of donor and acceptor, as well as their separation. The energy of the photon emitted by the compensation can be defined as follows:

$$h\nu = E_{\mathrm{gap}} - E_{\mathrm{A}} - E_{\mathrm{D}} + \frac{q^2}{\varepsilon r}. \tag{2.2}$$

The relationship between the emission energy is dependent on the constant energy of the band gap E_{gap}, as well the energies of the donor and acceptor states, E_{A} and E_{D}, respectively. These latter two are dependent on the nature and chemical identity of the defect, as well as their environment. The variable aspect of the relation is the Coulomb interaction between donor and acceptor, which increases with decreasing radius, increasing the photon energy. With a statistic distribution of defects in the solid the number of pairs increases with increasing radius, but recombination probabilities decrease at the same time. The number of recombinations and therefore signals intensity will consequently be at a maximum for an optimum donor–acceptor distance.

In an actual crystal there will be a finite number of defect pairs with discrete donor–acceptor distances and therefore discrete values for r. For the the small-distance – 1 nm to 4 nm – pairs $h\nu$ is strongly dependent on the defect distance, while it plays a minor role for pairs with larger separations (up to 20 nm).[76] This yields a distribution of donor–acceptor lines that are discrete for the high-energy side of the spectrum and becomes a continuum of overlapping states for the large distance, low energy recombinations.

For CdS the broad bands of the green signal that are so often observed derive from these overlapping narrow lines from high-distance pairs. There are also observations of the small-distance pair lines. Figure 2.5 shows the many high-energy CdS donor–acceptor pair lines and how the lines overlap into a broad signal at lower energies.[95]. The donor-acceptor signals have been marked with vertical lines. The lines overlay the larger bands of the I_1 line and its phonon replicas, as well as the excitation laser line and the LO phonon RAMAN signals.

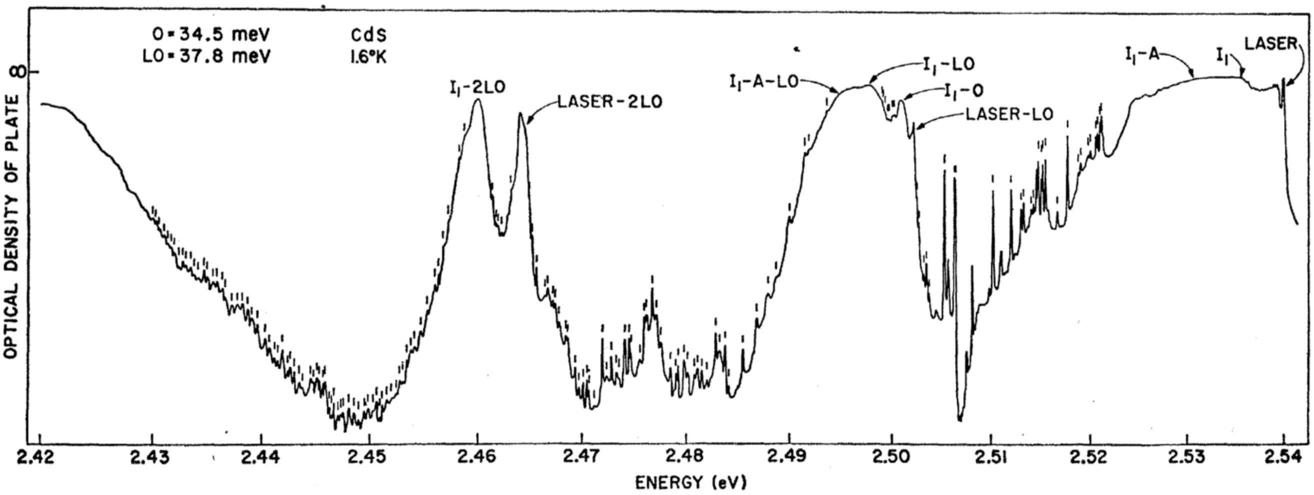

Figure 2.5: Donor–acceptor pair-lines in the spectrum of undoped wurtzite CdS. The narrow pair-lines are marked with vertical lines. On the low-energy side of the spectrum the lines become closer in energy and merge to form the typically observed broad green emission band.[95]

These results are heavily dependent on the experimental conditions. The lines only become visible at liquid helium temperature (1.6 K) and are much more intense when the crystal is excited with low intensity light with a wavelength below the band gap energy (e.g. 488.0 nm). High intensity excitations saturate the donor–acceptor pair transitions and the short-wavelength side of the spectrum is hence dominated by the I_1 line and its phonon replicas. Also, the free–to–bound transition – the X band – becomes more intense. This explains the dominance of the broad green band and its phonon replicas in most luminescence studies.

A later study by BROSER *et al.* shows through excitation spectroscopy, that the Y band is in fact caused by the compensation of ionised donor–acceptor pairs.[96] In 1985 they follow this work up with low-intensity excitation spectroscopy and luminescence measurements of the X and Y band, showing differing excitation mechanisms. From that they support the conclusion, that the X band that they observe is in fact due to a free–to–bound transition.[97] Even though, this work does not explain the fact that the X line is still visible at low excitation intensities – before saturation of the donor–acceptor pair line – and its remarkable width in comparison to a donor–acceptor pair-line.[95]

Most publications usually assign one zero–phonon line and identify it as a donor–acceptor pair compensation. An exact spectral assignment is also often not possible, due to the above-mentioned variation from crystal to crystal. Furthermore, the introduction of different dopants and their influence on the wavelength of the zero–phonon line complicate the exact identification of the origin of the signal without using additional methods to luminescence spectroscopy.

The doping experiments by Henry *et al.* show a direct relationship between green band strength and width, and the doping concentrations.[85] The green edge emission is visible in all their samples, including the undoped ones, but dramatically increases in strength with the introduction of dopants. The I_2 band – a strong signal in the PL spectra of undoped samples – decreases in relative and absolute intensity. The I_1 band increases relative to the I_2 band but also decreases in relation to the green emission. The change in the spectra with increasing doping concentration can be seen in figure 2.6. The spectra show the luminescence of samples that are – from bottom to top – undoped, doped with potassium, doped with lithium and doped with sodium. Arguments of ion solubility, based on the covalent radii of the metals and of cadmium, suggest that sodium should be incorporated the best into the crystal, followed by lithium and – by a margin – potassium. Therefore the doping concentration can be said to increase from the bottom spectrum to the top spectrum. This is also suggested by the increasing line width.

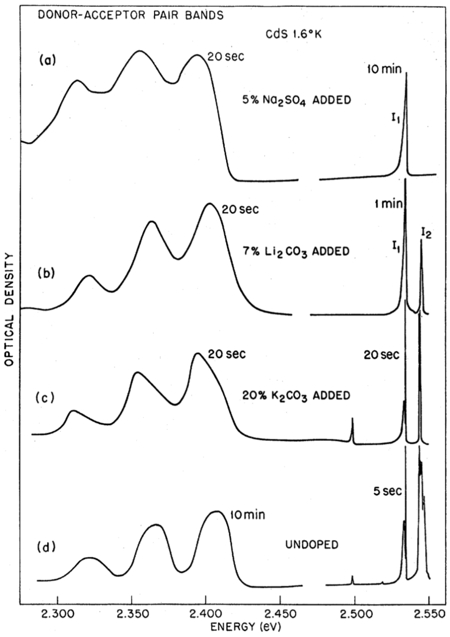

Figure 2.6: CdS samples pure and doped with different alkali metals. Due to better dopant solubility, the dopant concentration increases from the bottom spectrum to the top spectrum.[85]

The dopant concentration effect is explained by Henry *et al.* as stemming from the neutralization of ionised defects by the excitation light. This would favour the forming of bound excitons instead of localized single charge carriers. The complete neutralization is only possible up to a certain concentration of dopants, after which the localized charge carriers can also recombine.

The possible defects introduced by the alkali metals as proposed by Henry *et al.* is shown in figure 2.7. The alkali metals can act as both donors and acceptors, depending on how they are incorporated into the crystal. If the dopant replaces a cadmium atom it acts as an acceptor, if it is an interstitial, it acts as a donor. As sulphur is a group 16 element and cadmium a group 12 transition metal a native defect will compensate two alkali metal dopants. A native double donor would be able to trap two holes and could form two donor–acceptor pairs with two lithium acceptors (fig. 2.7a). Henry *et al.* also propose a complex of a native double donor with one alkali metal to form a single donor. This complex can be compensated with another single acceptor (fig. 2.7c). Lastly, an alkali metal acceptor can compensate an alkali metal donor (fig. 2.7b). The study also argues that the compensation by interstitial alkali metals is the most likely, as the authors were able to show the drifting of interstitial lithium in the lithium doped samples.

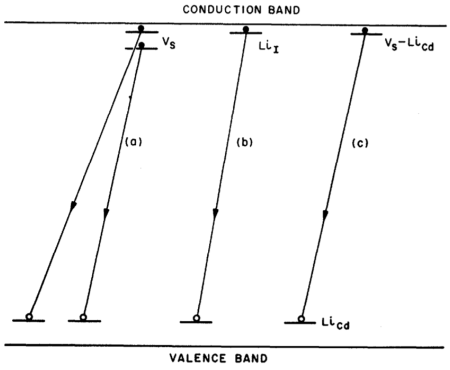

Figure 2.7: Possible recombination paths as proposed by Henry *et al.*. Lithium can act as both an acceptor (substituting cadmium), or – as an interstitial – as a donor; a) two Li acceptors can compensate a native double donor (S vacancy or Cd interstitial); b) one Li acceptor can be compensated by an interstitial Li donor; c) a complex of native double donor with a Li acceptor. [85]

The zero–phonon line, like the I_1 line, does appear at different energies for different dopants. The lines as reported by Henry *et al.* for lithium, sodium, and phosphorus are $\lambda^{\mathrm{Li}}_{\mathrm{DAP}} = 517.0\,\mathrm{nm}$ ($E^{\mathrm{Li}}_{\mathrm{DAP}} = 2.398\,\mathrm{eV}$), $\lambda^{\mathrm{Na}}_{\mathrm{DAP}} = 518.3\,\mathrm{nm}$ ($E^{\mathrm{Na}}_{\mathrm{DAP}} = 2.392\,\mathrm{eV}$) and $\lambda^{\mathrm{P}}_{\mathrm{DAP}} = 508.0\,\mathrm{nm}$ ($E^{\mathrm{P}}_{\mathrm{DAP}} = 2.441\,\mathrm{eV}$).[85]

The effect of selective doping on the photoluminescence , especially the green bands, of CdS has been shown by several other authors with different dopants. Shiraki *et al.* show the effect of the introduction lithium ions, nitrogen ions, phosphorus ions as well as neon ions into highly conductive, pure CdS samples. All of these impurities contribute to the formation of donor–acceptor pairs with the zero–phonon lines in the range of earlier reported signals (508 nm to 519 nm). [98] The phosphorus and lithium signal are in good agreement with the results by Henry *et al.*

2.1.4 *Deep bands*

In addition to the blue and green signals, in some cadmium sulphide samples several broad long wavelength bands can also be observed. In contrast to the signals discussed above, these bands, if present, are visible at room temperature. In fact, sometimes an orange, red or infrared (IR) band can be the only observed signal, like in the Dec. 1949 by FRERICHS. He measures the room temperature photoluminescence as a red signal situated in the range of 1.42 eV to 1.85 eV.[99]

The electron bombardment experiments by KULP & KELLEY show that the red luminescence they observe – in this case the experiments were conducted at liquid nitrogen temperature – can be intensified or even induced by sulphur displacement. This holds also true for the green fluorescence, both signals were also observed in the same crystal. KULP & KELLEY assign the red signal ($\lambda = 720.0\,\mathrm{nm}$, $E = 1.722\,\mathrm{eV}$) to sulphur vacancies.[7, 100] Additional experiments by KULP associate an orange band at 605.0 nm (2.049 eV) with cadmium interstitials.[101] HALSTED *et al.* report a second deep band seen in pure crystals at 1.40 eV (886 nm). They also review several studies on the luminescence of CdS samples doped with silver, gold and copper, which show broad bands at different points in the infrared to orange spectral range.[102] A band reported as related to a copper impurity is also reported by BRYANT & COX at 730 nm to 780 nm (1.7 eV to 1.6 eV).[100]

ERMOLOVICH *et al.* have conducted further experiments to characterise and find the origin of the deep bands. They find three groups of orange signals which show different changes in half-widths. All red and infrared bands show consistent behaviours.[103]

While the chemical identification of the involved defects can not be resolved by their study, ERMOLOVICH *et al.* contribute the general mechanism of recombination. The comparably large band with is most likely caused by an electron–phonon interaction during recombination. Other mechanisms can be excluded due to the asymmetry and T dependent behaviour of the band shape. All bands interact with different phonons. ERMOLOVICH *et al.* also exclude the a broad distribution of states in the band gap as a reason for the broad shape of the deep state signals, which is in contrast to the donor-acceptor pair luminescence.

While the studies above usually assume relatively simple defects RAMSDEN & GRÄTZEL show that, at least for sols that were synthesised by wet chemistry, some defects can compensate each other in a way that quenches luminescence.[104] The red luminescence of nominally undoped samples can be quenched by addition of relatively small amounts of methyl viologen, a strong acceptor. In the same way, copper-doped samples only showed the copper-associated red bands after treatment with oxygen. This was assumed by the authors to countervail the compensation by the chloride ions that were also introduced in the doping process. Wet chemical systems, especially those with high surface areas thus might show some effects that are not necessarily observed in very clean single crystals.

In general, the deep band fluorescence of cadmium sulphide is much less well investigated than the near band–edge signals and the green emission, maybe because of the large width of the bands that complicate statements about exact impurity energies.

All aforementioned unique signals are collected in tables 2.3 to 2.6.

2.2 *The luminescence of cadmium selenide*

Cadmium sulphide and cadmium selenide have many similar properties, as summarised in chapter 1.1. Nonetheless, the different chemical

Signal	Origin	Energy (eV)	Wavelength (λ)	$\Delta E(X_\mathrm{A})$ (eV)	$\Delta E(X_\mathrm{B})$ (eV)	T (K)	Comments	Source
Free excitons								
X_A	exciton vb A	2.546	487.0		0.017	0	calculated from pr spectroscopy data	[25]
X_B	exciton vb B	2.563	483.7	−0.017				[25]
X_A	exciton vb A	2.5537 (2.5540)	485.45		0.0149	1.6	calculated from pr spectroscopy data	[8]
X_B	exciton vb B	2.5686 (2.5689)	482.64	−0.0149				[8]

Table 2.3: The reported luminescence signals of CdS excitons . The values for $\Delta E(X_\mathrm{A})$ and $\Delta E(X_\mathrm{B})$ are always in relation to the exciton energies as measured in the respective experiments. Additional values in brackets have been recalculated from the measured values with current, full length constants. If the data was determined in the same study under the same conditions, the conditions and comments are not repeated for lines listed directly below. The list is continued for bound excitons in table 2.4.

Signal	Origin	Energy (eV)	Wavelength (λ)	$\Delta E(X_\mathrm{A})$ (eV)	$\Delta E(X_\mathrm{B})$ (eV)	T (K)	Comments	Source
Bound excitons								
I_1	A_0X_A complex	2.535 95 (2.5362)	488.85	0.0177		1.6	emission and absorption	[8, 9]
I_1^Li	$A_0^\mathrm{Li}X_\mathrm{A}$ complex	2.5362 2.5364	488.853 488.820	0.0178 0.0176		1.6	emission, doublet	[10, 85]
I_1^Na	$A_0^\mathrm{Na}X_\mathrm{A}$ complex	2.536 40	488.820	0.017 50		1.6	emission	[10, 85]
I_1^P	$A_0^\mathrm{P}X_\mathrm{A}$ complex	2.540 99	487.936	0.012 90		1.6		[85]
I_1^P	$A_0^\mathrm{P}X_\mathrm{A}$ complex	2.540 24	488.080	0.013 65		1.6		[85]
$I_{1\mathrm{B}}$	A_0X_B complex active for $E \parallel c$	2.548 87 (2.5492)	486.37		0.0198	1.6	emission and absorption	[9]
$I_{1\mathrm{B}}$	A_0X_B complex active for $E \perp c$	2.549 14			0.0196			[9]
$I_{1\mathrm{B}'}$	A_0X_B complex	2.5504 (2.5507)	486.08		0.0196			[9]
I_2	D_0X_A complex	2.5471 (2.547 37)	486.717	0.0183				[8, 9]
$I_{2\mathrm{B}}$	D_0X_B complex	2.5626 (2.5629)	483.77		0.0060			[9]
I_6	deeply bound exciton	2.445 45, 2.445 76 (2.445 84, 2.446 15)	506.918, 506.854	0.1082 0.1079		1.6	emission, doublet	[89]
I_7	unclear	2.5471 (2.437 93)	508.481	0.1161			emission	[89]

Table 2.4: The reported luminescence signals of CdS bound excitons signals. The values for $\Delta E(X_\mathrm{A})$ and $\Delta E(X_\mathrm{B})$ are always in relation to the exciton energies as measured in the respective experiments and the values measured by Hopfield & Thomas[8] if the exciton band was not measured. Additional values in brackets have been recalculated from the measured values with current, full length constants. If the data was determined in the same study under the same conditions, the conditions and comments are not repeated for lines listed directly below. The list is continued for free–to–bound and donor–acceptor pair emissions in table 2.5.

Signal	Origin	Energy (eV)	Wavelength (λ)	$\Delta E(X_\mathrm{A})$ (eV)	$\Delta E(X_\mathrm{B})$ (eV)	T (K)	Comments	Source
Green emission								
X	free–to–bound emission	2.415	513.3	0.139		22	emission, LO phonon replicas	[93]
		2.417	513.0	0.137		4.2		[94]
Y	donor–acceptor pair-emission D^+A^-	2.395	517.6	0.159		22	emission, LO phonon replicas	[93]
		2.396	517.5	0.158		4.2		[94]
	DAP$_\mathrm{Li}$	2.398	517.0	0.156		1.6	emission, LO phonon replicas	[85]
	DAP$_\mathrm{Na}$	2.392	518.3	0.162				[85]
	DAP$_\mathrm{P}$	2.441	508.0	0.113				[85]

Table 2.5: The reported luminescence signals of CdS green luminescence signals. The values for $\Delta E(X_\mathrm{A})$ and $\Delta E(X_\mathrm{B})$ are always in relation to the exciton energies as measured in the respective experiments and the values measured by HOPFIELD & THOMAS[8] if the exciton band was not measured. Additional values in brackets have been recalculated from the measured values with current, full length constants. If the data was determined in the same study under the same conditions, the conditions and comments are not repeated for lines listed directly below. The list is continued in table 2.6 for the deep trap luminescence.

Signal	Origin	Energy (eV)	Wavelength (λ)	$\Delta E(X_\mathrm{A})$ (eV)	$\Delta E(X_\mathrm{B})$ (eV)	T (K)	Comments	Source
Broad long-wavelength bands (deep traps)								
o	deep defect orange band I	2.102	589.8	0.452		77	emission, broad band	[103]
o	orange band II	2.067	599.8	0.487				[103]
o	orange band III	2.033	609.9	0.521				[103]
o	Cd interstitial	2.049	605.0	0.505		77	emission, broad band	[101]
k	deep defect red band	1.610, to1.476	770.09, to 840.00	0.994 to 1.078		~125		[103]
k		1.676	739.76	0.878		250		[103]
k	S vacancy	1.722	720.0	0.832		~300		[7]
k	Cu interstitials	1.7 to 1.6	730 to 780	0.85 to 0.95		~300		[100]
r	deep defect IR band	1.204 to 1,192	1030 to 1040	1.350 to 1.362		~125		[103]

Table 2.6: The reported luminescence deep trap signals of CdS signals. The values for $\Delta E(X_\mathrm{A})$ and $\Delta E(X_\mathrm{B})$ are always in relation to the exciton energies as measured in the respective experiments and the values measured by HOPFIELD & THOMAS[8] if the exciton band was not measured. Additional values in brackets have been recalculated from the measured values with current, full length constants. If the data was determined in the same study under the same conditions, the conditions and comments are not repeated for lines listed directly below.

composition and slightly different crystal lattice geometries lead to some relevant differences, that strongly influence the photoluminescence spectra.

The luminescence of hexagonal cadmium selenide – like the luminescence of hexagonal cadmium sulphide – shows a variety of different signals below the energy of the exciton recombination lines. Like with cadmium sulphide, a multitude of studies, mainly from the 1960s and 1970s, have been published. An extensive review of the findings have been published by Fasoli *et al.* in 2011.[105]

According to Fasoli *et al.*, the luminescence bands can be assigned to one of three main groups. These are the near band–edge signals, signals arising from shallow states and deep state recombinations. These bands distribute over an energy range of about 0.42 eV. In comparison, the CdS luminescence is reported to occur in a range of about 1.38 eV. This is already determined by the significantly smaller band gap of CdSe, limiting the depth of defect levels.

The high energy side of the spectrum appears similar, but a lot simpler than the reported multitude of lines for the CdS luminescence. The near band–edge group includes the free excitons – exciton A and exciton B – bound excitons and other states, such as excited donor states or states that could not be assigned to a particular complex.

In regards to the exciton signal, all literature as reviewed by Fasoli *et al.* does only report an A exciton line and no exciton lines, which is different to CdS exciton visible, but not B exciton, which is different to CdS. The energy difference between the two sub-bands is reported as 28 meV in CdSe[26], which would equate to a wavelength difference of about 10 nm, which would be easily resolvable in a spectrum. No C exciton lines are reported for either material.

In hexagonal CdS the recombination of clearly identified bound excitons is associated with a multitude of signals in a fairly broad energy range of almost 100 meV. In contrast, Fasoli *et al.* only mention three bound exciton signals. This includes two very close signals of an A exciton bound to one of two different donors and, at slightly lower energies, the signal of an A exciton bound to an acceptor. These bound exciton signals are not reported to be significantly narrower than the exciton band.

In addition to these bound excitons, two donor luminescence lines are reported. While the primary study[106] does not describe the recombination mechanism in detail, it is implied that the recombination would occur between one localized electron on a donor level and free hole. these signals are significantly broader than the bound exciton lines.

Other lines in the near band–edge include a biexciton and two bands that are not assigned to any specific kind of defect and recombination mechanism.

In contrast to the CdS luminescence studies there are no phonon replicas reported for any of the near band–edge lines. Instead, phonon replicas are reported for so-called shallow states. All of these bands with replicas are assigned to donor–acceptor pair recombinations. The zero phonon lines of these signals are observed within a 75 meV range. Band with is increased, when compared to near band–edge lines.

There are also reports about bands without phonon replicas. Some of them are assigned to donor–acceptor pair recombinations, another possibility for at least one line is an acceptor state. The recombination mechanism and involved impurities are not clearly or unambiguously assigned for most lines without phonon replicas. They are located in the general region of the donor–acceptor pair zero phonon lines and at slightly lower energies.

The least well investigated and described group of signals are the deep state bands. As in cadmium sulphide these signals are comparably broad and at least one band was observed at room temperature. The band maxima were observed in a energy range spanning 150 meV. most of them are not assigned to specific impurities. Two bands are linked to silver and copper doping, respectively. The reported deep defect bands in cadmium sulphide occur in a much more narrow energy range and have only been observed as visible light to near infrared wavelengths.

The lines as reviewed by Fasoli *et al.* are reproduced in table 2.7.

Fasoli *et al.* then go on to show that the luminescence of their nanowires can be assigned to the signals found in the bulk crystal studies. The samples synthesised by two different synthesis routes show different spectra, especially in the long-wavelength regions of the emission, with one route producing nanowires with much more defined, narrow bands in the red emission. The main difference between these two vapour–phase syntheses is the use and the omission of a gold catalyst. The gold-catalysed sample also shows more obvious morphological defect through bends and loops in the wires and also shows the broader bands, especially for ensemble samples. The differences between the luminescence of the two samples is assigned to these morphological defects. The low-energy bands of both samples are assigned two donor–acceptor pairs for both types of samples, while the near band–edge emission can also be correlated to recombination of exciton–defect complexes. No deep state luminescence is reported by Fasoli *et al.*

In the study by Franz *et al.* this bulk material based model is shown to be also applicable to explain the luminescence of QNWs, when the limited dimensions of the nanowires is factored in.[75] The study shows that all bands shift to the blue when the wire radius is below the exciton Bohr radius. While the defect bands – especially the shallow state bands with phonon replicas – do shift, they also do not show a fixed energy gap to the A exciton band. They rather occur within an energy range. This behaviour can be very well explained if the defect location within the wire is taken into account. Depending on the type and charge of defect and its location either the electron or the hole will be localized at the charged site. The opposite partner charge's probability density will be either situated around this neutralised defect or, if a second, appropriately charged defect site is available the charge can be localised there. The localisation of both charge carriers at oppositely charged defects corresponds to a neutralised donor–acceptor pair and the recombination luminescence would yield a DAP band.

Depending on the distance of the defects to the wire surface and, for the DAPs, the distance between defect pairs the energy of the complex will change, independent on its chemical identity. This explains the observed wide range in shallow state band recombination energy.

Signal	Origin	Energy (eV)	Wavelength (λ)	$\Delta E(X_A)$ (eV)	$\Delta E(X_B)$ (eV)	T (K)
Near band–edge						
X_A	exciton vb A	1.823 to 1.826	680.1 to 679.0		0.025 to 0.028	2 to 77
X_B	exciton vb B	1.851	669.8	−0.025 to −0.028		
D_1X_A	exciton bound to donor	1.821 to 1.822	680.5 to 680.9		0.001 to 0.002	3 to 10
D_2X_A	exciton bound to donor	1.820	681.2	0.003		2 to 10
A_1X_A	exciton bound to acceptor	1.814	683.5	0.009		2
XX	biexciton	1.812	684.2	0.011	0.039	4.2
D_1	donor state	1.813	683.9	0.010		5
D_2	donor state	1.795	690.7	0.028		5
NA_1	not assigned	1.810	685.0	0.013		77
NA_2	not assigned for single crystal, dap for polycrystalline	1.790	690.7	0.033		4.2
Shallow states						
A	dap with phonon replicas	1.755	706.5	0.068		2
B	dap with phonon replicas	1.725	718.7	0.098		4.2
C	dap with phonon replicas	1.784	695.0	0.039		10 to 70
D	dap with phonon replicas	1.784	725.5	0.114		10 to 70
E	dap with phonon replicas	1.732	715.8	0.091		77
$F1$–$F2$	dap	1.742 to 1.700	711.7 to 729.3	0.081 to 0.123		3
$G1$–$G2$	impurities or defects	1.675 to 1.630	740.2 to 760.6	0.148 to 0.193		10 to 70
H	dap or acceptor state	1.720	720.8	0.103		77
I	not assigned (powders)	1.690	733.6	0.133		300
Deep states						
J	Ag deep states	1.50	827	0.323		77
K	Cu deep states	1.33	932.2	0.493		77
L	not assigned	1.550	799.9	0.273		10
M	not assigned	1.420	873.7	0.403		10
N	not assigned (nanowire sample)	1.400	885.6	0.423		300

Table 2.7: Overview of CdSe bulk luminescence signals as reported in a number of studies. The data was compiled by Fasoli *et al.*[105] The near band–edge and shallow state luminescence is also observed for nanowires.

3

Methods

3.1 Confocal microscopy

The analysis of the interaction of light with matter can be used to probe different fundamental properties, for example through luminescence spectroscopy. Using microscopy these analyses can be performed in combination with imaging and spatially resolved measurements.

Most importantly, microscopy is primarily a method that can be used to record magnified images of microscopic structures, using lenses for magnification. This magnification, or rather the achievable resolution of small objects is limited by the resolution limit as formulated by ABBE.[107, 108] He found that the minimum distance s that two objects have that can still be resolved in a light microscopy image is dependent on the illumination light wavelength. Any objects that were located closer together would appear as one object. This dependence is shown equation 3.1.

$$s = \frac{\lambda}{n \sin \alpha} = \frac{\lambda}{NA} \tag{3.1}$$

In addition to the wavelength the equation factors in the use of a lens, which focusses the light into a cone with an opening angle $2 \cdot \alpha$, and the refractive index n of the medium between the lens and the sample. The angle α can in principle take on values between 0° to 90°. This product of refractive index and sine of half the opening angle is a characteristic number of the objective, the numerical aperture. For air objectives this number will be larger than 0 and smaller than 1.

The relationship shown in equation 3.1 describes the most simple case in which light is focussed with one lens. Additional optics – such as a condenser lens – can further improve the resolution to at most half the illumination wavelength λ, as can the use of a different medium between object and lens, such as with an oil immersion objective.[107]

For very small objects, especially in complex matrices, like in biological samples, another factor that complicates the imaging is the scattering of light from surrounding structures. This problem lead MINSKY to design a microscopy setup that blocks most of the scattered light from being detected.[109] MINSKY invented the confocal microscope in 1966 and patented it in 1961.[110] The fundamental principle behind the microscope is that the light is collected confocally from the sample, focussed through a pinhole to block the scattered light from any point outside of the focal point on the sample. The setup designed by MINSKY for his patent is shown in figure 3.1. In the patent the microscope is described as follows: A light source (10) is collected and focused by a parabolic mirror (12) through a pinhole (16) in a screen (14). The light is than focused by a lens (18) into a small, confocal spot that illuminates a small spot of a sample (22). The light from this spot is collected by a second lens

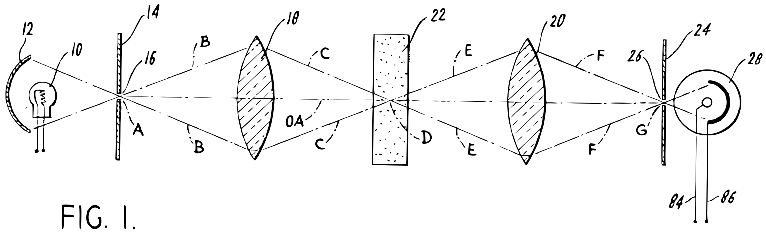

FIG. 1.

Figure 3.1: The setup of the confocal microscope from the original patent from 1961.[110]

(20) and focussed through a pinhole (26) in a second screen (14) onto a detector (28).

In this kind of setup the pinhole blocks most of the light that does not come from the focal point, with both a lateral and an axial resolution. A smaller pinhole will suppress more of the scattered light but also reduce the signal intensity. The resolution of such a microscope can be best approached with the radius r_{Airy} of the Airy disk of the focal spot:[111]

$$r_{\mathrm{Airy}} = 0.61 \frac{\lambda}{NA} \tag{3.2}$$

Any two points that are located a a distance equal larger than r_{Airy} can be resolved as two separate objects. This so-called Rayleigh criterion assumes that the two points radiate incoherently but is also generally correct for coherent confocal microscopy.[111] For confocal luminescence microscopy the light wavelength is that of the luminescence excitation light. For the axial resolution of a microscope the minimum distance z_{min} by which a microscope objective (or the position of a sample) has to be moved in axial direction to resolve two objects that are located along that axis is defined as follows:[111]

$$z_{\mathrm{min}} = \frac{2\lambda\eta}{NA^2} \tag{3.3}$$

The axial resolution is, in addition to the imaging light wavelength and the objective numerical aperture dependent on the sample refractive index η.

The main difference to a widefield microscope is that the illumination beam is focussed confocally onto the sample – this means that the light is detected only from a spot, whose size is limited by the light diffraction. Accordingly, the detected light does not contain no spatial information. To regain spatial information the sample or the beam can be through the beam or over the sample surface, respectively. For this any kind of scanner which can position sample or optics with sufficient precision and reproducibility can be used, such as a slip-stick piezo sample scanner or a galvanometric mirror scanner.

Depending on the application the microscope optics can be optimized for maximum resolution. In room temperature systems and with transparent samples the use of oil immersion objectives can yield the highest spatial resolution, reflective illumination schemes and vacuum and low temperature setups are limited to air objectives with working distances and NA influenced by the sample and conditions.

For illumination light sources, for luminescence and Raman measurements brilliant, monochromatic sources are preferable. Laser sources offer these qualities, as well as coherent, polarized light that whose properties can be easily controlled with the right optical parts. While all laser sources use the principle of stimulated emission to produce laser light, different laser media can be used as light sources with different properties, such as emission power, spectral with, tunability, continuous wave (cw) or pulsed operation. The choice of laser depends on the sample and method. Lasers are usually the light source used in confocal microscopy – or confocal laser scanning microscopy (clsm).

For detection, confocal imaging benefits from highly sensitive single photon detectors. For selection of specific spectral regions long pass and short pass filters can be used in front of an avalanche photo diode (APD) to measure intensity scan images with high efficiency. APDs also have the advantage that their chips are usually quite small (often below 100 µm in width) and can therefore function as the detection side pinhole. For spectral analysis instead of onto a point detector the beam can instead be focussed through the entry slit of a spectrometer and spectra at single image points can be taken with a charge-coupled device (CCD) camera.

In addition to the diffraction-limited measurement of elastically and inelastically scattered light confocal microscopy can also be used as the base for the super-resolution method stimulated emission depletion (STED) microscopy. In addition to the excitation laser a second, lower energy light is simultaneously coupled into the objective, but not as a Gauss mode but a circular doughnut-shape mode. In a sample that is marked with a suitable dye the circular laser mode can deplete the outside excited molecules while only a small inner spot remains, which is much smaller than the diffraction-limited excitation spot. This method was one of the optical super-resolution methods that were awarded the Nobel prize in chemistry in 2014.[112]

3.2 *Non-optical microscopy*

The above described resolution limitation of optical microscopes strongly limits the characterisation of structures smaller than half the light wavelength. This includes all nanostructures, such as nanocrystals and nanowires, which usually possess at least one dimension which extends much less than 100 nm.

Alternative methods that can be used to determine nanostructure size and surface topology are different methods of non-optical microscopy. These methods either employ the much smaller wavelength of electron radiation to increase the achievable spatial resolution or they use nanoscopic probes. The different methods are suited for different types of samples.

3.2.1 *Electron microscopy*

Like photons, other particles also posses both properties of particles and waves. The particle wavelength λ was postulated by de Broglie to depend only on the particle impulse $p = m$ in relation to the Planck constant h.[108] This is shown in the first part of equation 3.4.

$$\lambda = \frac{h}{p} = \frac{h}{\sqrt{2meU}} \tag{3.4}$$

Any charged particle can be accelerated in an electrical field, by an acceleration voltage U. The impulse of such a charged particle therefore depends on its mass m, its charge e and this acceleration voltage, as shown in the second part of equation 3.4. This equation is true for acceleration voltages up to 10 kV for electrons, as it does not take into account the relativistic effects at higher velocities. For electrons at an acceleration voltage of 1000 V the de Broglie wavelength is $\lambda = 0.039$ nm, which is a fraction of a chemical bond length. Considering the above-shown relationship between illumination radiation wavelength and the spatial resolution a microscope using electrons should easily be able to resolve single atoms. This principle was used in 1932 by Knoll & Ruska for the construction of the first electron microscope.[113]

In practice, this theoretical resolution cannot be reached with electron microscopes, as electron optics are not quite as efficient as optics used for visible light are. The electron beam is focused using magnetic lenses and these objectives cannot reach the same NA as optical components can. That said, electron microscopy has a significantly higher resolution than optical microscopy and can resolve single atoms in solids.[108]

In electron microscopy different methods are available which can be used depending on the sample. The two main methods are the transmission electron microscope (TEM) for samples that are to a certain degree transparent for the electron beam and scanning electron microscope (SEM) for samples that cannot be prepared on transparent substrate or systems that are too thick.

The TEM was the first electron microscope that could be realised. The general setup contains an electron source from which electrons are accelerated. The electron beam is adjusted and focused with magnetic lenses and apertures. The beam passes through the sample which is prepared on very thin membranes or films that consist of light atoms to minimize electron absorption and scattering. The electron beam that passes though the sample is then projected onto a luminescent screen and an image of the sample can be recorded through the detection of the light. While in a TEM image there are many aspects contributing to the image contrast, generally materials with high electron density will absorb or scatter more electrons and therefore appear darker in the image. Sufficiently high acceleration voltages and high performance lenses can make crystal structures and single ion species in the crystal visible.[108]

As the TEM is only suitable for very thin samples the nanoscale analysis of the surface of larger structures has to be performed by analysing backscattered electrons, as is done in the SEM. This kind of electron microscope was first reported in 1938 by von ARDENNE.[114] While in a TEM a widefield image of the sample is recorded, in the SEM the electron beam is focussed to a small point and then rastered over the sample. The electron probe can easily be 1 nm in diameter. To obtain an image the beam is rastered over the sample using deflecting coils. Both backscattered electrons and secondary electrons from the sample are detected by a detector located above the sample. This method enables the analysis of much thicker object than a transmission beam path and also the imaging of three dimensional objects. That said, the method is limited in spatial resolution due to diffusion effects and sample charging can also lead to artefacts in the images.[108]

3.2.2 *Atomic force microscopy*

While electron microscopy can easily solve the problem of resolution limitation present in optical methods, electron radiation is much harsher on delicate samples than even visible light. For any sample for which the electron radiation damage would impede the desired properties other methods, such as scanning probe microscopy, have to be considered. The most commonly used scanning probe method is atomic force microscope (AFM), which can be used for the surface characterisation of a broad array of samples under different conditions, without causing any damage or chemical changes to the sample.

AFM and all related scanning probe methods are relatively young, even in comparison to electron microscopy. The first scanning probe microscope, the scanning tunnelling microscope (STM), used a sharp tip hovering over a sample to characterize it, measuring the tunnelling current between sample and tip. The STM was first realised by BINNIG & ROHRER at IBM.[115] Derived from this, BINNIG *et al.* developed the AFM, which combined the nanoscopic tip probe with the measurement principle of a profilometer, tracing the height of the sample.[116]

An example for a general setup of an AFM is shown in figure 3.2. A metal tip at the top of a metal cantilever is fixed to a x, y, z–positioner. This positioner can scan the tip over the sample and adjust its height to the sample topography. Instead of a tip scanning setup there is also the option to place the sample on a similar positioner, which would be a sample scanning AFM. As the tip rasters the sample, the tip reaction to changes in topography is measured by shining a laser light onto the tip which is then detected by a quadrant diode. A displacement of the cantilever is mirrored by a change in diode signal. The tip – or the sample – can then be moved until the diode signal is returned to its initial value. While this scheme is the most common one, there is also an alternative for applications in which the setup geometry or requirements do not easily allow for the use of a deflection laser. In this case the AFM tip can be attached to one arm of a tuning fork and the changes in tuning fork vibration can be monitored.[117]

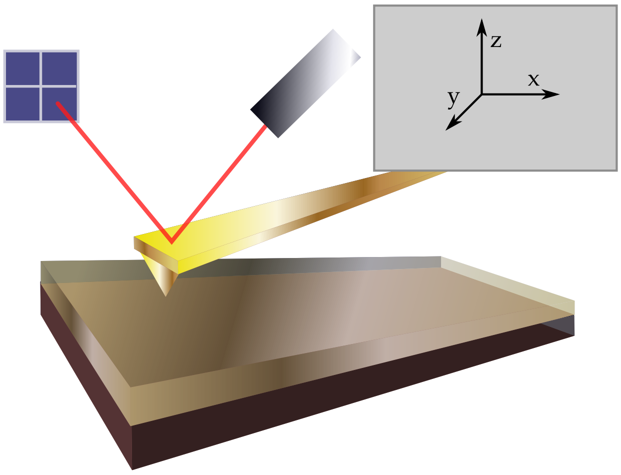

Figure 3.2: Schematic of a tip scanning AFM. A very sharp tip at the end of a cantilever is rastered over a sample. The displacement of the cantilever in the z direction by changes in sample topography can be measured by the movement of a laser reflected from the tip onto a quadrant detection diode.

Independent of the AFM setup and detection mode, the method always works by analysing the effect of the mechanical interaction between sample and tip by examining the cantilever movement. Fundamentally, the tip–sample interaction is contained in the Lennard–Jones potential, which is expressed in equation 3.5.

$$V = 4\varepsilon \left\{ \left(\frac{r_0}{r}\right)^{12} - \left(\frac{r_0}{r}\right)^{6} \right\} \tag{3.5}$$

The potential V acting on the AFM tip is depending on the distance r to the tip. The two distance-dependent terms are the attractive force – which includes Van–der–Waals forces and attractive interactions between dipoles – and the repulsive force, which is becomes active at closer distances and originates due to Pauli principle. The empirical value ε is the depth of the potential well and therefore the lowest potential energy the tip can reach. The force F affecting the AFM is the derivative of the potential, as shown in equation 3.6

$$F = \frac{\mathrm{d}V}{\mathrm{d}r} = \frac{24\varepsilon}{r_0} \left\{ 2\left(\frac{r_0}{r}\right)^{13} - \left(\frac{r_0}{r}\right)^{7} \right\} \tag{3.6}$$

This force is related to the z movement of the cantilever. The relationship is shown in figure 3.7.

$$F = C\Delta z \tag{3.7}$$

In this equation C is the cantilever spring constant and Δz is the change in tip z position.[2]

The AFM can now be operated with the tip being in different regimes of this potential curve. In non-contact mode the tip is placed at a distance from the sample at which the attractive forces dominate. The tip is moved over the sample and depending on changes in sample topography the magnitude of the attractive force changes, as does the tip z positions, which makes it possible to characterise the sample geometry by measuring that z position. In comparison, in contact mode, the tip is placed onto the sample surface and is kept in the repulsive force regime. Changes in sample topography will change the repulsive force affecting the cantilever and therefore also its z position. Finally, in intermittent-contact mode the cantilever is vibrated near one of its resonance frequencies, touching the sample at the lowest point of the vibration. Changes in sample topography will influence the tip vibration amplitude and phase and the necessary adjustment in z height necessary to return to the initial amplitude includes the information about the change in sample topography. This method also includes information about the sample mechanical properties in the change in the vibration phase.

3.3 *Wet-chemical synthesis of nanowires*

The synthesis of nanowires requires good control over the crystal growth conditions, to create the strongly anisotropic systems. These kind of syntheses are often performed using methods that require complex and costly setups and harsh reaction parameters, such as the chemical vapour deposition. Here a catalyst particle is molten one or multiple precursor substances are dissolved from the vapour state into the liquid particle. This solution saturates and a crystal forms, growing from the liquid. Anisotropy of the crystal plane energies leads to anisotropic crystal growth and the growth of whiskers or wire, whose size depends on the catalyst particle size. These reactions require temperatures of often several 100 degrees and evacuated reaction chambers.[118]

This mechanism of a solid growing from a liquid with precursors diffusing in from a vapour – the vapour–liquid–solid (VLS) mechanism[118] – could be transferred into a synthesis scheme that can be realized with standard wet chemical setups and reaction parameters. In the solution–liquid–solid (SLS) mechanism – as shown in figure 3.3 – the catalyst particle, usually a metal nanoparticle is suspended in a high boiling point solvent. The solvent is heated until the particles are liquefied. The solvent is usually chosen to also act as a coordinating solvent that will stabilise the nanocrystal surface. Then precursor substances are added, which are dissolved in the liquid metal until saturation and crystal formation. As with the VLS mechanism the anisotropy of the crystal growth will cause a growth in wire form.[119] In the SLS mechanism as well the wire diameter depends on the catalyst diameter. As precursors the use of multiple organometallic substances has been established, but the use of single-source clusters can lead to slightly different nanowire properties and slightly smaller diameters.[77]

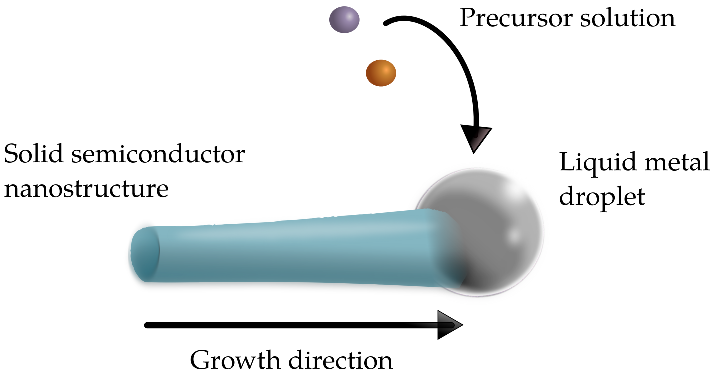

Figure 3.3: Schematic depiction of the Solution–Liquid–Solid mechanism as proposed by Trentler et al.[119]

In contrast to the SLS based syntheses it is also possible to synthesise some nanowires via a solvothermal route.[120] In this synthesis route ethylenediamine functions as a coordinating solvent which directs the crystal growth into the anisotropic direction. The reaction is performed at temperatures and pressures over the solvent critical point. The diameter and aspect ratio of the nanocrystals that are synthesised with this method depend on the used precursor and additives. No catalyst and no additional long chain ligand is used.

4

Experimental setup and procedures

4.1 The confocal setup

For the confocal measurements shown in this work a home-build low temperature microscopy setup was used. The setup was build by Dennis Franz within the scope of his PhD thesis[19] and modified to perform the desired experiments. It consists of a comprehensive illumination setup that can be used in its standard configuration to generate laser light from 350 nm to 1000 nm wavelength. The beam is then optimised, the sample illuminated and the luminescence signal isolated and detected. Both parts of the setup are described in the following section.

4.1.1 The illumination beam generation

The illumination light generation was done by using one or a combination of several lasers on one optical table, which was vibrationally coupled to a second, perpendicular table, on which the sample illumination and signal detection part of the setup was placed. A schematic of the top-view of the beam generation part of the setup is shown in figure 4.1 and the important parts of the setup are numbered.

Heart of the illumination part of the setup is a diode-pumped solid state (dpss) laser, a Coherent Verdi V10 (1). The laser uses two diode lasers to pump a crystal of neodymium-doped ytterbium vanadate to emit at 1064 nm. A non-linear optical crystal is used to double the laser light frequency and light with a wavelength of 532 nm is emitted from the device. This laser can be operated with emission powers from 0.01 W to 10 W. The lowest power can be used to directly illuminate the sample with cw laser light, while powers of 8 W to 10 W were used to pump the Ti-sapphire laser (2). If the light from the dpss laser was used directly, it was spectrally optimised with a laser line filter (ll532) to remove any remaining pump light and not frequency-doubled emission.

If the dpss laser is used as a pump laser the light is directly coupled into a Ti-sapphire laser, a Coherent Mira 900-F. In this laser the lasing medium is a Titanium-doped sapphire crystal which emits a broad emission between 700 nm to 1000 nm emission wavelength. The desired emission wavelength can be selected though wavelength-dependent polarising optics in combination with a polariser following afterwards. For time-resolved measurements the cw light can be converted into short laser pulses with a pulse width of 130 fs by introducing a vibrating glass plate into the beam path, which produces light pulses through intensity fluctuation. The remaining cw laser light can be blocked by a slit at the end of the resonator, as the refractive index of the lasing medium itself is dependent on the light's intensity and will therefore refract the momentarily intense pulses differently then the cw light. The pulse repetition

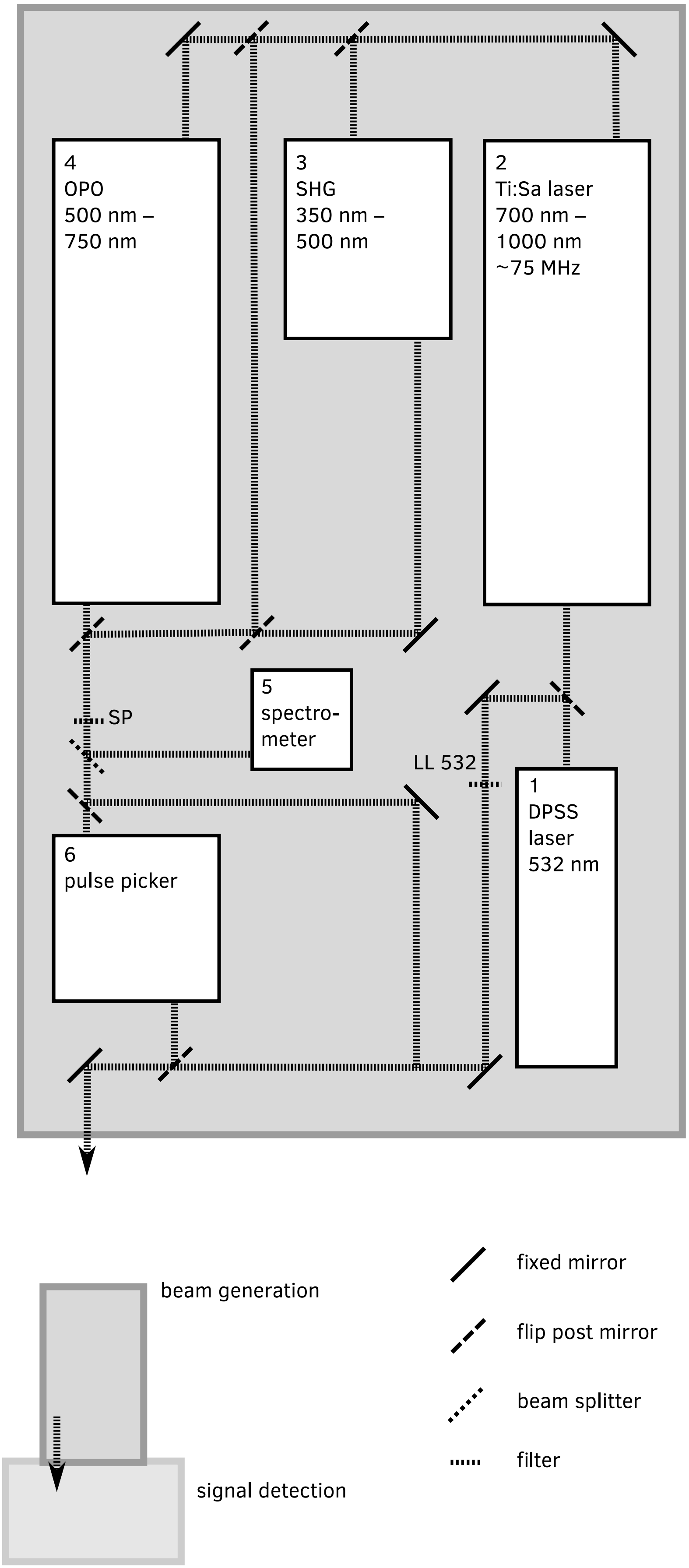

Figure 4.1: The illumination light generation part of the used home build confocal setup. (1) A DPSS laser emit CW light at 532 nm, either for direct sample illumination or to pump the Ti-sapphire laser (2) which can in turn emit light in low energy visible to near-IR range, 700 nm to 1000 nm. The light from the Ti-sapphire laser can again be used directly or after frequency doubling by an second harmonic generation (SHG) non-linear optical crystal to 350 nm to 700 nm. An optical parametric oscillator (OPO) (4) can be used to generate a frequency-doubled signal beam with a wavelength range from 500 nm to 750 nm. (5) A spectrometer is used to check the mode quality and emission wavelength and, if necessary a pulse picker (6) can reduce the repetition rate of the mode-locked emission.

rate of the used Ti-sapphire laser was about 75 MHz, which is equal to a time between pulses of ca. 13.3 ns.

The light from the Ti-sapphire laser can now either be used directly to illuminate the sample or, as done for the luminescence studies in this work, converted to higher frequencies. The first option for this is the APE HarmoniXX SHG (3) which uses a second harmonic generation (SHG) non-linear optical crystal for second harmonic generating, effectively halving the wavelength of the selected Ti-sapphire emission and therefore generating light with a wavelength from 350 nm to 500 nm.

The second option is to couple the emission of the Ti-sapphire laser into an optical parametric oscillator (4). The used optical parametric oscillator (OPO) is the Mira OPO by APE and Coherent. With an option of two non-linear optical crystals – pumped at either 775 nm or 830 nm – the photons of the pump beam are converted into two photons that make up the so-called signal and idler beam. The signal beam wavelength is between 1000 nm to 1600 nm, depending on the used crystal. The wavelength-dependent pulse speed in a dispersion element make it possible to use the resonator length to amplify a specific emission wavelength. The amplified signal beam can then be frequency-doubled by using a non-linear optical crystal.

The laser light from any of the three pulsed sources can subsequently be optimised by using a short pass filter (SP), with the specific filter chosen according to the specific laser light wavelength. The beam quality can further be controlled with a small spectrometer (5) and subsequently be directed onto the sample illumination and signal detection optical table. For a smaller pulse repetition rate the pulsed sources can also be coupled into a pulse picker (APE pulseSELECT) which uses the acousto-optical effect to select individual pulses with a BRAGG cell, with different division ratios, starting at $f/20$.

4.1.2 Excitation and signal detection

The light from the emission side of the setup is directed to optics on the second, vibrationally coupled optical table. The top-view schematic of the setup is shown in figure 4.2.

Firstly, in addition to the lasers on the first optical table the beam path gives the option to also use a diode laser (7). Different diode lasers heads can be placed in at the marked position and easily coupled into the existing beam-path. Also, a beam splitter in the beam path can be added to reflect part of the excitation light to a trigger diode (8) for the TCSPC system. The diode trigger signal synchronises the TCSPC electronic to the pulsed laser beam generated with the Ti-sapphire laser, the SHG system, or the OPO.

As the laser mode that are generated with the used laser do usually not exhibit a clean GAUSS function intensity profile a spatial filter – to lenses with a pinhole at their shared focal point – is used to optimise the intensity profile, as the pinhole blocks all light that is not focused to the lenses' focal point. Subsequently a $\lambda/2$ plate is used to rotate the linear polarised light. Together with a fixed polariser the fraction of transmitted light can be controlled with high precision by turning the $\lambda/2$ plate. After the polariser a $\lambda/4$ plate subsequently converts the linear polarised light to circular polarised light to avoid polarisation-dependent excitation effects. The light can then further be optimised by adequate filters – long pass, short pass and neutral density filters – depending on the specific source. After the filters a mirror in a flip mount fives access to an alternative wide-field illumination beam path.

The standard confocal beam microscopy beam path continues further on to a beam splitter, which reflects 4 % of the light onto the mirrors of a

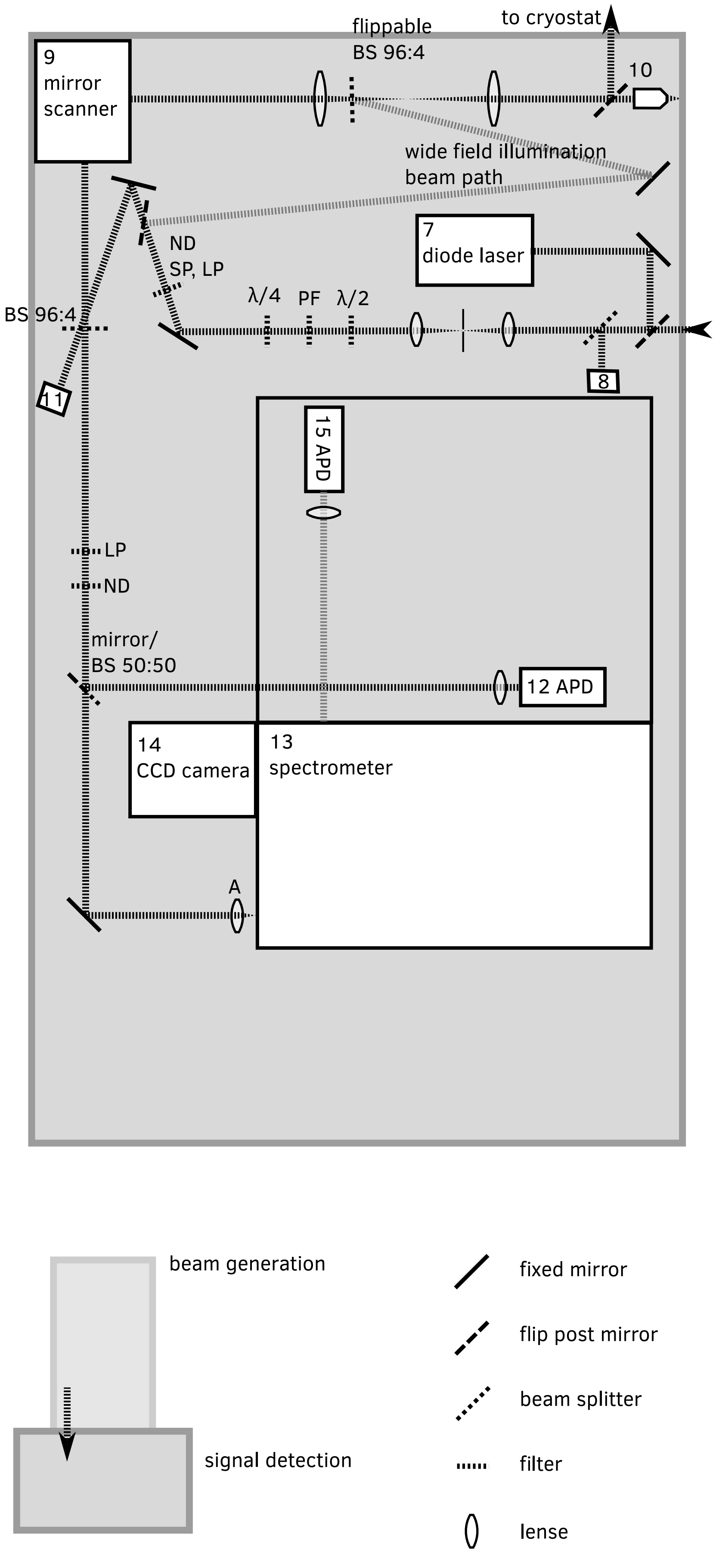

Figure 4.2: The sample illumination and signal detection part of the confocal setup. The excitation light is directed from the beam generation optical table or can be coupled in from a diode laser (7). A photo diode (8) can be used to measure the laser pulse repetition rate and puts out a trigger signal for the time correlated single photon counting (TCSPC) system. Further on, a pinhole and two lenses clean up the laser mode.The light intensity and polarisation is adjusted and the light is guided into a galvanic mirror scanner (9) which moves the light over the sample. This is possible due to a following set of telecentric lenses after which the light can (10) either be guided into an objective in front of a room temperature stage or into the cryostat. Illumination light intensity is measured with a power meter sensor (11). The reflected elastically scattered light or luminescence signals is either attenuated in intensity or filtered spectrally and subsequently detected. This can be done either with (12) an APD or, through a spectrometer and afterwards – spectrally resolved – with (14) a CCD or (15) a second APD.

galvanic mirror scanner (9), and ARGES OEM XY-Scanmodul. The other 96 % illuminate the sensor of a power meter(11). The galvanic mirror scanner is used, in combination with a system of telecentric lenses, to raster the confocal light spot over the sample. The scanner can move the installed mirrors with a repeatability of 15 μrad. The lenses of the telecentric lens system have each a focal length of 200 nm and a diameter of 2 in. They are positioned so that the mirror scanner is in the focal point of the first lens. The second lens is positioned at two times the focal length and finally the objective, both at room temperature and in the closed-cycle cryostat, is positioned at the focal point of the second lens. This makes it possible to scan the spot over the sample with a 400 μm diameter area covered. The scanner controller is connected to an ADwin Gold II box signal processor which is used to synchronise the mirror scanner with the optical signal recorded by the detectors that are described below.

(10) The setup can be used for both measurements at room temperature and to measure samples in the closed-cycle cryostat by attocube systems AG. A magnetic mount makes it possible to install a mirror that reflects the mirror up into the cryostat chamber. In the cryostat a 100× objective (Olympus LMPLFLN 100×, $NA = 0.8$) is installed which is thermally coupled to the outside of the chamber, but vibrationally coupled to the sample low temperature stage. The sample hangs from the 4 K cold stage, directly above the objective. This possible due to the long working distance of the objective of 3.4 mm. Rough positioning of the sample within the cryostat chamber is done via stepper piezo positioners. The sample temperature is measured directly above the sample. The chamber also offers twenty electrical connectors that can be used to apply voltages and perform transport measurements with a connected sample.

If the mirror directing the light into the cryostat is removed, the light is instead directly focused with the same objective that is installed in the cryostat. It is mounted in on an x, y, z micrometer stage for rough positioning and focussing.

No matter if the illumination beam path at room temperature or in the cryostat is used, the objective used for illumination is also used to collect the reflected light and, most importantly, any luminescence. The light is directed back through the telecentric lenses, through the mirror scanner. Depending on the measurement different filters can be used to both reduce the light intensity with wavelength-independent neutral density filters, ND, or isolate any emission by cutting out the excitation laser light with a long pass filter, LP.

The light can then be detected, either its entire intensity, or spectrally resolved. For the former method it is reflected, usually by a flip mount mirror to an APD (Micron Photo Devices PDM series APD) (12). an APD is a small photodiode that has a high reverse bias voltage applied. If a photon is absorbed by the diode the generated charge carrier pairs are separated and accelerated to such high velocities that their kinetic energy is sufficient to create new charge carrier pairs and induce a charge avalanche, amplifying the current that is caused by the absorption of a single photon. Through synchronisation with the mirror scanner movements through the ADwin Gold II box the number of photon detection events can be measured for a chosen integration time at a defined number of positions of the confocal beam, creating an intensity scan image. For single point measurements the intensity can be recorded with time resolution, as the APD is connected to a PicoQuant PicoHarp 300 TCSPC system, which can record luminescence decay curves with a time bin resolution of 4 ns and also TTTR data that can tag every single reported event with a time tag and reconstruct the event information into intensity time traces.

Instead of pure intensity detection the signal can also be coupled into a spectrometer (13), an Acton SpectraPro-2558, using a 100 mm lens A. A narrow entry slit at the entrance of the spectrometer blocks any diffusely scattered light from entering the spectrometer.

The spectrometer has a focal length of 500 mm and a three-grid replaceable turret. The standard turret held a 300 l/mm grid as well as a 1200 l/mm grid, blazing wavelength 750 nm, as well as a mirror for alignment and wide-field imaging . For some spectra a turret with a mirror, a 50 l/mm grid, and a 150 l/mm grid, blazing wavelength 600 nm for both grids, was substituted. The light shining onto the grating is diffracted with the diffraction angle depending on the light wavelength, effectively mapping the light energy axis onto a spatial axis.

The spectrally fanned-out light is now detected with a detector with spatial resolution, a CCD (14). The CCD chip consists of a two-dimensional matrix of gated diodes, creating a grid of potential wells. When illuminated, charge carriers that are generated in the vicinity of a well are collected in there, for the desired frame of integration time. After the end of integration time, the charge carriers in the wells can be shifted to the edge of the chip well for well, the current generated from the charge of the pixels can be recorded and assigned to an intensity value or count value, recreating an intensity image pixel by pixel. The CCD camera used in this setup is a back-illumination deep depletion Pixis 400 CCD by Princeton Instruments with a pixel count of 1340 × 400.

Finally, the light from the spectrometer could also be coupled out to a second APD (15), instead of illuminating the CCD for wavelength-resolved point detection and time-resolved measurements. Alternatively instead of a mirror reflecting the light to the first APD (12), a 50 %:50 % beam splitter was also used, making it possible to record data with the APD and spectra at the same time. By triggering spectra acquisition with the ADwin Gold II box, these measurements could also be synchronised to the mirror scanner movement.

4.2 Experimental procedures

4.2.1 Sample preparation for confocal microscopy

Nanowires samples for confocal measurements were prepared through drop casting the nanowire solution onto substrates of highly doped silicon with a 300 nm insulating layer of SiO_2 (Max-Plack-Institut für Festkörperforschung, Stuttgart). Pre-written electrode structures were present for The substrates were cleaned in an ultrasound bath, submerging them for 5 minutes in high performance liquid chromatography (HPLC) grade acetone twice, HPLC grade isopropyl alcohol, and ultrapure water, each. The substrates were subsequently treated in an air plasma for 3 minutes.

Afterwards 5 μL of the wire solutions, which had been treated with ultrasound for a few seconds beforehand, were drop cast onto the substrates and excess liquid was removed with air flow.

For one sample, CdS bulk nanowires were prepared on 40 nm SiO_2 TEM membrane (PLANO GmbH) with a Si waver as a carrier. This membrane was treated with air plasma for 3 minutes and the nanowires were drop cast as described above.

The nanowires that were prepared and characterised within the scope of this work are summarised in table 4.1 for the CdSe nanowires and table 4.2. The wires were synthesised and kindly supplied by different people, who are also credited in the tables. If available electron micrographs or scanning probe images are shown to show the sample morphology. The syntheses types used to prepare the wires are also shown. Details on the CdSe syntheses in solutions can be found in the work by Wang *et al.*[77], the wires synthesis directly on substrates is described below, and the CdS solvothermal nanowires synthesis was originally described by Böttcher[120].

sample name	material	synthesis	TEM/AFM	synthesised by
CHSCdSe1	CdSe	SLS mol. precursor	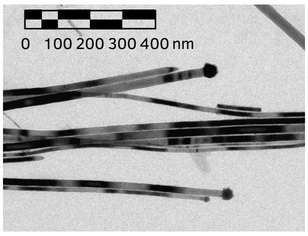	Christoph Schloen
CdSe-C	CdSe	SLS cluster	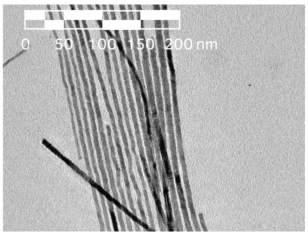	Zhe Wang
CdSe-A	CdSe	SLS cluster	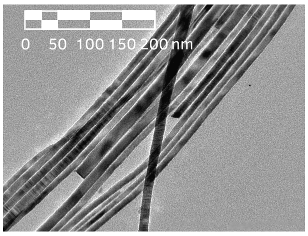	Zhe Wang
CdSe-B	CdSe	SLS cluster	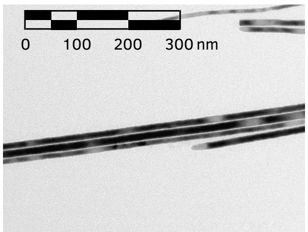	Sara Grunewald
KAT1	CdSe	SLS cluster on Si substrate	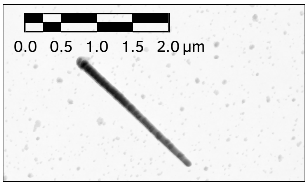	Katharina Braun

Table 4.1: List of investigated CdSe nanowire samples

4.2.2 *Single wire contacting via optical lithography*

For some samples single nanowires were contacted via optical lithography. After the nanowires had been deposited on the silicon samples their locations were mapped using optical microscopy or AFM and the prewritten electrode and marker structures. Contacts to those electrode structures were designed and then created via optical lithography.

The nanowire sample, as prepared above, were coated with ECI3012 positive resist (MicroChemicals GmbH). 15 µL of the resist were deposited and the sample was coated for 60 s, spinning at 10 000 rpm. This was followed by baking for 90 s at 90 °C. The resist was exposed using a MicroWriter ML2 laser writer by Durham Magneto Optics Ltd. After exposure the sample was baked again for 90 s at 90 °C and, after cooling, was developed for 60 s in AZ 826 MIF developer (MicroChemicals GmbH). Development was stopped by submerging the sample in ultrapure water.

After the resist mask was checked with an optical microscope 10 nm Ti and 50 nm Au were evaporated onto the substrates. Lift-off was performed by submerging the substrate in HPLC grade acetone which was

sample name	material	synthesis	SEM	synthesised by
CdS-02	CdS	solvothermal single source	—	Dino Behn
CdS-01	CdS	solvothermal single source	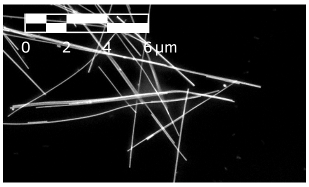	Dino Behn

Table 4.2: List of investigated CdS nanowire samples

stirred with a magnetic stirrer.

The electrode structures to which the nanowires were now electrically contacted were subsequently bonded to a chip holder, which was in turn build into a small circuit board sample holder. This holder was designed and realized by Jan Flügge and could be easily mounted onto the 4 K stage of the cryostat. Is shown in figure 4.3 The 20 contacts on the chip holder to which the sample can be bonded are electrically connected via the circuits on the sample holder to twenty wires that were equipped with plugs that fit the electrical connections that lead from the inside of the cryostat to the outside and to which any power supply could be connected via BNC connectors.

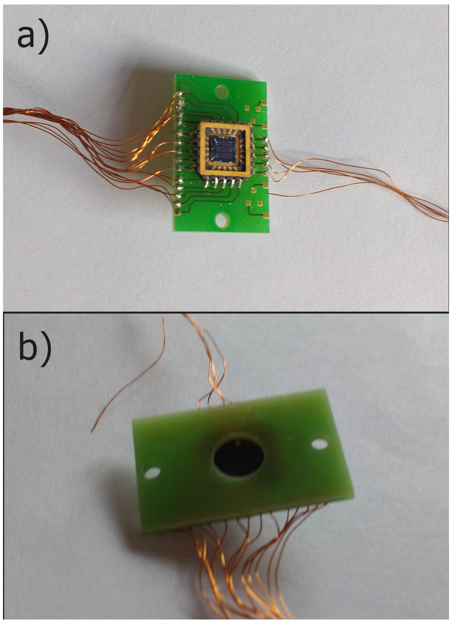

Figure 4.3: a) The front and b) the back of the sample holder for contacted sample that was designed and realized by Jan Flügge specifically for the measurements of contacted samples within the scope of this work. A bonded sample can be seen in the front view, while the back shows the circular hole that could be used to contact the chip holder thermally to the cryostat cold stage by inserting a copper disk.

4.2.3 *Synthesis of bulk CdSe nanowires*

The CdSe bulk nanowires were synthesised within the scope of the Bachelor's thesis of Braun.[121] The wires were synthesised directly on the Si substrates that were also normally used for sample preparation. The synthesis was performed in accordance with the work by Wang *et al.*, but instead of a Bi nanoparticle solution as a growth catalyst, Bi particles fixed on the substrates were used.

Preparation of fixed Bi nanoparticles

The immobilised Bi nanoparticles were made via electron beam lithography. Poly(methyl methacrylate) (PMMA) resist (ALLRESIST GmbH) was used in a two layer system. First, PMMA 50 k was spin coated for 60 s at 6000 rpm onto the substrates, which were cleaned beforehand as described for the sample preparation above. The coated sample was baked at 150 °C for 90 s Afterwards PMMA 950 k was spin coated onto the samples at 4000 rpm for 60 s. The sample was again baked for 90 s at 150 °C.

The samples were exposed in the SEM with an acceleration voltage of 30 kV. The written pattern was a grid of 4 × 4 point exposures at a distance of 20 µm from each other, at an exposure charge of 0.1 pC. The exposed mask was developed in isopropyl alcohol for 90 s and a layer of 10 nm Tungsten was sputtered, was well as 20 nm bismuth evaporated onto the sample. The mask was lifted off by submerging the sample in acetone.

Synthesis of trioctylphosphine selenium reactant

To synthesise a 2 mole/L concentration trioctylphosphine (TOP) selenium solution 0.8 g (10 mmol) of selenium were stirred in 5.0 mL TOP in nitrogen atmosphere until the powder was completely dissolved.

Synthesis of CdSe clusters

As a precursor for the CdSe nanowire synthesis CdSe clusters were synthesised. 104.5 mg (0.814 mmol) CdO were suspended in 1.2 mL (7.572 mmol) octanoic acid, stirred and evacuated until there was no longer any gas evaporation to be observed. Afterwards the the suspension was stirred for 40 min under nitrogen atmosphere.

6 mL of trioctylphosphine were subsequently added and the suspension was heated to 310 °C and stirred throughout. The suspended solid was dissolved during heating and a clear solution remained. The solution was kept at 310 °C for 5min and then slowly cooled to 65 °C and 0.4 mL of the TOP–Se solution was added. The solution was stirred for 6 days, until the UV–visible (VIS) absorption spectra did not show any more changes and the expected absorption peak of the clusters at about 400 nm could be clearly identified.

Synthesis of immobilised CdSe bulk nanowires.

For the synthesis of CdSe nanowires from the immobilised Bi nanoparticles 3 g trioctylphosphine oxide were melted and dried in vacuum at 100 °C. The solvent was then heated to 250 °C and the substrate, was well as 1.5 mL of the CdSe cluster solution were added rapidly while stirring the solution carefully.

After 10 min the solution was cooled rapidly to 100 °C and the reaction was stopped by adding toluene to the mixture. The Bi particle substrate was removed from the solution and washed several times with toluene. The synthesised nanowires were located on the substrate, which was confirmed by light widefield microscopy, AFM and confocal microscopy at room temperature.

4.2.4 Low temperature confocal measurements

Samples were measured with excitation wavelengths of 540 nm (2.30 eV) for the CdSe nanowires and 470 nm (2.64 eV) for the CdS nanowires. The longpass filters used were a longpass 532 nm (Semrock EdgeBasic BLP01-594R-25) and a longpass 473 nm (Semrock RazorEdge LP02-473RU-25). Illumination powers on the sample were usually kept around 100 nW (51 W/cm^2, 6.8×10^{-7} J/cm^2 at 75 MHz repetition rate) for both material systems. If not otherwise mentioned the measurements were performed with this power density. Other used illumination powers ranged from 20 nW (10 W/cm^2, 1.3×10^{-7} J/cm^2 at 75 MHz repetition rate) to 30 µW (1530 W/cm^2, 2.0×10^{-4} J/cm^2at 75 MHz repetition rate). Other significant measurement parameters will be detailed in the text describing the results.

The data shown in this work was partly measured within the scope of students' bachelor theses. The students who contributed measurements were namely Henri Hagelmann[122] and Nora Jannsen [123].

5

Dynamics in the CdSe quantum nanowire luminescence

The low temperature CdSe quantum nanowire luminescence has been examined and described by us before.[75] Looking mainly at single, static spectra, the spectrally resolved luminescence signal could be easily divided into two groups. The high energy near band–edge lines that appear narrow and should include – according to the literature[105] – free and weakly bound excitons and the lower energy trap-associated T bands which exhibit at least two characteristic LO phonon replicas. Both of these groups are shown in the spectrum in figure 5.1a.

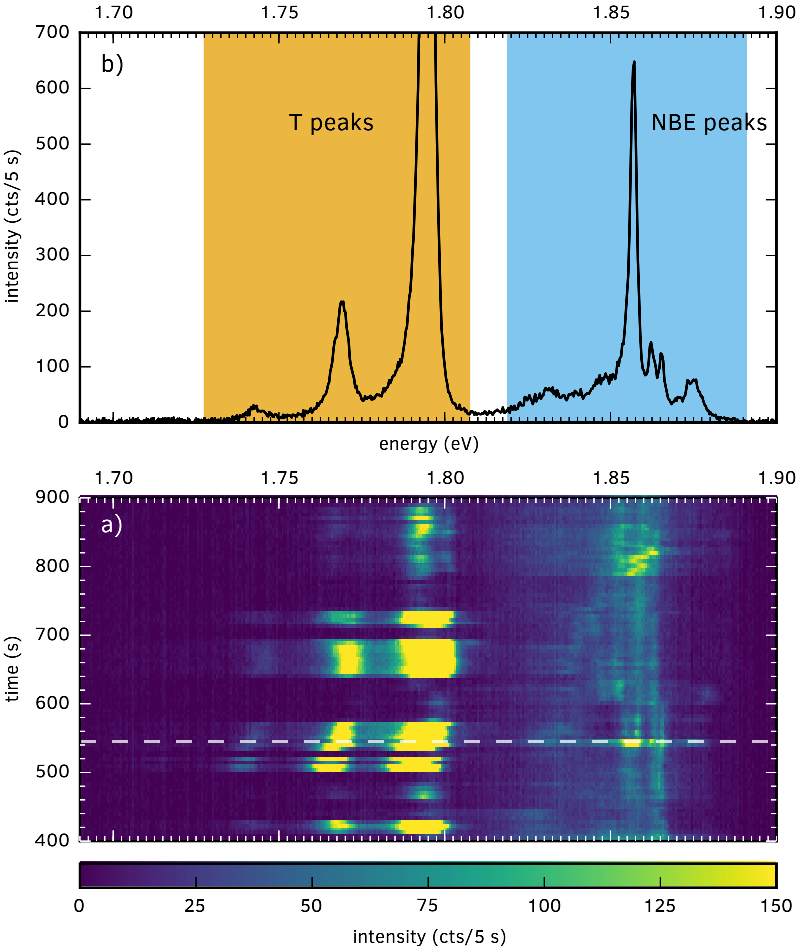

Figure 5.1: The typical spectrum as reported by us before. a) The luminescence signal can clearly be divided into two groups. At low energies the characteristic trap signal (T peaks, highlighted in orange) with phonon replicas can be made out. At higher energies several NBE signals (highlighted in blue) can also be seen. b) Observing these spectra over time shows that both signal groups show dynamics in terms of intensity and emission energy. The point of the spectral trace that corresponds to the spectrum above is marked with a white, dashed line.

The low-energy T peaks – a very intense zero-phonon line and two evenly spaced LO phonon replicas – and the NBE lines are marked in yellow and blue, respectively. The spectrum is scaled to show as many lines as possible clearly, cropping the high intensity zero-phonon line.

In our previous study the T bands' energy shift relative to the free exciton line in dependence on the QNW diameter could be very well described by simulations that modelled the interaction of the photo-generated charge carriers with point charges placed at different locations in the nanowire. If both charge carriers were localised at a point charge – representing a donor and acceptor defect – the distance between defects, as well as the location relative to the wire surface would determine the energy of such a donor–acceptor pair. This explained the wide variety of the zero-phonon line energies that were observed, ranging from 20 meV to 100 meV.

Figure 5.1a shows a good example of such a spectrum. The zero-phonon line in this case is situated at a distance of 80 meV from the quite faint highest energy signal at 1.875 eV. The NBE signals are closely spaced and comparably narrow.

A property of the luminescence that was only briefly touched upon in this first study was the time-dependent dynamics of the luminescence. Indeed, the spectrum shown in figure 5.1a is only a single frame from a long series of spectra, of which an excerpt of 100 individual 5 s spectra is shown in figure 5.1b as a false-colour plot. The point in time from which the single spectrum was extracted is marked with a dashed, white line.

In the spectral time trace strong dynamics of all spectral bands in both intensity and emission energy are immediately visible. The trap (T) bands and their replicas change between at least one high and low intensity state, each. The dynamics of the NBE bands seem even more complex and many more bands than the static spectrum suggests appear and disappear over time.

The dynamics of the two signal groups appear to be independent. And in fact, the bands can be observed independently of each other. This is emphasised in the spectrally resolved luminescence dynamics. The false-colour spectral traces in figure 5.2 show the usual spectra with NBE lines and T lines in a, but a series of spectra with no characteristic T–T-LO pattern in b.

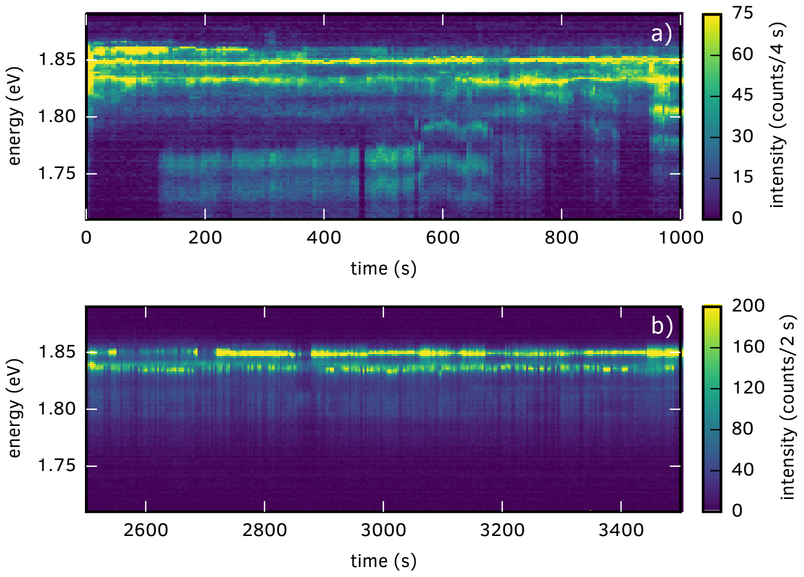

Figure 5.2: Two CdSe QNW spectral traces spanning a 1000 s timeframe. a) A trace showing both blinking NBE and T bands. b) A trace showing only blinking NBE bands.

This shows that appearance of the NBE bands and their blinking are independent of the T band appearance. Additionally, as there are not T bands visible in figure 5.2b, they do not obscure the width of the NBE luminescence, which can be seen to be much broader than the few meV that are known for neutral exciton–defect complexes.[21, 105, 124] This observation calls for a more detailed and differentiated description of the luminescence mechanism to account for all signals. The investigation of the dynamics of both groups – the energy shift and the non-radiative recombinations – as well as the better classification and characterisation of the origin of all NBE signals is therefore the focus of this work.

5.1 The measured data: scope, dimensions, and resolution

For the analysis of the single CdSe QNW luminescence dynamics it is desirable to record the luminescence intensity and its changes, the spectra of this luminescence and the change in spectra, as well as the decay time and its change. These measurements should be performed at the same time as to correlate the data sets with each other. Maximum time resolution and sensitivity is desirable for all these measurements. Excitation parameters should be chosen to be comparable to previous measurements. Long measurements are also preferable to collect as much data as possible for statistic analyses.

Figure 5.3 shows an example for a data set for which the compromise of resolution to signal intensity was found to be adequate for most means of data analysis: A spectral trace was recorded with a CCD and is shown as a false-colour image in fig 5.3a. As the spectra of CdSe nanowires can be rather broad and at the same time a good resolution of spectral lines is desirable, a compromise between detector sensitivity, resolution and size has to be found. The spectrum integration time for the performed measurements and consequently the spectral trace time resolution for the vast majority of the traces could be chosen as short as 1 s to 5 s while still achieving a signal–to–noise ratio that made fitting most of the luminescence bands feasible for the majority of frames.

As can be seen in the trace, spectral changes and dynamics of bands across the spectrum can be made out well at this time resolution. A sum of all, or any number of spectra, as shown in fig 5.3b can be easily computed to show the long term spectral properties of the investigated spot on the wire.

From this series of spectra an intensity trace can be extracted, as shown in figure 5.3c. By splitting the emission light and recording half of it with an APD a simultaneous recording of a TTTR intensity trace could be made via TCSPC technique. This trace is shown in figure 5.3e. The signal can be directly correlated to the trace extracted from the spectra. This yields a trace with high, adjustable time resolution. For both traces different intensity levels can be visualised in the respective intensity histograms in figure 5.3d and f.

The TTTR measurement also yields a time-tagged fluorescence lifetime measurement, which can be expressed in a lifetime trace – figure 5.3g – or as single decay curves – figure 5.3h – for any desired point and frame of time.

Another aspect that plays an important role in the chosen procedure of data acquisition is the synchronisation of the different data traces, which can be sufficiently assured after the measurement. A single point of the time axis of the spectral trace is equal to the spectrum integration time plus a small period of time in which the CCD chip is read out and the data is processed. For long measurements this time can be easily determined by assigning points at the beginning and end of the trace to the corresponding exact time from the time tag of the TTTR trace. The difference between the set spectrum integration time and the actual time needed to record a spectrum has been found to lie between 30 ms to

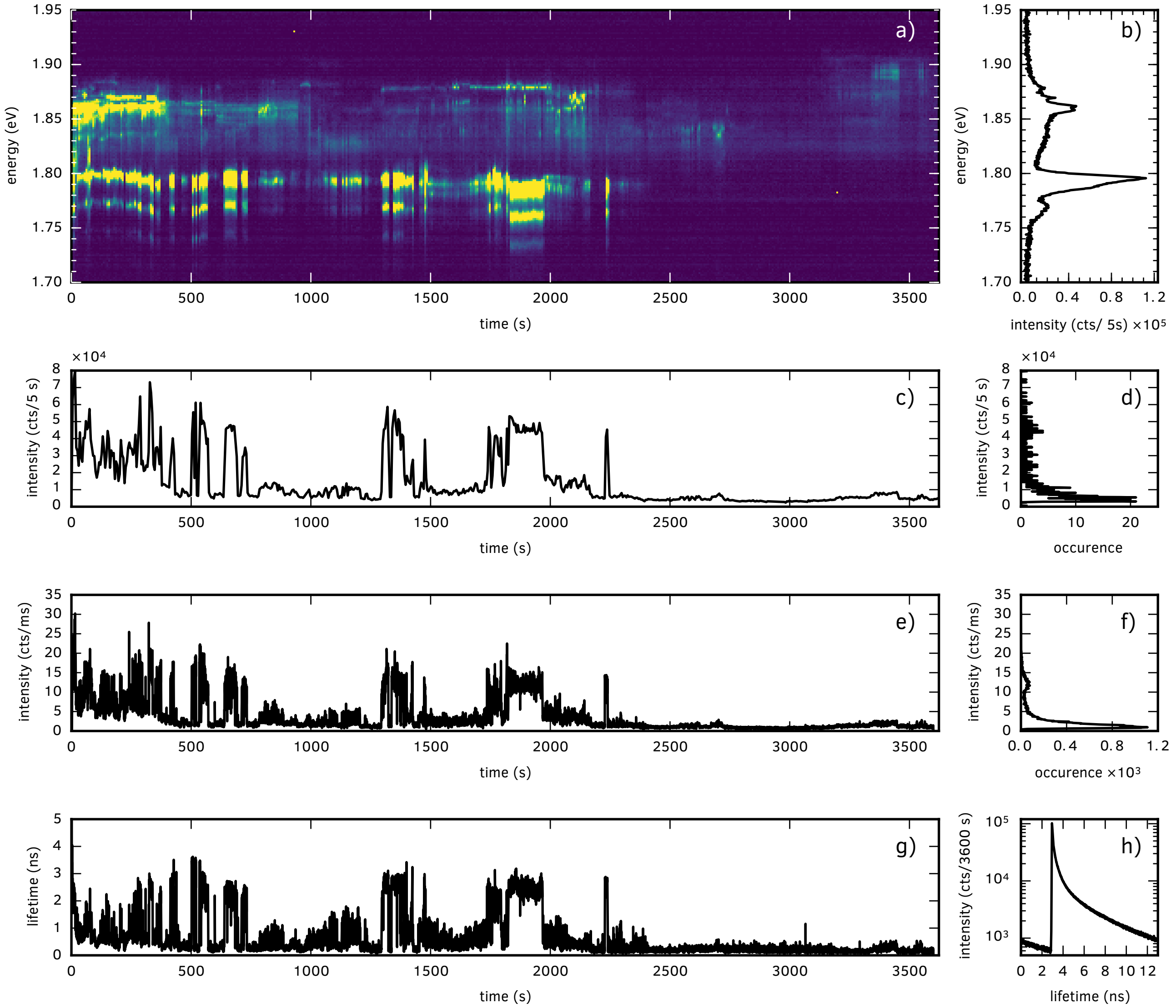

Figure 5.3: Example data set for the characterisation of the luminescence dynamics of a confocal spot of a single CdSe nanowire. Simultaneously measured were a) a series of spectra which show the energy-resolved luminescence dynamics as a false-colour image or b) the snapshots at any desired point in the measurement for a sum of any desired number of spectra. The sum of the intensity of each spectrum can combine to show an intensity trace (c) with a characteristic intensity histogram (d). The plots in e) and f) show the TTTR trace and intensity histogram which were recorded simultaneously and can be directly correlated to the respective data extracted from the spectrum. Also from the TTTR trace can be extracted a lifetime trace (g), as well as luminescence decay curves (h) for any point in the trace and any duration, limited only by the TCSPC minimum time resolution in theory and signal–to–noise ratio in practice.

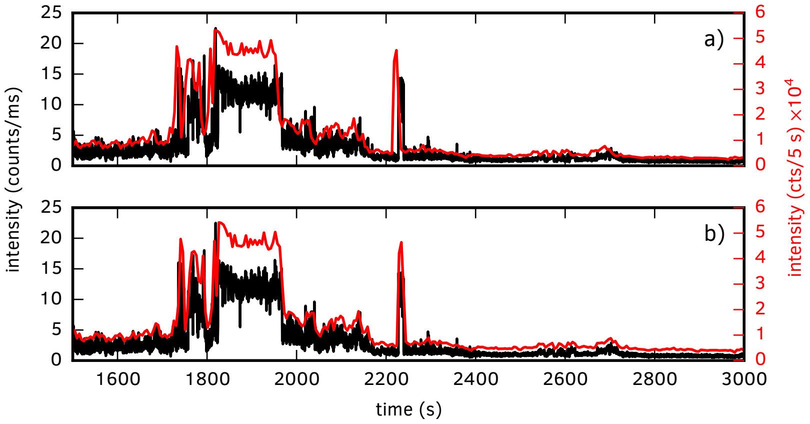

Figure 5.4: A comparison of the TTTR intensity trace and the intensity trace extracted from a spectral series a) with the spectral trace time axis not considering read-out and data-processing time, b) with the spectral trace time axis corrected by read-out and data-processing time as determined from the TTTR time axis.

50 ms and to differ between all measured traces. Figure 5.4a shows how this difference affects the synchronisation of a TTTR intensity trace (black) and the the intensity trace extracted from the corresponding spectral series. Especially later features are offset by several seconds, as the small time difference adds up over the recording of several hundred spectra.

By assigning two distinct features – at the beginning and the end of the trace – the time from the same feature in the TTTR trace, the actual measurement time, can be calculated by distributing the time frame between both points to the number of spectra between the two features. The resulting corrected spectra time axis can be seen in figure 5.4b. The good overlap of the red and black curve, even late in the measurement, show that the traces can be synchronised quite well.

In the further discussions of the data, the spectrum integration time plus the read-out and processing time will be called *spectrum measurement time*. As the actual read-out time is very short, if data (for example decay curve data from a TTTR file) is added up over a multiple of spectrum measurement times the value in the text and the axis legend will be rounded to the next 0.1 s for readability's sake.

While the chosen experimental approach necessitates the use of several detectors at once and records different parameters with different temporal resolutions, these are small drawbacks in comparison to the much reduced sensitivity of for example a streak camera, which would record this data at once. As it stands, the employed procedure of data collection could be optimised for the luminescence intensity and complexity of the investigated system.

5.1.1 Time resolution limitations and decay time determination

The limitations of and approaches to evaluating the associated data sets is an important aspect for any further discussions. Especially the time resolution limitations of the spectral traces, the signal–to–noise ratio of the highly resolved decay curves, as well as the precision of the synchronisation of the two data types are important aspects when correlations between exactly these data types are of interest. All these aspects are visualised in figure 5.5.

As can be seen in figure 5.5a and b, when compared with the 100 ms resolution TTTR trace, the resolution limitation of the 5 s integration time becomes quite noticeable. While the highly resolved trace shows distinct jumps in intensity, the low-intensity and high intensity phases overlap into the same bin in the less resolved spectral trace, which creates intermediate intensity levels not present in the high-resolution data. Also, some fast intensity dynamics become visible in the 100 ms TTTR trace which are not resolvable in the spectra, such as very fast spikes in intensity.

Nonetheless, combining the high time resolution intensity trace and the low resolution spectral trace can be used to characterise the clearly defined high-intensity and low-intensity states. Spectra from the spectral trace can be assigned to both a clearly low intensity (blue) or high intensity (yellow) phase of the measured intensity, extracted and plotted (figure 5.5c) and the changes in emission lines between the two can be compared, while avoiding the spectra that show the bin time related artefacts. The combination of two differently resolved traces also makes the identification of the main blinking band clear and therefore gives clues about the actual time-scale of – in case of this example – the blinking of the intense band just below 1.80 eV.

In addition the respective decay times can be extracted from the TTTR trace. In figure 5.5d, the decay curve including all photons from the 600 s measurement time frame shown in the traces is shown. In figures 5.5e and f the decay curve bin time was chosen to represent the spectra integration

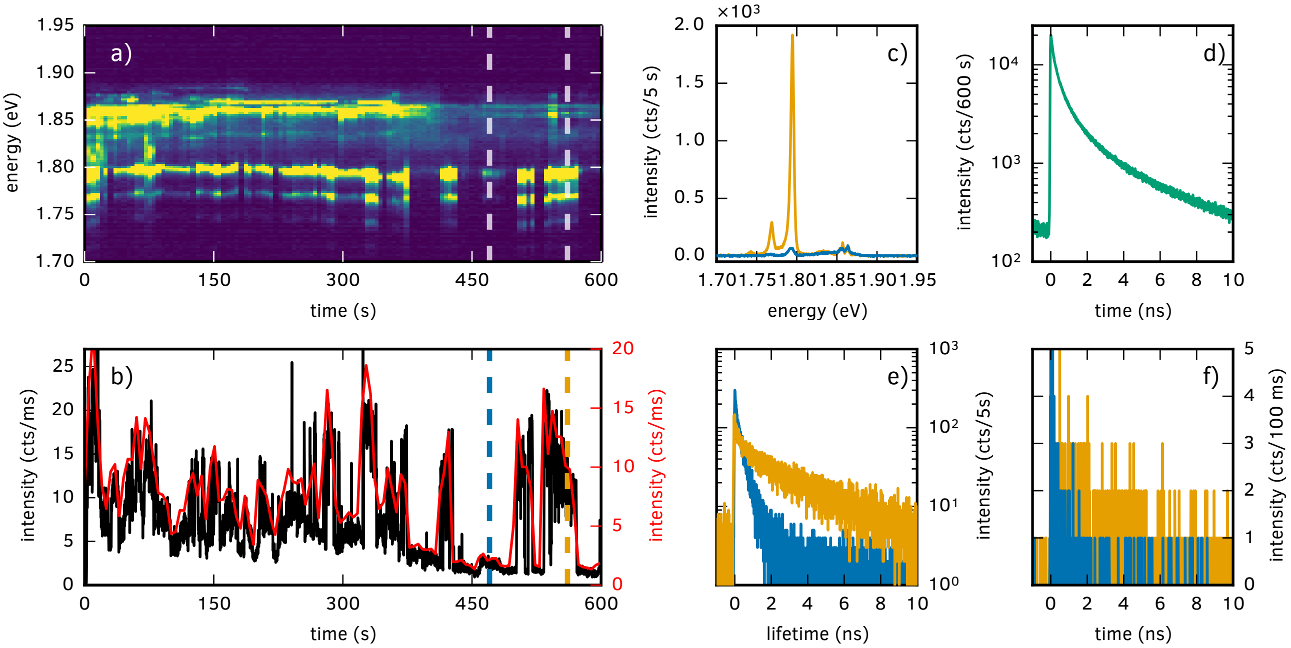

Figure 5.5: The time resolution limit of different data types and the extraction of spectra and decay curves with consideration of bin time artefacts: a) shows a typical spectral trace with a 5 s spectrum integration time and two points in the trace marked in a low intensity and high intensity phase of the wire luminescence, respectively, b) shows an intensity trace with 100 ms (black) time bin and a second trace with bins equal the spectrum measurement time (red), as well as two lines marking the same low-intensity (blue) and high-intensity (yellow) points in the trace. c) shows the spectra extracted at each of the points, colour-coded respectively. d) shows the decay curve that incorporates all photons recorded in the 600 s time frame of the trace. e) and f) show decay curves recorded at the two marked positions. The curves in e) represent a 5 s integration time and the curves in f) a 100 ms integration time.

time and the TTTR trace bin time. The curves are colour-coded according to their respective position in the time trace.

The shape of CdSe nanowire low temperature luminescence decay curves is strongly dependent chosen bin time, which in turn is adjusted depending on the goal of the evaluation. This means, a short 100 ms bin decay curve will appear quite different to a spectrum measurement time bin decay curve and again different to a decay curve extracted from a ten minute – or even longer – measurement. This is nicely visualised by the curves in the figures 5.5d to f. The logarithmic y-axes of the decay curves 5.5d and e should show decays following an exponential function as straight lines. Instead the 600 s integration decay is a smooth curve for the whole examined time frame, suggesting a more complex decay mechanism with a broad distribution of decay times.

The 5 s integration time decay curves in figure 5.5e in comparisons suggest more simple decays with two to three exponential decay times with a clear difference in decay times. And finally, the TTTR time bin curves in figure 5.5f show roughly the same difference in decay time but with such a small absolute signal fitting any function to the curves is not feasible.

Despite these differences in complexity and signal strength an at least average decay time value that, in the best case, is derived by a unified method and yields comparable values is desirable. For a detailed and distinctive analysis of the decay curves a clear but preferably simple mathematical model, such as a multi-exponential fit, would be ideal to describe the luminescence mechanism.

The general equation describing an n^{th} degree exponential decay can be expressed as follows:

$$I(t) = y_0 + \sum_{i=1}^{n} A_i \cdot e^{-(t/\tau_i)} \tag{5.1}$$

In equation 5.1 the luminescence intensity I is a function of the time t, and a background level y_0 is assumed. The multi-exponential decay is described as a sum of n single exponential decays, with A_i being the intensity amplitude and τ_i the time constant, respectively. For the luminescence mechanism in the nanowire, a multi-exponential decay with a limited n can be understood to imply n different decay channels through which a recombination with a certain rate $1/\tau_i$ can take place. This suggests that each decay might be assigned to a specific decay mechanism, such as the free exciton, a free–to–bound transition, or a donor–acceptor pair recombination, which occurs with a certain rate. But, as described before, if an exponential function is to be used, all three types of decay curves in figure 5.5b–d have to be treated differently due to strong differences in the curves' complexity, or cannot be described at all.

The luminescence decay of CdSe nanowires has previously been reported – and reproduced in my own work at low temperatures – as fitting a third degree exponential function[19, 20, 74]. This behaviour can be also observed for the spectrum measurement time bin decay curves in figure 5.5e.

The luminescence decay curve of the whole ten minute trajectory shows much higher complexity and a fourth degree exponential decay would have to be employed to fit the curve. In fact, most long term decay time measurements performed in the frame of this work do require at least a fourth degree exponential decay to fit the data, many require even higher degrees of complexity. Like the spectral data, the decay times fluctuate and the longer the measurement the more individual components will add to the complexity of the data. As these high complexity functions have only limited value in terms of a description of the luminescence only the short-term low-complexity curves that can be correlated with single spectra would yield exponential decay curves where an analysis of the components would be meaningful.

But sometimes an average decay time over a long time measurement is desirable for the sake of comparison between nanowires. Also, a comparison of a small time frame of the wire to the long-term average behaviour might be worthwhile. To compare decay times reliably without interference of the decay curve complexity, one option is to look at the time after which a certain fraction of the events of the curve have occurred. The best exponential fits for the above curves and the times at which 0.5 and 0.75 of the photons of the decay have been recorded is shown in table 5.1.

bin time/ measurement	τ_{ave} (ns)	$t_{0.5}$ (ns)	$t_{0.75}$ (ns)
600 s	3.33	1.39	4.38
~5 s; yellow curve	3.99	2.64	5.84
~5 s; blue curve	0.64	0.48	2.52
100 ms; yellow curve	—	2.86	5.78
100 ms; blue curve	—	0.60	2.14
IRF	0.09	0.16	0.17

Table 5.1: A comparison of the results of different methods of average decay time determination.

For comparison and reference the instrument response function (IRF) of the TCSPC system was also recorded and fit with a second degree exponential decay. The curve, fit and residual are shown in fig. 5.6a and b, respectively.

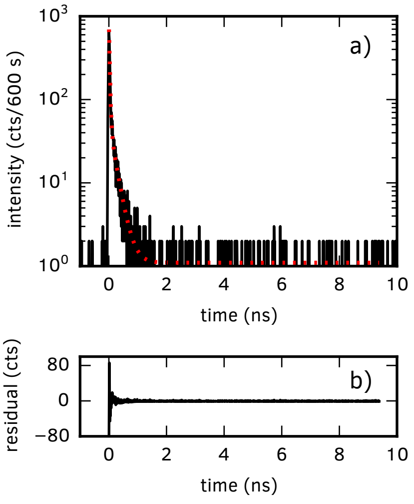

Figure 5.6: IRF, second degree exponential fit and residual.

Firstly, the alternative decay time determination works for all curves, even the low signal 100 ms bin time curves. The times are in fact comparable to the times that were determined for the 5 s integration time decay curves extracted around the same times in the TTTR trace. The method therefore offers an option for the analysis of highly resolved decay time traces, even if the luminescence signal is very small. It also makes the average decay times of decay curves recorded over different time frames feasible.

In terms of what exact ratio of photons to use for the decay time determination, a comparison with the average decay times from the exponential decay are a good measure. The time at 50 % of photons usually underestimates the decay time in comparison to the exponential fits. The time at 75 % of measured events in turn yields larger values, but overestimates the shorter decays.

Especially for the low intensity decays from the 100 ms time bin, the decay times are much larger for the 75 % times than for the times at 50 % of registered photons. Also, the time at a larger fraction is easily skewed to unusable large values for lower intensities, as single events occurring statistically at longer decay times and any kind of background noise impact the value much more strongly. As this method was to be used specifically for the evaluation of fast dynamics, for all analyses shown in the future any decay times – if not specified differently – are the times at 50 % of registered photons.

5.1.2 *The nanowire photostability and long-term statistics*

Very similarly to CdSe nanocrystals[125] a bleaching-process is often observed in the long-term intensity trajectories. Many of the traces recorded within the scope of this work show a loss of luminescence intensity, but not all do.

An example for a trace with no significant reduction of intensity and a trace showing an obvious bleaching process is shown in figure 5.7a and b, respectively. The traces were both recorded with pulse fluences of 0.7 µJ/cm^2 and with a pulse repetition rate of ~75 MHz.

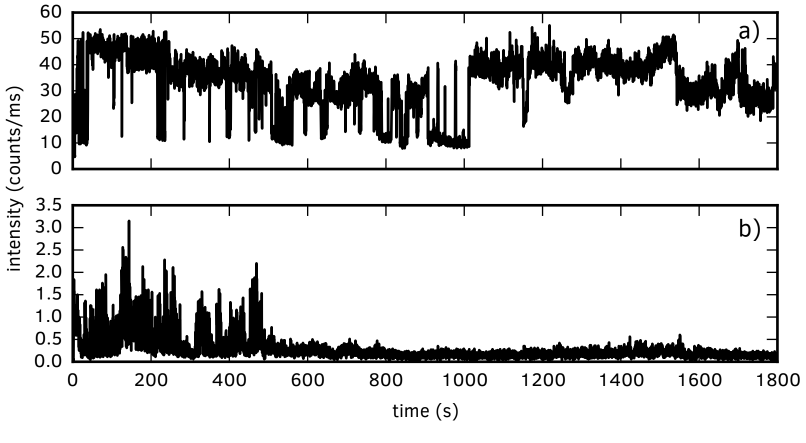

Figure 5.7: Example intensity traces that show a) no photobleaching within the measurement time; b) significant photobleaching within a time frame of 10 minutes.

In general, the trace in figure 5.7a does exhibit much larger fluorescence intensities than the trace in figure 5.7b. This is due to the wires being prepared from different synthesis batches. The trace with no bleaching shows an example of a wire with very high intensity, constant luminescence during a time frame of 30 minutes. The second trace shows strongly blinking luminescence in the first ten minutes of the measurement and a strongly reduced signal with some visible dynamics afterwards.

Both behaviours – bleaching and no bleaching – could be observed for all samples for which a larger number of nanowires were examined over longer measurement times. In comparison to the photo-bleaching of CdSe quantum dots, the luminescence does usually not vanish completely, but a residual small luminescence remains. This is analogous to the reaction of nanowires that were exposed to very high excitation powers. Wires have been shown before to being bleached after a power series and a very small luminescence remaining.[19, 20]

For nanocrystals, bleaching processes are usually described as eliminating all luminescence.[125] For the description of all quenching processes two different mechanisms and results are considered – the total quenching of all luminescence, also called static quenching and the creation of a competing fast non-radiative decay channel, also called dynamic quenching.[126, 127] For an ensemble of dots the first process reduces the luminescence with no change in luminescence decay time while the second process just quenches the slow processes, as the new, fast non-radiative process is preferred.

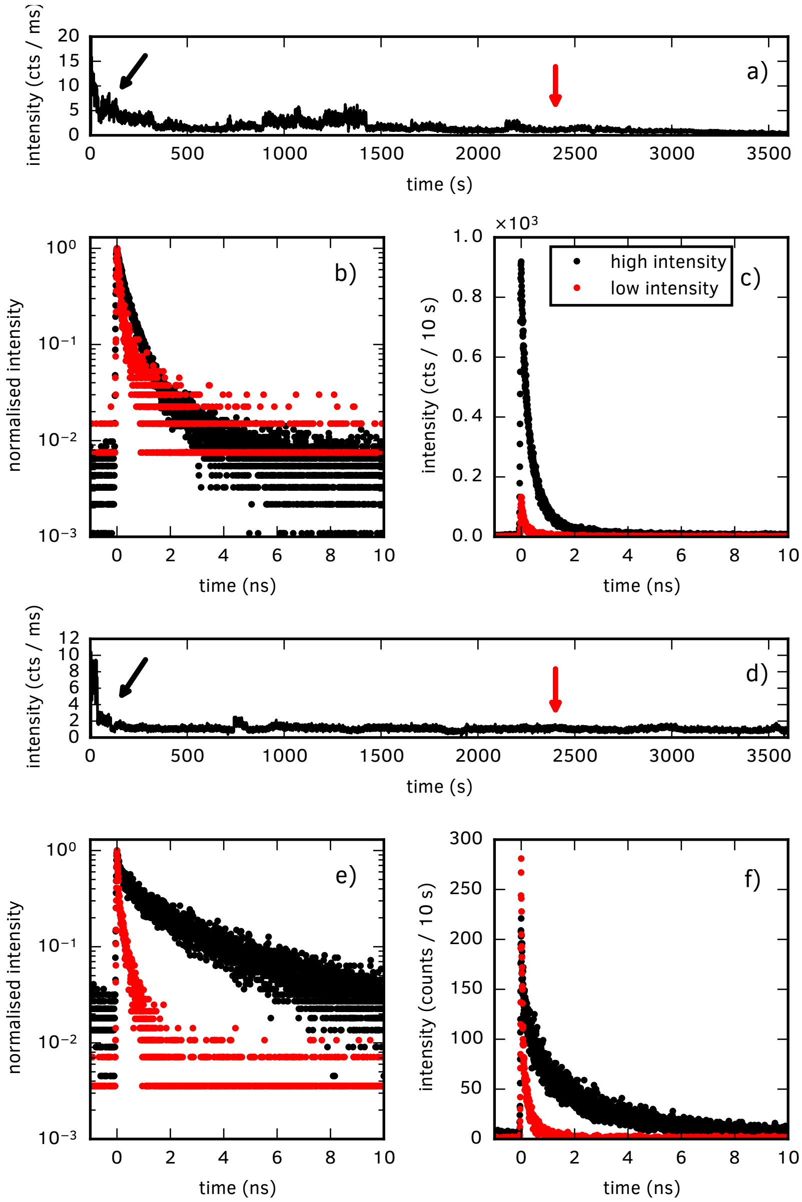

Figure 5.8: Bleaching of single CdSe QNWs with and without a decrease in decay time. a), d) Intensity traces of a single wires which show strong bleaching, the black and red arrow mark the point in time from which the luminescence decays of ten second segments in the high intensity (black) and low intensity (red) phases are plotted with a b), e) logarithmic and c), f) linear intensity axis.

A comparison of the high intensity luminescence decays of two different intensity traces is shown in figure 5.8. The two traces can be seen in figure 5.8a and d. Both show a rapid decrease in luminescence, down to a base luminescence intensity. From the TTTR data, decay curves were extracted that correspond to ten second time frames at the high luminescence intensity beginning of each trace (black arrow) and the later bleached luminescence (red arrow). Both curves are plotted in the same graphs, once normalised and with a logarithmic axis in figures 5.8b and e. To the right of each decay curve plot the same curves are plotted again, this time showing the absolute intensities and using a linear axis (figures 5.8c and f).

The two time traces are very similar. The initial bleaching happens quite fast for both sets of data – in the first 100 s – and some further reduction of luminescence also happens on a larger time scale. A big difference can be made out in the decay curves. In the logarithmic, normalised plot the decay curves belonging to the upper trace show no obvious change in decay time, while the curves extracted from the data of the lower trace show a significant decrease of decay time. This is confirmed by the $t_{0.5}$ decay times, which actually slightly increase from 0.56 ns to 0.61 ns for the first trace. In contrast, $t_{0.5}$ decreases in figure 5.8e from 2.08 ns to 0.4 ns.

This is further illustrated by the non-normalised linear plots in figure 5.8c and f. For the first data set, the intensity of the whole decay curve is significantly reduced, while for the second data set only the long decay time tail vanishes, while the intensity at very small decay times actually increases.

This behaviour points to two mechanisms of luminescence bleaching, one, where a fast, competing decay channel opens and the number of radiationless decays increases subsequently. For the other case the excited charge carriers are removed to a completely different recombination path, which does not compete for the excitons with the radiative decay channels. In many of the recorded trajectories both processes can be observed to some extend.

Any dynamic quenching process can be intuitively explained, even without knowing the specific chemical processes involved. A light-induced surface modification or ionisation can open new non-radiative decay channels, either through the creation of energetically close defect states that allow more charge carriers to recombine non-radiatively at the same time, or the creation of new surface trap sites that can separate charge carrier pairs and enable Auger-recombinations at formerly emitting defect sites.

As this bleaching process is observed for single nanowires and a residual luminescence is preserved, the ensemble mechanism as described for quantum dot static quenching is not applicable. Instead, a mechanism of bleaching that is neutral in terms of decay time is necessary.

One option would be the removal of, for example, hot electrons immediately after excitation. This is the mechanism for the so-called B type blinking, as proposed by Galland *et al.*[68] According to the model a quasi-band of energetically close surface states can trap hot electrons, a process competing with the relaxation to the band gap.

This fits with the consensus of the bleaching originating from photo-induced surface changes. van Sark *et al.* show that the bleaching in air correlates with a blue shift of the luminescence, pointing to the surface oxidation of the quantum dot and a subsequent reduction of size of the actual CdSe emitter.[125] Also, bleaching has been shown to be greatly reduced for quantum dots with very thick ('giant') shells.[128] Higher photon densities, as in pulsed excitation, have also been shown to induce the bleaching much faster.[129]

As all of the measurements in this work have not been performed in air but in vacuum and at low temperatures (5 K to 7 K) a reaction of the surface with gaseous oxygen is not likely. Nonetheless, the examined nanowires do not possess any protecting shell but only an organic ligand layer and are therefore highly sensitive to any kind of surface processes. While excitation powers have been kept low for this work (50 W /cm^2 to 250 W /cm^2 in comparison to 20 000 W /cm^2 in the work by van Sark *et al.*) the excitation light might be able to break the bond between ligand and the nanowire surface atoms, leaving sites with incomplete valences and creating new charge traps or surface states.

Coming back to the fact that not all traces bleach, the chosen experimental conditions can be assumed to be highly stabilising for the sensitive nanowires. Also, it highlights how different individual wires are from each other, with some much more stable than others within the same synthesis batch.

In the end, any long term statistic analysis would have to be performed on wires where no drastic change of the wire electronic structure has taken place, meaning only until the bleaching sets in. This change could happen as early as 170 s into the measurement or be not observed at all in a one hour trace. In the end, twenty traces with an average constant luminescence time of 1751 s – almost half an hour – could be used for the long term statistic evaluations in this work.

5.2 The CdSe nanowire luminescence signal groups: identification and dynamics

The previous comparison of the different appearances of the spectral traces shows that different signal groups will show different dynamics. A distinct difference between the NBE emission and the T band and its dynamics is easily visible.

While the T emission assignment to donor–acceptor pairs is solidly supported by our calculations employing the effective mass approximation [75] the NBE emission is not nearly as well described. Especially on a longer time scale for a sufficient nanowire sample size the NBE lines can appear in a fairly large energy range and while they might not always be the channels through which the majority of radiative recombinations take place the number of lines is usually much larger than that of the T or rather DAP emission.

As noted above, past CdSe bulk crystal luminescence studies have shown that the highest energy lines within 9 meV of the exciton should be assigned to the exciton bound to neutral donors and acceptors.[124] These are the bands whose origin is clearly assigned[105] and which we defined as the NBE emission in previous studies. But the actual span within which the narrow emission lines without phonon replicas can be observed is in fact much wider than these 10 meV. Also, one wire will show a multitude of lines when observed for a longer time frame and lines will also shift in energy.

To properly quantify these lines and the distribution of emission energies for each group of lines all spectral series were evaluated on whether they showed defined and sufficiently intense lines throughout most of the trace that would make fitting the individual lines with a LORENTZ function possible. A number of 16 spectral traces fit these criteria for the NBE emission and 9 for the T emission. The distinction between high energy T bands and low energy NBE bands was made by the presence or absence of phonon replicas, respectively. For T bands only the position of the zero phonon line was included. In cases where the suspected zero phonon line was so low in intensity that an eventual phonon replica could not be expected to be visible in the noise the band was not included in the statistic.

As the spectra and lines to be fit had to be identified and chosen manually the maximum number of spectra was limited to a maximum of 50 to keep the time needed for the analysis feasible. The histogram of these extracted line positions relative to the respective highest energy line recorded for each series is shown in figure 5.9.

The NBE emission was further divided into the group of free exciton and excitons bound to neutral donors and acceptors as defined above– the

Figure 5.9: Histogram of signals observed at different emission energies relative to the highest energy signal observed during the entire trace.

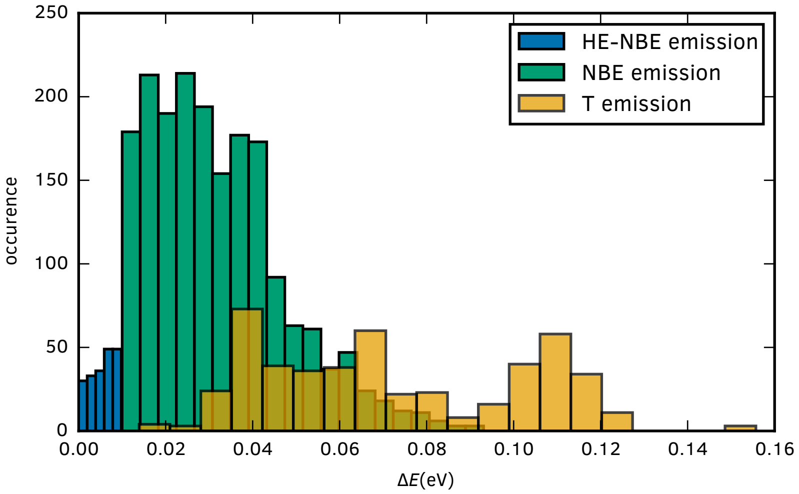

high energy NBE emission – as well as the low energy NBE. The cut-off for a line to belong to the high energy NBE emission was an emission energy closer than 10 meV to the highest recorded energy line. This value was chosen according to the values reported in the literature for the bound exciton complexes (see table 2.7). Histogram bin sizes of 10 for the high energy NBE and 20 for the low energy NBE and T signals were chosen to account for the number of observed bands from each group.

The emission line histogram shows a comprehensive summary of the observed occurrence of the three line types. High energy NBE lines are only seldom observed. While the slightly more stabilised weakly bound excitons are observed more often the difference is small in comparison to the low energy NBE emission. These lines are confined mostly to the energy region between 10 meV to 50 meV with some signals shifted even further to the red. The general shape of the histogram looks at first glance like a symmetric distribution that is truncated at high energies.

The T bands on the other hand are not as numerous but the majority is spread out over an energy range slightly larger than 90 meV. The observed high energy T peaks overlap energetically with the low energy NBE signals. In fact, this is one of the reasons that makes manual identification and fitting necessary, as phonon replicas can be observed that are easily identified by eye but – due to signal–to–noise ratios close to the limit of detection – not with means of data evaluation algorithms. The T band histogram does not seem to follow a distinct distribution. Also, the absolute number of identified and fit T bands is much lower than that of the low energy NBE bands.

While the assignment shown in the histogram in figure 5.9 may seem arbitrary, they can be supported by the CdSe QNW photoluminescence spectra and their dynamics. These three signal groups are clearly distinguishable by their spectral appearance and dynamic behaviour. Setting all these different kinds of bands in relation to each other – describing their independent and dependent dynamics – and supporting the current or identifying a new possible model for the emission lines' origin is the goal of the following chapters.

5.2.1 *Identifying the high energy CdSe luminescence signals*

The CdSe nanowires that were analysed in this work were all CdSe quantum nanowires. All emission bands of wires with a radius below the exciton Bohr radius have been found by us before[22, 75, 77] to shift to larger energies with increasing confinement. Absolute energies are therefore less meaningful than the signal energy relative to the wire band gap or – as it should be possible to extracted this from a luminescence spectrum – the energy of the free exciton.

This illustrates the importance of identifying the actual high-energy lines of a CdSe QNWs. To determine any relative energy value the exciton line and the emission lines of weakly bound exciton recombinations should ideally be identified for every analysed wire's emission.

The high energy NBE lines can be considered their own group of emission lines with similar properties within the group which distinguish them from the other lines in the spectrum. Onward these emission lines will be called just high energy (HE) lines to distinguish them from the more intense, red-shifted fraction of the NBE lines.

Especially in long spectral series the identification of the HE lines has to take their intensity fluctuations into account. In fact, they are easily distinguishable from the other emission groups in the spectra by observing their blinking and flickering. Or, from a different perspective, a certain observation time is necessary to clearly identify these lines.

An example for the independent behaviour of an example HE band can be seen in figure 5.10.

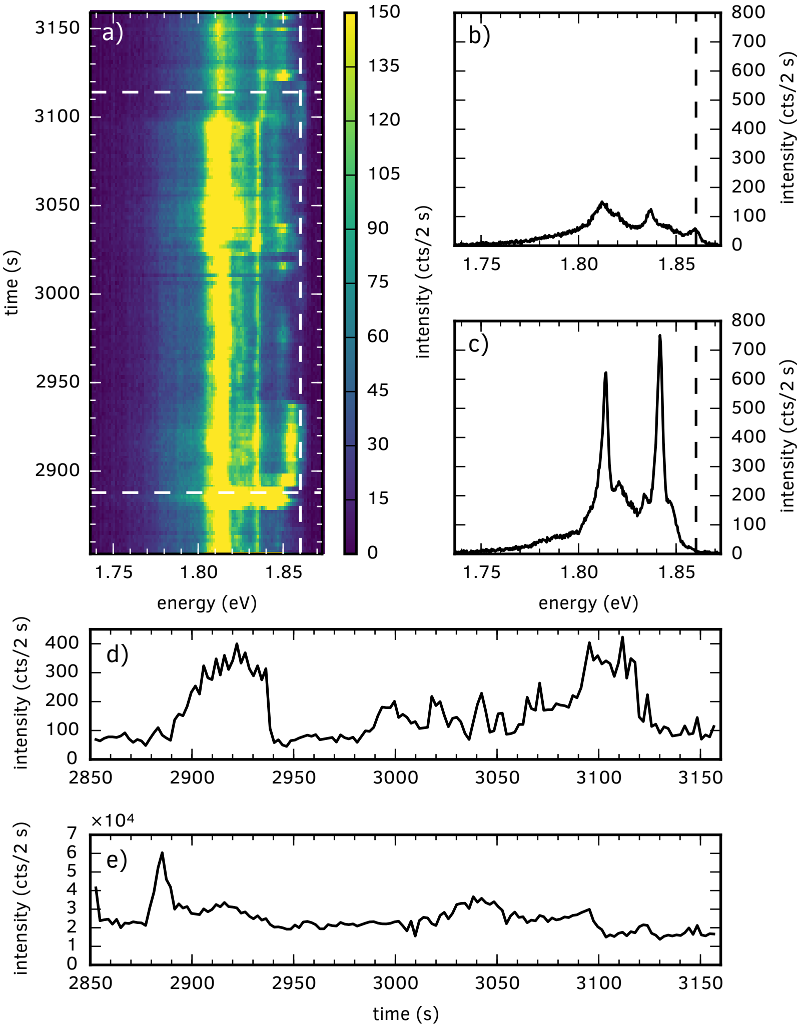

Figure 5.10: Behaviour of a high energy NBE line, independent of the other emission bands. a) False colour plot of an example spectral series, each spectrum was recorded with an integration time of 2 s. Dashed lines mark extraction times and energies for the spectra in b and c, as well as the time trace in d. b) Spectrum extracted at the time marked by the upper horizontal line in a. A high energy emission peak is visible and marked with a dashed line. c) Spectrum extracted at the time marked by the lower dashed horizontal line in a. The high energy line is not visible at this point in time. d) Intensity trace extracted at the energy of the high energy line. e) Intensity trace of the entire spectrum.

The figure shows an example spectral trace as a false colour plot in 5.10a. Horizontal dashed lines mark the points in time from which the spectra in b (upper line) and c (lower line) were extracted. A vertical dashed line shows the spectral position from which the intensity trace in d was extracted. The trace in e shows the intensity trace of the complete spectrum.

As the colour scale of the false colour plot is adjusted to show as many features as possible, the high energy emission can only made out as a faint hint at the high energy side of the spectra, due to its low intensity. The line plot of the first example spectrum shows the high energy emission much more clearly. A dashed line marks a high energy peak which is relatively low in intensity but still distinctly visible. In comparison, the second spectrum shows the fluctuation of this emission to a dark state. The signal vanishes completely.

The two intensity traces – the fluctuation of that distinct high energy signal and the intensity fluctuation of the spectrum as a whole – show no similarities. This implies that the high energy emission and the remaining spectrum fluctuate in a completely independent manner. This is especially interesting, as the shown trace shows on several occasions intensity fluctuations that apparently affect the entirety of the spectrum (e.g. at ca. 3010 s).

The relationship between the overall nanowire luminescence intensity and the HE emission depends on each individual wire and each point in time. Sometimes the emission dynamics will follow the dynamic of the entire spectrum and sometimes it will change in an entirely independent manner.

This is illustrated with three examples in figure 5.11. The example traces show differently long time frames, trace 5.11a bleaching within 1000 s, the other showing consistent luminescence intensities for 2200 s (figure 5.11b) and 3600 s (figure 5.11c). The intensity of the HE emission is furthermore compared in intensity traces that were extracted from the spectral traces. The summed intensity of the entire spectrum is shown as a grey area and the intensity of the HE emission band is superimposed as a black lines in the figures 5.11d–f. The spectral series and the intensity traces are affiliated as follows: the uppermost trace 5.11d shows the intensity of the spectra in the leftmost series 5.11a, e shows b, and f shows c, respectively.

Looking at the leftmost spectral series and the corresponding intensity traces (figures 5.11a,d) the most noticeable characteristic is that the HE emission will follow the general trend of the nanowire bleaching, but the detailed dynamics are mostly independent of the remaining bands. At a few points – for example around 500 s – the luminescence does follow the overall decrease and increase of the rest of the spectrum. In the spectral traces this is visible as a strong decrease of all bands, including the comparably intense T band.

In comparison, the HE emission in the spectral and intensity trace with the constant luminescence intensity (figures 5.11b,e) shows a HE luminescence whose average intensity is fairly constant during the whole recorded time frame. The fluctuation of the HE bands sometimes follow the fluctuation of the entire trace – for example between 800 s to 1000 s – but often it does not increase or decrease with the other bands and shows independent fluctuations (between 1300 s to 1500 s).

As a third example, the last traces (figures 5.11c,f) show an increase of the HE luminescence intensity while the overall luminescence intensity of the nanowire stays constant. The HE luminescence increases by almost two orders of magnitude during the 3600 s of the measurement. As in the other traces the HE band luminescence intensity sometimes follows the general intensity dynamics but often behaves independently.

In summary, the HE bands show both dependent and independent luminescence dynamics. In some cases a general blinking of the spectrally independent luminescence intensity will also influence the availability of free and weakly bound excitons for radiative recombinations. In other cases the overall luminescence intensity will be constant or show completely different dynamics than the HE bands. In all cases, the HE luminescence does not show a binary *On/Off* behaviour commonly re-

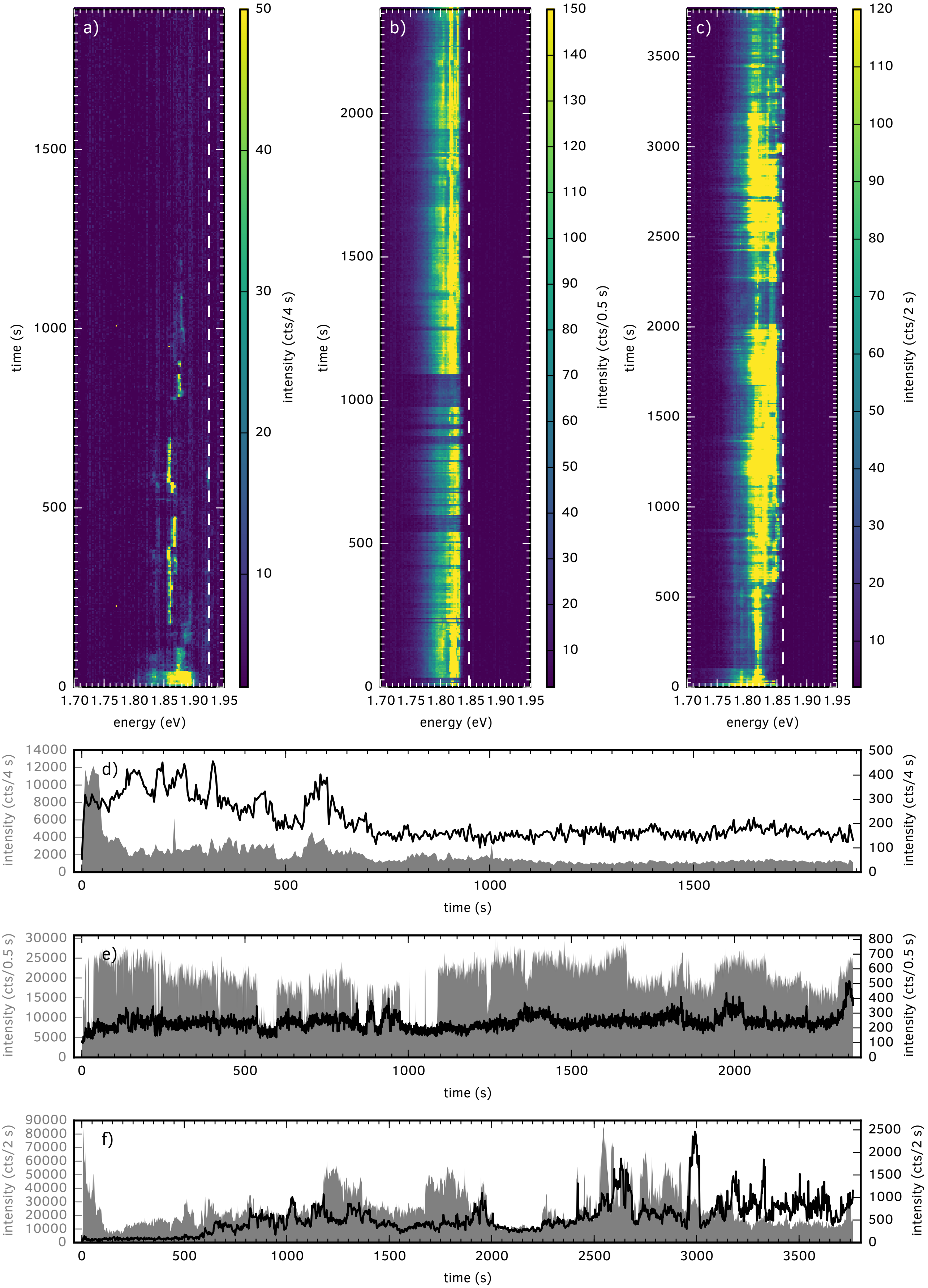

Figure 5.11: Different behaviours of the NBE emission for different kind of time traces. a), b), and c): Three spectral traces with different HE band behaviour. d) e) and f): the respective intensity traces of the HE emission (black line) and the entire spectrum (grey area).

ported for CdSe nanocrystals.[15] Instead the luminescence is distributed over a range of emission intensities.

This behaviour of the HE emission can fairly easily be explained by considering the fundamental processes of radiative and non-radiative decays as well as the competition between different decay channels, no matter if radiative or non-radiative. As the energy of the free and weakly bound excitons is considerably higher than that of complexes with more strongly bound charge carriers any energy barrier that has to be crossed to access for example surface defect bands is much smaller than for a more stabilised charge carrier pair. Also, a free or weakly bound exciton will often have the opportunity to bind more strongly to a defect, resulting in a competition with the more red-shifted radiative decays.[76]

The above described processes imply a strong competition of the high energy NBE recombinations with both non-radiative and radiative decays. This fits well with the generally observed low intensity of the HE bands.

The nature of excitons that are not or only very weakly stabilised as described above is also illustrated by the states' luminescence decay time. The spectra in figure 5.12a were taken at different points in time during the measurement of a spectral trace. While the quite low intensity spectra show only NBE luminescence bands, from the lower (red) spectrum to the upper (black) spectrum the HE emission increases notably at the high energy side of the spectrum.

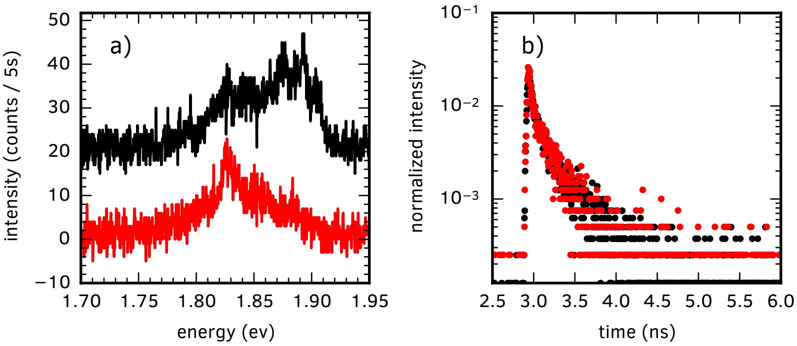

Figure 5.12: The effect of a significant increase in HE luminescence shown a) two spectra and b) the associated decay curves that were recorded at the same time. The strong spectral change and increase in emission intensity does not influence the decay curves. The decay curve areas are normalised.

At the same time, the two decay curves in figure 5.12b show no significant difference. With an increase in luminescence intensity an increase in decay time would usually be expected,[68] if a mechanism such as Auger recombination is assumed the cause for a competing non-radiative decay. This is not the case for the data shown here and implies that the HE emission intensity is mainly influenced at the level of the hot charge carriers before they relax to the band gap. Hot electrons in the conduction band can either relax to the band edge or access non-radiative recombination pathways that can only be accessed from higher energy levels.

While at first one might assume that in reverse, the very shortest of decays are contributed by only the emission of weakly bound excitons, this cannot be confirmed by investigation of emission spectra and decay time dynamics. Figure 5.13 shows three spectra extracted at different times of a spectral trace. The spectra are offset for clarity and plotted sequentially from bottom to top. Same goes for the normalised decay curves that were extracted for each spectrum from the TTTR trace, with a bin time of 10 s, same as the spectrum measurement time.

In the spectra a strong decrease in intensity can be observed over time. At the same time the decay time decreases strongly. All decay curves could be fitted with second degree exponential functions. Both components – both near the IRF resolution limitation – decrease by about one third of their initial value from 0.36 ns to 0.20 ns and from 0.06 ns to

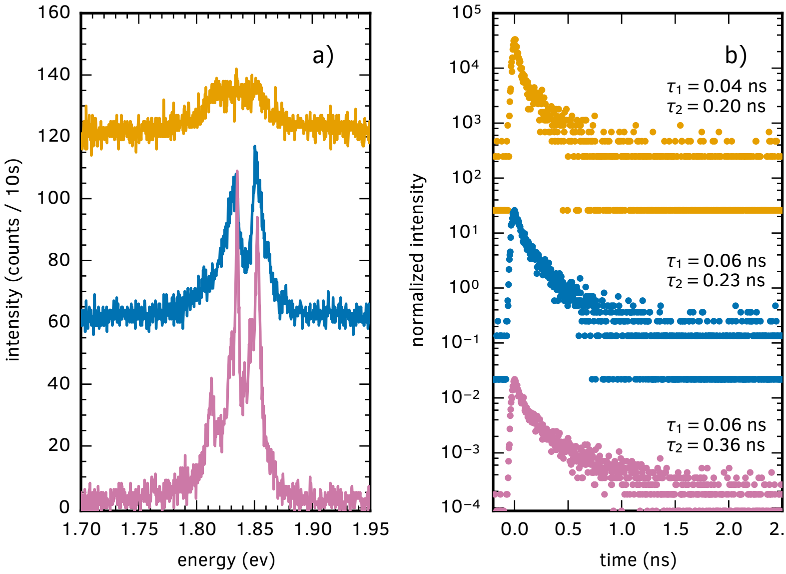

Figure 5.13: Correlation of short luminescence decay times and certain spectral shapes. a) Decreases of luminescence intensity from the same spectral trace. The spectra were extracted at different points in time with the measurement time advancing from the bottom spectrum to the top spectrum. The spectrum with the lowest intensity still exhibits a with of at least 70 meV. b) The decay curves extracted from the TTTR trace at the respective times of spectra extraction. The decay time decreases with decreasing intensity. A second degree exponential decay function reveals an acceleration of both radiative decay channels.

0.04 ns. The relative contribution of each channel only changes slightly. The amplitude fraction of the short component increases from 37 % to 39 % and finally 47 %, bottom to top. This means the shortening of all non-radiative lifetimes is the dominating process and not the relative increase of the shorter radiative component.

At the same time the spectral distribution of the emission stays broad – while distinct bands can not be assigned anymore, the emission width spans at least 50 meV. The highest energy emission band at 1.855 eV is only visible in the high intensity spectrum. This means that while the HE emission has a very short lifetime, emission bands from the lower energy parts of the spectrum also contribute with short lifetime radiative decay routes.

The single bands of the HE emission do show both independent and dependent dynamics within the signal group. In the specific case shown in figure 5.14 the HE emission could easily be distinguished, as it switches *On* at about 850 s and can be continuously observed for more than 1500 s before switching *Off* again. The respective excerpt of the spectral trace is shown in figure 5.14a as a false-colour plot. The intensity colour scale is adjusted to best show the dynamics of the entire spectrum. A white rectangle marks the magnified data area shown in figure 5.14b, now plotted with a colour scale adjusted to best show the HE emission. The vertical lines in the two false-colour plots mark the wavelengths at which time-dependent intensity traces were extracted, which are shown in figure 5.14f and g. An intensity trace showing the sum of all dynamics can be seen in figure 5.14h. The horizontal lines in figure 5.14b show the temporal positions of the three spectral frames shown in figures 5.14c,d,e. The top-to-bottom order of the horizontal lines in the false-colour plot is equal to the top-to-bottom order of the three spectra.

The significant difference in colour scaling between the two false-colour plots illustrates the significant difference in emission intensity between the HE emission and the remaining spectrum. The intensity range maximum has to be set to one fifth of the original value to sufficiently show the highest energy emission line. At 1.8751 eV and 1.8602 eV the two lines that switch *On* and *Off* together during the measurement can be made out, with the higher energy line – presumably the exciton emission – much less intense. The intensity of these two lines is plotted as time traces figures 5.14f and g for comparison, while figures 5.14d and e show spectra in which the signals are visible. It has to be remarked that

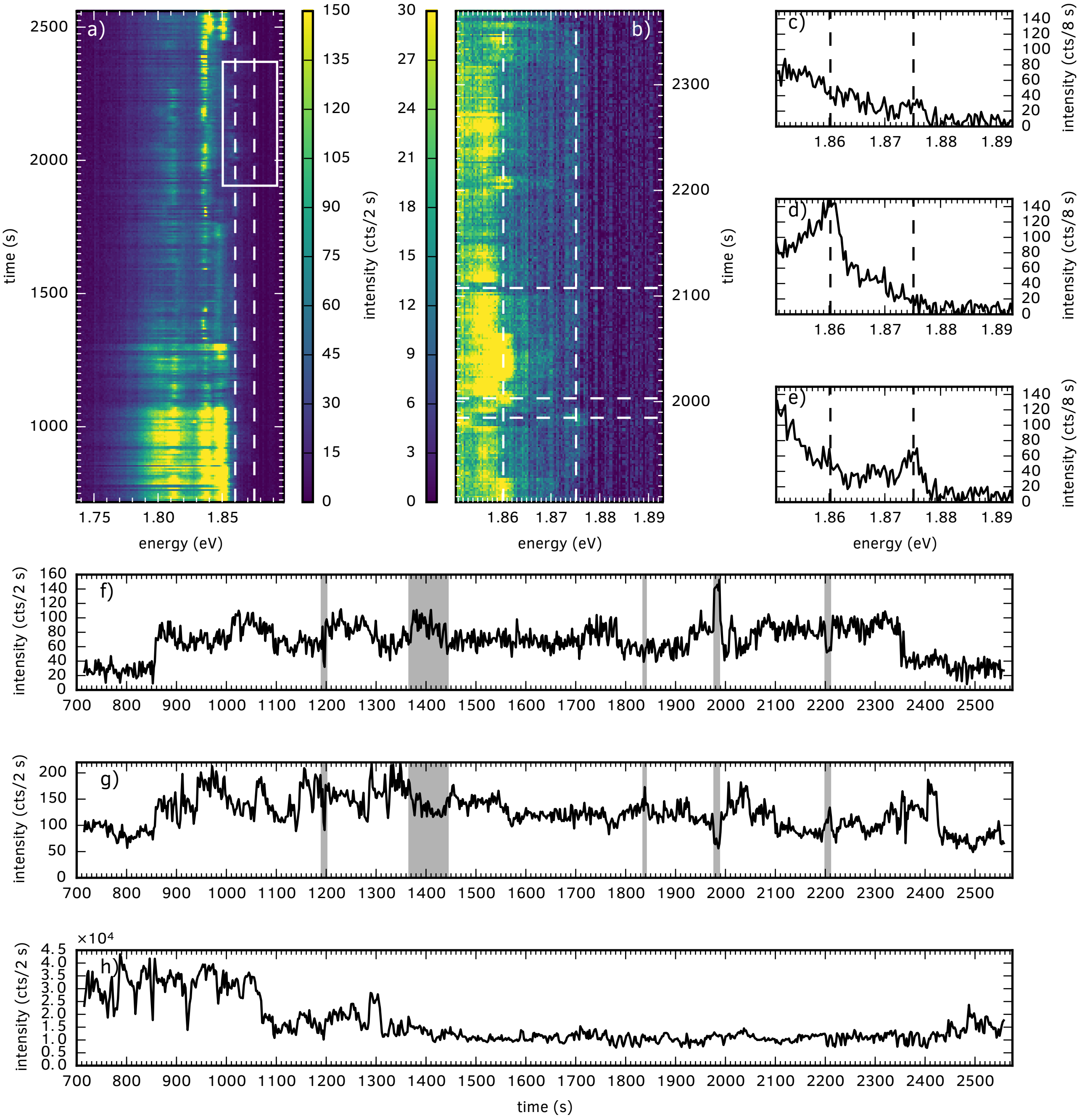

Figure 5.14: Blinking behaviour of the individual HE emission group bands. a) In comparison to the other bands in the spectrum the HE emission is very low in intensity. The colour scale is adjusted to show the majority of the bands and their dynamics. The colour scale is adjusted in b) – a plot of the detail marked with a square in the previous image – to the HE emission intensity, which is one-fifth of the original value. The spectra in c), d) and e) were extracted from the three horizontal dashed lines in the detail image. The arrangement of the spectra – top to bottom – is the same as the the top to bottom order of the lines in the image. The traces f) and g) show the intensity traces extracted from the spectral trace at the emission energies marked with the vertical dashed line in both false colour images. The trace in h) shows the intensity trace added up over the entire spectrum.

while the two lines are easily distinguished as part of the same group, the energetic difference is significantly larger than the maximum 9 meV mentioned above. As this wire shows strong quantum confinement it is likely that the relative HE emission position can also be influenced by the wire diameter and the particular environment of the involved defects, as reported by us for the donor–acceptor pair emission.

The close relationship of the two lines can be observed at different points during the 1500 s emission duration of the group. The intensity traces of both signals in figures 5.14f and g show – apart from the synchronous appearance of the band – mostly independent behaviour. In fact, the band at lower energy can be observed a bit longer than the high energy emission. But looking closer, both positive and negative correlations can be found between both bands' intensities. Examples for the positive correlation are the synchronous appearance as well as the intensity dip at 1200 s, marked in grey. Several negative correlations are also marked in grey around 1400 s, 1840 s, 1980 s and 2200 s. Either band can gain in intensity while the other becomes less intense. These correlations are further illustrated by the three spectra extracted at the points in time marked by the horizontal lines in the magnified spectral trace. In contrast, the intensity trace of the entire spectrum (figure 5.14h) does not show any correlation with either of the HE traces.

In summary, the HE emission is a group of emission bands with quite low emission intensity. The relaxing states have very short lifetimes but are not the only short-lifetime emission lines of the spectrum. The luminescence dynamics are mostly independent of the other emission groups, but some intensity changes do influence the entire spectrum.

The spectral position of the bands and the behaviour described above mostly fit with the before mentioned assignment as excitons and bound excitons for these specific lines. The low emission intensity is easily explained by the abundance of defects which can form much more stable complexes with the optically created charge carriers than free or bound excitons. Also, an exciton will more easily be re-excited which increases the chances of a non-radiative recombination of the involved charge carriers.[76]

For a specific assignment of the lines, the highest energy emission will usually at most be the A band exciton. This is likely, as the B band exciton decays very fast. Its lifetime has been measured to be less than 0.9 ps until relaxation of the electron to the A conduction band.[130, 131] Also, the A exciton emission has been reported as very weak in comparison to that of bound excitons.[132] As the multiple bands that were observed in this work for the HE emission region likely arise from the recombination of bound excitons and are already quite weak in emission, chances are, the even weaker free exciton emission might not be observed at all.

In fact, multiple lines spread over an energy range as far as 20 meV from the exciton emission have been reported by REYNOLDS *et al.*.[133] These lines are assigned to be excitons bound to both neutral and ionised donors and acceptors. This energy range explains any lines observed in the HE region of any spectral trace recorded within the scope of this work. Additionally, the recombination of an exciton bound to a neutral trap site can also excite the charge neutralising the defect.[132] These recombinations and simultaneous excitations would result in even lower energy emission lines, giving a certain flexibility and breadth of emission line position without even considering local trap site potential and the influence of the nanowire on that.

In general, exciton complexes, especially those bound to neutral trap sites are not easily, or sometimes not at all described by the model we used to calculate the DAP energies, before,[75] but could only be sufficiently identified by observing their behaviour in the magnetic field.[133]

Nonetheless, observing the coherent emission line behaviours and noting the energetic region where the lines occur, it can be said with quite some certainty that these emissions arise from the recombination of free and bound excitons. What can not be said is if we see in fact the free exciton emission line. It might well be, that the highest energy line that could be observed in some of the recorded spectral traces is in fact a bound and not the free exciton. While this has to be taken into account for any future evaluation of relative emission energies, the possible error is only in the magnitude of a few meV.

5.2.2 *The CdSe trap luminescence and its dynamics*

In stark contrast to the weak HE bands, if the T band group of signals can be observed in the spectrum of a CdSe nanowire it immediately draws the eye and seems to dominate. Even if the T signal group is by no means always the emission with the highest intensity – it often doesn't occur at all – the one or two bands with their usually two phonon replicas are the most recognizable spectral pattern of the CdSe nanowire luminescence. This appearance is typical for donor–acceptor pair emission.[105, 134–139] In nanowire luminescence the bands within this group often show a lot of dynamics, both in terms of emission energy, as well as intensity. These very prominent characteristics are why we described this emission and its origin before in detail.[75] As our earlier study showed the strong dynamics without analysing them further the following chapter will describe the main behaviours of the bands with the goal to better define the related properties of the emission and consequently the nanowire.

Typical appearance of the T band over time.

For all the recorded long-term spectral traces where a T band was observed the bands retained certain properties over longer observation periods. Examples for this behaviour are shown in the spectral traces in figure 5.15a and b. The example spectra in figure 5.15 c and d below the respective traces were extracted at the times marked with a white dashed line in the false-colour plots. The zero phonon line of the dominant T emission, as well as the highest observed HE band are marked in red in the two line plots.

The first mostly constant property of a T band is its general energy. While the exact emission energy certainly fluctuates, this happens within a comparably small range of usually not more than ~20 meV in comparison to the energy range in which these kind of bands could be observed (~100 meV). The T band at about 1.85 eV in figure 5.15c (marked in red) only shows an energetic distance of 25 meV to the highest energy peak observed in this measurement (also marked in red). As can be seen in the false-colour plot of the spectral series in figure 5.15a the band will shift slightly in energy, but always within the before mentioned narrow range.

Other constant properties of the T bands are the width of the band and the maximum intensity relative to the rest of the spectrum. In figure 5.15a and c the T band zero phonon line dominates the spectrum during its *On* times and retains its narrow width. In comparison, the T band zero phonon line in figure 5.15b and d has a much lower maximum intensity than the other lines that are visible in the spectrum. It is also fairly broad and stays so during the measurement.

These constants in the emission band behaviour fit very well within the model of donor–acceptor pair recombination as proposed by us before.[75] While the concrete influence on the emission intensity and line width are not explained directly by the model, the emission energy

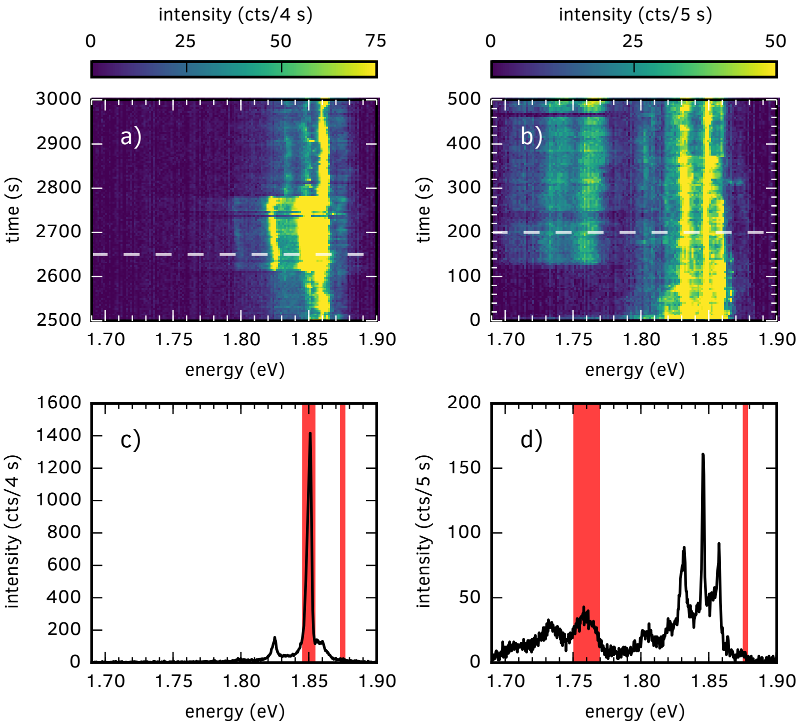

Figure 5.15: False-colour plots of example spectral traces – a) and b) – with T bands with different energetic positions and maximum intensities. These properties are retained over longer time periods. The spectra in c) and d) are extracted from the traces at the points marked with the dashed lines. and illustrate how different these properties can be between different nanowires.

and the long-term stability of these emission properties is. The basic properties of the lines can be associated with the specific defect sites at which the charge carriers are localised. This is the main defining aspect of the emission, as the defects stabilise the charge carriers, define their distance and wave function overlap as well as their potential environment, depending on the defect position relative to the wire surface.

These stable properties can now be influenced by changes in the defect site potential environment. The over time behaviour of the T bands can, depending on each wire and signal, be radically different. Three very differently behaving T band emissions are shown in figure 5.16.

The false-colour plots of the spectral traces are shown in figures 5.16a–c. The respective $t_{0.5}$ lifetime traces are shown in figures 5.16d–f and the 100 ms time bin intensity traces in figures 5.16g–i. Each measurement shows a 500 s time frame from a longer time trace, with $t = 0$ being the start of the measurement and also the beginning of the constant illumination of the wire.

The main differences between the three traces can be briefly summarised and compared as follows: The spectra in figure 5.16a show a very intense and constant set of two T bands that barely fluctuate in either position or emission intensity; the spectra in figure 5.16b show two strong T band signals with strong fluctuations, both in the band intensity and position; the spectra in figure 5.16c do barely show a T band at all, the signal only blinks *On* for short periods of time.

For all three traces the luminescence decay time is increased when the T bands are visible. A constant T band intensity equals a constant luminescence decay time. If the T band switches *Off*, a decay time decrease is observed – with one exception at the end of the spectral series in figure 5.16a.

In the trace in figure 5.16b the effect of the dynamics of the emission energy are nicely illustrated: Stretches of constant T emission energy between 2600 s to 2700 s show constant luminescence decay times, while the very dynamic emission energies between 2750 s to 2900 s also show increased lifetime flickering. A closer look at the spectral shifting of the T band and its influence on the emission lifetime will be discussed below.

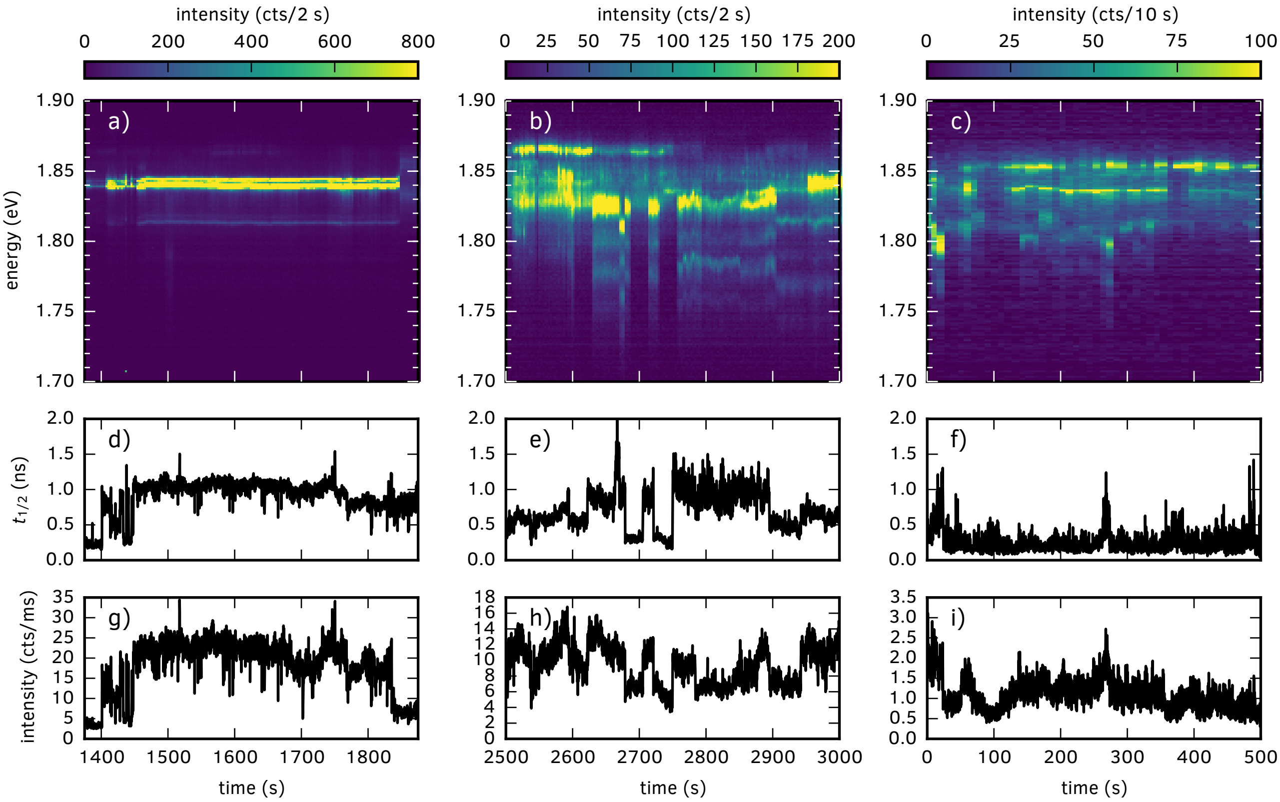

Figure 5.16: Different blinking behaviour of T bands. a), b), c) show three differently behaving T band spectral series as false colour plots. d), e), f) show the respective $t_{0.5}$ lifetime traces. g), h), i) show the respective 100 ms time bin intensity traces.

T band emission dynamics and decay times

A closer look at the T band dynamics is taken in the figure 5.17. From the spectral trace shown in the false-colour plot in figure 5.17a spectra and – from the TTTR trace – decay curves measured at the exact same time were extracted at the two points marked with vertical dashed lines. The decay curve bin time was chosen equal to the spectrum recording time of about 5 s.

The first point for the extraction of the spectra was chosen to represent a point in time where the T emission was especially high in intensity (yellow curves in figure 5.17b,c), while the second represents a low intensity phase of the T emission (blue curves in figure 5.17b,c). The stark contrast in emission intensity of the T emission zero phonon line at 1.791 eV is visible both in the false-colour trace, as well in comparison of the two spectra. At the same time, the NBE and HE emission only show very small changes, mostly a slight redistribution of emission to lines at smaller energies.

The change in decay curves that accompanies this spectral change is a strong decrease of the luminescence decay time. The maximum intensity of both curves is almost constant (141 counts to 130 counts). Exponential fits of both curves reveal the contribution of different channels to the decays. The yellow high intensity curve can be fit best with a third degree exponential decay, which yields the following contributions: a short-lived decay channel with $\tau = 0.03$ ns, which is in the range of the instrumental response function; a decay channel with a decay time of $\tau = 0.48$ ns; a decay channel with a distinctly longer decay time of $\tau = 4.49$ ns. These components contribute to the entire decay with magnitudes of respectively 0.4 %, 8.6 %, and 91.0 %. This means that the long decay and presumably also the T emission dominates the spectrum. In contrast the low intensity decay curve is best fit with a third degree exponential decay with the a 14.2 % contribution of a 0.05 ns decay, a

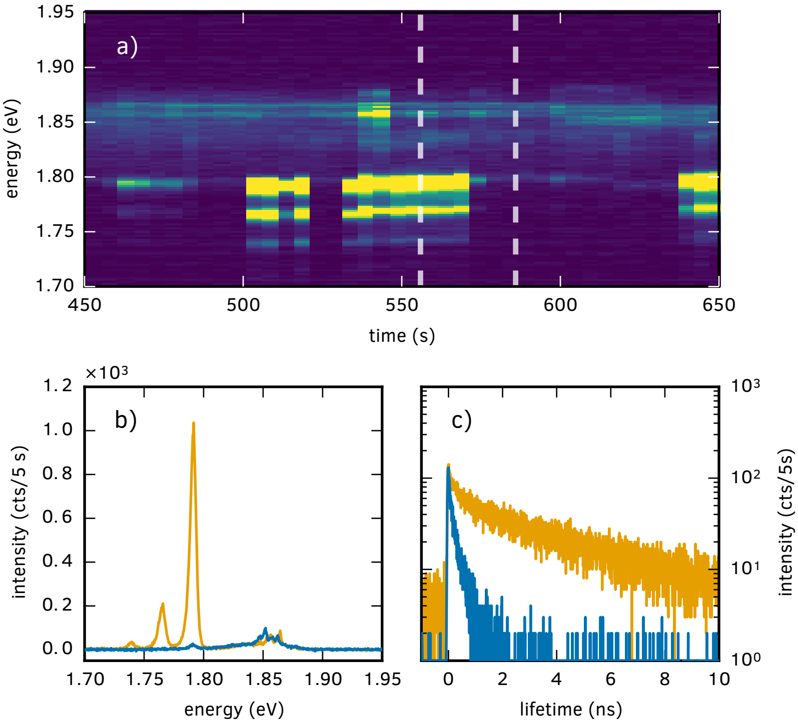

Figure 5.17: a) A spectral trace of showing a blinking T band over a time frame of 200 s. On phases show a well defined triplet of line from 1.791 eV onwards. Two vertical dashed lines mark the points where the two spectra in b) were extracted. The yellow spectrum shows a snapshot of high T band intensity and the blue spectrum a moment of low T band intensity. The respective luminescence decay curves are shown in c) with the colour coding the same as for the spectra.

62.9 % contribution of a 0.26 ns decay, as well as a 22.9 % contribution of a 0.85 ns decay.

For the low intensity decay curve a second degree exponential decay curve – a 0.06 ns component (20.8 %) and a 0.35 ns component (79.2 %) – fits the data just as well. Nonetheless, the more complex mathematical model does describe the data better, especially in regards to the spectral changes.

Under the premise that all three decay curve components are retained and can be assigned to a group of emission bands, the switch between the T peak *On* and *Off* or rather *On* and *grey* states can be described as follows: In the highly emissive state the T band recombination is not competing with a faster recombination mechanism. Through a change in the nanowire defect potential landscape the emission of this specific DAP recombination is quenched strongly – relaxation happens through much faster, competing non-radiative decay channels.

This description is reliant on the clear assignment of the very long decay with $\tau = 4.49$ ns to the T emission. This can for one be done by looking at the area of the T emission relative to the spectrum. In the example shown in figure 5.17, the T emission in high intensity spectrum (yellow line) accounts for 83.2 % of the recorded photons. In the low intensity spectrum the emission is reduced to 16.1 percent of all recorded photons. Both values underestimate the contribution of the slowest luminescence decay for both *On* and *grey* state. Subsequently, other emission bands than the T emission should arise from longer lived charge carrier complexes.

The reverse test of the assignment of the long component to the T emission is the comparison of the spectrally gated T emission trace to the decay time gated TTTR trace. This is shown in figure 5.18. From the spectral trace in figure 5.18a an intensity trace was extracted from the energy region in between the two dashed lines. This trace is plotted in figure 5.18b. To extract the long lifetime component of the trace the last 500 decay curve channels (last 1.63 ns of the ~ 13 ns decay time range) were extracted and an intensity trace consisting only of the photons registered in these channels plotted.

Figure 5.18: Comparison of the blinking of a single CdSe nanowire a) spectrally resolved, b) extracted by specifically adding the T band luminescence c) extracted by defining a decay time gate for the last 500 decay channels (last 1.63 ns of the about 13 ns decay time range). The decay time gate clearly extracts the T band ON state blinking.

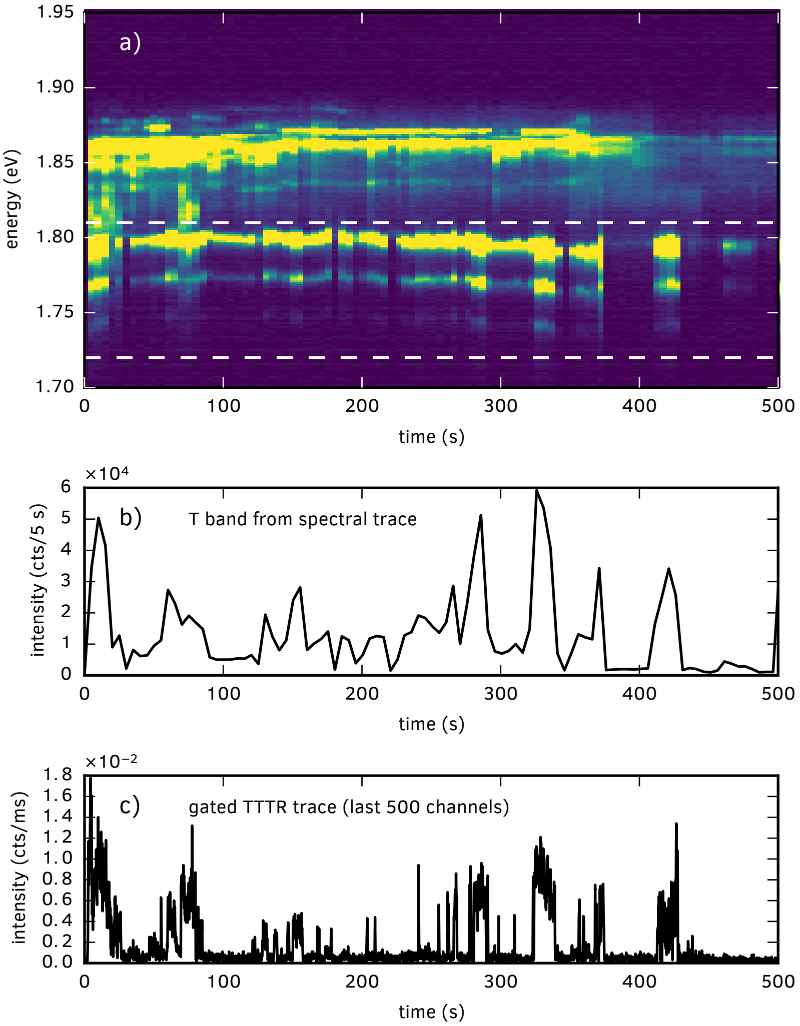

Ignoring the much higher temporal resolution of the 100 ms time bin TTTR trace the main difference between the two intensity trajectories is the much clearer *Off* state in the gated TTTR trace. The *On* phases correlate very well in both traces. At the same time the NBE emission and its dynamics does not noticeably influence the slow decay emission.

Lifetime gating removes the short components, both from the high energy side but also some of the grey states of the T luminescence. This results in flat, defined *OFF* states and well distinguishable *ON* states which – by comparison of spectral trace and both intensity trajectories – can be clearly assigned to belong to the T luminescence. Lifetime gating is therefore an efficient method to extract intensity trajectories of combined intensity fluctuations that are caused by the activation and deactivation of a fast decay route competing directly with the T emission.

In the analysis of CdSe quantum dots every decay of a specific species – the exciton, a charged crystal trion or a biexciton – is usually assigned a specific lifetime[140] or lifetime range.[59] For the nanowire luminescence the two-dimensional charge carrier confinement – and the resulting free movement along the long axis of the wire – will result in different recombination mechanisms. In room-temperature studies this results in much shorter lifetimes – Vietmeyer *et al.* report a third degree exponential decay with the slowest component of about 2.5 ns contributing less than 1 % of the emission.[74] The strong phonon coupling of the nanocrystal emission visible at low temperatures[141] is similar to that of the nanowire T emission. In both cases it implies a strong separation of the electron and hole and a resulting lattice deformation. This also results in longer decay times. For the spectra dominated by T bands this slow decay also dominates the emission lifetime.

In comparison, the reported decay time of bound excitons[11] in CdSe is 0.5 ns to 0.8 ns, which in the *ON* state decay curve corresponds to the second-fastest decay. The *grey* state emission on the other hand shows an acceleration of all components and a redistribution of the emission to mostly the second-fastest decay. In the spectra a simultaneous increase of the low-energy NBE emission can be observed.

Summarising the above, a third degree exponential decay describes a decay curve from a spectrum measurement time size bin well, for spectra showing both NBE and T emission. The T band can be assigned the slower decays and the NBE emission groups the faster ones. Nonetheless, ratios of spectral bands and decay curve – while similar – do not match exactly. When the T emission of a wire switches from the *On* state to the *grey* state all components accelerate while at the same time the ratios of each emission channel is redistributed to the faster decay channels. This implies that the mechanism of luminescence quenching must influence both the specific T band recombination as well as all other radiative decay channels.

T band spectral shifting and decay times

The T bands – and with them their phonon replicas – can show either very sudden spectral changes or a continuous shifting to different wavelengths. These processes are reversible and an emission band's behaviour can change from staying relatively stable to strong shifts or back–and–forth jittering.

For a clear observation of a sudden spectral shift a look at a very clear example is shown in figure 5.19. The spectrum shows a pair of two T bands with phonon replicas which emit at fairly constant energies for about 40 s before both bands jump to higher energies. The energy shift is 14 meV for both bands. The jump is highlighted in the false-colour plot of the spectral series in figure 5.19.

The six spectra from the highlighted area are plotted in figure 5.19b. The intensities of the spectra are offset for clarity. Red crosses mark the maximum intensity of each spectrum. The connecting red line is guide to the eye. In grey the respective decay time $t_{0.5}$ is plotted for each of the shown spectra. The y-value expresses the association to the respective spectra. The connecting line is, again, a guide to the eye.

The energy jump of the emission line is large enough to be very clearly visible in both the false-colour plot, as well as the single line plots. The lines shift, stay at the new, lower energies for slightly longer than the duration of two spectrum integration times (2 × 2 s), and consequently return to their previous positions. The spectra just before and after the complete shift show both lines, as the spectrum integration time is too large to clearly resolve the shift.

This shift of 14 meV strongly influences the luminescence decay time. The $t_{0.5}$ doubles from 1 ns to 2 ns, implying that the new state is significantly more stable then the one before. With the return to the original emission energy, the lifetime also returns to its original value.

Looking at third degree exponential decays, the effect of the jump only affects the slowest of the three components, τ_3, as can be seen in the results of the fits in table 5.2. The two fast components, τ_1 and τ_2 stay mostly the same before, during and after the T band energy shift, as do their amplitude contribution. Only the slowest component increases by more than threefold, from about 2 ns to 6.5 ns. The return of the T band emission energy to its original value is also accompanied by the return of the slow component to 2.3 ns. The relative contribution of the slow

τ_1[ns] (%)	τ_2[ns] (%)	τ_3[ns] (%)
0.07 (4)	0.39 (29)	2.07 (67)
0.08 (4)	0.39 (25)	6.54 (71)
0.09 (5)	0.39 (24)	2.29 (71)

Table 5.2: Results of the third degree exponential fit of curves extracted – top to bottom – before the sudden energy shift, during and after the return to the original emission energy. The values in parentheses are the components' relative contribution to signal amplitude.

Figure 5.19: A strong and sudden spectral shift of the T emission of a single nanowire, a) shown in a spectral trace, b) shown in single spectra. The maximum intensity T line is marked with a red cross and connected with a line as a guide to the eye. The average decay time for the respective points in the trace are plotted at the same y-values as the spectra as grey crosses and also connected with a line as a guide to the eye.

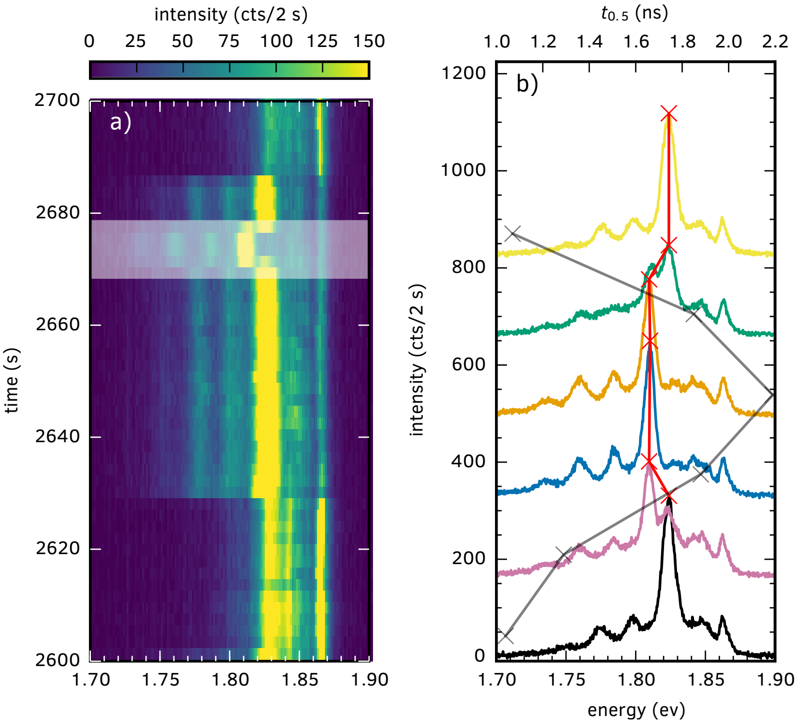

component stays more or less constant during this process.

These observations confirm the attribution of the slowest decay component to the T bands, as spectral change and lifetime change can be directly correlated. They also imply that the mechanism behind the change in emission energy must cause a quite strong effect – the change in emission energy and lifetime is quite significant. It must also be a very local occurrence, influencing only a very limited area or number of sites with the remainder of the spectrum and luminescence lifetime components not being affected.

Also, as this effect influences two clearly separate T lines certain assumptions for the cause of the shift and also the nature of the defects contributing to the emission mechanism can be made. For one the involved defects, or at least one of the two species of the DAP have to be close enough to be influenced by the same effect, as their potential changes by the same amount. These could include two neighbouring defects, or, maybe even more likely, one species – either the donor or the acceptor – being the same defect and alternately interacting with two different counterparts. This assumption also allows more flexibility for the effect causing the jump. A single charge in the vicinity influencing the potential around a single defect is much more likely than a charge influencing two defects equally.

Another important observation is that the position, intensity, and general appearance of the other bands in the spectrum are not influenced at all by the jump, but are in fact influenced by the T-bands switching *On* and *Off*.

While the above sudden jump in emission energy is a clear example which can be easily analysed, it is a small sample of one very specific dynamic. For traces spanning longer time periods a T band – or group of T bands – can also shift gradually, shift back and show intensity dynamics.

The false-colour plot of a 2000 s spectral trace with a T band with various energy dynamics is shown in figure 5.20a. The corresponding TTTR intensity and lifetime traces are shown in figure 5.20b and c. The spectral centroid of the T band was calculated for the area between the two white lines in the false colour plot as a representation of the T band spectral shifting. The spectral centroid is shown as red line in both the TTTR intensity trajectory and the lifetime trajectory. To ease comparison with the other traces the centroid y-axis is reversed.

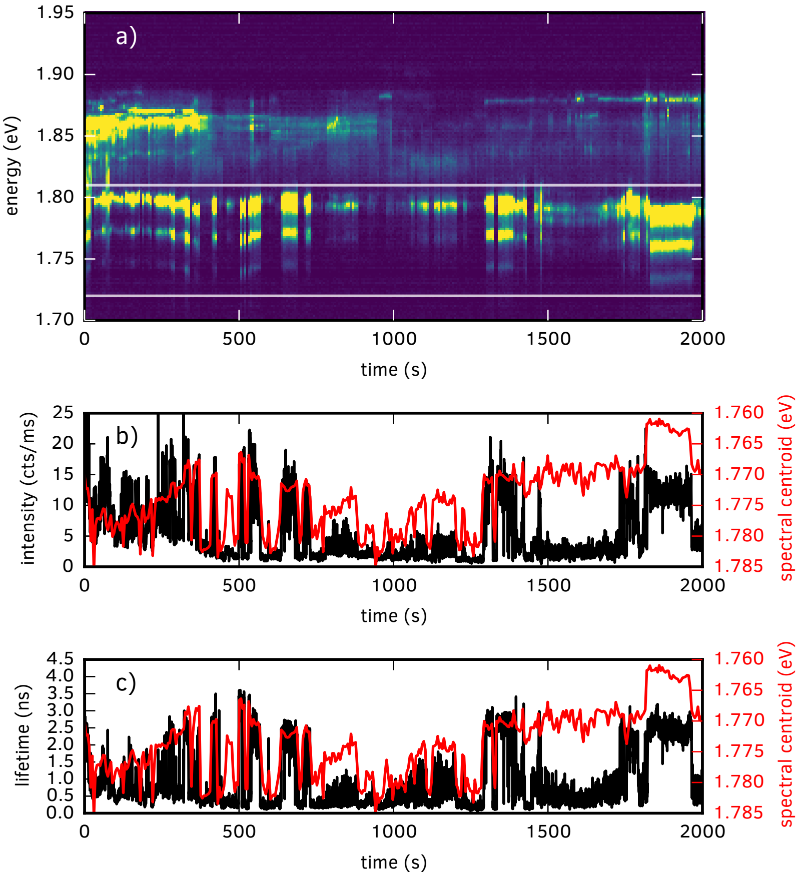

Figure 5.20: Continuous shifting of the T band. a) Shows a spectral trace with a very intense T band with a strong continuous emission wavelength shift. This shift is expressed by the T band spectral centroid plotted in b) with the emission intensity and in c) with the emission lifetime of the whole trace. While the absolute emission intensity does not directly correlate with the spectral centroid, the lifetime does so over long periods of time. Nonetheless there are other factors influencing the emission lifetime as seen in the last 500 s of the trace where the direct correlation is not preserved.

The comparison of the traces shows that while a correlation between changes in T band emission wavelength and intensity exist, the actual values do not correlate. In contrast, a correlation between the emission wavelength and the lifetime is visible, especially in the first half of the lifetime trace. The spectral centroid nicely follows the curved lifetime increase and decrease from 0 s to 1000 s.

As the lifetime of the luminescence is also tied to other factors, such as the luminescence intensity, the scaling of the centroid overlay has to be adjusted from one part of the trace to another. While the TTTR intensity includes the higher energy bands of the emission, a comparison of the low-resolution traces as extracted from the different spectral regions of the spectral trace still do not match the centroid values as well as the lifetime trace does. In reverse, a relative increase in high energy luminescence decreases the absolute lifetime and makes the trace match not as well at some points.

Additionally, for this specific T band in some regions (for example at 1500 s onwards) a strong intensity–lifetime relationship can also be observed, implying additional non-radiative recombinations that do not influence the T band emission energy. The influence of the effects visible in the emission as well as those only influencing the invisible recombinations have to be considered when the emission lifetime is analysed. Interestingly, especially in the later part of the trace, a further decrease in average emission energy does not increase the lifetime further.

T–T-LO phonon coupling

The previous descriptions of the spectral shift always refer to the zero–phonon line. An analysis of the phonon replicas can also give valuable information about the changing environment of the involved defects.

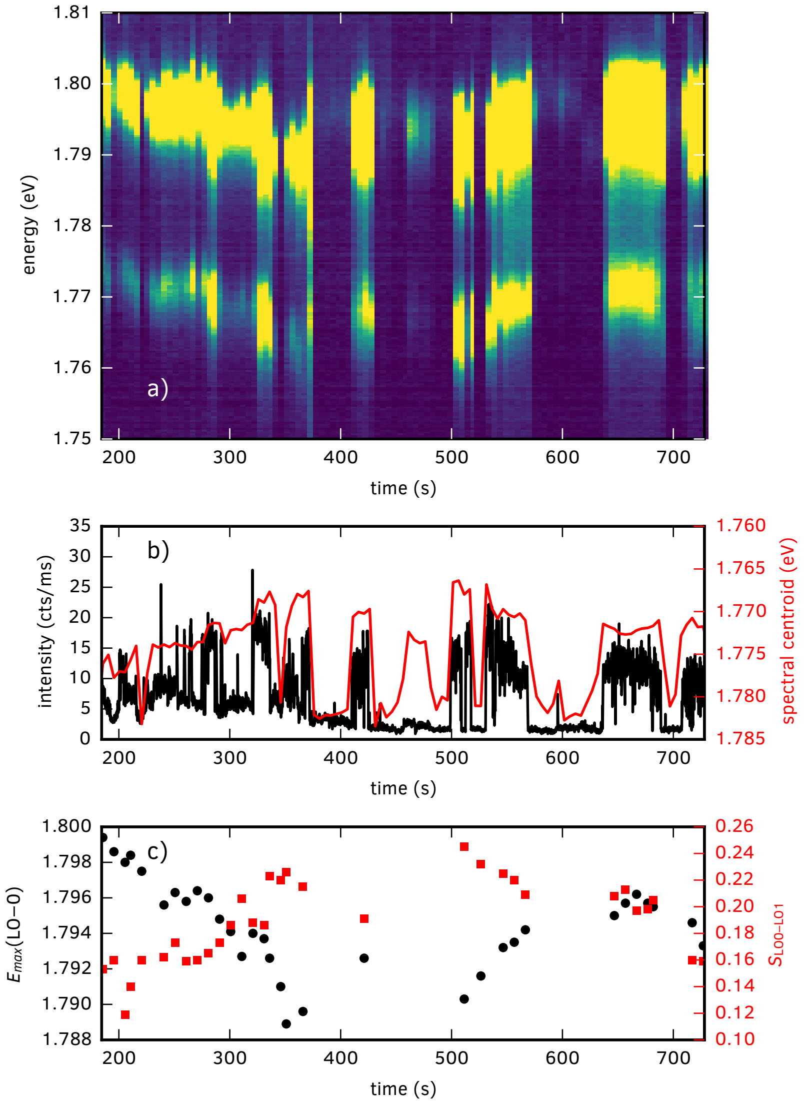

Figure 5.21: T band emission energy shifting and the correlation with phonon coupling of the band. a) shows a ca. 500 s long excerpt of a blinking and shifting T band. The emission intensity and spectral centroid of the T band are shown in the trajectories in b). The zero-phonon line position and the respective Huang-Rhys factor for a selection of sufficiently intense bands is shown in c). It is clear that the phonon coupling increases with decreasing emission energy, which is also linked to an increasing emission lifetime and independent to the emission intensity.

The phonon coupling as a parameter is visible in the relative intensity of a phonon replica to the zero phonon line. The intensity I_n of the n^{th} phonon replica is given as follows:

$$I_n = I_0 \frac{S^n}{n!} \tag{5.2}$$

In equation 5.2 I_0 is the intensity of the zero phonon line and S the Huang–Rhys factor which expresses the magnitude of the phonon coupling. For the first replica the dependence of the Huang–Rhys factor on the emission intensity is reduced to the following expression:

$$S = \frac{I_0}{I_1} \tag{5.3}$$

For an analysis of the phonon coupling of the T band phonon replicas a multitude of spectra were extracted from a spectral trace for a 500 s time frame. The spectra in which the zero phonon line and first phonon replica had sufficient intensity were selected and their intensity and the zero phonon line energetic position were determined.

The false-colour plot of the spectral series, the respective intensity trace and T band spectral centroid, as well as the zero phonon line position and the Huang–Rhys factor are shown in figure 5.21a, b, and c.

The zero phonon line shows a clear blue shift in both the false-colour plot as well as the values determined from the individual spectra. While it is not as clearly pronounced in the spectral centroid, a continuous red shift and then a blue shift back can be made out..

As the energy of the zero phonon line shifts to lower energies in figure 5.21 the phonon coupling increases. The general behaviour of the coupling is clearly opposite to that of the emission energy. The shift of the band energy in this case is 11 meV while the Huang–Rhys factor doubles from 0.12 to 0.24.

Additionally, a plot of the Huang–Rhys factor as a function of the emission energy is shown in figure 5.22. Like the chronological plot suggested, a linear dependence of the coupling is clearly visible.

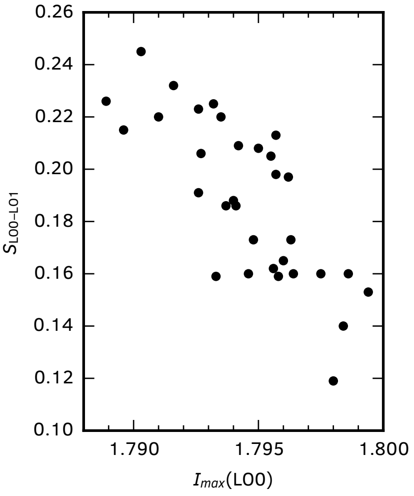

Figure 5.22: Phonon coupling of the first phonon replica dependent on the zero phonon line position.

A comparison of several bands from spectral traces from different wires reproduce this linear trend. The data is compiled in figure 5.23 and shows the phonon coupling of four different T bands from measurements on four different wires from different synthesis batches. The Huang–Rhys factor is plotted against the energy difference of the zero phonon line to the highest energy NBE line observed in each spectral series. This energetic difference serves as the best expression of the DAP state binding energy, which is a more comparable measure than the absolute energy of the line, as this is strongly dependent on the wire diameter and therefore also varies strongly between individual wires.

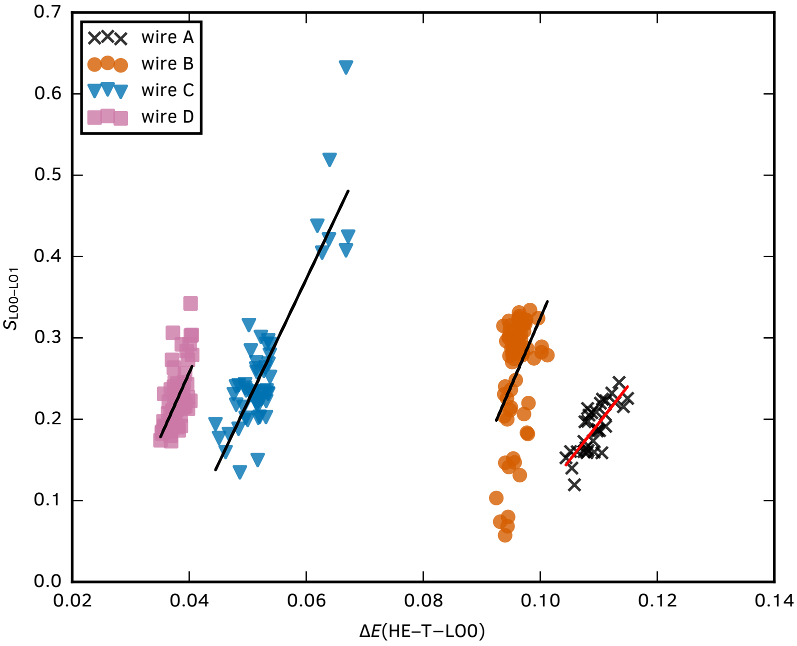

Figure 5.23: Energy dependent phonon coupling for several bands of several wires. The correlation is linear with no clear dependence of the slope discernible.

The data of the sampled signals show a very apparent linear dependence of the phonon coupling to the relative zero phonon line energy. The linear regression for each set of data points is also shown (red line for wire A, black line for wires B, C, and D). The wire A data is the same data that was shown above in figures 5.22 and 5.23.

The phonon coupling shows a strong dependence on the emission energy for all data samples. The slopes of the each linear fit functions are all situated between an increase in Huang–Rhys factor of 0.009 /meV to 0.017 /meV. No dependence of the slope on the relative emission line energy could be found.

In the case of the wire B data, the slope might be even larger than the fit suggests. Due to only very few data points at small S values, the larger amount of points at larger values yield the shown fit.

Another interesting example is the wire C data set. The data points span the largest ranges of both emission energies, as well as Huang–Rhys factors – 0.044 eV to 0.067 eV and 0.135 to 0.632, respectively. These ranges of values are not covered continuously, there is a noticeable gap in data points between S =0.3 to 0.4. This indicates a strong, binary jump in luminescence energy through a process that also strongly increases phonon coupling. In fact, the data points shown in this plot originate from the band shown before in figure 5.19 on page 90. The excerpt of the spectral series showed a large, reversible spectral jump. This indicates a strong change in the potential landscape surrounding one of the involved defects.

An aspect that further emphasises the strong influence of the potential landscape around each individual defect is the care which has to be taken when evaluating the phonon replicas. Each line in the wire spectrum has its own specific magnitude of phonon coupling and its own dependence on the emission energy. Large, long-term samples that conflate multiple emission lines will therefore not show the clear linear increase, but a wide distribution of values.

Phonon coupling of optical emission lines implies that the excited state from whose decay the line arises influences the polarisation of the lattice atoms. As the CdSe lattice does possess an ionic nature, the nominally charged cadmium and selenium atoms will be influenced by both, the existence of any kind of defect and also by the localisation of excitons, and even more so single charge carriers at defect sites. This polar deformation potential interaction – the Fröhlich interaction – leads to the excitation of LO phonon modes.[142]

For the phonon coupling of donor–acceptor pair emissions the interaction between the ionic atoms and the charges is easily visualised. Each charge will repulse the equal charges and attract the opposite charges, polarising the surrounding atoms accordingly. The further electron and hole are apart, the stronger the local effect of the charge, as their mutual charge compensation is reduced with increasing distance.

An increase of the DAP luminescence phonon coupling with decreasing emission energy would now imply a change in the nanowire potential that would both stabilise the DAP and increase the deformation of the surrounding potential landscape.

The following section will take the above described emission properties of the T band into account and describe the possible processes of radiative recombinations as thoroughly as possible.

Summary and emission mechanism

In our previous works[19, 20, 75] the T emission was assigned to donor–acceptor pair recombinations on the basis of literature review of bulk studies. The mechanism had to allow for both a wire diameter dependent emission energy and a certain range of energies at which the zero phonon line could be observed at, for the same wire diameter.

Both the diameter dependence and the apparently random variation in emission energy of the T band could be explained by describing the donor–acceptor pair emission as a radiative recombination of the electron and hole localized at ionised defects, modelled as simple point charges within the cylindrical potential of the nanowire. With the wire diameter and the resulting quantum confinement supplying the energy baseline for the free exciton recombination the localisation at the point charges would now stabilize the charge carriers to a certain degree, depending on their absolute and relative locations. Two extreme cases are shown in figure 5.24.

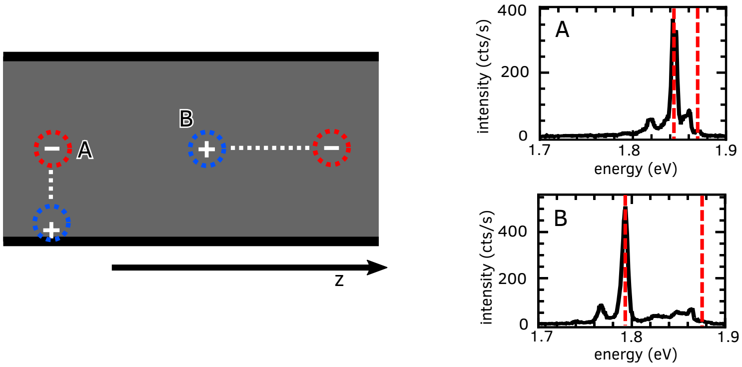

Figure 5.24: Previously proposed emission mechanism for DAP emission in nanowires. The emission energy is dependent on the distance of the two defect sites but also their absolute position within the wire.

The schematic on the left side of the graphic shows for case A two very close defects, symbolised by the minus sign – for the acceptor and a plus sign + for the donor. around the point defects the electron and hole are symbolized by the blue and red circle. In the left case the donor is also very close to the wire surface which further restricts the electron probability density. In case B the two defects are on the other hand much further apart and located in the middle of the wire. This leads to a much more stable donor–acceptor pair complex of the two charge carriers. These two extreme cases explain why two spectra with almost the same HE emission energy can exhibit radically different T emission zero phonon line energies – as shown in the two spectra on the right.

Before continuing the discussion of the T band emission mechanism it has to be said that the above shown schematic of the bound electrons and holes are strongly simplified for the sake of clearly demonstrating the principle of the bound charge carrier complexes. The actual expected wave function of the charge carriers – especially that of the electron – are much more strongly influenced by the wire shape and the limited diameter of the CdSe QNW. To illustrate this, the calculated electron and hole wave function of a DAP in the radial centre of a two-dimensional nanowire slice is shown in figure 5.25. The nanowire has a diameter of 6 nm and exhibits significant confinement on the short x-axis of the shown potential landscape. The hole is much more localized to the acceptor and only barely confined by the limited nanowire diameter.

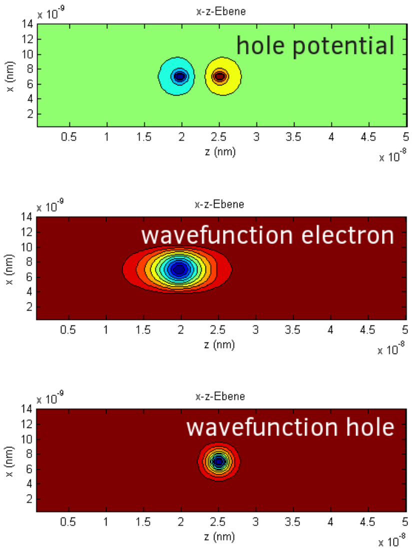

Figure 5.25: Calculated potential landscape for an electron and a hole in a two-dimensional slice of a nanowire.

This effect on charge carrier wave function will always influence the DAP recombination energy. But as it is not crucial for the following explanations it will not be considered. Also, for the sake of clarity, the nanowire will be drawn much larger than it would be in reality.

Now, coming back to the actually observed nanowire luminescence, the comparably simple description of the complexes from which the T emission originates would imply that each T line would have to be extremely narrow in emission energy as its energy would follow the same dependence as it does for every single DAP as defined in equation 2.2. Now, as described above, in the bulk the actually visible broad DAP emission originates from the simultaneous emission from the recombination of DAPs with similar distances between defects. Due to the strong dependence of the position of the defects within the wire potential cylinder this strong energetic similarities between pairs is not likely, with the shifting of the entire T emission not even considered.

A certain emission band width can be explained when considering that pure CdSe is usually n-type.[21, 139] This means that the majority of defects are actually donors. This can lead to the configuration shown in figure 5.26a. A hole localized at a single acceptor can interact and consequently recombine with an electron which can be localised at a multitude of ionised donors. In figure 5.26b the energy diagram of a single donor and single acceptor level is shown next to an energy diagram

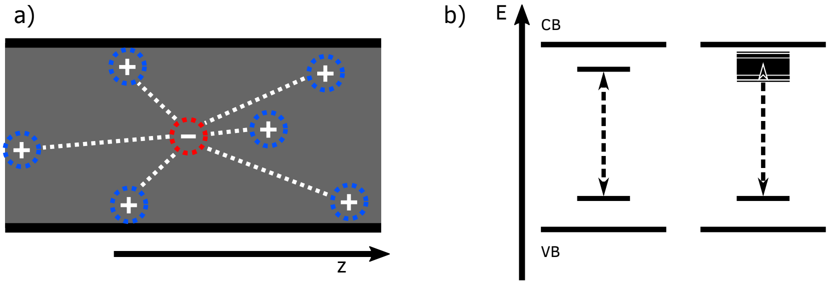

Figure 5.26: A plausible emission mechanism for the T bands has to take into account the width of the emission bands. a) This can easily be done by considering that CdSe is usually n-doped and that multiple donors are available to localize the electron of a photogenerated charge carrier pair. b) Comparison of the energy diagram for the previously formulated mechanism which would infer a narrow emission line (left) and the diagram resulting from the proposed mechanism.

describing the schematic in figure 5.26a. While both the left schematic and the energy diagram show several donor–acceptor pairs at once, this is the result of an observation of a system over time. For each excitation an even number of electrons and holes will be generated. As a hole is localized at an acceptor, there is a certain chance for the electron to be localized at one of the many donors in the same vicinity. Over time the hole localisation spot is constant, while the electron localisation at all the spots is possible. As a certain observation time (= spectrum recording time) results in a spectrum that shows many of the most probable defect pair recombinations at once, in this schematic and all following schematics all possible combinations are shown at the same time.

A spectrum, recorded over the frame of several seconds, will show multiple recombinations of different pair configuration. Like with bulk donor–acceptor pairs, the line width and position is a compromise between availability of recombination partners and wave function overlap – there is a higher chance for closer pairs to recombine but statistically, the farther one looks from the acceptor–hole complex, the more matching donor–electron complexes will be available. This will lead to a certain donor energy range and a distinct acceptor energy (dependent on the defect positions within the wire) yielding the broad emission band.

Within this proposed mechanism of the T band luminescence shifts and jumps of the zero phonon line have to be accounted for. As the emission energy of the T band is strongly dependent on the potential landscape around the involved defects, a reversible change of this landscape is the likely cause of the spectral changes. Also, as the change in phonon coupling is also directly dependent on the change in T emission energy the underlying mechanism also has to influence the charge-carrier related lattice deformation.

A great influence in all nanostructure electronic properties is the relatively large surface. In nanocrystals the strong emission dynamics are generally assigned to surface states and their charging and neutralisation[15, 68, 128, 143]. It is also a readily available source of surface states due to dangling bonds and crystal defects.[144, 145] It is therefore an evident conclusion that the trapping of charges at the surface is a potential change that easily influences the energy of any close DAPs while the system of defects within the wire stays intact. A proposed mechanism for both the shifting and the sudden energy jump is shown in figure 5.27a.

The graphic shows a hole localized in one of the many empty cadmium orbitals on the nanowire surface[144], represented here by positive charges. Due to the closeness and overlap of these empty orbitals the charge can now wander, changing the potential landscape for the defect–charge carrier complexes within the nanowire. Now, a neutralisation of these surface states – either through surface state recombination or through charge transfer to the substrate – will change the potential landscape suddenly, which would be expressed in the spectrum as a sudden energy jump of the T band.

The two processes described above are also expressed as energy diagrams in figure 5.27b. On the left hand side the potential change caused

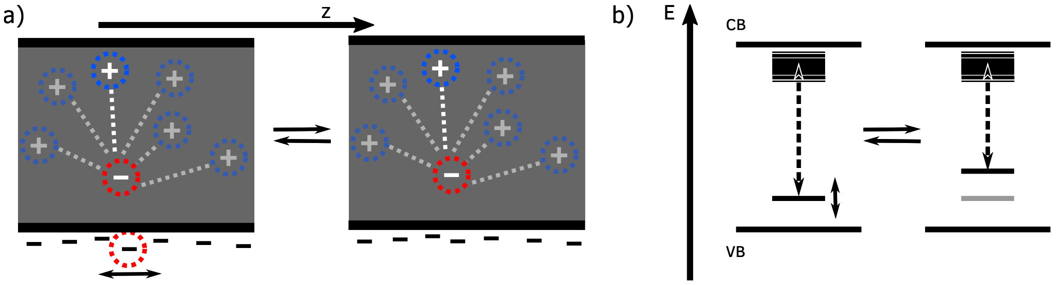

Figure 5.27: A possible mechanism for the shifting and jumping of the T band. a) The localisation of a charge – here an electron – on the wire surface can influence the potential of the defect sites in the nanowire, including the lattice deformation. If the charge carrier moves from defect site to defect site its influence will change gradually, leading to a change in emission wavelength. Through surface recombination this charge can be neutralised, leading to sudden energy jumps. b) Shows the related energy diagrams of these processes.

by the wandering electron will in the shown case mainly influence the energy of the acceptor state which will also change gradually. A sudden neutralisation of the surface state will also suddenly change the acceptor state energy. As the donor states are spread much further spatially they will be influenced differently by a specific surface charge and in their sum to a much lesser degree.

A charge on the nanowire surface will also influence the deformation of the lattice and the phonon coupling of the donor–acceptor pair emission. As a stronger coupling is tied to a smaller emission energy, this means that either the donor and acceptor energies are increased, or that the donor–acceptor distance is reduced. For the case pictured in the schematic, a charged surface state would not decrease the DAP distance, but would rather influence the potential landscape in such a way that the hole probability density would have stronger overlap with that of an electron localised in the wire, as it would be repulsed by the positive charge. This would increase the emission energy of the complex which always goes hand in hand with a decreased phonon coupling.

Now, the discussion of the phonon coupling quickly shows that the actual nanowire is a much more complex system than can be expressed with schematics and simple energy diagrams. It is fairly unlikely that only one charge is present on the surface and, of course, the donor sites will also be influenced by any change in potential. But, as a clear correlation of the amount and direction of the energy shift of all investigated zero-phonon lines with the phonon coupling can be observed, it is likely to be linked to the potential landscape around the one minority defect and its effect on the surrounding crystal lattice.

As a last aspect to be discussed, T bands sometimes do not appear as a single but as multiple, energetically close bands – an example is shown in figure 5.28c – a description within the above detailed recombination mechanism is necessary. This is of special importance as dynamics such as synchronous shifting and jumping of multiple bands can be observed regularly (such as in figure 5.19). The two likely possible origins for such behaviour is pictured schematically in figure 5.28a can be assumed. Either a single acceptor complex will interact with two significantly different clusters of donor complexes, e.g. a certain amount of defect complexes at very similar positions and distances to the acceptor complexes. This will lead to the energy diagram on the left of figure 5.28b, where two distinguishable broad donor energy levels are available for recombinations with holes on the one discrete acceptor level.

The second option is that of two slightly differently situated acceptor–hole complexes being in the vicinity of the same donor complexes. The resulting energy diagram is that of one broad donor band and two discrete acceptor levels.

It cannot be said with certainty if one of these mechanisms happens predominantly. Especially when considering the synchronous dynamics

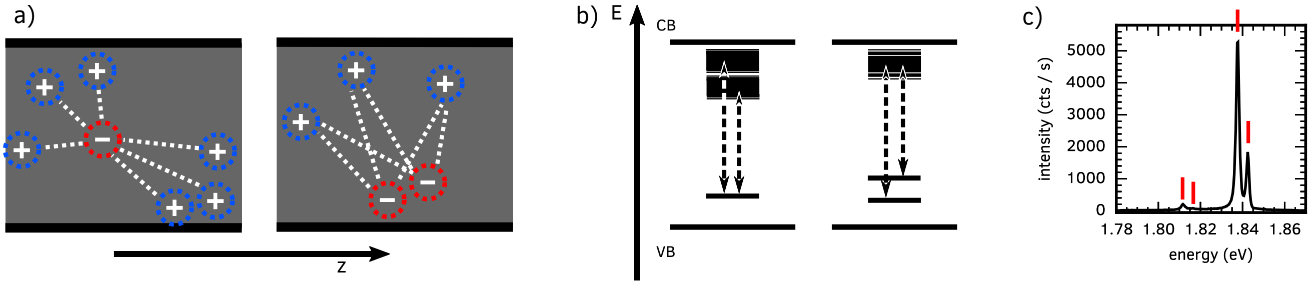

Figure 5.28: Possible mechanism leading to the appearance of two T bands that show the same dynamics. a) Schematics of a single acceptor interacting with two sufficiently different groups of similar donors and two similar acceptors that can interact with the same donors. b) The respective energy diagrams. c) An example spectrum of such a T band pair.

a single acceptor–hole complex appears to be the more likely option as two distinct complexes would be influenced to slightly different degrees by e.g. surface charges. At the same time a case as shown in figure 5.28c where the higher energy band would be lower in intensity would be much less likely, as these spatially closer DAPS would recombine with much higher likelihood. In the end the experimental data cannot exclude either of the mechanisms but not entirely support them either.

The above only describe the radiative recombinations and their dynamics in terms of emission energy. The possible mechanism of the non-radiative dynamics will be discussed below in the chapter 5.3

5.2.3 *The CdSe near band edge luminescence and its dynamics*

Typical appearance

When dividing the CdSe nanowire luminescence by energy and appearance into the two previously described groups with the associated radiative recombination mechanisms a large part of the observable emission bands can not be assigned to either group. A group of bands at distinctly longer emission wavelengths than the HE emission but consisting mostly of quite narrow signals with no distinguishable phonon replicas can be observed for every nanowire. These bands are easily assigned into a third group, as they show very similar if not coherent behaviour within the group. Their dynamics are also very different from that of the two other groups.

This group of nanowire emission can be observed at energies that have previously been assigned as the window where the T band emission would be observed. Going back to figure 5.9 This is nicely visualised in the emission band histogram. The NBE bands could be observed at up to 90 meV lower energies than the highest energy NBE band and the highest energy T emission is shifted only by 20 meV.

These energy ranges overlap quite widely. Two show how the two groups can be differentiated two example emission traces and a representative spectrum below have been plotted in figure 5.29. The spectral trace in figure 5.29a shows nanowire luminescence that consists only of HE and NBE emission. The trace in figure 5.29b shows additional T band luminescence. The white dashed lines in the trace mark the points in time at which the spectra in figures 5.29c and d have been extracted.

The 500 s trace in figure 5.29a shows several quite narrow bands with different intensities. The band with the highest energy is located at about 1.839 eV and can only be observed in spectra later in the trace. The bands with the highest emission intensities are located from energies of about 1.827 eV onwards, which implies a larger stabilisation than most complexes between an exciton and a neutral defect can provide (see section 5.2.1).

All together the trace excerpt shows about ten unique emission band,

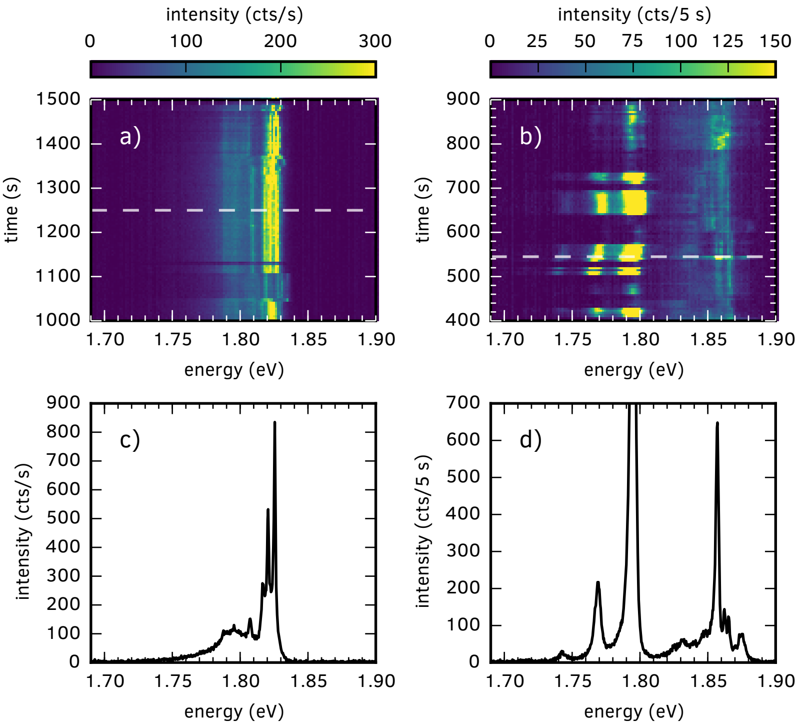

Figure 5.29: Possible appearance of the NBE emission. The signals can appear both exclusively or alongside T emission. a) Shows a 500 s excerpt of a spectral series of a spectrum consisting only of NBE signals, while in b) both NBE and T emission is visible. The dashed horizontal lines in both series mark the point at which the spectra were extracted that are shown below the respective series in c) and d). The spectra are scaled to show the NBE emission. Even with a strongly dominant T emission as shown in d) the general shape of the NBE lines is very similar to that of the spectrum in c), implying that these are the same kind of emission lines.

most of them in the energy range formerly only assigned to T bands. None of the bands shows distinguishable phonon replicas. Over time two kinds of dynamics can be observed. Single bands can shift and switch on and off and, quite clearly seen between 1000 s to 1150 s, the entire luminescence signal group can decrease and increase in intensity.

An overview over the relative emission intensities gives the spectrum in figure 5.29c. A closely spaced group of narrow high intensity bands occupy an energy range of about 20 meV. The emission reaches much further into the red, with the tail of the a decreasingly defined cluster of signals reaching down to almost 1.75 eV. This division into two groups can be observed for all wires, but better for those with high-intensity NBE emission.

An example for the reproduction of this pattern in a mostly T band dominated luminescence is shown in figures 5.29b and d. In this case the T band is shifted exceptionally strongly to the red and the overlap with the NBE emission is minimal. The T emission is easily recognised by the two – at times even three – phonon replicas and its almost binary intensity behaviour. The NBE emission seems quite faint in comparison, but as in the previous example single narrow bands switch on and off and the entire emission group also shows intensity dynamics. Scaling one of the spectra to ideally show the NBE emission reveals the group of narrow intense bands and the broadening tail as seen before in figure 5.29c.

The broad tail and its dynamics is closer examined in the waterfall plot in figure 5.30. From spectrum to spectrum it becomes clear that several narrow bands do in fact contribute to the broad emission. Comparing the different spectra, single local maxima can be assumed as far to the red as at about 1.783 eV (50 meV from the blue-most HE line) a shoulder can be made out at this energy in the black spectrum. Maxima of several narrow bands appear at other energies in the other spectra, implying that the overall width of the emission can be caused by an overlap of a multitude of states with slightly different energies.

In terms of intensity fluctuations of the NBE emission two different processes can be differentiated. One is the fluctuation of single lines and the other is a decrease and increase of the emission intensity of the entire

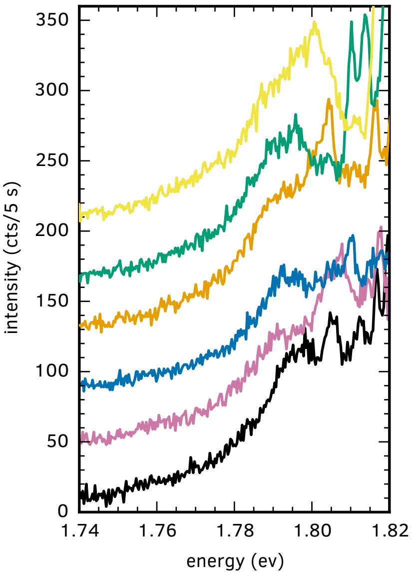

Figure 5.30: The low intensity broad low energy side of the globally blinking spectra also suggest a fine structure which changes over time.

spectrum. In all spectral traces with a sufficiently intense NBE emission both processes can be observed. An example showing a spectral trace and intensity trajectories extracted from different wavelength regions of the trace are shown in figure 5.31. The five traces in figures 5.31b–f were extracted from the trace in figure 5.31 for b) the entire wavelength range and c–f) only at the wavelengths marked with the dashed lines, coloured exactly like the lines in the respective line plots, showing the extracted traces top to bottom from high to low energy. The width of respective wavelength ranges was kept as large as possible to account for shifts in emission energy but this was restricted as close emission lines often overlap.

A comparison at first glance shows that some intensity changes are visible for all bands, as well the overall luminescence intensity. Three different intensity phases – relatively high in the first third , then a significant reduction in the second third and a slight recovery for the last third of the observation time – can be made out at most wavelengths. If the signal intensity is sufficient, the traces show some of the same intensity changes – increases and decreases. An example for a general intensity decrease is marked with the leftmost dashed vertical line in the intensity traces, just below the 500 s mark. The decrease is visible at the same time in all traces, even if the individual traces show very different fluctuations in the direct vicinity of the shared event. The second black dashed vertical line (at about 1300 s) shows a wavelength independent increase in intensity. These wavelength-independent decreases and increases in intensity can be found throughout the whole trace.

Nonetheless, all bands also show individual fluctuations that the others do not and the red-most band in figure 5.31 even seems to switch into a *grey* emission state completely in the second emission phase of the nanowire. Examples for emission fluctuations that are only visible in the traces in figure 5.31c and d are marked with vertical dashed lines, coloured like the respective intensity trajectories, at about 2700 s and 2200 s. These wavelength dependent events can be regularly observed in the traces of each individual emission line. Generally, especially the more intense high energy bands can be observed to fluctuate individually between an *On* state and a *grey* state, very similarly to the T emission.

While single bands can be extracted and analysed to a certain degree, they cannot be as cleanly extracted from the spectral trace as the T band emission. This is due to the very bands appearing very close in energy and also shifting in energy over time. An example of the overlap between bands is shown in figure 5.32. This magnification of a segment from the trace in figure 5.31a shows at least three distinguishable emission lines with the mean maxima of emission at about 1.850 eV, 1.840 eV and 1.835 eV.

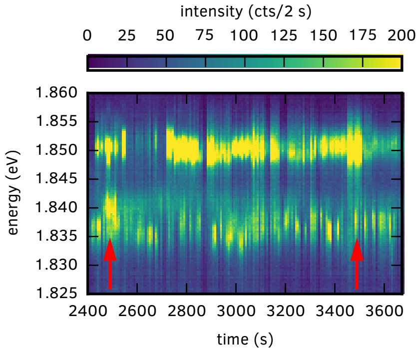

Figure 5.32: The shifting and overlap of distinct NBE emission lines. All three NBE lines show energy dynamics that lead to overlap at certain points of the series, as shown at the points marked with red arrows. This makes the exact extraction of intensity traces of single lines nigh impossible.

While especially the two closer lines overlap repeatedly, even the slightly further blue line does shift in such a way that the emission distribution reaches into the middle line. Examples for times in the trace at which the overlap of the emission bands is visible are marked with red arrows. The first arrow at just below 2500 s shows the two bands at lower energies clearly overlapping due to the energy shift of both signals. The second arrow at about 3500 s shows how even the much farther, high energy emission can overlap with the two other band, in cases of high emission intensities. the actual contribution of the band at 1.840 eV is not clearly distinguishable at this point in time. For a single line analysis the observed overlap makes clear distinction of certain dynamics nigh impossible.

Like the nanowire fluorescence dominated by T bands, wires that only exhibit NBE emission also show lifetime blinking. Example changes in emission spectra and the related lifetime changes are shown in fig-

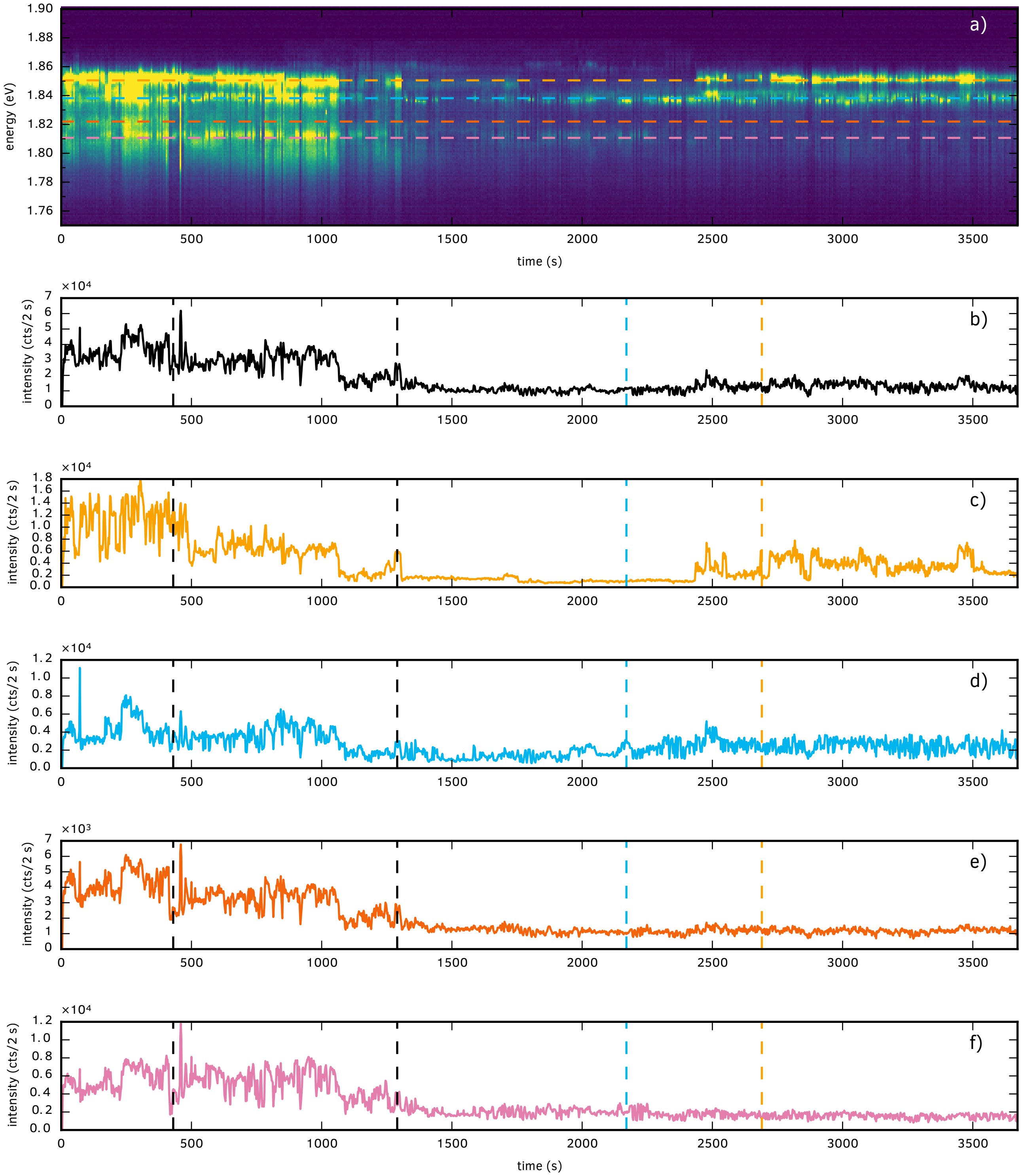

Figure 5.31: The emission energy dependent intensity fluctuations of the NBE emission. a) Spectral trace of NBE dominated wire luminescence. The dashed horizontal lines show at which energies intensity traces were extracted from the spectral series. The colour coding is the same as for the respective traces in the plots c)–f). b) The intensity summed up over the entire spectrum. c)–f) The intensities summed up over 4nm spectral ranges with the centre at the respectively coloured horizontal lines. While single lines can show individual fluctuations (coloured vertical dashed lines) strong emission intensity changes (black vertical dashed lines) can be observed throughout the whole spectrum.

ure 5.33a and b, respectively.

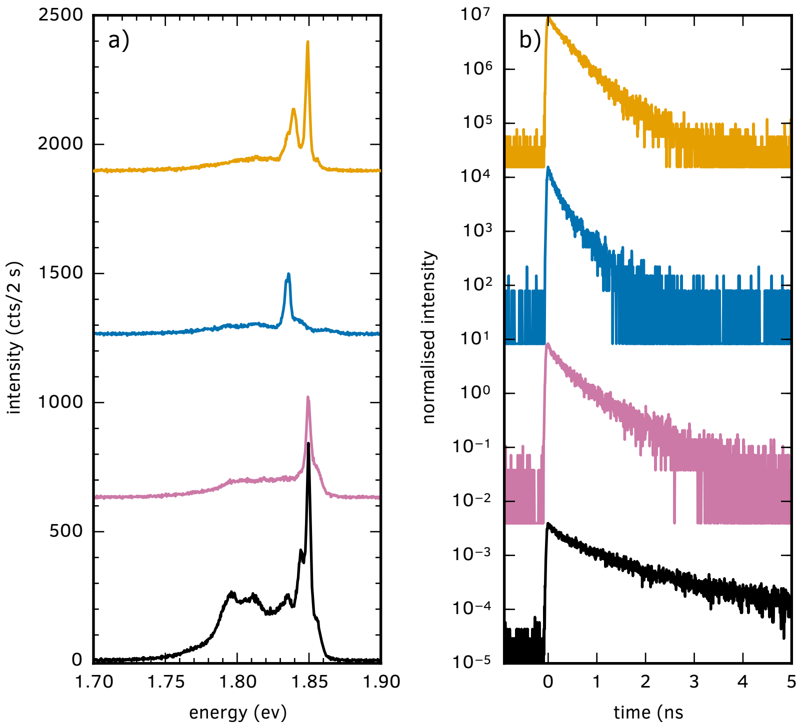

Figure 5.33: Changes in NBE emission and decay time. a) Spectra recorded at different points in time of a longer emission trace. Spectra are offset for clarity. b) The respective decay curves, as extracted from a simultaneously recorded TTTR trace. The curves are offset for clarity. The offset and colour coding correspond to that of the spectra.

The fluorescence lifetime of the NBE emission is dependent on the emission intensity and not the exact radiative NBE decay channels active at any time. The main emitting bands change strongly between the spectra, but a red shift in the main emission can go together with a strong acceleration of the luminescence decay if a a general decrease of intensity is simultaneously observed.

τ_1[ns] (%)	τ_2[ns] (%)	E_c[eV]
0.49 (30)	2.24 (70)	1.819
0.26 (32)	0.82 (68)	1.823
0.11 (28)	0.39 (72)	1.814
0.24 (26)	0.52 (74)	1.824

Table 5.3: Results of the second degree exponential fit of curves extracted – bottom to top – at different points of a 3600 s spectral trace.. The values in parentheses are the components' relative contribution to signal amplitude.

This is quantified further by the values of the second degree exponential fit and the respective spectral centroid listed in table 5.3 At all extracted snapshots of different points of the emission trace show the same pattern of a short decay component that contributes around 30 % of emitted photons and a second, slower component that contains around 70 % of emission. During a change in emission lifetime the relative contributions stay almost constant, while both components equally decrease or increase in value. The spectral centroid – the weighted mean of the emission energy – shows no connection to the lifetime changes.

In summary, a change in emission intensity of the NBE emission directly affects the emission lifetime – an increase is correlated with a deceleration of the radiative decay while a decrease correlates with an acceleration. The overall intensity in- and decreases are usually not wavelength-dependent. In- and decreases of individual bands do not appear to significantly change the emission lifetime. This implies that the states leading to the NBE emission are quite similar in kind and therefore have quite similar lifetimes, much more so than the T emission. The strong dependence on emission intensity points to a the lifetime being strongly dependent on the lifetimes of the available competing non-radiative decays.

Interaction between bands

The above described similarity between the NBE bands and the distinct difference to the T bands can be further seen in the interdependent fluctuations of different bands. These dependent dynamics or interactions can be well observed in spectral traces but are hard to extract in the form of intensity trajectories due to the above described emission band shift and overlap. An example that shows the interdepending disappearance and reappearance of certain narrow NBE bands is shown in figure 5.34.

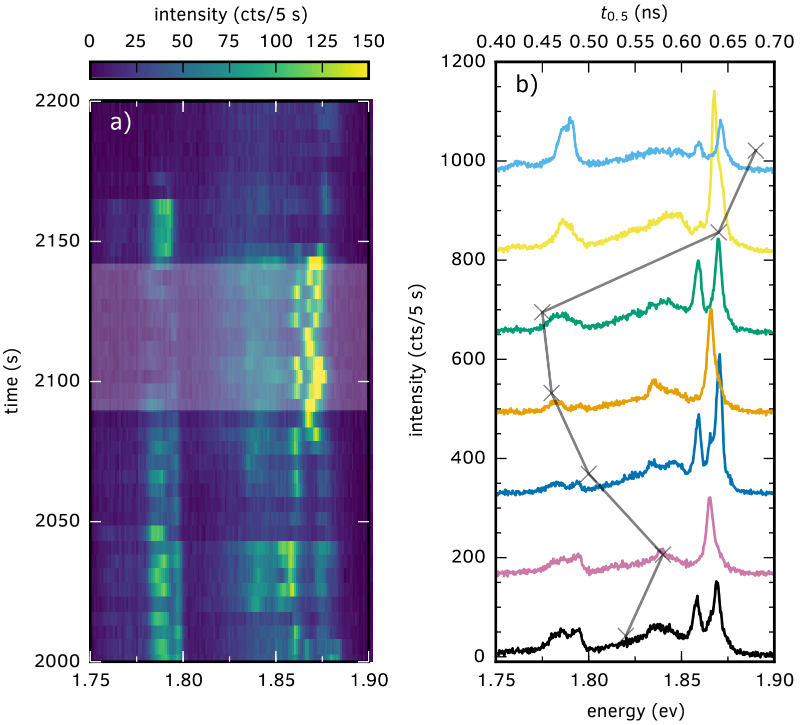

Figure 5.34: Interaction between NBE bands. Spectra are offset for clarity. a) Spectral series in which the NBE lines around 1.86 eV change within the spectrum integration time from a single signal to a pair of signals just to the blue and red of the original line. The relevant time frame is marked as slightly lighter in the trace. b) A selection of spectra from the time frame marked in the in the spectral trace. Over the offset spectra the respective average decay times are shown with the grey line functioning as a guide to the eye. It is clear, that the decay time is much more strongly influenced by the intensity fluctuations of the T emission than the spectral change of NBE emission.

The NBE signals in the energy range between 1.850 eV to 1.875 eV either appear as a single narrow line, or two lines, one to the red and one to the blue of the single signal. In the spectral trace – figure 5.34a – this is visible especially well in the area marked with a slightly lighter square. The change between the two states does not happen regularly and only in a time window of about one minute. But within this timeframe and the spectral time resolution the change can be made out several times, as can be seen in the selected spectra in figure 5.34b. The spectra are shown in chronological order, bottom to top, but spectra in which no change was visible are omitted. The grey crosses plotted at the same y-value of each spectrum represent the average lifetime $t_{0.5}$ extracted from decay curves at the same time as the recording of each spectrum and with a bin time equal the spectrum recording time.

The change between the single emission band and the pair of emission bands can be easily made out on the high energy side of the spectrum. Within the several seconds integration time sometimes all three of the bands can be observed, which suggests either a change significantly faster than the 5 s integration time or the possibility of the different bands being not exclusionary. As the observation of only either the single signal or the signal pair can be nicely repeated within the selected time frame, the former is more likely.

The described interdependent change in emission luminescence does not significantly change the decay time of the luminescence. In fact, the decrease and subsequent recovery of the intensity of the sometimes much less intense T emission at 1.89 eV is a much more significant influence on the average decay time.

The above observation supports the assumed similarity of the origin of individual NBE bands but also implies that the mechanism have to consider the possibility that different types of states – such as complexes between defects and charge carriers – can influence each other.

A further observation that has to be taken into consideration when

Figure 5.35: Interaction between NBE bands and T bands. a) A spectral trace showing a clear connection between the high-intensity or *On* state of a group of T signals and the intensity of the NBE emission. horizontal white lines show the points in time at which spectra have been extracted that have been plotted in b). Spectra are offset for clarity. Grey crosses at same offset level as the spectra show the average decay time at the time of the recording of the spectra. The grey lines are a guide to the eye and highlight the clear increase in decay time with the increase in T emission.

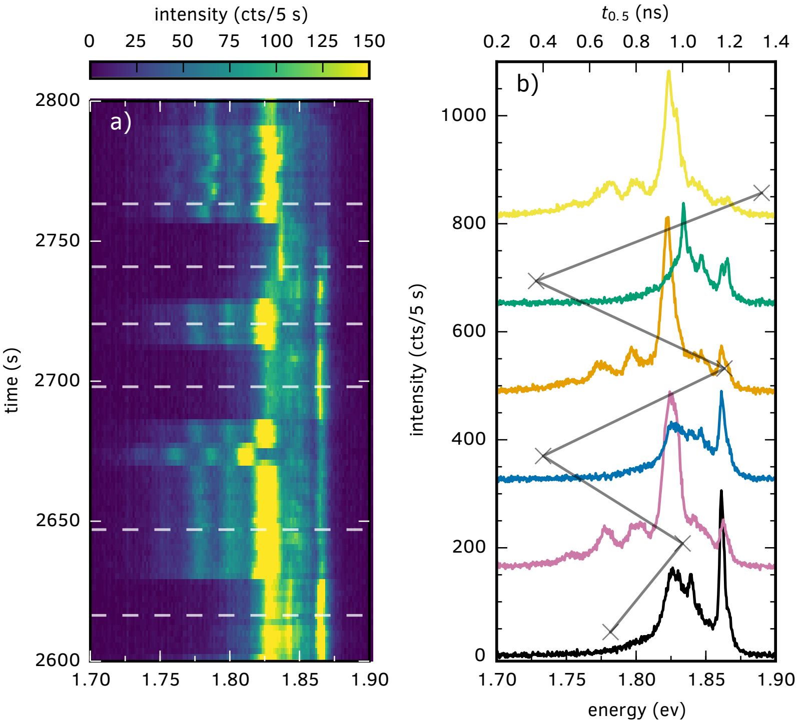

formulating a NBE band emission mechanism is the interaction between T bands and NBE emission, as seen in figure 5.35. As is clearly seen in the spectral trace in figure 5.35a the appearance of the two T bands and their phonon replicas (the first zero phonon line is visible at 1.825 eV) correlates with a marked decrease in NBE emission intensity, but not a complete disappearance.

The vertical dashed lines mark the positions from which spectra have been extracted an plotted in a waterfall plot in figure 5.35b. The arrangement bottom–to–top coincides with the chronological order in which the spectra have been recorded. Grey crosses again mark the average decay time $t_{0.5}$ at the same y-height of the respective associated spectra. The connecting line is a guide for the eye.

As can be seen, with the appearance of the T emission in the spectrum the formerly dominant NBE bands decrease in intensity. This is most noticeable for the single, defined emission lines, which often are still visible in the spectra with visible T bands. The distinct pattern of zero phonon lines and replicas in turn cannot be made out in the emission phases with strong NBE emission, suggesting a very low intensity *grey* state or even an *Off* state.

The average decay time is also strongly linked to the spectral change. The fluorescence decay slows down from 0.4 , to 1.4 , almost tripling. This strong change is easily linked to the appearance of the T emission.

The above observations imply that the NBE emission and the T emission involve at least partly the same defects, but that the DAP complexes as a source of the T band recombinations are much more stable than the species whose recombination yields the NBE emission.

The above example shows a switching between a NBE-dominated emission and a T band-dominated emission that is also correlated with a significant increase in emission intensity. This could imply that the increase in emission lifetime might also be mainly dependent on the emission intensity for the T emission.

The spectral trace shown in figure 5.36 shows that this in fact not the case. In this spectral series the emission is NBE-dominated in the beginning and, around 400 s changes to show a T band with phonon

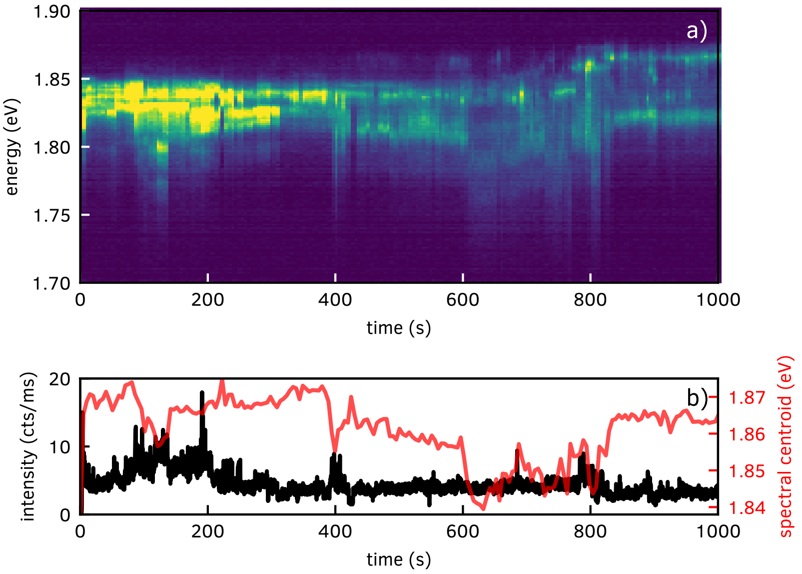

Figure 5.36: Changes in emission wavelength without a significant change in average emission intensity. a) Spectral trace that shows strong changes between 400 s to 800 s with the appearance of T emission in a spectrum that before only showed NBE emission. b) Intensity trajectory (black) and spectral centroid (red) show that the emission intensity is fairly constant from 300 s onwards. While the spectral centroid shows strong fluctuations of the weighted average emission energy, the emission intensity is not influenced by that.

replicas. This happens without a significant change in overall emission intensity, as can be seen in the intensity trajectory shown as a black line in figure 5.36b. The red line in the same plot is the respective spectral centroid, which changes significantly at around the 400 s mark, shifting to smaller energies. The value returns to fairly constantly high energies just after 800 s, at which point the spectra also return to a NBE-dominated emission, albeit one with different bands showing more intensely.

In short, the radiative recombinations are more or less redistributed from one kind of recombination channel to the others. This redistribution can be seen well in single spectra extracted from different points in time of this trace. A collection of spectra, one before the appearance of the T emission, three from different points of time during the presence of the T bands, as well as one spectra after the return to only NBE emission is shown in figure 5.37. The spectra are shown chronologically, bottom to top.

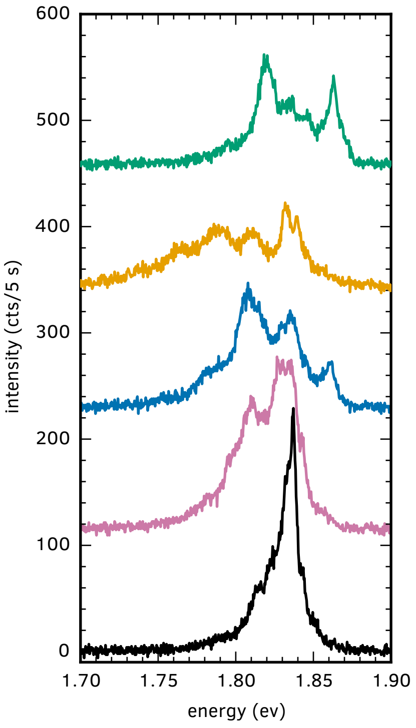

Figure 5.37: Different spectra at different points in time during the emission energy redistribution as shown in 5.36. The spectra change from an emission without T lines to a a state in which T emission dominates. At last, the spectra return to a state with no T emission but spectrally different NBE emission.

The most significant marker in these spectra as to whether a high-intensity emission signal can be assigned to the NBE or the T emission group are the phonon replicas. The zero phonon line and two replicas each are marked in the three middle spectra. All in all, the spectra look all quite different and a significant decrease in maximum luminescence intensity can be observed from the first, bottom spectrum to the last spectrum, with the width increasing significantly. From the first to the last spectrum, bands to both the blue and the red of the former emission maximum increase in intensity, resulting in a slight net red shift.

The impact of this spectral shift on the emission lifetime is shown in figure 5.38. The figures 5.38c and d show an intensity trajectory and a lifetime trajectory respectively, extracted from the TTTR file. The plot of each of these intensity values against the lifetime values is shown in figure 5.38b, with each dot representing a measurement time bin and the heat colourscale further representing the density of the dots. This FLID shows the intensity change between a short lifetime state and a long lifetime state, usually between an *Off* and *On* state. In the shown example, both lifetime and intensity either show intermediate states or change faster than the chosen time bin allows to resolve, leading to streaks between the recorded maxima.

For this nanowire specifically the average lifetime $t_{0.5}$ recorded the most is around 0.5 ns at an emission intensity of 3 counts/s. Many of the states with significantly higher emission intensities follow the intensity–

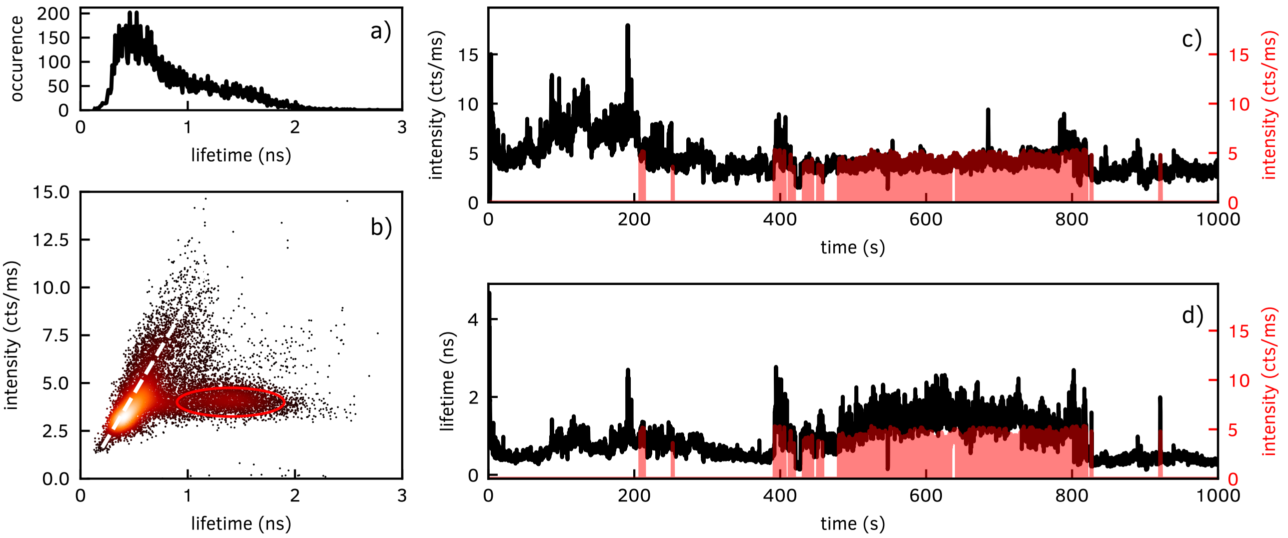

Figure 5.38: Intensity–lifetime relationship for the nanowire luminescence shown in the spectral trace in figure 5.36. a) Lifetime histogram. b) Fluorescence lifetime–intensity diagram. There are clearly two different intensity–lifetime relationships visible. The dashed white line is a guide to the eye and marks the change between a quickly decaying low intensity state and a high intensity state with a longer lifetime. The change happens much quicker than the 100 ms trace bin time. Marked by a red ellipse is the third state or cluster of states which shows a broad lifetime distribution at the same intensity level. The events within the ellipse are marked in the intensity trace and the lifetime trace in c) and d) and can be clearly linked to the spectral area of intensity redistribution.

lifetime relationship marked by the dashed line. As the points scatter significantly, the line is meant as a guide for the eye. Generally, while the exact amount of intensity increase tied to a certain lifetime increase falls into more of a range than it is a distinct value the two are tied nonetheless.

This stands in contrast to the cluster of events stretching in-between average lifetimes of 0.5 ns at an emission intensity of roughly 4 cts/ms. It is marked in the FLID by a red ellipse. This lifetime increase is clearly intensity-independent.

The events within the ellipse are marked in the two trajectories in figure 5.38c and d by a red overlay. It shows that this specific lifetime–intensity behaviour is connected to the times when the T band can be made out in the spectra. This shows the clear distinction between the T band emission and the NBE signals.

In figure 5.38a the associated lifetime histogram is shown. It reinforces that the T band emission lifetimes largely depends on the emission mechanism and the stabilised DAP complex, while the NBE emission lifetime , even if it can be sometimes found at similar energetic distances from the HE emission, is much more strongly influenced by the competing non-radiative emissions.

The above also implies a saturation of the T states. As they are long-lived but can also be seen at relatively low emission intensities the emission pathway is either preferred to the short-lived non-radiative emissions or can only be seen when these non-radiative emission channels are not available.

The above shows that the make-up of the emitting states will change over time with slower recombination pathways emerging, while the number of excitons available for radiative recombination stays the same. A faster recombination path should always be preferred, this means that the previously available fast recombination is not available anymore, at least not to the previous extent, when the slower radiative paths become visible in the spectrum. When a new, fast radiative decay becomes available the recombination will preferably use this pathway.

The previous behaviours therefore show both that the actual number of radiatively recombining charge carriers is not only determined by the competition with non-radiative pathways and that also the available different radiative pathways can change and compete for the charge carrier pairs.

5.2.4 Near band edge emission mechanism: expanding the existing model

Looking at the literature describing the bulk CdSe mechanism mostly the DAP emission and the HE emission are described and reported.[21, 105] Emission lines that are energetically situated between the two groups often are assigned to non-specific defect-related recombinations or to DAP recombinations.[105]

As can be seen in the CdSe emission dynamic, the luminescence has to be divided into three groups. Considering the three very different behaviours, a third recombination mechanism has to be considered in addition to the HE recombination of weakly bound excitons and the DAP–recombination-caused T emission.

Looking at those publications that assign specific mechanisms to lines within the proper energy range that do not have phonon replicas the results are inconclusive. The review by Fasoli *et al.* assign a line without a phonon replica at 33 meV energy distance from the exciton to a DAP for polycrystalline material and another line at 36 meV – originally from the report by Arora & Ramdas[106] – to a not further defined donor state. Other lines that their sources report either fall within the HE energy range or are assigned to DAP recombinations or deep states.

The publications that report bands with the observed appearance in the right energy range are fairly small in number. Arora & Compton report some lines in the range between 10 meV to 37 meV that are all assigned to complexes of excitons with neutral and ionised donors, their excited states, as well as their phonon replicas.[135]

Tarbaev and Gnatenko *et al.* report emission signals with a very similar spectral shape at energies between 20 meV to 60 meV.[139, 146, 147] They assign these to defects caused by the strain of crystal defects. In the publication by Tarbaev the formation of a dislocation rosette in the prismatic plane after indentation of the {0001} phase and the {1010} phase are specifically named.

In contrast, Jäger-Waldau *et al.* assign the band that they observe at 60 meV energy distance specifically to a free–to–bound transition and any bands at lower energies to DAP recombinations.[148]

Considering the very distinct behaviour of the DAP-related T emission of CdSe nanowires only two emission mechanism can be considered as likely sources of the non-HE NBE emission. The complexes whose recombination can be considered are pictured schematically in figure 5.39.

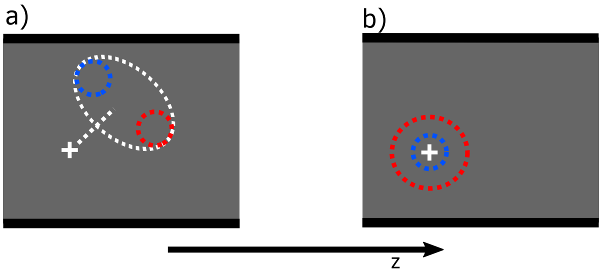

Figure 5.39: The two possible charge carrier pair–defect complexes leading to NBE emission. a) An exciton bound to a ionised donor. b) A free–to–bound complex with one charge carrier pair (here the electron) strongly localised at the defect while the other is comparably delocalised.

The first prerequisite that both options have to fulfil is for one that they have to lie energetically lower than the excitons bound to neutral defect sites but higher than the lowest expected DAPs. The two possible complexes between defects and excitons or charge carrier pairs are the exciton bound to a ionised defect site (figure 5.39a) and the partially localized charge carrier pair (figure 5.39b). These are also the two options agreeing best with the assignments found in the literature above. As native defects in CdSe are more likely donors, these are shown in the two schematics and will also be used in all schematics further on. The second prerequisite is that the emission line behaviour – narrow in energy, less likely to have a lattice contribution in the recombination process, shifting and blinking dynamics – has to match the observations in the recorded data.

The self-consistent calculations as done by Christian Strelow and Tobias Kipp and described by us in [75] have been successfully used to explain the formerly reported two signal groups – HE-NBE and T emission. This leaves the above two species of charge carrier–defect complexes to be investigate as the possible cause for remaining NBE emission, namely those involving the interaction with one ionised defect.

The potential landscape of such a nanowire segment containing one defect and an exciton – the charge potential, the potential for the hole, and the wave functions of both electron and hole after optimization – is shown in figures 5.40, 5.41, and 5.42. As before this is a two-dimensional cross section of a nanowire with a 6 nm diameter that does not consider relative positions within a three-dimensional body.

Figure 5.40 shows the localisation of a charge carrier pair at an ionised donor. In this case electron is localized at the donor, while the hole is localized to one side of the defect. The wave functions of both charge carriers are strongly confined due to the small wire radius. The electron and hole wave functions still show significant overlap, suggesting that the exciton is stable. This case would fit best to the description of an exciton bound to a charged defect.

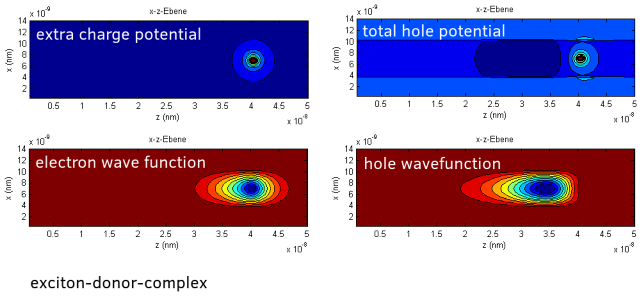

Figure 5.40: Potential landscape for an donor–exciton interaction with the defect situated in the centre of the wire.

Figure 5.41 on the other hand shows the localisation of a charge carrier pair at an ionised acceptor that is located at the centre of the wire. While the hole is strongly localised at the defect, the electron is strongly delocalised, with no increased localisation near the bound hole. This implies that the charge carrier pair is not bound anymore, ergo the exciton is not stable. This case is closest to one would expect to be the excited state leading to a free–to–bound transition.

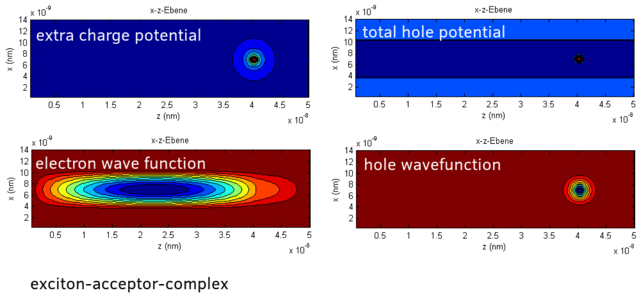

Figure 5.41: Potential landscape for an acceptor–exciton interaction with the defect situated in the centre of the wire.

In contrast, if the charged acceptor is located closely to the wire surface, as shown in figure 5.42, the hole localisation is slightly reduced and the electron wave function localises more strongly near the defect–hole complex. Electron and hole are likely to be bound to each other, ergo the exciton is preserved. This case shows that the preservation of the exciton and the nature of the excited state which possibly yields the NBE luminescence – bound exciton recombination or free–to–bound recombination – might be strongly dependent on the actual position of the involved defect in the wire. It also implies that the two states are not necessarily binary but likely include a range of wave function overlaps.

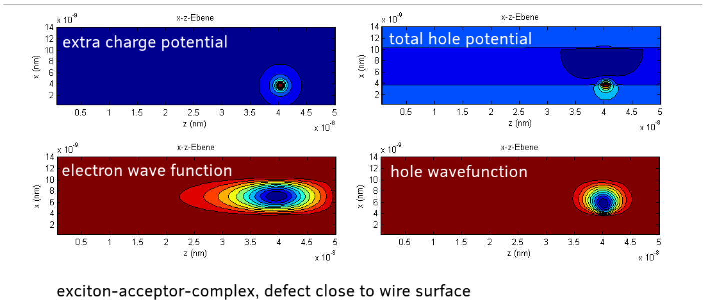

Figure 5.42: Potential landscape for an acceptor–exciton interaction with the defect situated close to the wire surface.

Figure 5.43 shows the absolute and relative energies of the specific complexes, dependent on wire radius. Figure 5.43a shows the absolute energies of exciton, two different DAPs and exciton–defect complexes for donors and acceptors both in the radial middle of the wire and close to its surface. Figure 5.43b shows the wire radius–dependent energy difference of these complexes to the exciton energy. Illustrations of the respective charge carrier–defect complexes are shown in an additional image in the figure description. These calculated energy reductions by interaction of charge carriers with defects, especially those with single defects can sufficiently explain the observed signals. This is illustrated by figure 5.44. It shows the same histogram that was already shown in figure 5.9 at the beginning of this chapter, but now the lowest and highest energy difference of the different single ionised defect–charge carrier pairs are shown as vertical dashed lines. The orange lines represent the lowest an highest energy that complexes between an ionised donor and a charge carrier pair were calculated to have and the turquoise lines represent the same for complexes with ionised acceptors.

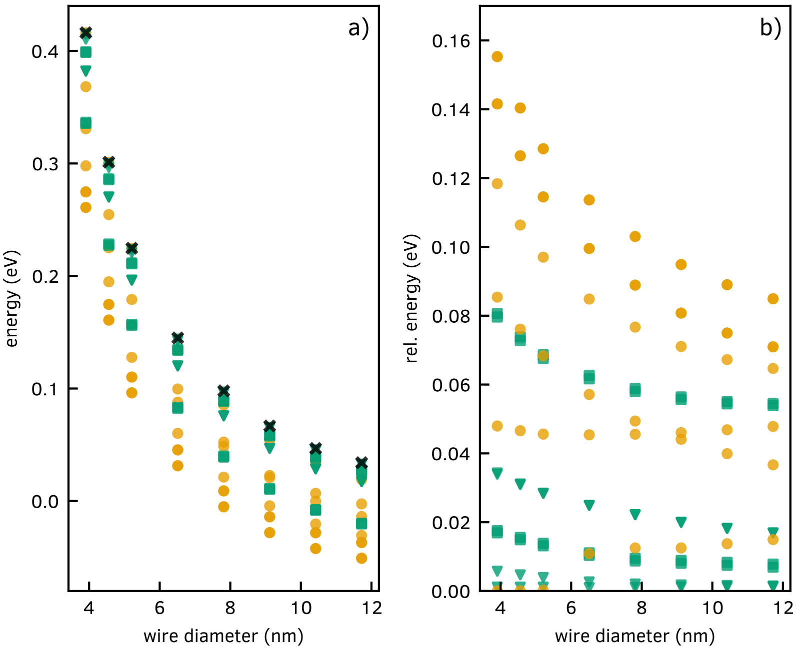

Figure 5.43: Results of the self-consistent calculations for different charge carrier–defect complexes. a) Wire diameter related energy of different charge carrier–defect complexes involving one electron hole pair and different types and combinations of defects and defect pairs at different spatial positions in the wire. b) Energy of the same complexes relative to the calculated free exciton energy. An illustration of the complexes and the corresponding symbols used in the plot is shown below. lower energies correspond to lower positions in the schematic.

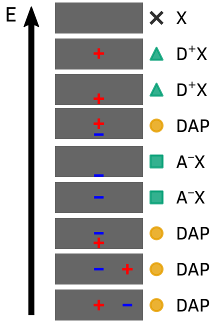

Figure 5.44: Histogram of signals observed at different emission energies relative to the highest energy signal observed during the entire trace. The minimum and maximum energies for ionised donor and acceptor bound charge carrier pairs are marked with dashed lines.

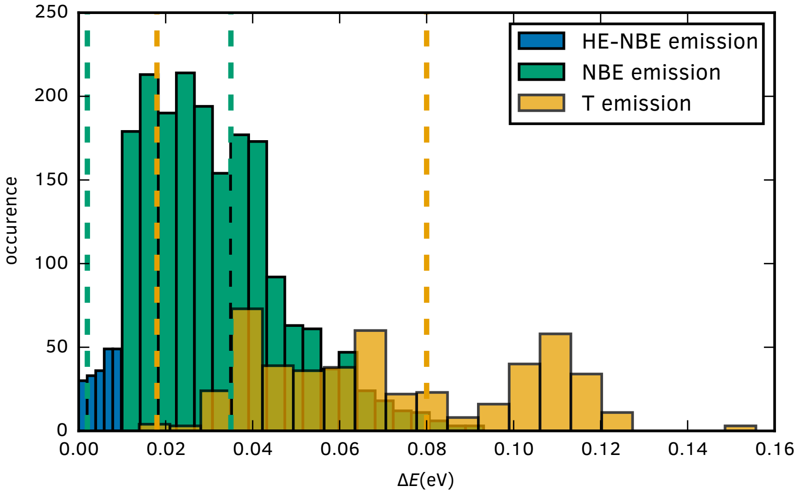

The calculated energy ranges represent the measured data fairly well. The donor complexes represent those lines rising from only slightly stabilised charge carrier pairs. The acceptor complexes are more strongly stabilised, to the point that the charge carriers are no longer bound to each other. The highest density of NBE states can be observed around the overlap of the two energy ranges. At the high energy side of the ionised donor–bound states there is definite overlap with the range assigned according to literature to HE emission. There is also strong overlap with the very broad T emission. This is consistent with the much more narrow range of possible energies of the one-defect complexes in comparison to the many DAP combinations. The larger number of NBE lines also fit within this model, as single ionised defects are more likely to be present in the wire than matching DAPS.

Assigning the observed emission lines to the respective complexes implies that acceptors have to be present in the wire to sufficiently explain the observed lines, or that certain donor species also have to lead to free–to–bound complexes, or that some very low energy bound exciton complexes due to for example the specific species of defects have to be considered. This can not be provided by this straightforward model but rather needs additional experimental measurements that can identify specific dopants and their influence on the nanowire luminescence.

While the above enables to narrow down the origin of the NBE emission just by virtue of looking at the relative emission energies, the other behaviours of the lines are also important to explain. It is reasonable to do this with a focus on the free–to–bound transitions, as these cover the broadest energy range and, as will be clear below, offer very reasonable explanations for several observed phenomena. The broad energy range of NBE emissions that themselves are fairly narrow emission lines are sketched in figure 5.45.

Figure 5.45: A possible mechanism behind the appearance of multiple different NBE bands with different emission energies. a) Defects can be located at many different radial and relative positions within the nanowire. b) Energy schematics of a single charge carrier-defect complex (left) and multiple charge carrier–defect complexes at slightly different positions within the nanowire. As the more free charge carrier is more delocalised in this very simple model the effect of the defect position is not as relevant as it is for the localised charge carrier.

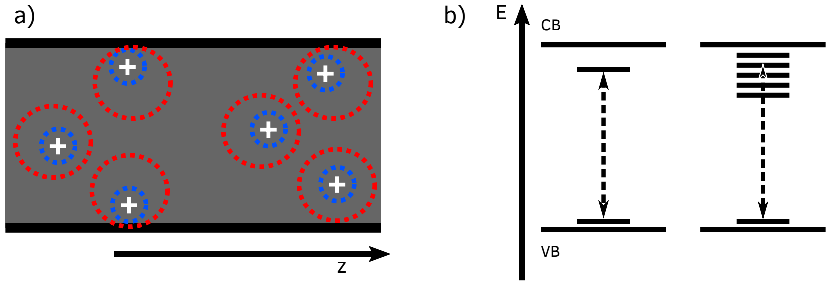

In a nanowire a certain number of ionised donors can localize a charge carrier pair each, as shown in figure 5.45a. Each complex has a distinct energy which depends on its surroundings – the proximity to other defects, as well as to the wire surface. A single of these complexes' recombinations will emit a quite distinct energy, as shown in the left energy diagram in figure 5.45b. Multiple of these complexes will emit at similar but slightly different energies, as shown at in the right energy diagram, yielding a spectrum with many narrow, energetically close luminescence signals. In comparison to the DAP emission these complexes offer a more narrow energy range in which they can potentially be found, as well as a lower lattice deformation, as one charge carrier is still delocalised around the charge carrier–defect–complex and therefore does not deform the crystal lattice to the same degree as a charge carrier localized at a charged defect. As a certain localization around the neutralized defect might be assumed, the hole energy in this diagram is not assumed that of a completely free hole, but as slightly stabilised.

As with the T emission, the NBE emission behaviour can be explained within bounds that match with the proposed free–to–bound recombination. First of, the shifting of the emission energy of the single emission lines can be explained analogous to the shifting of the T band, as can be seen in figure 5.46. Figure 5.46a shows schematically the possible influence of a hole trapped in a negative surface state. The delocalised holes are repelled by this charge. As the charge migrates along the wire surface the potential landscape and respectively the free–to–bound complex energy changes, as the delocalised hole wave functions are influenced.

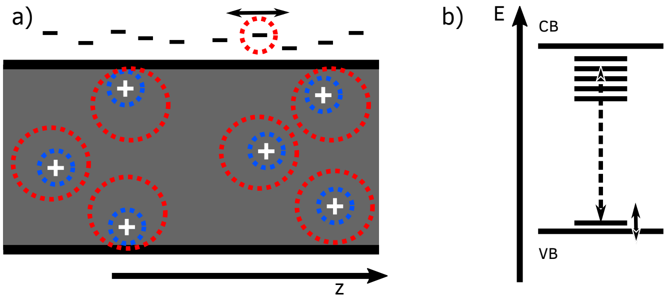

Figure 5.46: The shifting of the NBE emission explained in the established model. a) The location and movement of a charge carrier on the nanowire surface will strongly influence the wave function of the delocalised charge carrier b) This results in a energetic movement of this otherwise relatively fixed level, at least for individual complexes.

The changing potential landscape along the wire surface might also be an explanation for the intensity dynamics of single bands. Charged sites in the vicinity of the contributing defect will for one influence the availability of nearby trap sites that can alternatively trap one half of the charge carrier pair. On the other hand, nearby charges can contribute to Auger recombinations or simply repel certain charges that will alternatively localize at a energetically more favourable site.

Other very distinct fluctuations that have to be explained are those of interdependently alternating bands, as characterised in figures 5.34 and 5.35.

For the interdependent NBE bands – a single band alternating with two bands to the red and blue of that original band – the following complexes can be proposed: As schematically depicted in figure 5.47a, the state emitting a single line would possibly involve two very close defect sites but only one being able to trap a charge carrier pair. As the ionised defect not trapping an exciton can be considered rather unlikely, it might be considered that the involved trap state might actually be ionised by a lone charge, with the complementary charge being trapped for example in a surface state. Auger processes or other recombination routes can re-ionise the defect state, enabling it again to trap charge carrier pairs.

If this spatially close defect again traps a charge carrier pair, this would change the potential landscape around the first defect, shifting its energy. Due to their closeness, both complexes are likely situated in very similar surroundings and, if they have the same chemical identity, would be very close in energy. The switching between the one active

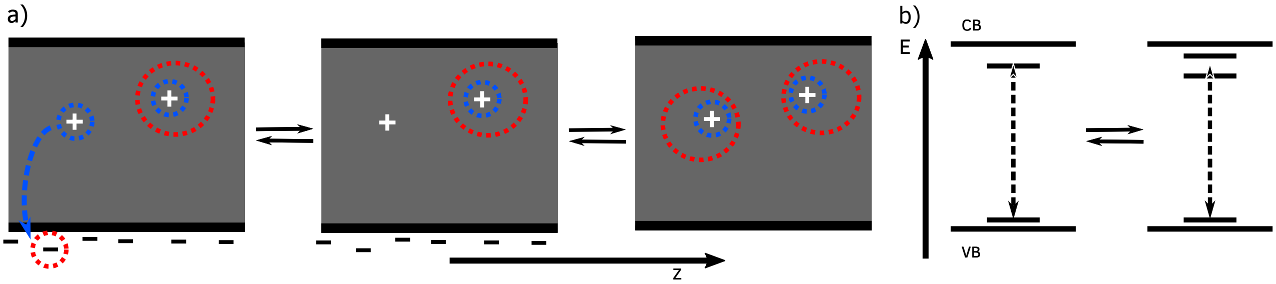

Figure 5.47: Possible mechanisms for the dynamics of the NBE emission intensity with interchanging bands. a) A three step process can be described for this observation. In the first case, with only one emission band being visible, the close proximity of an ionised and a neutral defect are assumed. The ionised defect can trap charge carrier pairs. When the second defect is also neutralised it can also trap charge carrier pairs. This will also change the potential landscape of the first defect and the respective complex. b) The respective energy diagram of the process described in a). The one recombination energy is shifted by the change in potential landscape and a second recombination path opens up.

trapping site and the two sites is also depicted in en energy diagram in figure 5.47b

For the interactions between the NBE emission and the T emission shown in figure 5.35, the proposed switching mechanism between the two emitting states is shown in figure 5.48. In the NBE dominated state, the majority defects localize charge carrier pairs, these complexes decay radiatively. The available minority defect is not ionised. The hole that is localised at the defect can be trapped in a surface state, leaving an empty hole trap within the wire and within the reach of the two delocalised holes of the free–to–bound complexes. Each of these hole can now localize at the trap, and donor acceptor pair recombinations are now possible. The NBE recombinations are still possible, as their is only very limited bandwidth for DAP recombinations, which is consistent with the NBE emission being lower in intensity but still observable in those spectra where the T emission can also be made out. This also narrows down the mechanism responsible for the multiple T bands in the example in figure 5.28. As the mechanism hinges on the activation of a single complementing charge, it is more likely that the observed pair of T bands is due to a two clusters of majority defects that interact with the same single minority defect

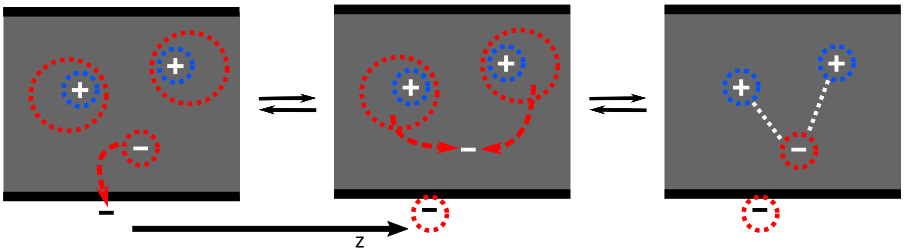

Figure 5.48: The proposed mechanism of the NBE dependent switching of a T emission signal. While a majority of donors are present that yield NBE emission, there is also a neutral acceptor on sufficient proximity. When the acceptor is ionised instead of the less stable one-defect complexes, the delocalised charge carrier will be localised at the newly free defect, yielding DAP complexes and therefore T emission.

In summary, the above processes describe a recombination mechanism that explains the clear difference of the NBE emission to both the T emission and the HE emission. The assumed localisation of only one charge carrier is in agreement with the observed lifetime that is generally smaller than that of the T emission. The stability of the free–to–bound complex (or a similar complex) would be smaller than that of a DAP and more likely to be observed in a system with a majority defect species. That the NBE signals are the most numerous, as counted and shown in figure 5.9 also fits within that explanation. The mechanism also explains the interdependent emission dynamics observed for the T and NBE bands. While this description of the CdSe nanowire luminescence is quite simplified and does not include for example the contribution of surface states to radiative recombinations, it is nonetheless a comprehensive description of the possible mechanisms behind each group of luminescence signals.

A point to be discussed it the strict distinction criteria between NBE emission and T emission by the absence or presence of phonon replicas. phonon replicas have been observed in CdSe luminescence signals Other than DAP recombinations[124] and some emission signals without phonon replicas have been assigned to DAP recombinations[105] respectively.

A clear distinction between the different recombination mechanisms can only be achieved by for example measuring the characteristic splitting of each emission line of a specific origin in the magnetic field.[149] As the quite strong dynamics of the individual line would complicate these measurements tremendously and this measurement and the the additional experimental requirements present themselves as a task far beyond the scope of this work. It might be assumed that there is some possibility that some emission lines assigned to the NBE group and some assigned to the T group belong in fact to the other group. But as coherent behaviour within the same kind of emission lines could be observed quite well, the consequence of these possible mistaken assignments can be considered negligible.

Also, the proposed model of the luminescence dynamics missing a mathematical foundation, which future work can contribute through simulations, calculations and the resulting models.

5.3 *Nanowire blinking statistics*

As shown in the chapters above, the nanowire luminescence shows dynamics both with and without changes in decay time. Different emission channels, likely originating from the recombination of different charge carrier complexes, contribute to the overall emission, each with their own luminescence lifetime and intensity dynamics. While the spectral investigation of these bands confirms their independence in term of dynamics and therefore mechanism, the spectra are too complex and emission bands overlap too closely for the dynamics to be separated on the energy scale with sufficient signal–to–noise ratio.

The complexity of the intensity dynamics of the nanowire luminescence is easily expressed in the intensity histogram of a TCSPC intensity trace, as shown in figure 5.49. As can be seen, at least five individual intensity levels above the noise level (just between 0 cts/ms to 1 cts/ms) can be made out, here fitted with a Gauss function, each.

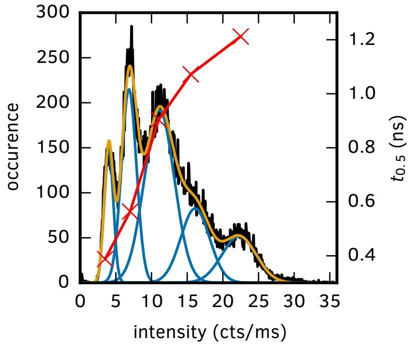

Figure 5.49: Intensity levels of a single nanowire intensity trajectory. Different levels are fitted with a Gauss distribution, shown in blue. The sum of all fit functions is shown in yellow over the black line of the data. The average lifetime $t_{0.5}$ of the decay curve extracted from the events contributing to each intensity levels is shown as an overlay of red crosses. The crosses are connected with a red line as a guide for the eye. The average lifetime clearly increases for the higher intensity levels.

Regarding the high complexity of the nanowire spectra and the high number of potentially involved recombination mechanisms this is not surprising. What might be is that the multitude of levels is not so different from the intensity histograms of single nanocrystals, as demonstrated by Zhang *et al.* and Malko *et al.*, who found similar distributions and numbers of emission levels – dependent on illumination power and shell thickness.[64, 66] In these nanocrystal studies higher luminescence intensities correlate with slower luminescence decays and this is also generally true for the nanowire luminescence, as illustrated by the red crosses in figure 5.49, which show $t_{0.5}$ for each of the apparently quite discrete intensity levels. The lifetime values could be extracted by reconstructing the luminescence decay curves via gating by intensity level, as described by Malko *et al.*.

The existence of multiple distinct emissive states can be further seen in the FLIDs of the nanowire luminescence. Examples for typical FLIDs can be seen in figure 5.50a–c. In these plots the intensity values have been normalised to the respective maxima to ease comparison while the lifetime axis is absolute and the same scale is used in all three images. Above

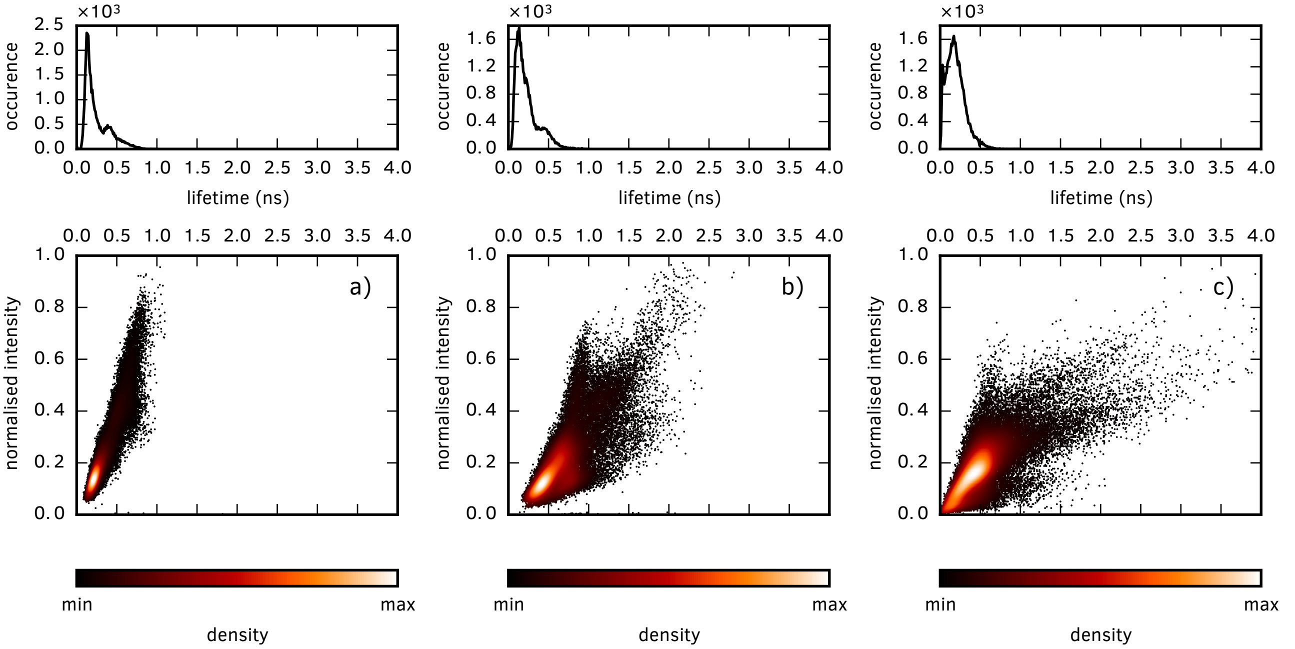

Figure 5.50: The FLIDs extracted from the TTTR data of single CdSe quantum nanowires showing different spectral patterns. Events are plotted with small circles and event density is also encoded with a false colour map. The respective lifetime histograms are shown over the FLIDs. a) Nanowire luminescence showing only NBE bands b) A different nanowire showing only NBE bands c) A nanowire showing both NBE and primarily T emission.

each FLID the respective lifetime histogram is shown. Event densities are also indicated by a colour scale.

A general look and comparison of the FLIDs shows that none of the fluorescence–lifetime distributions show completely binary high and low intensity states but that plenty of intermediate intensities and lifetimes are registered. The spread of the distribution on each axis can be quite different in magnitude, with the distribution in figure 5.50a showing a more narrow spread and the other two FLIDs fairly broad ones. The complexity of the lifetime histogram is not necessarily reduced by a more narrow distribution.

As described above, the nanowire luminescence spectra can show different complexities with either only NBE bands being observed or additional T bands. The appearance of the nanowire spectra do not noticeably influence the appearance of the FLIDs. This is illustrated by the fact that the FLID in figure 5.50a is that of a nanowire without any T emission, as is the one in figure 5.50b, which looks quite different. In contrast, the FLID in figure 5.50c – which is very similar in its lifetime–intensity distribution as the one in figure 5.50b – belongs to a wire with spectra that show strong T emission. The respective spectral traces can be found in the appendix as figures A.1, figure A.2, as well as figure A.3

When compared to nanocrystal luminescence, the intensity–lifetime relationship of the nanowire emission appears much more complex. Nanocrystals show usually a very low intensity *Off* state in addition to a high intensity *On* state which dependent on the nanocrystal charge. Galland *et al.* show that these states are either clearly separated or, in the case of flickering, connected by in-between states, either by a straight line of events or a slightly curved one.[68] As seen in the above FLIDs the nanowire luminescence generally shows plenty of states that are connected by intensity–lifetime events to the lowest intensity emission state. This state usually is the one with the highest density of measured events, as indicated by the scatter plot colouring. This event is equal to the baseline luminescence of the nanowire.

At higher intensities events can be observed to spread along different lines to different states. also, in the case of figure 5.50b and c, close to the baseline luminescence further clusters of events at certain intensity–lifetime values can be observed, in figure 5.50c one of these states is even the one with the highest event density.

Generally, the CdSe nanowire luminescence intensity–lifetime relationship as shown in the FLIDS is, as the low temperature luminescence spectra suggest, much more complex than that of CdSe nanocrystals. The dominance of the baseline luminescence is likely directly tied to the low nanowire quantum efficiency, which is not surprising for a system with such a low volume–surface ratio and no protective shell.

Just as TTTR data can be selected to gate decay curves by intensity the opposite – gating intensity traces by the decay curve channels – can be done. As the above intensity histogram with the corresponding decay time averages in figure 5.49 implies, the vast majority of those photons recorded in the last channels of the decay curve contribute to the highest intensity state in that histogram. Gating the intensity trace to show only the photons registered in the last 500 decay curve channels, as shown in figure 5.51, leads to a significant simplification of the intensity trajectories to usually a low intensity (*Off*) state and high intensity (*On*) state.

As described in the earlier parts of this chapter, the traces that were recorded within the frame of this work can be divided into two types: Those that show only HE and NBE emission and those that also show T emission. An increase in luminescence intensity can both mean an intensity increase for the whole spectrum or the independent blinking of T luminescence bands. The first case implies that the overall number of cooled excitons that can recombine through a radiative decay path increases. The second case means that in addition to the relatively fast HE and NBE recombinations a slower T recombination path opens and that, often, this comes in addition to an overall increase in wire brightness. These two processes can be clearly distinguished by the spectral traces.

These lifetime-relevant dynamics can now be extracted through lifetime gating. First, the spectral series were preselected for sufficient signal–to–noise ration and were then divided into two groups – those showing no T emission and consequently mostly spectrally independent dynamics and those showing clear T emission blinking. The result of gating each type of spectral trace are shown in figure 5.52 and 5.53.

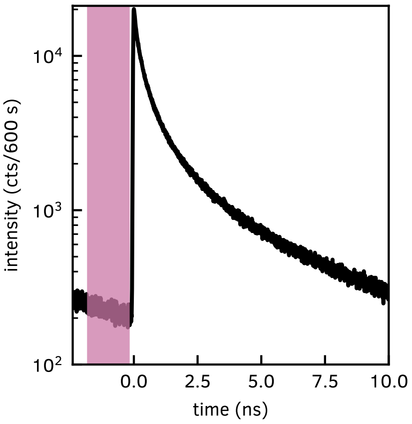

Figure 5.51: A decay curve with the channels marked that were considered for the analysis of the decay time related intensity-blinking.

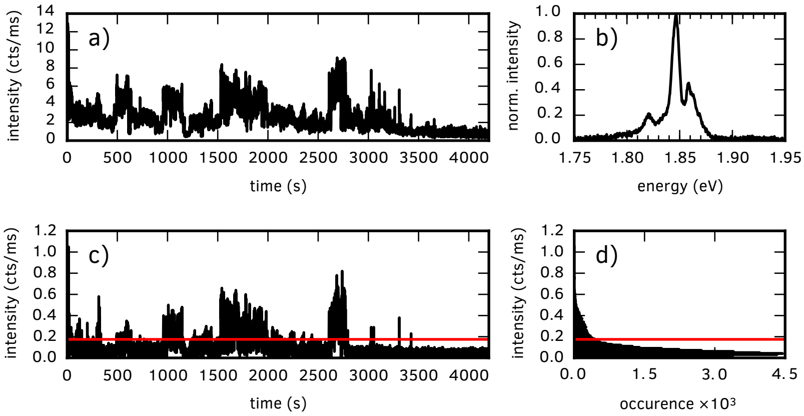

Figure 5.52: Result of the lifetime gating of an intensity trajectory of the nanowire luminescence that shows T type emission. a) The trace without any lifetime gate applied. A baseline luminescence is clearly visible throughout the trace. b) The respective summed spectrum. The NBE and T emission overlap. c) The intensity trajectory gated to show only the photons arriving within the last 500 channels of the decay curve. The red line shows an *On*–*Off* threshold chosen according to the intensity distributions in the related intensity histogram. d) The respective intensity histogram. It is clear, that a narrow, dominant *Off* state can be seen just above 0 counts. The *On* states have a continuous distribution. A cut-off intensity for the distinction between the two states is shown in red, chosen to efficiently cut off all *Off* events but count a maximum amount of *On* events.

For spectral traces with the slow T luminescence blinking being the relevant dynamic process the lifetime gating as described above is shown in figure 5.52. The complete trace without a gate applied can be seen in figure 5.52a. While quite distinct high intensity phases can be distinguished, there is also a varying luminescence baseline that overlaps with some of the less intense high luminescence states. The sum of all spectra of the respective spectral trace shows a fairly narrow spectrum with a strong T emission (zero–phonon line visible at 1.847 meV, with one distinct LO phonon replica at lower energies). The NBE and T emission clearly overlap, which would make it impossible to separate the signal dynamics spectrally. Figure 5.52c shows the gated intensity traces, which now shows a distinct *Off* state, while the high intensity states still differ in luminescence intensity. This is also expressed by the intensity histogram in figure 5.52d. It shows a very distinct low-intensity or rather *Off* state but a much broader distribution of *On* states.

For the sake of statistic analysis an *On*–*Off* threshold has to be chosen. In this study this was chosen according to the intensity histogram of the gated trace and the trace itself with the goal to cut off the vast majority of *Off* states while still counting as many emitting states as such as possible. In the example of figure 5.52c and d the red line shows the threshold as it was set for this trace. The distinct peak of *Off* states lies below the threshold, which is nonetheless quite close to the peak's flank. This is a compromise to allow the relatively large number of high intensity states between about 0.2 cts/ms to 0.4 cts/ms to be counted as *ON* and gives a more accurate representation of the system.

As has been shown before in figure 5.18 on page 88 the lifetime gating of a time trace with strong T emission does quite reliably result in a T intensity trajectory, without the drawbacks that come with the extraction from spectra, such as the low time resolution and the overlap with NBE emission. What cannot be ascertained through this methods is the extraction of the dynamics of only a single T signal. It is in fact likely that, if there are multiple signals stemming from different defect, that these will be convoluted into one trace. What has to be kept in mind for these observed traces though is that even in multiple signals were observed, one would show significantly higher signal intensities and that signals of comparable height often showed dependent or synchronous dynamics - meaning that the emission mechanism would likely be related to the same defects and shared *Off* states might likely be due to the same quenching mechanism.

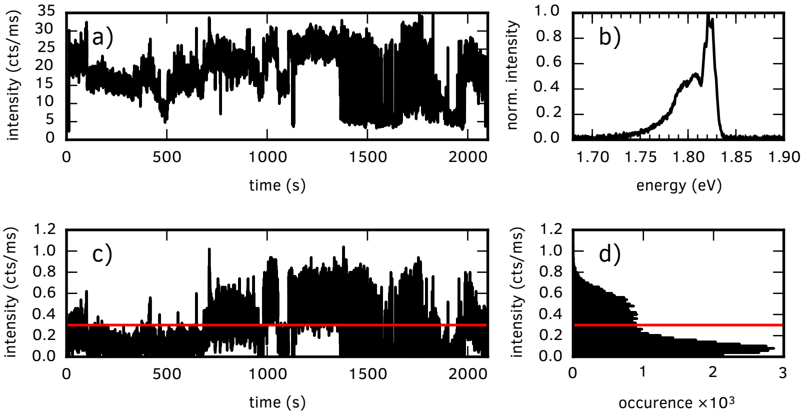

Figure 5.53: Result of the lifetime gating of an intensity trajectory of the nanowire luminescence that shows only NBE and HE type emission. a) The trace without any lifetime gate applied. As with the trace showing T emission a baseline luminescence can be seen. b) The summed-up spectrum of all spectral trace frames. c) The trajectory gated to shown only the last 500 channels. In red the *On*–*Off* cut-off threshold is shown. d) As with the above trace, a distinct *Off* state, as well as a distribution off *On* states can be made out and a threshold value determined.

Like for those traces with a significant T emission, those traces consisting only of HE and NBE emission also possess a baseline luminescence which can be eliminated through lifetime gating. This is shown in figure 5.53.

As in the example in figure 5.52, figure 5.53a shows the entire TTTR intensity trajectory without any gating applied. The spectrum in figure 5.53b shows the summed up spectrum, which is about as broad as the above spectrum with t emission, but shows in comparison no phonon replicas. The most intense emission lines are also much closer to the high energy edge of the spectrum.

Gating the TTTR file as described above yields the trace in figure 5.53c with the respective intensity histogram in figure 5.53d. For this trace the result of the gating is insofar interesting that especially in the first 500 s the eliminated baseline is quite high in intensity. This means that at this point the radiative decays were significantly accelerated. This high intensity phase of the emission therefore does not show up in the gated trace. In comparison, a redistribution of intensity from fast to slow decays as shown in figure 5.36 with no change in overall emission intensity would also appear as an intensity increase in the gated trace.

Otherwise, the intensity histogram in figure 5.53d qualitatively shows a very similar intensity distribution to the one of the trace with the gated T luminescence. The main differences are a relatively higher number of *On* states. The *Off* state also shows a significantly broader distribution, which implies the possible existence of a low intensity *grey* state very close to the the *Off* state in intensity. Nonetheless, for this trace also a threshold between *On* and *Off* can be determined which is again shown as a red line in the gated trace and histogram.

On the basis of the above described processing of the time trace data statistic analysis of the lifetime-relevant blinking was performed for both the *On* and *Off* time distributions.

In figure 5.54a and b the *On* and *Off* time probability densities for the long decay time component of five representative nanowire intensity traces showing only HE and NBE bands and therefore mainly spectrally independent intensity fluctuations is shown. The chosen time bin for all traces was 100 ms. The probability densities data points were weighted to account for the low data point density for long *On* and *Off* times in accordance with the method used by Kuno *et al.*[15] For both axes logarithmic scaling is used. The data sets are offset along the *y*-axis to ease comparison. Corresponding *On* and *Off* probability densities are plotted with the same *y* offset.

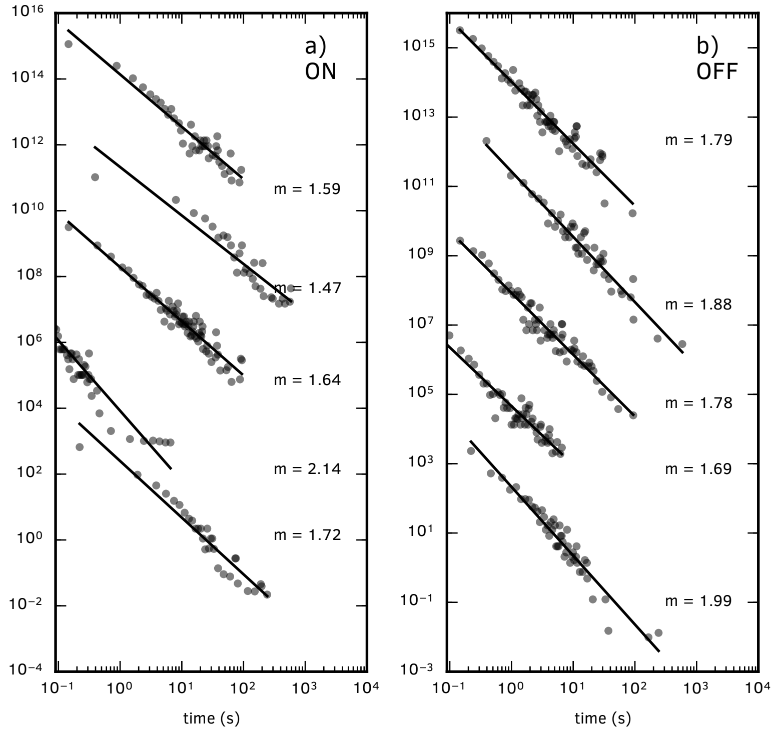

Figure 5.54: The blinking probability density plots of gated nanowire luminescence that does not show T emission. a) shows the *On* time statistics, while b) shows the *Off* time statistics.

All of the traces can be fit with a negative power law, as defined in equation 1.10. The value of the exponent *m* is shown next to each data set. They fall within the previously reported range that encompasses both nanowire and also nanocrystal blinking.[15, 36, 44, 45, 50, 125, 129] The average exponents *m* are 1.71 for the *On* times and *1.83* for the *Off* times. What is exceptional for this data set is the broad range of the values which range from 1.47 to 2.14. This implies a strong heterogeneity of each blinking emitter. The corresponding *On* and *Off* exponents do not show an obvious correlation. For most traces m_{Off} is larger, but there is one exception.

What is interesting is that the expected probability density truncation[47] cannot be observed. This is in agreement with the previously reported temperature dependence of this phenomenon in nanocrystals[45], but temperature dependent studies would be necessary to also confirm this correlation for nanowires. Traces usually span at least three decades of *On* and *Off* times, with the lowest being in the 100 ms range, which corresponds to the resolution given by the bin time. At the same time individual traces show only very few events close to this resolution limit, meaning that most of the dynamics are slower. This also indicates that the intensity gradient of the *On* state is rather due to the actual blinking mechanism then multiple binary events being registered in a single band and therefore convoluted into an intermediate intensity. This supports the model by ZHANG *et al.* that explains these intermediate states with charge diffusion in nanocrystal shells.

The largest values are situated for most traces within the 100 s magnitude, with some values coming quite close to 1000 s, both for *On* and *Off* times. Generally, If a wire is found to have shorter *On* times it will also exhibit shorter *Off* times at the chosen experimental conditions, showing that wire blinking speed varies depending on the individual emitters.

Figure 5.55a and b show the T band probability density plot for the *On* and *Off* times each. The traces are offset in the same manner as the traces of the NBE blinking. All traces show clear power law behaviour for both the *On* and *Off* times. The average power law exponent for the *On* and *Off* time probability distributions are $m_{\mathrm{On}} = 1.66$ and $m_{\mathrm{On}} = 1.68$ respectively. As with the distributions in figure 5.54 there is no apparent dependence of the exponents on each other and the values scatter in a comparable range (1.49 to 1.93). A further similarity is the range of event duration which again spans about three orders of magnitude with the smallest numbers lying in the 100 ms range and going up to 1000 s. As

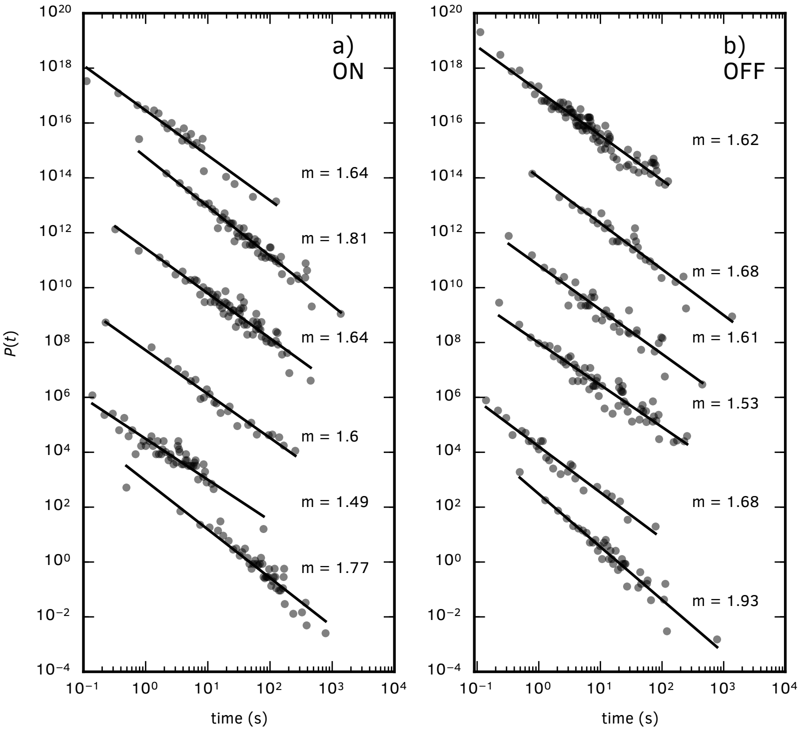

Figure 5.55: The blinking probability density plots of gated nanowire luminescence that does show strong T emission. The analysed blinking can be considered to only show the T band blinking. a) shows the *On* time statistics, while b) shows the *Off* time statistics.

in the traces in figure 5.54 most events are not recorded near the bin time dependent resolution limit and for some nanowires the fastest dynamics even just start in the range of seconds.

The strong similarity in blinking behaviour of the long lifetime fluorescence of nanowires with very different spectral signatures is an important aspect to keep in mind when contemplating the mechanisms responsible for the dynamics. As has been shown in the previous chapter the mechanism of the radiative decays have to be assumed to arise from different types of charge carrier complexes, which is supported by the difference in luminescence properties. At the same time, the dynamics of NBE and T bands are clearly independent - this means that a similar mechanism that can at the same time influence individual trap sites independently has to be assumed. Also, the low-temperature CdSe nanowire blinking has not shown any strong difference to the blinking of single CdSe nanocrystals, even though these system have markedly different electronic properties.

5.3.1 Possible mechanisms behind the nanowire blinking

Both the strong similarity between different types of nanowire blinking and also that to the blinking of nanocrystals has to be taken into account when considering a mechanism for these fluorescence behaviours. At the same time, while the focus might be on the temporary quenching of emitters an the related mechanism, this also says something about the nature of the radiative recombination channels – these also have to be considered to be quite similar in nature.

The above analysis of the radiative recombinations in CdSe nanowires are based mainly of the interaction of the photogenerated charge carrier pairs with defect sites – and for those recombinations that lead to the majority of emissions the this leads directly to dissolution of the excitons and the formation of complexes with ionised defects in which at least one charge carrier is strongly confined.

Any proposed mechanism must plausibly explain the reoccurring dynamics of individual, defect-related emission lines. This means that there are generally three options that have to be considered: The first is the dissolution or maybe even prevention of the formation of the emissively recombining charge carrier–defect complexes by influencing the charge carriers. The second it the prevention of the formation of the complexes by changing for example the charge of the defect site. And the third is by removing or moving the defects sites themselves. Any valid option has to be reversible and in agreement with the observations that have been made for the radiative recombination spectra and dynamics.

Defect site creation and diffusion

The first option that will be discussed is a possible dynamic of the defect sites themselves. For this two different mechanisms will have to be considered. One is the repeated creation and subsequent elimination of a defect site and the other is its movement within the crystal.

For both processes an activation with the light used to irradiate the sample for fluorescence measurements would be assumed. The two mechanisms are illustrated in figure 5.56a and b. The cartoon in figure 5.56a shows a schematic drawing of a wire segment with no defects that is irradiated with light. This irradiation induces both a donor and an acceptor in the wire – for example by the displacement of a single ion into an interstitial position. Through further irradiation the interstitial as well as the vacancy might be activated to move within the crystal. If the ion returns to its original position both defect sites are eliminated again. A sketch of the change in energy levels of the nanowire through these

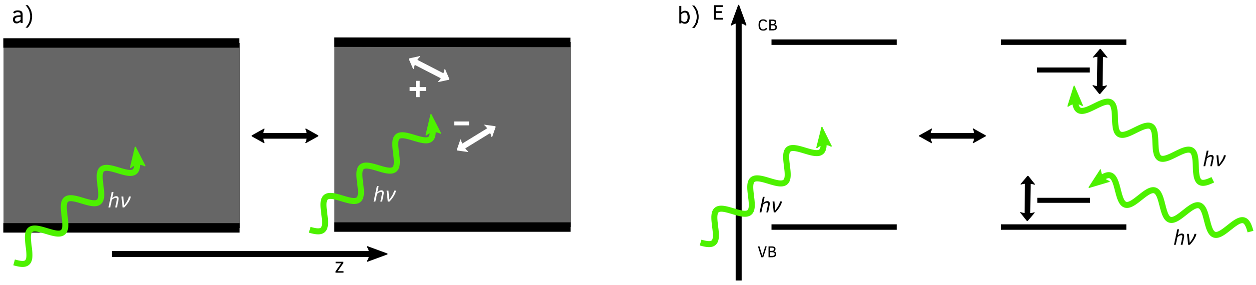

Figure 5.56: The possible mechanism of defect creation and spatial fluctuation. a) The possible process of radiation-induced creation of defects and their migration within the volume of the nanowire. b) The respective energy schematic of defect creation and subsequent migration within the wire. In this mechanism the illumination of the defects itself switches the luminescence on and off and also moves the defects to different positions within the potential landscape of the nanowire.

two processes is shown in figure 5.56b. In the first step the nanowire without defects only has a valence band and a conduction band. Through the irradiation both a donor level just below the conduction band and an acceptor level just above the valence band are created. The position changes induced by further irradiation would now influence the potential landscape of the nanowire and the exact energy of the levels.

The first mechanism of defect fluctuation is the creation of interstitials and vacancies by displacing ions from their lattice position. This process is usually induced when the material is irradiated with high energy radiation.[150] As the samples in long term luminescence studies are constantly irradiated with photons, this mechanism has to be examined further.

The mechanism and magnitude of defect creation through radiation strongly depends on the type of radiation. Bombardment with ions usually induce a cascade of displacements with the ion weight influencing the number and spatial distribution. Electron bombardment induces single defects close to the material surface, but only if a threshold velocity is achieved for the accelerated electrons.[150]

To induce defects that can contribute to the luminescence of a material with a single, defined band a creation of a single defect is necessary. As electron irradiation is the process that can result in these kind of defects a comparison with studies that perform exactly that experiment is useful. Kulp did perform irradiation studies of CdSe single crystals in which also the luminescence of the crystals was probed and the displacement energy for both ions was determined. The study shows that at 77 K the increasing irradiation induces indeed a defect luminescence band, but it is a quite broad band and in the IR spectral range. The displacement energies that were determined were 6.0 eV for the cadmium ion and 8.6 eV for the selenide.[151]

These values exceed any of the radiation energy that the nanowire sample was exposed to (in comparison: the typical illumination wavelength of 532 nm is equal to a photon energy of 2.33 eV). Also, displacement for the mechanism behind the luminescence blinking would have to include the constant and quick creation and elimination of the same or at least very similar defect sites. This is a highly unlikely process and no example in the literature for this or a similar process could be found.

The second possible process of defect fluctuations is that of defect diffusion. As the investigated nanowires are not specifically doped the certainly relevant mechanism is that of self diffusion, meaning the diffusion of vacancies and Cd or Se interstitials. For n-type CdSe a higher occurrence of Se vacancies as well as Cd interstitials would be assumed. This means that mostly moving cadmium atoms would be assumed – either in-between the regular lattice positions or around the selenium vacancy, moving it through the crystal. As any kind of diffusion process self diffusion is also very much dependent on the outside condition of the material. This includes any chemical gradient, component vapour pressure, and the sample temperature.[150, 152]

While activation energies for diffusion processes in CdSe have been determined to lie within a range that could be reached just by illumination (for example 0.41 eV and 1.03 eV[152]) the studies are usually performed at high temperatures (several hundred °C). Also, no studies in vacuum could be found. As the diffusion processes would be highly dependent on the sample temperature the above activation energies become meaningless if the goal is to make a statement about the low temperature processes in nanowires.

In addition to the above considerations, it is not quite clear what kind of continuous diffusion mechanism could lead to a distinct blinking behaviour as observed and shown above. It might contribute to band shifting, but even that is process can be easier explained by expanding on already existing models that are used to explain the same phenomena in other nanostructures such as nanocrystals.

Additionally, there is one phenomenon that can be observed for the nanowire luminescence that contradicts the notion that a defect related luminescence will regularly be created during the observation time. This phenomenon is a short (one or two spectral frames) phase in which the luminescence is especially high, just after the beginning of sample illumination. This short intensity flash could be observed for all nanowire luminescence traces in which the illumination was only switched on after spectra acquisition was started, albeit with different magnitudes for different nanowires.

An example for this kind luminescence behaviour is shown in figure 5.57. The first 1000 s of the trace are shown in a false-colour image in figure 5.57a. Different regions of the emission spectrum are marked with dashed lines. At these emission energies the spectrum intensities were extracted and plotted in the intensity trajectories in figures 5.57b to f. The trace in b shows the intensity sum of the whole individual spectra, while c to f show the intensity of the emission lying under the lines, from top to bottom. The plot colour is also the same as that of the respective dashed lines.

What can be seen in the spectral trace in figure 5.57a is the one high intensity frame in the beginning of the trace. This is also reflected in the summed intensity trajectory in figure 5.57b in which the intensity at illumination quickly spikes and then starts blinking as expected.

Looking at the spectrally resolved traces of the nanowire luminescence, the high energy edge intensity trajectory in figure 5.57c does not reflect the intensity flash but shows independent emission blinking. Going to lower energies – and therefore luminescence that involves the recombination of charge carrier pairs bound to defects – the emission flash reappears and is also quite strong in regions of the spectrum that show relatively low absolute luminescence intensities. All in all the intensity trajectories show the intensity flash at any point of the spectrum that will show luminescence at later points in the measurement period – except for the HE emission region, for which the flash is not observed.

This indicates that the trap sites that are involved in the luminescence processes are present in the nanowire from the outset and that a reversible equilibrium state is reached in which not all of them can contribute to radiative recombination mechanisms all the time.

Ionisation processes

In the context of the earlier parts of this chapter the easiest way to describe a possible blinking mechanism is to look at the most important prerequisite for most of the radiative transitions: The presence of a charged defect

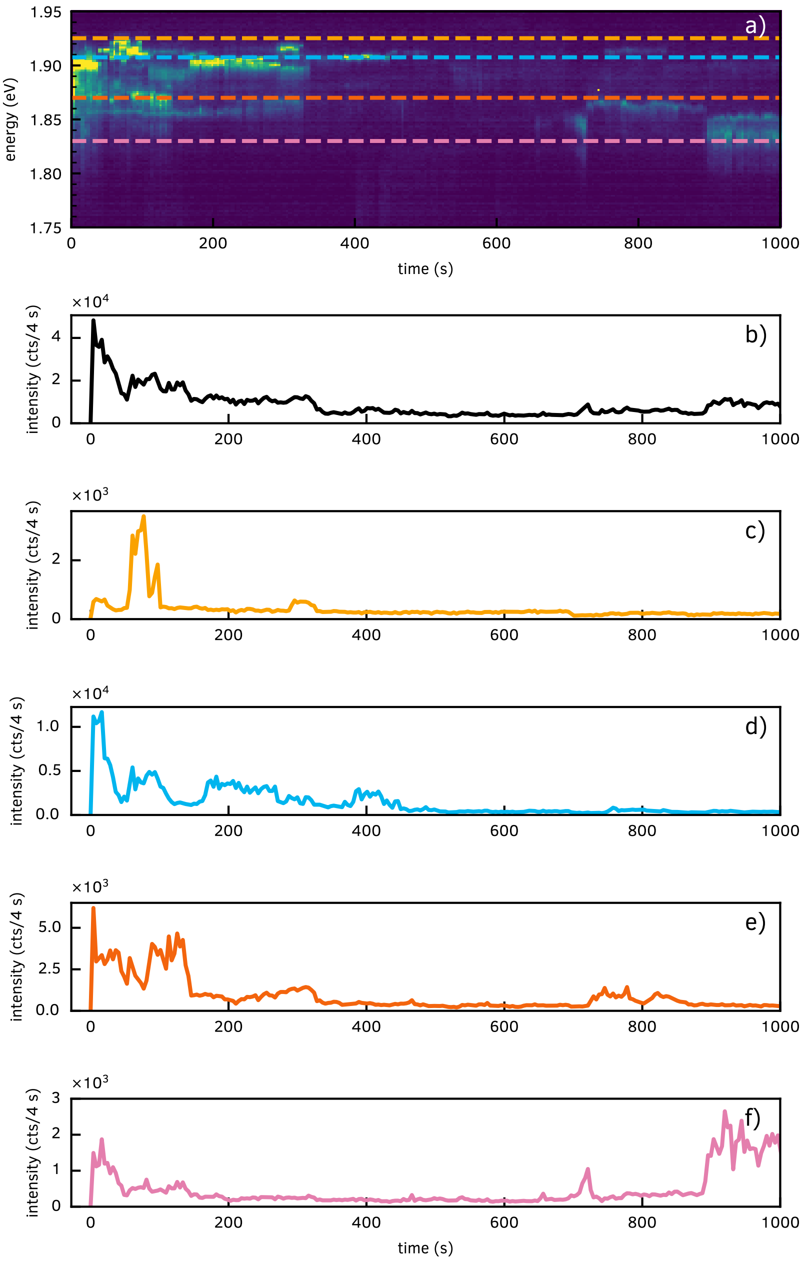

Figure 5.57: The peculiar intensity flash at the beginning of wire illumination. a) The spectra trace of a typical CdSe quantum nanowire showing both NBE and T emission. b) The intensity trace of the entire spectrum. A high intensity flash at the beginning of the measurement is visible, just after the beginning of the illumination of the nanowire. The traces in c), d), e) and f) show the intensity trace for the marked emission energies, top to bottom, or blue to red. The intensity flash is only present for those emission lines that stem from defect related recombinations.

site. At low temperatures an interstitial or a vacancy will be in itself neutral but in a position in the crystal that will not supply the chemically ideal binding conditions that the ions in the crystal have, leading to a local excess or deficiency of electrons. This is why a relatively small amount of energy can ionise these sites, either delocalising an electron from a donor site into the conduction band or localising an electron to an acceptor site and respectively creating a delocalised hole in the valence band. These charged sites then will in turn interact with charge carrier pairs as described in the sections above.

The ionisation of defect sites at low temperatures is illustrated in figure 5.58. In a simplified energy diagram in figure 5.58a the wire is shown in its ground state with both a neutral donor and acceptor. Irradiation with light will ionize the defects by elevating an electron from the donor into the conduction band or a hole into the valence band respectively. These charge carriers can at any time return to the ionised defect sites. The localisation of photogenerated charge carriers at the defect sites is only possible in the ionised state which would make a return of the charge carrier impossible for the time of the existence of the complex.

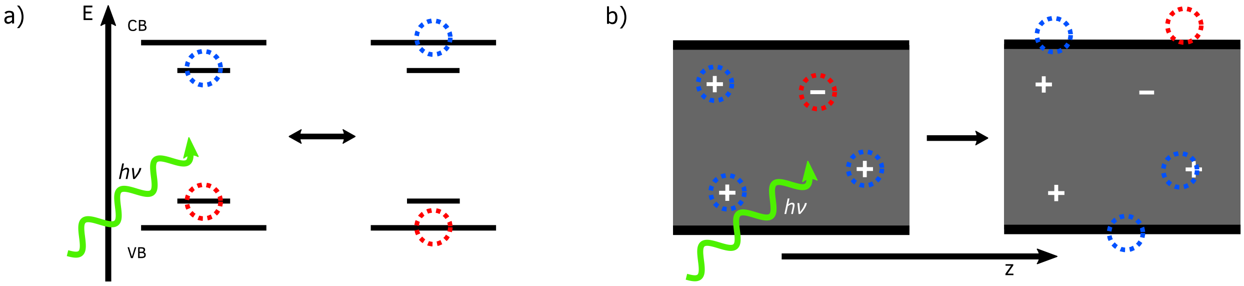

Figure 5.58: The photoionisation of intrinsic defects in a CdSe nanowire. a) The schematic energy diagram of the photoionisation of a donor and acceptor in a nanowire. The excess charges are excited into the conduction band and valence band, respectively and can be considered to behave like any electron–hole pair after relaxation to the band edge. b) The same process but illustrated within the space of the nanowire. Defect concentrations must be considered to not be the same for donors and acceptors. As the excitation energy is high enough to excite an electron from the valence band into the conduction band the ionisation from the defect sites happens with a large amount of excess energy which makes an excitation into surface states likely.

In figure 5.58b a schematic of the wire shows a possible mechanism of what happens with the charge carriers at ionisation. The neutral sites are ionised by the incident light and the charges are trapped in not further specified surface states. The ionised sites are now available for the formation of complexes with photogenerated carrier pairs. Some charges might also be immediately trapped in another trap site, neutralising and therefore deactivating it for the formation of these complexes. Considering that the vast majority of the low temperature nanowire luminescence is arising from these complexes the luminescence intensity is directly related to the number of free, ionised sites. This means it depends on the number of available surface traps and the ionisation and return rates to and from these sites.

During the photoexcitation of the nanowire the ionisation of defect sites but also their neutralisation can be assumed to happen simultaneously and constantly as excited charge carriers return to their ground state. Due to the photon flux being constant and recombinations having a certain velocity depending on the specific recombination path the nanowire can be assumed to reach a state in which a certain number of charged sites will be ionised while the rest is not. While the number of charged sites will reach a steady state, the individual defect can at any point be ionised and subsequently return to its neutral state through the return of the right charge carrier. This could either be the single charge that is explicitly missing or a charge carrier pair – which would form a complex which would also decay, emitting either NBE or T emission.

So, the emission intensity of a single line – assuming that it indeed arises from a single complex – would be dependent on the charge state of the individual defect sites and its behaviour over time. This is an attractive model insofar as descriptions of nanocrystal blinking can be easily applied to this. The charging process and the persistence of that charge is dependent on the single charge being kept away from the defect. This can be imagined through the capture of the charge for example in other trap states, which would follow the same rules as the charge carrier trapping in nanocrystals would, with the same statistic considerations applying. This of course does not give an insight into the exact trap site or process that leads to the ionisation and the question remains what exactly happens to the charge carriers – as with nanocrystals the exact path from *On* to *Off* remains a mystery.

What can be at least basically described within this treatment of the nanowire blinking is an *On*–*Off* fluctuation but also potentially the intensity flash in the beginning of each measurement. Considering a distribution of lifetimes for the charge carrier traps, before a steady state of constant ionisation and recombinations is reached the luminescence process will start with a sudden ionisation of the maximum number of defect sites.

As excitons are also generated the photogenerated charge carriers bind to the sites and recombine. As not all trap sites will let their charges return at the same speed the number of ionised sites will depend on the absolute number of free charge carriers and excitons in the system and the number of charged sites – and also available radiative and non-radiative recombination channels – will reach an equilibrium which in turn determines the steady state fluorescence intensity.

In fact, the room temperature photoexcitation of CdSe nanowires and derivative structures has been shown to charge both the nanowire itself outside of the illumination focus but also the surrounding substrate, implying a strong and far-reaching trapping of charge carriers.[71, 153] As this charging has been shown to change over time[154] the steady state formation over seconds and maybe even a long term change in luminescence can be explained by a process which leads to an overall charge imbalance in the wire. While this might increase the number of one type of ionised defect sides, it also increases the chance for Auger processes involving the access charges.

The above described binary switching of the defect sites would also lead to a binary switching of the luminescence intensity. For the observed intermediate levels one would either have to assume that they result from the limited temporal resolution or a mechanism similar to that proposed by Zhang *et al.*[64] that assumes that an excess charge carrier can be trapped at different distances to the exciton which will lead to a different likelihood for non-radiative recombinations. This can easily be imagined for nanowires – no matter the actual identity of the charge carrier traps necessary for the ionisation of the defect sites, there is ample opportunity for these sites to distribute within the wire volume and on the wire surface.

A similar aspect that will certainly influence any complex between defects and photogenerated charge carrier pairs is that the likely present intrinsic defects – Cd and Se vacancies and interstitials – are double donors and acceptors.[85] This means that any defect site be ionised twice and also in turn also localise two charge carriers. This close proximity of an additional charge to the localised exciton can as a possible contributor to Auger recombinations be involved in the other processes to be considered – the non-radiative recombination paths.

Non-radiative recombination paths

From the four different mechanisms of non-radiative recombination that are proposed for bulk semiconductor crystals[76] for nanostructures two are of special importance. One is the Auger process and the second is the recombination through a continuous band of surface states.

The high likelihood of these two mechanism is a result of the small sizes and the high surface–to–volume ratio of the structures. In a small crystal any additional charge will always be close to a photogenerated exciton and in fact increasing nanocrystal size and shell thickness will reduce the occurrence of *Off* states significantly.[66] At the same time the exciton diffusion length of in CdSe has been reported to be between 1 µm to 2 µm at 7 K sample temperature.[155] Diffusion lengths of single carriers are reported to be at least around 10 nm, usually more,[21], even for the minority charge carriers. This means that the surface of the wire is always within reach of most charge carriers, especially in wires with small diameters.

Calculations by Pokrant & Whaley have shown that CdSe nanocrystals have a continuous surface state band due to dangling bonds.[58] The resulting densities of states for different binding conditions are shown in figure 5.59. What is clearly visible is that for all considered systems the surface orbitals or dangling bonds will form a band within the band gap, which can be part of a stepwise recombination from conduction band to valence band. Due to the similar diameters a surface band formation can also be expected to occur in nanowires. In fact, along the long axis of the wire orbitals are likely to overlap quite well just for geometric reasons, while the strain due to the strong surface curvature in the short axes increases the likelihood of surface defects and dangling bonds that can

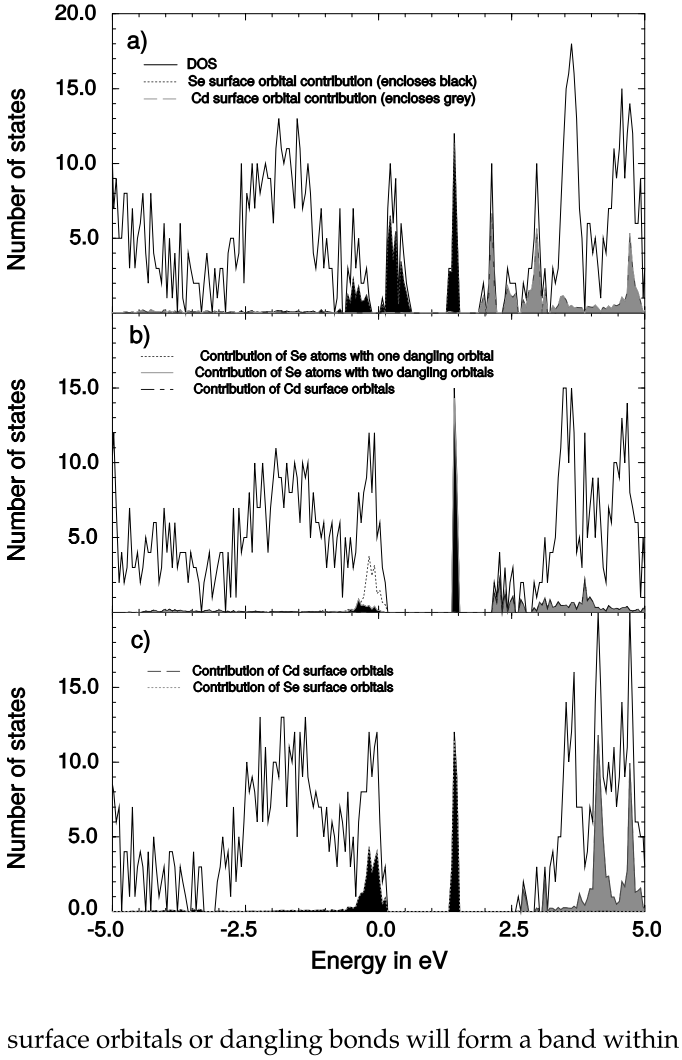

Figure 5.59: Calculated surface levels in the density of states of a single CdSe quantum dot.[58]

contribute to this band.

In bulk descriptions of semiconductor surface states a continuous band connecting conduction band and valence band can be assumed for an even distribution of states. The non-radiative recombination of electron and hole through this band directly competes with the radiative recombination. This is illustrated in figure 5.60a and b. While figure 5.60a shows the respective energy schematic figure 5.60b shows a cartoon of a wire section and two charge carriers with the possibility to either directly recombine or alternatively diffuse to the surface and recombine there. In the image as shown the direct recombination would be the likely step as there are neither defects in the wire that the charge carriers can interact with nor the specific traps or states on the wire surface shown that the charge carriers can diffuse into. As these state are to my knowledge not well known for CdSe wire surfaces it can only be speculated that a diffusion to the surface is likely due what has been reported for nanocrystals and what is assumed for the bulk.

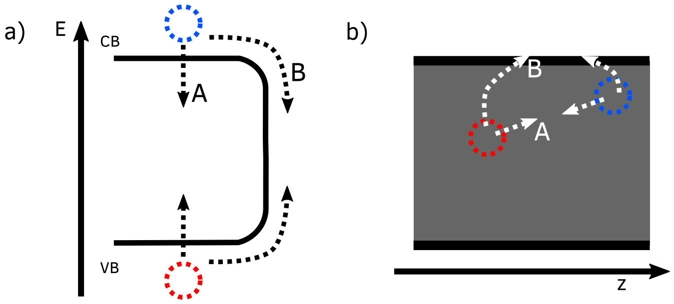

Figure 5.60: The process of surface state recombinations as applicable for a nanowire. a) The general energy diagram illumination of the surface band recombination. The surface states form a continuous band if states that the charge carrier pairs can recombine through radiationless. b) The process illustrated for a nanowire. instead of an exciton forming and recombining the charge carriers have to migrate to the surface and recombine there.

One necessary consideration regarding the recombination through surface states is that of a potential barrier between valence and conduction band and the surface states. As described by Pankove in [76] internal surfaces – surface-like states caused by inclusions in the bulk crystal – function like external surface bands, but usually exhibit an energy barrier for the charge carriers to cross over or tunnel through. These non-radiative recombination centres are ascribed to local deformations and charges or local strain. Due to the nature of the nanowire surface these are likely also to occur there. These internal surface states can only be accessed if the electron, the hole or both charge carriers can overcome an energy barrier.

If the blinking was due to surface state recombinations only, the most important question to answer would be the energetic position of this band, especially if an energy barrier has to be overcome. While this is certainly possible in a continuously irradiated system, it is much more likely that the non-radiative recombinations happening through this channel are those of hot electrons directly after excitation into the conduction band, especially if the surface band highest levels might be even lying above the conduction band edge. This would lead to the so-called B-type blinking, as described by Galland *et al.*[68]. In this process charge carrier pairs are pre-emptively removed from the system and no competition between the radiative and non-radiative recombination paths through the band gap takes place. This leads to an intensity blinking without a lifetime blinking, which also has been observed at least for some periods of time for some of the investigated nanowires – see for example the traces in figure 5.16b, e and h.

In addition to surface recombinations, like in nanocrystals the probability and possible mechanisms of Auger recombinations have to be considered. For example, a defect site sitting closely to a second defect or a dap will, if neutral, be able to be involved in Auger recombinations. The principle of Auger processes in nanowires is illustrated in figure 5.61a and b. Figure 5.61a shows the energy diagram of intrinsic donors and acceptors that are ionised once. Both the cadmium and selenium ions in CdSe are nominally charged twice – which means that an interstitial and or a vacancy also carry two excess charges. Ionisation is much more likely to only happen once then twice, as the second ionisation energy is higher.[21] This means that one excess charge remains at either defect site after ionisation by incident light, as shown in the schematic. If this once ionised site now forms a complex with a photogenerated charge carrier pair the second charge carrier can be excited at recombination instead of emission of a photon. This process is illustrated in figure 5.61b.

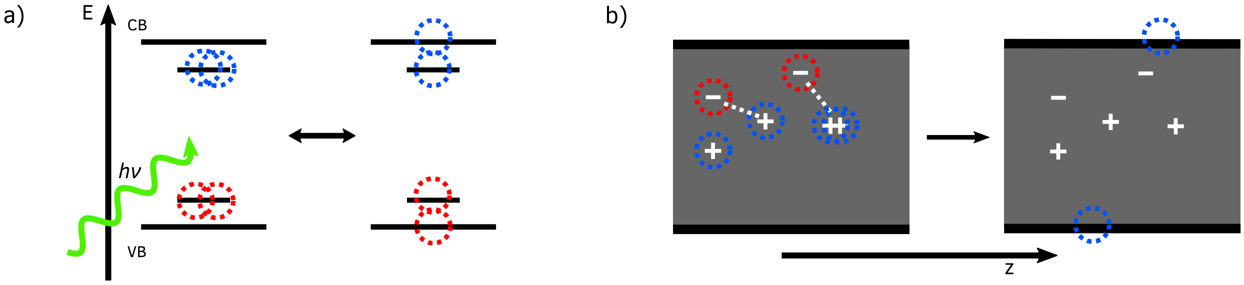

Figure 5.61: The Auger processes that can be imagined specifically for II-VI nanowires. a) Illustration of the peculiarity of the native defects in II-VI materials: These defects can be charged twice, but will be usually only charged once, leaving and access charge carrier at the defect site. b) The two imaginable Auger processes in such a nanowire. For the singly chargeable defects a second defect close to a donor–acceptor pair can contribute a charge that can absorb the recombination energy of the DAP and be excited, for example to the surface. The second example involves a DAP with at least one bivalent defect involved. At recombination the energy can be absorbed by the excess carrier.

Remaining charges at the defect sites can be excited by the energy getting released when a charge carrier pair that forms a complex with a defect recombines – for example into nanowire surface states.

As the observations that were described above for the radiative recombination pathways imply an ample amount of defect sites in the nanowire, this would also imply a higher likelihood of Auger recombinations[76] Considering that the only possibility to determine if Auger recombinations take place is the detection of hot carriers this non-radiative recombination path way can be assumed to probably occur but not be confirmed but neither refuted. The one aspect that has to be especially considered is that for the observed intermediate intensity states a certain mobility of the trapped charge carrier or multiple trap sites at different distances would be necessary.

6

Low-temperature luminescence of CdS bulk nanowires.

The analysis of the CdSe nanowire low temperature luminescence, as done in the previous chapter, shows that these nanowires are especially complex systems. The large number of overlapping signals that can be made out for small segments of these already very confined systems make it more or less impossible to analyse individual spectral lines and their dynamics. This means that in the end no definite statement about the behaviour of these lines can be made and any proposed model will remain, to a certain degree, conjecture.

One option to simplify the luminescence signal would be to look at systems without quantum confinement, meaning nanowires with diameters larger then twice the exciton Bohr radius. This would reduce the influence of the surface on the charge carrier levels and make it possible to directly compare to bulk literature spectra.

For CdSe nanowires, this is size control is not as easily done, at least not with the means of wet chemical synthesis. While synthesising thicker nanowires is comparably easy it has to be done through significant changes in synthesis parameters, which in turn changes the optical properties strongly, as has been shown by Li *et al.* and Wang *et al.*[77, 156].

Especially the second work shows a dramatic difference in optical quality between the two types of precursors used, even in room temperature spectra.[77] This difference in optical properties is further amplified at low temperatures. This can be clearly observed in the three single wire spectra in figure 6.1.

The spectra in figure 6.1a to c have been recorded by analysing single wires from the synthesis batches from which representative tem images are shown in figure 6.1d to f. All spectra were measured at about 7 K sample temperature and with the same illumination parameters (illumination wavelength $\lambda = 540\,\text{nm}$, pulse fluence of $E = 7\,\mu\text{J/cm}^2$, repetition rate of $f = {\sim}75\,\text{MHz}$). The tem images are shown to the right of the spectra that are representative for the wire luminescence from the same synthesis batch. The general location of the trap and nbe signals in each spectra are indicated with an arrow.

It is quite clear between the three spectra that different nanowire samples can show very different luminescence signals, without showing any significant differences in their morphology, as represented by the tem images. The three representative spectra show for one very different spectral line widths. The spectrum in figure 6.1a exhibits very narrow and intense luminescence signals. The tem image in figure 6.1d highlights that the nanowires are thin, they show no visible structural defects. This tem analysis of the second sample, shown in figure 6.1e, shows a very

Figure 6.1: Comparison of the low-temperature luminescence of CdSe nanowires from different synthesis batches. a) and d) as well as b) and e) show the low temperature luminescence spectrum and respective TEM micrograph for cluster synthesis CdSe quantum nanowires. c) and f) show the low temperature luminescence spectrum and the respective TEM micrograph of a molecular precursor nanowire batch showing no strong quantum confinement.

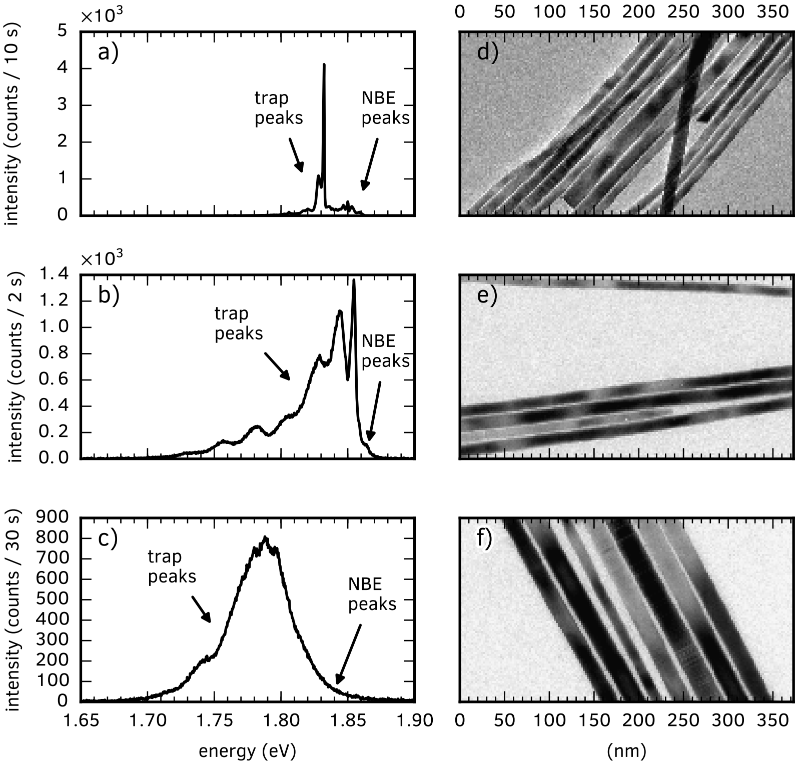

similar picture, with wires being thin and regular, with no obvious defect. While these nanowires look almost the same in the electron micrograph as those in the previously discussed sample, the spectra that is shown in figure 6.1b looks very different. The T signals are much broader and more numerous. Both samples show their highest energy peaks in very similar energy ranges, due to the very similar nanowire diameters.

While the two previous samples showed very different spectral line width and patterns, they both showed clearly distinguishable NBE and T peaks. This is in stark contrast to the spectrum in figure 6.1c. This luminescence is one very broad signal with minimal fine structure. The NBE peaks are not distinguishable within the broad blue shoulder of the spectrum and while some T peaks can be made out, the typical pattern with phonon replicas vanishes into a very broad energetic continuum of the emission. Also, emission intensity is significantly reduced, which limits the possibility of any time-resolved analysis.

This stark difference of emission properties to the other two samples is quite surprising when the representative TEM micrograph in figure 6.1f. The wire of this specific sample are very homogeneous in appearance, if significantly larger in diameter. The comparison between all three samples shows that the appearance in electron micrographs cannot predict the emission properties and therefore neither the electronic properties of CdSe nanowires. Also, as shown here in an example, the thicker nanowires that were sampled in this work usually showed the broadened signals that can also be observed in figure 6.1c. The reason for this strong heterogeneity between samples is unknown. Some influence might be ascribed to the precursors used in the synthesis as cluster precursors would usually lead to thinner wires, higher luminescence intensities and thinner wires, while using molecular precursors results in thicker wires that show much lower intensity luminescence. This has been before shown in synthesis studies by Wang *et al.*[77] at room temperature. At low temperatures the additional broadening of the spectrum could be observed.

As the problem of acquiring no-confinement CdSe nanowires with good optical properties via chemical synthesis is to this day not solved in this work a different but related systems were used for comparison. These systems are CdS bulk nanowires that were synthesised via a single-source precursor solvothermal method.[120] These nanowires were found to show stable, reproducible luminescence properties with high luminescence intensities at room temperature and could also be easily contacted and integrated into nanoscale devices for opto-electronic analysis.[157]

The following section will therefore analyse the low temperature luminescence of these nanowires and compare these to the luminescence of the CdSe quantum nanowires.

6.1 CdS bulk nanowire static luminescence properties

The luminescence signal of CdS bulk nanowires – or rather, of bulk CdS in general – is much broader in energy than that of CdSe. This is more or less due to the much larger band gap which permits a large distribution of trap states. This leads to defect-related luminescence signals that can be observed from 0.01 eV to 1.36 eV of the free exciton signal. A comprehensive review of studies analysing the CdS bulk luminescence signals and their origins can be found in section 1.1 and will be referenced for any peak assignment in the following section.

The bulk CdS nanowire luminescence at room temperature has been described extensively in the work of Behn. The luminescence usually shows a narrow near ban–edge signal and a very broad deep trap band. This could be easily reproduced, as can be seen in the pink spectrum in figure 6.2. The low-temperature spectrum recorded at the same position of the wire at 5 K sample temperature is shown as a blue line. Both spectra were recorded with the same illumination power and wavelength ($P = 100\,\text{nW}$, $\lambda = 440\,\text{nm}$ at $\sim 75\,\text{MHz}$ pulse repetition rate), but with 30 s integration time for the room temperature spectrum instead of the 10 s integration time used at 10 K sample temperature. Both spectra are normalized to the maximum intensity.

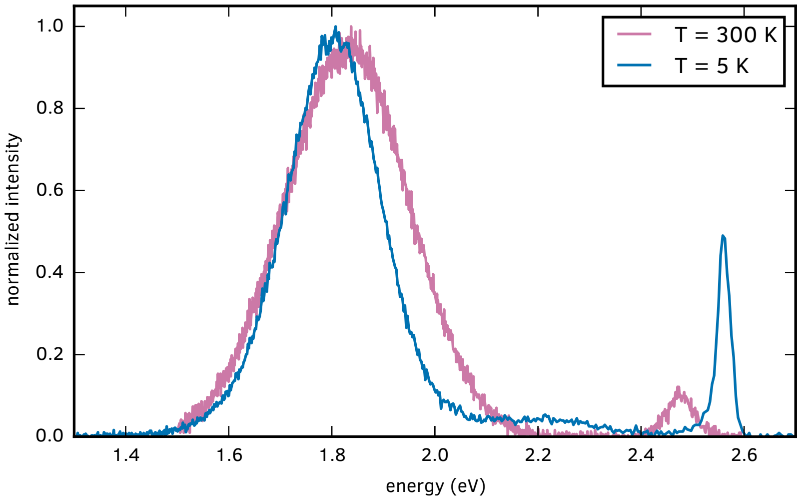

Figure 6.2: Comparison of the luminescence spectra of a single CdS bulk wire taken at 300 K (pink) and 5 K sample temperature, respectively.

The room temperature spectrum of the representative CdS nanowire shows two signals – one small and narrow band at 2.4708 eV and a very broad band with its maximum at 1.8279 eV. The low energy band is located 642.9 meV from the high energy – potentially exciton-related – emission line, relating it to deep traps.

In comparison, the spectrum in blue – taken at the same position of the same wire – shows three distinguishable signals at 2.5574 eV, 2.2239 eV and 1.8031 eV. The narrow line at the blue edge of the spectrum can be expected to contain the free exciton transition (with good agreement with the values listed in 2.3) as well as very close bound exciton complexes, which is implied by the slightly asymmetric shape. The two lower energy bands are both very broad and located at 333.5 meV and 754.3 meV from the high-energy peak maximum. This places them in the group of the deep traps. The consulted literature of bulk CdS analysis did not contain any deep trap luminescence bands at exactly these energies, which means that no specific defects can be assigned.

The spectral changes between room temperature and 5 K sample temperature can be summarized as follow: The exciton-related NBE emission shifts, as expected, to the blue. The deep trap emission splits into two bands, a low intensity band at higher energies and a high intensity band at lower energies. Considering that the positions of these bands relative to each other and the exciton level are much further away then the room temperature thermal energy the reason for these spectral changes have to go beyond energy level population changes.

The above described spectral shape was typical for the analysed nanowires. While there was a fine structure to be observed in the excitonic peak region, the often-reported *I* lines (exciton complexes with neutral and charged defects), as well as the DAP and free–to–bound green bands (tables 2.4 and 2.5) could not be observed in most spectra.

Another aspect of nanowire luminescence that has been observed before – both for CdSe quantum nanowires and CdS bulk wires – is the luminescence intensity modulation through the injection of charge carriers. This has been done before, for one by injection through a conductive AFM tip[71] but also by conducting single CdS bulk wires on one side and applying a modulated voltage.[157] These experiments were repeated within the scope of this work to repeat the experiments at low temperatures with the goal to observe the modulation at low temperatures and resolve the modulation of individual spectral bands that can only be seen at low sample temperatures.

The first step in these experiments was to reproduce these modulations at room temperature. Single nanowires were contacted via optical lithography and a sine-modulated voltage was applied. The intensity of the complete nanowire luminescence was recorded in a TTTR file. Intensity trajectories with a time bin chose appropriately for the applied modulation frequency were exported and fast FOURIER transform (FFT) was used to analyse any periodic intensity changes of the luminescence.

Two example traces of the modulated CdS luminescence at room temperature are shown in figure 6.3a and c. The FFTs of these traces are shown in figure 6.3b and d, respectively. For both traces a voltage of 10 V peak–to–peak was applied, at 1 Hz for the trace in figure 6.3a and at 100 Hz for the trace in figure 6.3c. These frequencies are confirmed by the strong peaks at these frequencies in figures figure 6.3b and d. Figure 6.3d also shows several peaks that are introduced by the electronics used for the application of voltage, for example at about 50 Hz and 150 Hz. These peaks are not present when no voltage is applied to the wire.

The modulation of the luminescence at 1 Hz is nicely observable in figure 6.3a, in which the luminescence intensity visibly follows the 1 Hz sine function. At the same time scale the 100 Hz modulation in figure 6.3b is, of course, not resolved. Generally, the modulation of the luminescence could not be observed by eye due to the much stronger noise of the luminescence signal, figure 6.3a was one of the few exceptions. In a typical trace only the FFT would reveal the modulation from within the luminescence intensity noise. This is very unlike the previous experiments that have been done by BEHN with the same material system, where the modulation was normally visible by eye at much lower voltage amplitudes.[157]

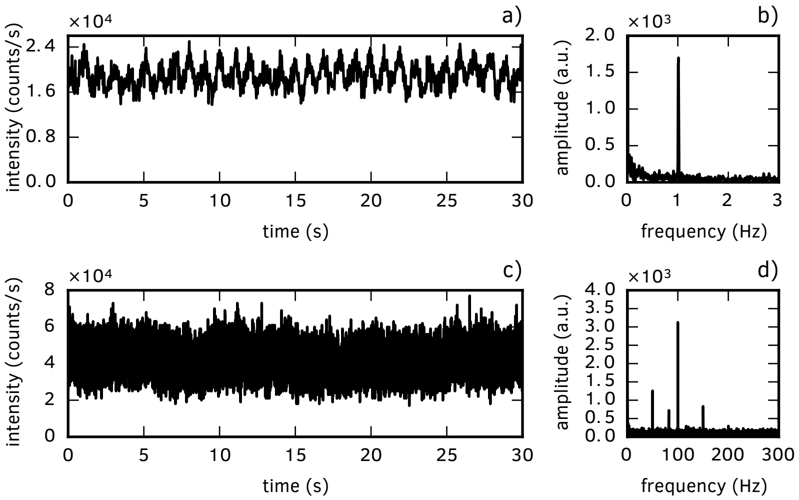

Figure 6.3: The intensity modulation of the CdS bulk nanowire luminescence through the injection of charges. a) The intensity trajectory showing a 1 Hz modulation. b) The FFT of the trajectory with 1 Hz modulation. c) An intensity trajectory that is modulated at 100 Hz and d) the respective plot of the FFT.

The much lower intensity modulation amplitudes observed in this work are possibly related to two reasons. One is the changed lithography process that was used for writing the contacts. As in the previous work electron beam lithography was used and in this current work optical lithography it might be that the resist residues would increase the resistivity between nanowire and metal contact, even though the same contact material was used. Also, not the same batches of nanowires were used. Depending on the dopant levels and especially the concentration the injection of charge carriers might not have been very efficient.

At low temperatures the luminescence modulation was reproduced as well. This experiment confirmed the high barrier between the conduction band and the metal Fermi level. Figure 6.4a to c show the FFTs of the intensity trajectories recorded at the points A to C marked in figure 6.4d. The applied voltage had a peak-to-peak amplitude of 30 V and a frequency of 200 Hz.

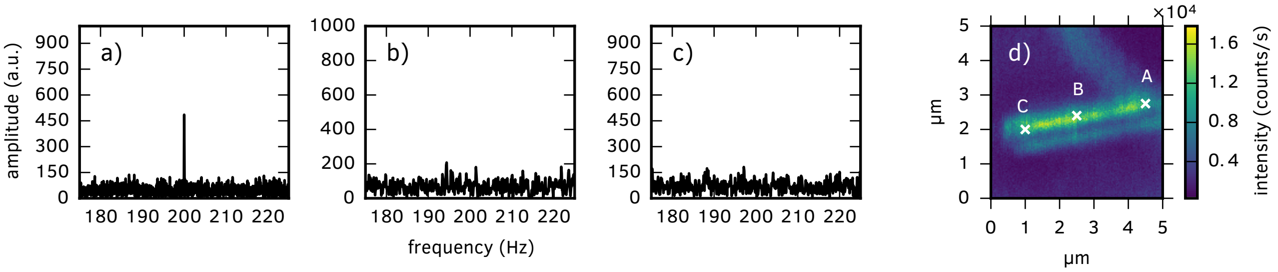

Figure 6.4: The dependence of the low temperature intensity modulation magnitude on the distance to the electrical contact. The FFT plots in a), b), and c) belong to the points marked respectively A, B, and C in d).

The FFTs of the three recorded intensity trajectories show that the modulation is only visible if the illumination and light collection is performed at the contact–wire interface. Illuminating the wire at a larger to the contact (located on the right side of the nanowire, as shown in figure 6.4d) will not lead to a modulated luminescence intensity, even if the voltage is applied. This implies that the potential barrier between the metal Fermi level and the nanowire conduction band is rather large. For the illumination at the interface the potential barrier will be lowered through the excitation of charge carriers over the potential barriers, thus making an injection of charge into the wire possible.

While the luminescence intensity modulation measurements suggest a really low doping concentration for the CdS bulk nanowires synthesised via a solvothermal synthesis route luminescence spectra show that there is some variation in defect concentration along a single nanowire. This is illustrated in the spectra in figure 6.5a. These were taken along the nanowire shown in a luminescence image in figure 6.5b. The points at which the spectra were taken are marked in figure 6.5c. The marks top to bottom represent the positions of the respective spectra top to bottom. All spectra were taken with the same illumination intensity as well as the same integration time of 10 s per spectrum.

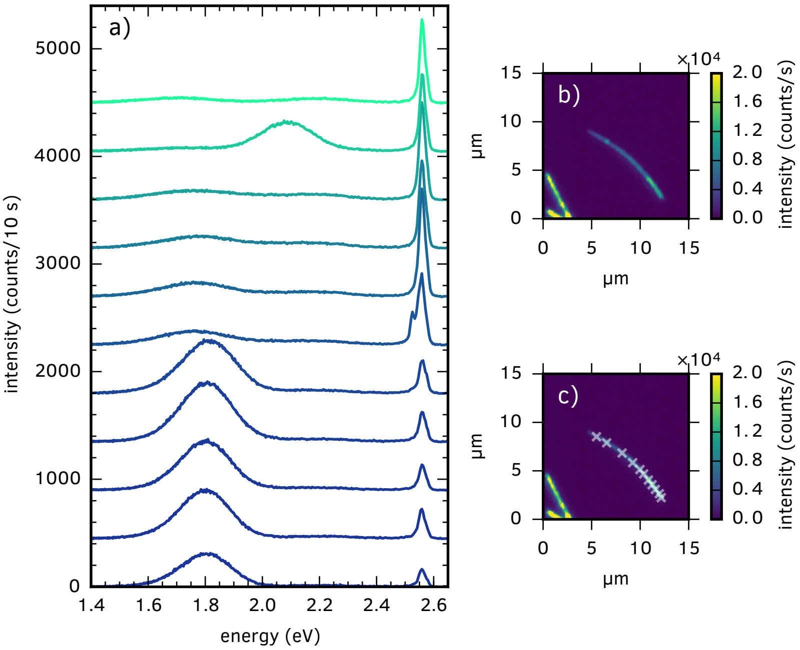

Figure 6.5: The spectral variations along a single CdS bulk nanowire. a) The waterfall plot of the spectra recorded from a single wire. b) The confocal luminescence image of said wire. c) The positions of spectra acquisition marked in the confocal image.

What can be already seen in the low temperature luminescence scan images is that the nanowires show variations in luminescence intensity along their long axis. These intensity changes correlate, as can be seen in the respective spectra, with the appearance of different deep trap bands, to the point that these bands become the main luminescence line. That said, in many spectra the exciton related recombinations contribute as the highest intensity band.

On first glance the luminescence of CdS nanowires behaves quite differently to that of CdSe quantum nanowires. The deep traps that are so dominant for the charge carrier recombination paths in CdS are usually not even visible at all in the CdSe quantum nanowire luminescence while the NBE and T bands that cause the very distinct shape and show the complex dynamics in the CdSe quantum nanowire luminescence seem completely absent – as seem the dynamics.

While the exciton–related emission and the deep traps are usually the dominating spectral features a closer look at the blue edge of the spectrum reveals that there are other, not as obvious spectral changes. These also concern lines that are much more narrow and located much closer to the exciton line of the CdS nanowires.

An example is shown in the two spectra shown in figure 6.6. The two spectra were taken at different locations off the same nanowire. the spectra are normalized to the same peak at 2.5586 eV. The black spectrum shows a excitonic signal region that consists of one relatively broad signal, if compared to the very narrow CdSe emission. The signal shape implies maybe a slight shoulder in the blue but is otherwise quite smooth. In comparison the spectrum shown in red shows a strong second peak at 2.5257 eV.

This second peak is located 32.9 meV from the highest intensity peak, which locates it within the range of reported bound exciton lines (see

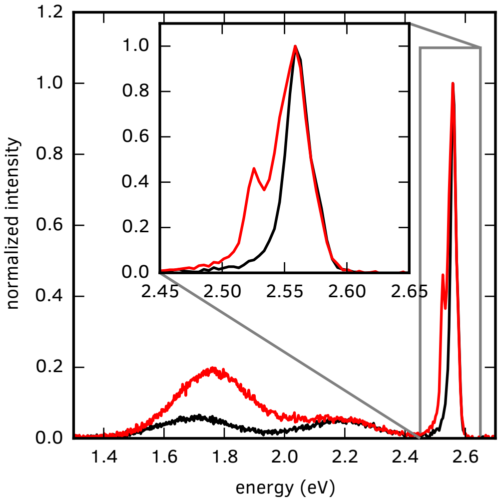

Figure 6.6: The fine structure of the CdS bulk nanowire luminescence at different points of the same wire. The inset shows the significant changes in the narrow high energy region of the spectrum.

table 2.4). This shows that CdS bulk nanowires do indeed emit what was classified within this work NBE emission for CdSe quantum nanowires.

One reason why these might not be easily resolved is the spectral resolution of the above shown CdS bulk nanowire spectra. To record the entire nanowire spectrum without the need to move the spectrograph turret and stitch together multiple spectral regions gratings with a small number of lines per millimetre have to be used. This of course reduces the spectral region tremendously and can lead to some lines not being resolved clearly. Also, signals as observed in the red spectrum in figure 6.6 were present only at very few spots. To nonetheless analyse these kind of signals wires were analysed not only at specific points but along their whole length through spatially resolved techniques. These are discussed in the following section.

6.2 *Spatially resolved analysis through hyperspectral and fluorescence lifetime imaging*

As seen in the spectra above the CdS bulk nanowire luminescence is not heterogeneous between different sections of the nanowires. This is quite similar to the CdSe quantum nanowire luminescence, as I already showed within the scope of my master's thesis.[20] In comparison to the CdSe quantum nanowires the spectral changes are much less frequent and the non-excitonic signals are much less intense.

The CdS nanowires that were analysed in this study have a few key differences to the CdSe nanowires, in addition to the different material properties. For one, they are not covered with a long chain ligand for stabilisation. In addition the bulk nanowires have a diameter around 40 nm. With an exciton BOHR radius of 3 nm the charge carrier pairs can be expected to not be confined in any spatial direction while in CdSe quantum nanowires the charge carrier pairs are strongly confined in two dimensions. This also implies a much smaller surface–to–volume ratio for the bulk wires. A representative example for the morphology of the bulk nanowires is shown in figure 6.7. The SEM micrograph shows one long nanowire with a length of about 3 µm and a shorter, 1 µm segment at the top aligned parallel to the long wire. Both segments are almost identical in apparent diameter and very smooth and homogeneous in appearance. This implies that any defects that would contribute to nanowire luminescence are more likely to be related to point defects than any larger defects such as larger crystal structure defects.

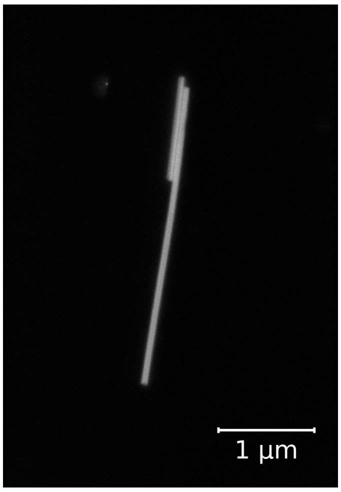

Figure 6.7: The SEM micrograph of a CdS bulk nanowire pair analysed spectrally. No structural defects can be made out for either nanowire.

Due to the low density of defects to clearly characterise those defects present hyperspectral luminescence imaging is a powerful method. For a hyperspectral measurement the sample is scanned confocally, but instead of detecting the entire luminescence signal with a point detector the light is split spectrally in a spectrograph and detected with a CCD camera. While this method increases the measurement time per pixel from 10 ms to 20 ms to one to several seconds it yields complete spectral information for every point of the wire.

These resulting hyperspectral maps are especially useful in identifying signals that can only be measured in select spots along the wire that might be missed with single spot measurements. The data can be sliced along the spectral axis and the intensity of single spectral bands can be plotted spatially resolved. A representative example for such slices from the same measurements can be seen in figure 6.8. The spectra were recorded with an illumination power density of 109 W/cm² at about 75 MHz pulse repetition rate, which comes down to a pulse energy density of 1358 J/cm² at an illumination light wavelength of 460 nm. The integration time per spectrum was 1 s.

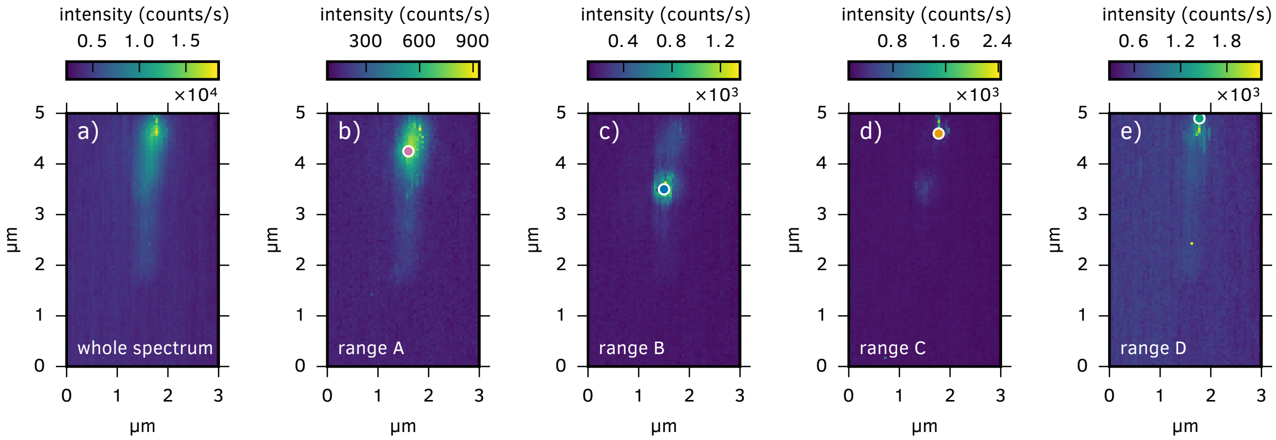

Figure 6.8: Spectral intensity slices extracted from a hyperspectral imaging (HSI) of the above-shown wire pair. The different spectral ranges are marked in the spectra in figure 6.9. The images show a) the whole spectrum, b) range A, c) range B, d) range C, and e) range D. Different slices show different intensity distributions.

Figure 6.8a shows the summed intensity of the whole spectrum, while figures 6.8b through e show the intensity of different spectral slices of the ranges A to D. These ranges are marked as grey areas in the spectra in figure 6.9. The width of the ranges were selected to both contain the specific emission bands and allow for a sufficient signal–to–noise ration in the HSI slice images. The spectra in figure 6.9 were extracted at the points marked in the images with circles. The spectra are normalized to their respective maximum intensity value. The lowermost spectrum is a sum of the spectra of all image points. The spectra from the second lowest to the spectrum at the top were extracted at the points marked in the images from figure 6.8b to e. The spectra are plotted with the line coloured the same as the fill colour of the circles marking the positions.

The first observation to be made is, that the sum of all recorded spectra is dominated by the excitonic emission but does show some small signals at lower energies. In turn, the not energy resolved intensity map shows mostly very homogeneous intensity along the nanowire. The area in which the shorter wire segment is located is overall higher in intensity. There is a small area at the top of the two wires that shows a few brighter pixels.

Considering the different defect related emitting charge carrier complexes, different parts of the spectrum should map the occurrence of these specific complexes. As the exciton line of these nanowires should

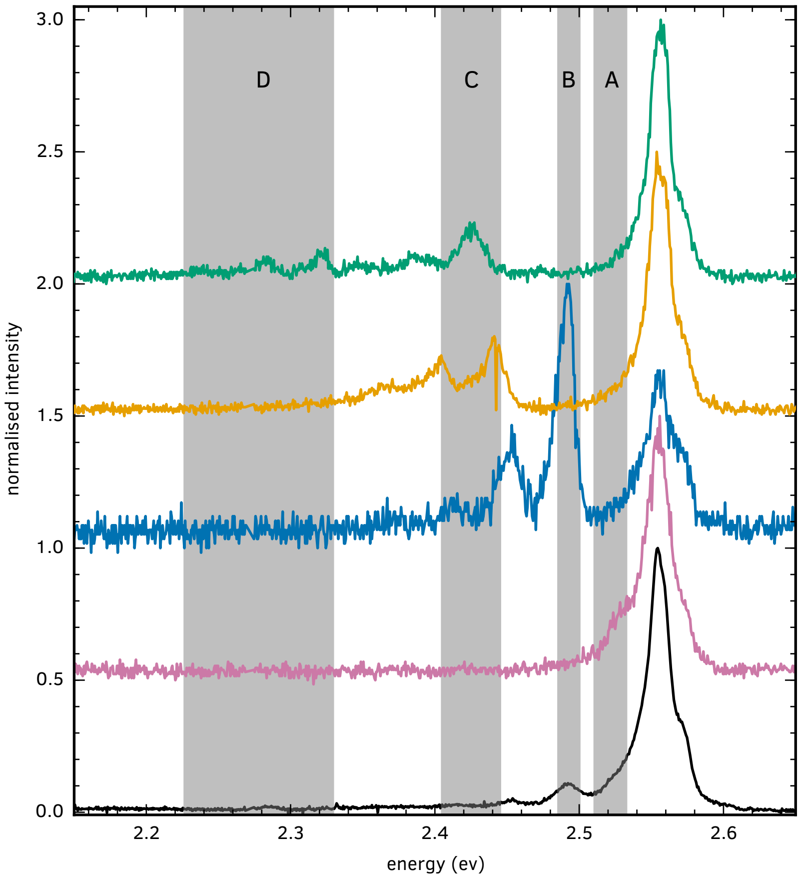

Figure 6.9: Spectra extracted from the HSI measurement at the points shown in figure 6.8. The spectra are, bottom to top, the sum of all spectra (black line), the spectrum from the point marked in figure 6.8a, the spectrum from the point marked in figure 6.8b (pink), the spectrum from the point marked in figure 6.8c (blue), the spectrum from the point marked in figure 6.8d (yellow), and the spectrum from the point marked in figure 6.8e (green).

not be shifted by quantum confinement the energetic difference between the emission of the blue edge of the spectrum and the lower energy complex emissions should be directly comparable to those values reported for the bulk crystal emission.

In all spectra shown in figure 6.9 the two same lines at high energy can be seen. They appear at 2.571 eV and 2.555 eV, which is a good match for the reported energies of the B exciton and the A exciton, respectively. The reported literature values can be found in table 2.3. These two excitonic lines can be observed irrespective of position along the wire.

As the vast majority of the reported charge carrier pair–defect site complexes are those of the A exciton (table 2.4) the energy difference to the A exciton emission will be listed in the text below. The first of the lines that can be assigned to these complexes is that at 2.527 eV, or at 28 meV to the exciton line. This emission is well visible in the second spectrum from below and marked with the range A spectral region. This signal is located quite a bit lower in energy than most of the bound excitons listed in table 2.4 which are reported between 14 meV to 18 meV but still not nearly as low as the deeply bound excitons, listed in the same table and in table 2.2 (108 meV to 116 meV).

Considering that bound excitons are often reported to appear as very thin emission lines and have phonon replicas in the bulk[21] this shoulder at the red side of the excitonic signals can also likely be a broad, not resolvable distribution of multiple bands and potential replicas.

The spatial distribution of this specific band within the nanowire is shown in figure 6.8b. Some emission in this region can be observed in every part of the wire, but the distribution is noticeable different to that of the spectrally integrated luminescence. markedly the centre of the short wire segment shows increased luminescence in this spectral region, as well as some single pixels at different positions of this wire. As the spatial resolution of the confocal microscope – determined by the light spot size – is much larger than a single image pixel step – determined by the step resolution of the mirror scanner that was used to move the beam over the sample – these single pixel intensity spikes can usually be interpreted as a blinking process – if an emission band exhibits sudden, short intensity spikes during the measurement this can be visible as a single pixel. The measurement time per pixel for this HSI data set was 1 s per pixel, which implies that the intensity dynamics would have to occur on a time scale close to this value to be visible in the image.

Moving to the most prominent emission line in the third spectrum in figure 6.9, the highest intensity signal at 2.491 eV with a prominent LO phonon replica at 2.453 eV is contained within the spectral range B. This range's spatial emission distribution is shown in figure 6.8c and is much more confined to a very distinct sections of the nanowires. Some single pixel intensity again imply intensity fluctuations on the single second time scale. The identity of this emission band can again not be clearly determined by consulting the bulk literature. It's located 64 meV from the exciton peak, falling again between the group of weakly bound excitons and the deep bound excitons. This band is also quite broad in appearance, similar to the reported appearance of the green DAP and free–to–bound emissions which are expected at even lower energies (see table 2.5).

Finally, the two top spectra show signals that can be generally assigned to the group of green emission bands, as listed in table 2.5. The zero phonon lines of these emission appear at 2.442 eV, 2.425 eV, as well as 2.321 eV at respective energetic distances of 113 meV, 130 meV, and 234 meV. While the first two emission lines (contained in spectral range C) fit clearly within the reports of green bands in the bulk literature, the third band (contained in range D) is shifted much more strongly to the red and a clear identification of the emission is not possible. For the two other lines, both a free–to–bound complex, as well as a DAP complex are possible origins for the observed emission.

Considering the spatial distribution of the two bands in the spectral range C, this signal is the one that is visible in only very small areas of the wire, namely the two ends of the small wire segment. This implies that the defects that contribute to the signal are located more at the ends of the wire.

For the strongly shifted signal in range D the distribution is slightly different. The signal–to–noise ratio of the emission band is not as high in comparison and the highest intensity pixels are located at the upper end of both nanowires. For both spectral ranges single high intensity pixels can be observed, especially at the upper end of the two wires, implying intensity dynamics on the pixel integration time scale.

One aspect that strongly differentiates the CdS nanowire luminescence from that of the CdSe quantum nanowire luminescence is that the defect related radiative recombinations are much less frequently observed at similar measurement parameters. Regarding these very parameters, one aspect that could be found to influence the luminescence spectra and therefore the processes in the nanowire was the excitation power or photon fluence. This can be seen in the hyperspectral study of the very same nanowire duo as before, but this time with a tenth of the illumination power used (20 nW or 136 J/cm^2 at a 75 MHz repetition rate). To adjust for the smaller number of generated charge carrier pairs and subsequent drop in signal–to–noise ratio the integration time per pixel was increased to 10 s. The resulting HSI images, with the slices showing the same energy regions as in figure 6.8, are shown in figure 6.10a to e.

As can be seen in all spectral slices, the intensity along the wire is much more heterogeneous, even for the spectrally integrated intensity image in figure 6.10a. All spectral slices show single pixel intensity spikes,

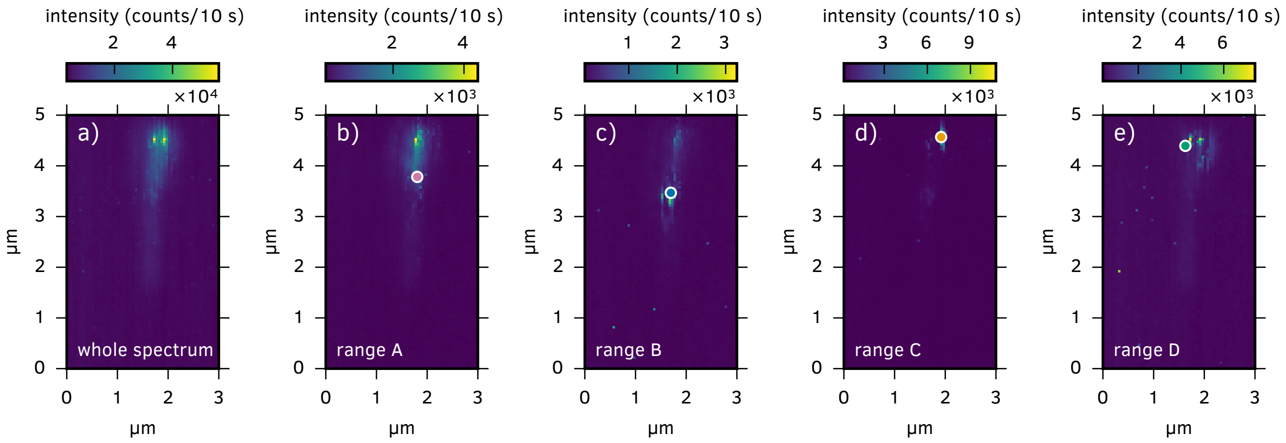

Figure 6.10: Spectral intensity slices extracted from a HSI of the above-shown wire pair, but with a tenth of the before-used illumination power. The different spectral ranges are marked in the spectra in figure 6.11. The images show a) the whole spectrum, b) range A, c) range B, d) range C, and e) range D. Different slices show different intensity distributions.

which means that intensity variations even on the 10 s integration time scale can be observed.

As with the HSI taken with standard illumination parameters spectra were extracted at pixel with particularly high intensity for each spectral slice. These spectra are shown in figure 6.11. The spectra were normalized to their respective maximum intensity value and plotted with an offset for clarity. The lowermost spectrum is again the sum of all recorded spectra, the spectra extracted from the pixels marked in the figure 6.10b to e were plotted in the same order from the second lowest to the highest spectrum. The colour of the marker in the respective intensity images responds to the colour of the plot line of the respective spectrum.

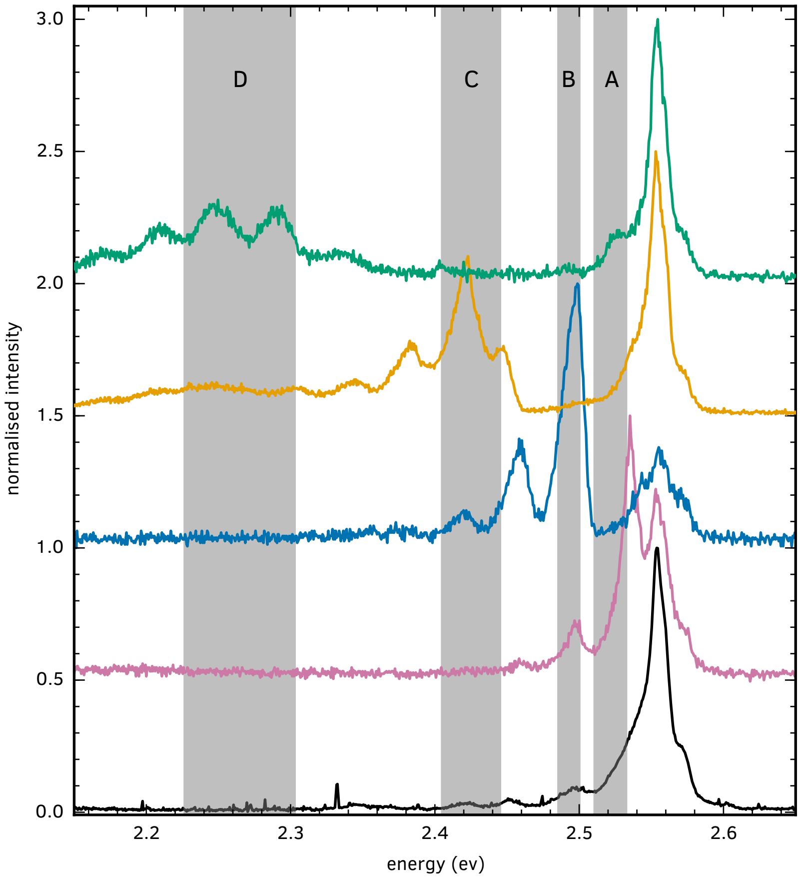

Figure 6.11: Spectra extracted from the HSI measurement at the points shown in figure 6.10. The spectra are, bottom to top, the sum of all spectra (black line), the spectrum from the point marked in figure 6.10a, the spectrum from the point marked in figure 6.10b (pink), the spectrum from the point marked in figure 6.10c (blue), the spectrum from the point marked in figure 6.10d (yellow), and the spectrum from the point marked in figure 6.10e (green).

At first glance the main difference to the measurements with an illumination power of 200 nW is that the lower energy defect-related bands are much more prominent in appearance in the images recorded with one tenth of the illumination power. There are also several new bands that appeared throughout the shown energy range. That said, interestingly the sum of all spectra did not change significantly.

The illumination bands that could be observed at 20 nW of illumination power are as follows: Firstly, the exciton bands of the A and B exciton could be observed again with no spectral shift. The energetic shift of the defect recombination emission will again be given as the difference to the 2.555 eV A exciton. That said, in addition to those exciton bands the relatively broad high energy signal can now be resolved into several signals, as can be seen in the second spectrum from the bottom. This spectrum shows an additional signal between the A and the B exciton at 2.5574 eV, which means a shift of 13 meV to the red of the B exciton.

Also, an additional line is now visible around 2.536 eV, shifted 19 meV from the A exciton signal. I also exhibits two LO phonon replicas. Looking closely at the zero phonon line, it can be seen to consist of at least three different signals at energies of 2.540 eV, 2.535 eV, and 2.533 eV. This is equal to a shift of 15 meV, 20 meV and 22 meV from the A exciton line. These three lines are quite close to the reported values for the exciton-defect complexes that have been reported in the literature before (see table 2.4), if shifted a bit more strongly to the red. This observation strengthens the assumption that the excitonic emission as observed at 200 nW is broadened due to the presence of a distribution of bands.

Interestingly the preciously observed shoulder at 2.527 eV is still visible at other points of the wire, as can be seen in the green, topmost spectrum.

Coming to the main spectral signal in spectral range B, the middle spectrum again shows the strong emission with LO phonon replicas, apparently at the same position. Looking at the exact emission energy, this band's maximum is now located at 2.498 eV or 57 meV from the exciton emission. This is a band shift in comparison to the measurement at 200 nW of 7 meV. Considering that the intensity images already imply intensity dynamics, spectral dynamics are also likely to occur and it is quite safe to assume that this is the same band as observed in the middle spectrum in figure 6.9.

Finally, the spectral regions that contain the previously observed green emission signals can still be only observed in very specific parts of the two nanowires. both emissions are located at points on the nanowires that should not be possible to be differentiated through confocal microscopy – this means that what looks like the spectra originating at different positions in the HSI is actual a difference in time: At certain moments emission in region C was observed, while at other emission region D was visible.

The main green bands that could be observed for the yellow spectrum (region C, second from the top in figure 6.11) are located at 2.447 eV and 2.422 eV, or at 108 meV and 133 meV from the A exciton line. Lo phonon replicas are visible and the energetic positions are well within the reported region of DAP emission (see table 2.5).

For spectral region B – top green spectrum – the three observed green bands are located at 2.335 eV, 2.290 eV and 2.247 eV. All three bands have the typical slightly broadened appearance of the reported green bands, and LO phonon replicas are also visible for the mire intense emission, but the location of the bands is shifted unusually strong: The emission maxima are located at 220 meV, 265 meV, and 308 meV from the exciton emission. These values lie much lower than the usually reported bulk DAP emission lines, but are still considerably higher in energy than the often observed deep trap emissions.

The hyperspectral images of CdS bulk nanowires reveal two important aspects about the property of the solvothermally synthesized bulk nanowires. For one, the strong dependence of the luminescence spectra on the excitation power – much stronger than has been observed for CdSe quantum nanowires[19, 20] – implies a quick saturation of the recombination path through the formation of charge carrier–defect complexes. This implies that these complexes are probably very long-lived and, more likely, the defect concentration much lower than in the CdSe quantum nanowires. Additionally, while the bulk appearance of the defect-related luminescence lines is easily reproduced for the bulk nanowires, the position of these lines is not. Both bound exciton lines, and green free–to–bound and DAP emissions are observed in a much broader energy range, implying a nano-scale-dependent effect on electronic properties, even in the nominally bulk system.

6.2.1 *The relationship between the luminescence spectra and the luminescence decay time*

As the defect-related luminescence involves the recombination of a stabilised charge-carrier pairs these excited states should have longer lifetimes than the free exciton. A spectral heterogeneity in regards to position on the nanowire should therefore be expected to lead to a lifetime heterogeneity. At the same time defect related non-radiative recombinations should in turn lead to a decrease in fluorescence lifetime, as these quick processes compete with the radiative pathways.

One option to probe the spatial heterogeneity of the luminescence lifetime is to record a FLIM. As with hyperspectral imaging for every pixel the recorded photons are not only counted but also resolved, but this time the additional dimension is not an energy axis but a time axis, relative to the excitation pulse, in this case by using TCSPC. The FLIM that was recorded at 20 nW illumination power of the two nanowires analysed spectrally above can be seen in figure 6.12

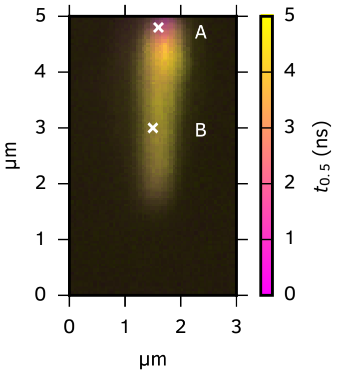

Figure 6.12: fluorescence lifetime image (FLIM) of the nanowire pair that was analysed spectrally in the text above. The brighter the colour, the higher the emission intensity. The lifetime ($t_{0.5}$, the time at which half of the photons were registered) is coded with a false-colour colour map from pink to yellow. These particular nanowires do not show a strong spatial heterogeneity in terms of luminescence lifetime.

The FLIM of the above analysed nanowire pair appears a lot less heterogeneous than the recorded spectra would suggest. most of the nanowire shows an average luminescence lifetime between 4 ns to 5 ns. There is only a small area at the top of the wire where a significantly shorter lifetime is visible. Looking at the lifetime recorded at different pixels of the FLIM – the two positions marked with A and B – the lifetimes in the small area of short luminescence lifetimes is $t_{0.5}(\mathrm{A}) = 2.34$ ns and in the majority long luminescence lifetime area is $t_{0.5}(\mathrm{B}) = 4.32$ ns. While there is a significant difference to be observed between these two areas, the meaning of the absolute decay time values is not clear. Also, none of the single pixel intensity differences, that could be observed for the HSI slices are visible in this FLIM.

An example that provides context for the above data is that of a nanowire in which radiative defects could be induced using very high illumination intensity. This process was a one time occurrence and could not be reproduced, but gives nonetheless valuable insight into the properties of defect-related luminescence.

The images in figure 6.13a to c show a single CdS nanowire confocal luminescence image recorded after one another with different illumination powers. The scan in figure 6.13a was taken first, with an illumination power of 200 nW at 460 nm light wavelength and a laser repetition rate of 75 MHz. The scan in figure 6.13b was taken after at 20 µW illumination power and the scan in figure 6.13c was taken last, using 20 nW of illumination power. For the scan in figure 6.13b neutral density filters were used in front of the detection beam path to reduce the detected luminescence to 1/1000.

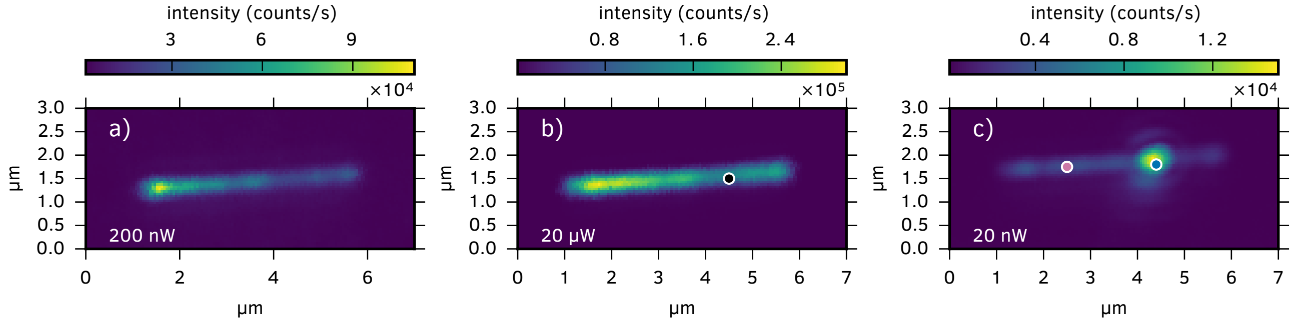

Figure 6.13: Confocal luminescence images of a single CdS nanowire with a) 200 nW, b) 20 µW, c) 20 nW illumination power. After the high intensity confocal scan local photobrightening could be observed at one spot of the wire. The marked points show the positions at which the spectra shown in figure 6.14 were taken.

As can be seen, the intensity distribution along the nanowire does not change significantly from figure 6.13a to b. The distribution is maybe a little more even. The spectrum taken at 20 µW illumination power at the spot marked in figure 6.13b is shown as the lowermost spectrum in figure 6.14, plotted in a black line. All spectra in the plot are normalized to the maximum intensity and the spectra are offset along the y axis for ease of comparison. The spectrum of the high intensity illumination measurement shows only one broad band at 2.566 eV, around the energetic area of excitonic emission. The emission is broadened even beyond the longpass filter edge around 2.625 eV in the blue and beyond 2.5 eV in the red. No defined defect related emission bands can be observed.

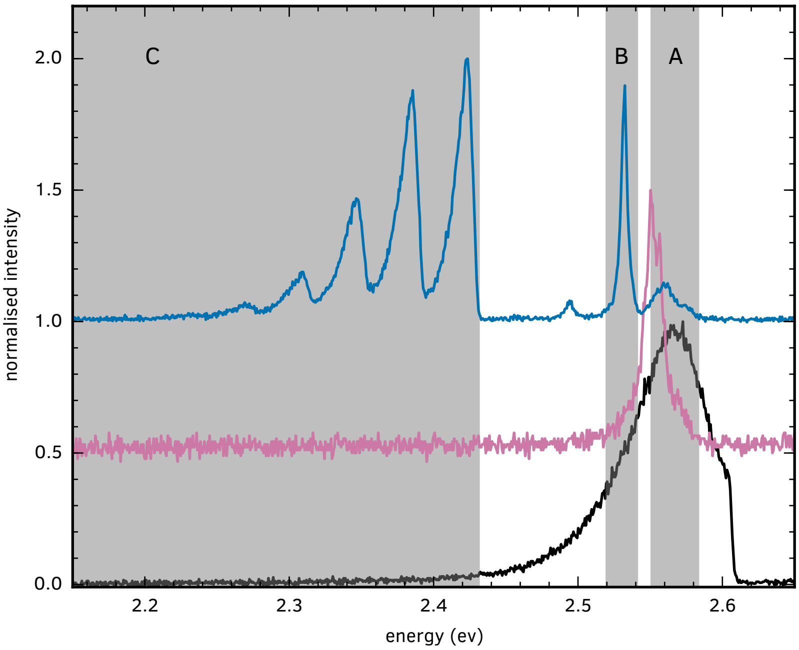

Figure 6.14: Spectra taken at the positions shown in figure 6.13b and c. The lowermost spectrum (black) shows the spectrum taken at 20 µW illumination intensity, at the point marked in figure 6.13b, while the other two (pink and blue) were taken afterwards with an illumination power of 20 nW at the two accordingly coloured spots marked in figure 6.13c.

In comparison, the scan image taken after the high power illumination using an especially low illumination power of 20 nW show a strong change in luminescence intensity at one specific spot. This photo brightening in this one specific area could be observed permanently in the same spot through repeating confocal scans. The two marked spots in the confocal image – a pink filled circle in a low intensity part of the wire and a blue filled circle in the photo brightened part of the nanowire – show the spots at which the respective middle and top spectra shown in figure 6.14 were recorded.

The middle spectrum from the nanowire low intensity area in figure 6.14 shows that the main emission of the nanowire still consists of the excitonic peak group – the A and B exciton emissions are still present at 2.555 eV and 2.570 eV and a few weakly bound exciton lines are also present, mainly one at 2.551 eV, 4 meV from the A exciton peak. Additional shoulders and slight broadening imply the presence of further, not clearly resolved bound exciton lines. This spectrum is very much like most spectra recorded at low temperatures on CdS nanowires within this work.

In comparison, the spectrum taken at the spot that experienced the photo brightening (topmost spectrum in figure 6.14) looks markedly different. In addition to the excitonic signal group two intense signals with LO phonon replicas can be made out. The first is located at 2.533 eV, which is located at 22 meV from the A exciton line. This signal can be assigned to belong to excitons bound to a defect site, with a slightly bigger energy shift than reported in the literature (see table 2.4). due to the broadened signal shape the observed signal is likely to different complexes at slightly different energies. The phonon coupling can be clearly observed, but is much smaller than that of the green emission band at 2.423 eV or 132 meV from the exciton emission. The emission is very broad, implying the presence of a broad distribution of states and a strong localisation of the charge carriers due to the strong phonon coupling. The emission energy cannot be assigned to any exact reported DAP or free–to–bound states – see table table 2.5. Nonetheless, the emission appearance and general energetic location make it clear that this band is very likely originating from DAP recombinations.

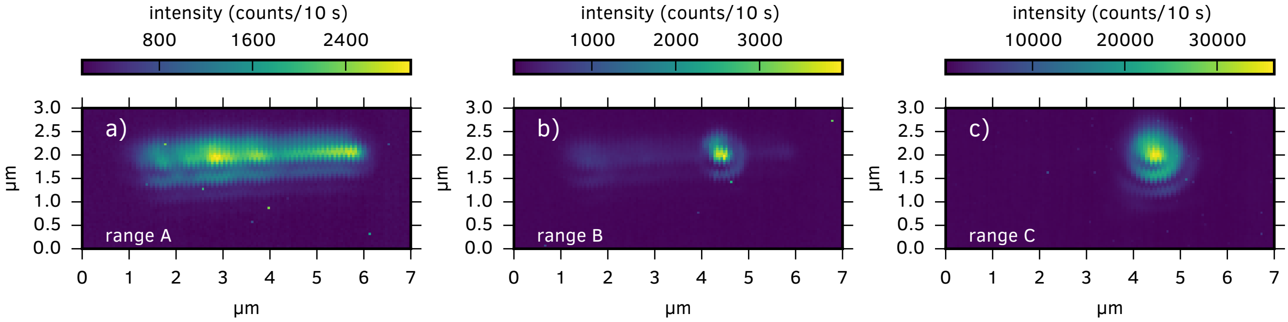

Figure 6.15: Spectral intensity slices extracted from a HSI of the photo-brightened nanowire. The different spectral ranges are marked in the spectra in figure 6.14. The images show a) range A, b) range B, and c) range C. The slices show that the intense green bands are confined to the newly bright spot.

The most likely reason for the appearance of this strong green emission can most easily be explained by the simple assumption that the strong illumination power triggered a local photoreaction, for example a photochemical process, which lead to the creation to a defect site that is able to stabilize charge carrier pairs that can subsequently recombine radiatively. This process was strongly localised, as the HSI of the photo brightened wire confirms. The spectral slices A to C of the HSI recorded with an illumination power of 20 nW are marked in figure 6.14 in grey and the intensity maps are shown in figure 6.15a to c. The parts of the spectrum that are mapped in these images can also be described as follows: figure 6.15a shows the range A, the excitonic emission, figure 6.15b with range B the emission from bound excitons and figure 6.15c the green emission contained in range C. In all images the focal plane of the setup was slightly misaligned, leading to the wire appearing with slight halos around it.

What can be clearly seen for the intensity distribution of the different spectral ranges is that the excitonic emission is not strongly influenced by the photo brightening process. There might be a small reduction of excitonic recombinations, but this can also be attributed to the availability of competing radiative recombinations for the charge carriers that are generated in the area of this nanowire. Looking in turn at the distribution of luminescence originating from the recombination of bound excitons, while these happen to a certain degree along the whole wire, they are much more numerous in the region of that was brightened. Finally, the luminescence of the green band can only be observed at the brightened spot.

The above observations confirm that the solvothermally synthesised nanowires seem to have relatively low defect concentrations. In this case the low defect concentration actually leads to a reduced luminescence in comparison to the nanowire segment in which defects seem to have been created that increased the luminescence in comparison to the nanowire's native state.

The significant punctual change in electronic properties is also confirmed by the FLIM of the nanowire. The three states – before the brightening at 200 nW illumination, during the high power 20 µW scan and afterwards at 20 nW illumination – are shown in figure 6.16a through c.

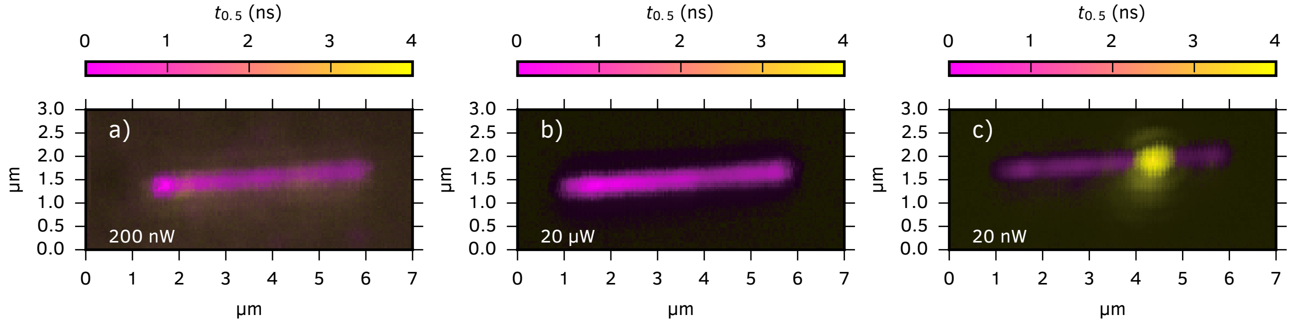

Figure 6.16: The FLIM images of the CdS nanowire a) before, b) during, and c) after the photo-brightening of the green band. The brightened spot clearly shows increased luminescence decay times.

While the images in figure 6.15a and b clearly show a general quick luminescence decay with no inhomogeneities the image in figure 6.15c shows that the luminescence from the brightened spot is now clearly dominated by the defect luminescence. As the defect stabilise the generated charge carrier pairs in complexes they are much more long-lived – which in turn increases the average luminescence lifetime from 1 ns and below to 4 ns.

This shows that the defects in CdS nanowires play a very similar role for the luminescence of the CdS bulk nanowires as the defects in CdSe quantum nanowires do. Another aspect that has also been observed throughout the shown spectra and images is that the exact positions of the defect bands are only in the area of the lines reported in the literature and that luminescence dynamics can already be assumed from the static confocal images and spectra.

6.3 Dynamics in bulk systems: CdS bulk nanowire photoluminescence blinking

As evidence occurrence of luminescence intensity dynamics in CdS bulk nanowires was already visible in the HSIs the direct observation of these dynamics was observed. Considering that for most CdS bulk wires both the bound exciton lines (the *I* lines in the bulk literature, see table 2.4) and the green emission – DAP and free–to–bound lines as listed in table 2.5 – are only present in very few spots on most nanowires. In a few spots, discovered through spectral slicing of HSIs in the observed regions of the *I* and green emission, for both types of emissions bands could be found for which intensity fluctuations could be observed.

The bound exciton intensity fluctuations of the CdS bulk nanowire bound exciton luminescence was measured for one wire with the standard excitation parameters (excitation light wavelength 460 nm, 75 MHz repetition rate, 200 nW excitation power) measuring one spectrum per second for 2400 spectra. Three 300 s excerpts from different points of the spectral trace – from the beginning, middle, and end of the measure can be seen in figure 6.17a to c.

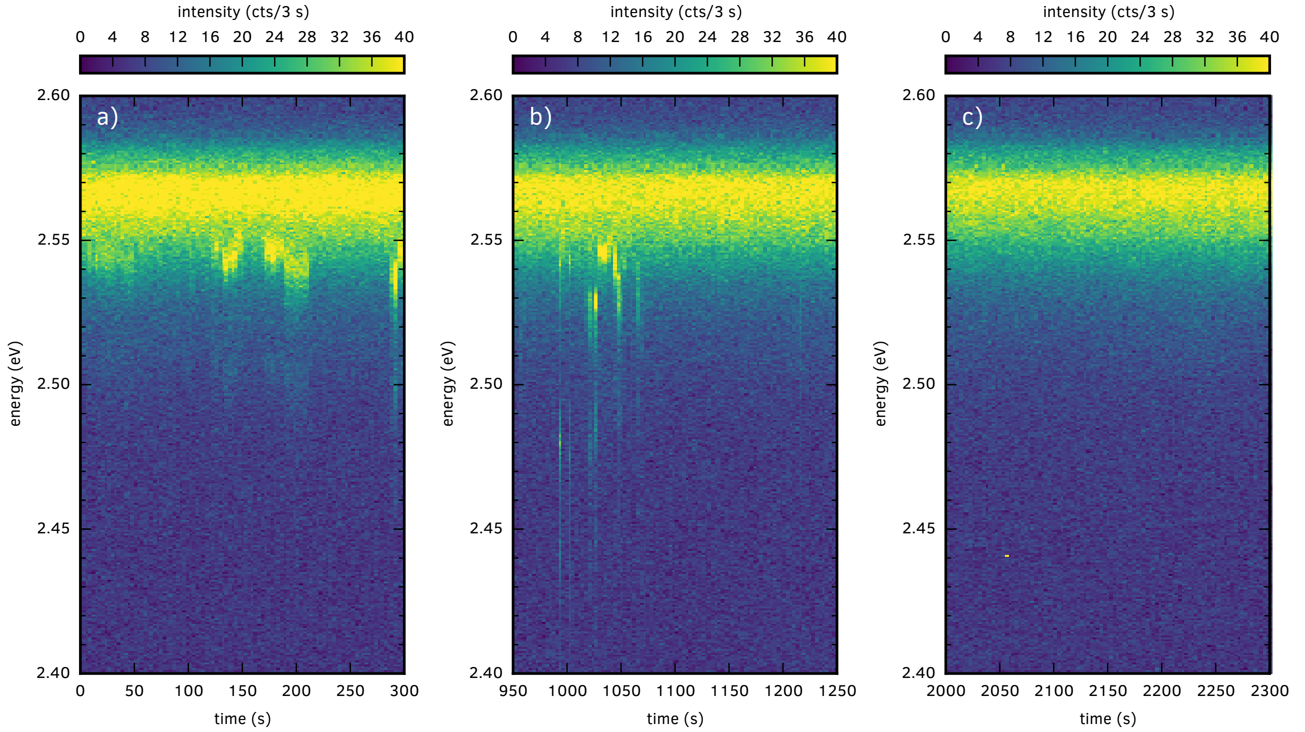

Figure 6.17: The luminescence dynamics of the *I* band of a single CdS bulk nanowire. Three different excerpts of a 2400 s trace are shown. a) The trace segment from 0 s to 300 s. b) The trace segment from 950 1250s. c) The trace segment from 2000 2300s.

The first observation that can be made for the long time luminescence measurement of the CdS nanowires is that the exciton emission does not show any significant dynamics. At any time during the measurement the fairly broad exciton emission bands are stable in both intensity and shape, as can be seen in all three spectral traces in figure 6.17a to c.

The luminescence blinking observed for this nanowire is that of a band that likely originates from the recombination of a bound exciton, considering the the emission's energetic location and appearance. The signals all exhibit LO phonon replicas and can be seen in the figures 6.17a and b. In both time frames – 0 s to 300 s and 950 s to 1250 s – the *I* luminescence band appears and disappears again for random time periods and at random intervals. In most frames the bound exciton bands are not observable in this case, only the high energy group containing the exciton bands can be made out. Over time the fluctuating luminescence band extinguishes for the rest of the measurement, and in the time from 2000 s to 2300 s, which can be seen in the trace in figure 6.17c, the signal does not reappear.

What is clearly visible in the traces is that the emission does not only fluctuate in intensity, but it also shifts dramatically in terms of energy. For some parts of the trace – for example in figure 6.17a from 100 s to 200 s – the bands shift continuously in energy, while in other parts – for example in figure 6.17b from 1000 s to 1050 s– the emission jumps suddenly for sometimes more then 10 meV at a time.

The large range of different bound exciton bands that can be observed in this trace is illustrated in figure 6.18. Different spectra from the spectral

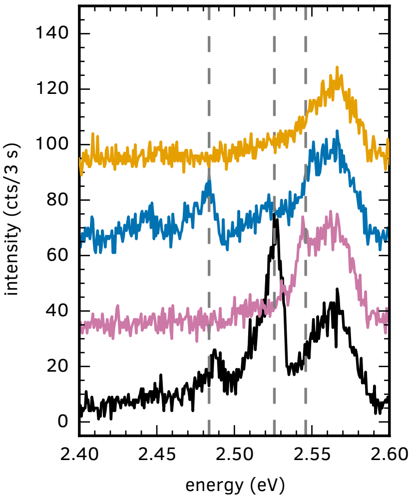

Figure 6.18: Spectra from different points of the spectral trace shown in figure,6.17. The *I* emission zero phonon line in each spectrum is marked with a grey dashed line.

trace are shown, the spectra are plotted with a y value offset for ease of comparison.

From bottom to top the first three spectra – plotted as black, pink, and blue lines – show bound exciton lines at different energy positions. In the uppermost spectrum – plotted as a yellow line – no bound exciton line with significant intensity can be made out. In the other three spectra three bound exciton lines can be made out clearly, one in each spectrum. In the black spectrum at the bottom the most intense I line can be observed at 2.526 eV or 29 meV from the A exciton emission line. In the pink spectrum above that the I emission line is visible just at the edge of the excitonic HE emission. The line has no clearly discernible phonon replica and appears, insofar as that can be said, considering the overlap with the HE emission, quite narrow. It is located at 2.546 eV, or 9 meV from the A exciton emission. These two bands are quite close to the range of reported I bands. These have been reported in the literature as occurring between 13 meV to 18 meV from the A exciton. As the bands are quite close to this range it is likely that their origin stems from similar complexes as have been identified in the bulk literature. That said, the slight difference, both to the red and the blue from this range, implies a difference in electronic structure in comparison to the bulk luminescence. Finally, the third spectrum from the bottom, shown as a blue line, shows the I line at 2.484 eV, or 71 meV from the exciton line. This is much much lower than the I lines reported for bulk spectra, but not shifted quite enough to fall into the reported range of green emission (from 113 eV from the A line downwards).

One observation that can be clearly made for the recorded spectra is that the I bands observed in this trace do not appear simultaneously. While the observation of only single I signals might be due to the spectra recording parameters, but as it is quite reproducible it might even be a single recombination channel whose availability and recombination energy is influenced by the same changes in potential landscape as the defect related recombinations in CdSe quantum nanowires leading to both emission blinking and changes in emission energy.

The above described fluctuations in emission intensity and energy were not only visible for bands in or near the I range energy, but also for those bands that appear in the range of the green emission, as referenced in table 2.5. These signals were observed over a time frame of 47 000 s on the same spot of the same nanowire. Three 400 s excerpt of the trace are shown in figure 6.19a to c for time frames in the beginning, middle, and end of the entire measurement time. Measurement parameters was an excitation intensity of 120 nW with 460 nm light and a repetition frequency of 75 MHz with a spectrum integration time of 1 s. The false colour scale was adjusted to ease the identification of the blinking bands, which in some cases leads to a not quite ideal presentation of the HE spectral region.

For these signals also the LO phonon replicas can be made our clearly. Especially in figure 6.19a the replicas can be seen to shift with the zero phonon line. The appearance of the bands resembles strongly that of the shifting T bands in the luminescence in CdSe quantum nanowires. The bands fluctuate in emission intensity and exhibit strong spectral shifts and jumps. The emission changes strongly within the time frame of the 47 000 s (about 13 hours) measurement. The band's maximum intensity starts out high(figure 6.19a), dwindles to barely noticeable (figure 6.19b) and reappears, exhibiting general lower intensities and stronger spectral shifts towards the end of the measurement (figure 6.19c).

The magnitude of the spectral shifts and jumps are again easily visible in single extracted spectra from the trace. These spectra are shown, offset along the y-axis for ease of comparison, in figure 6.20. The spectra are

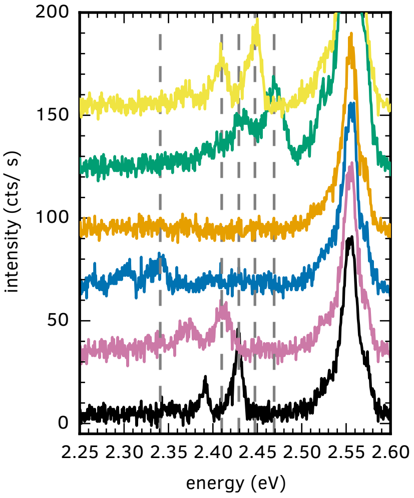

Figure 6.20: Spectra extracted at different points of the spectral trace shown in figure 6.19. The zero phonon lines of the green emission are marked with grey dashed lines.

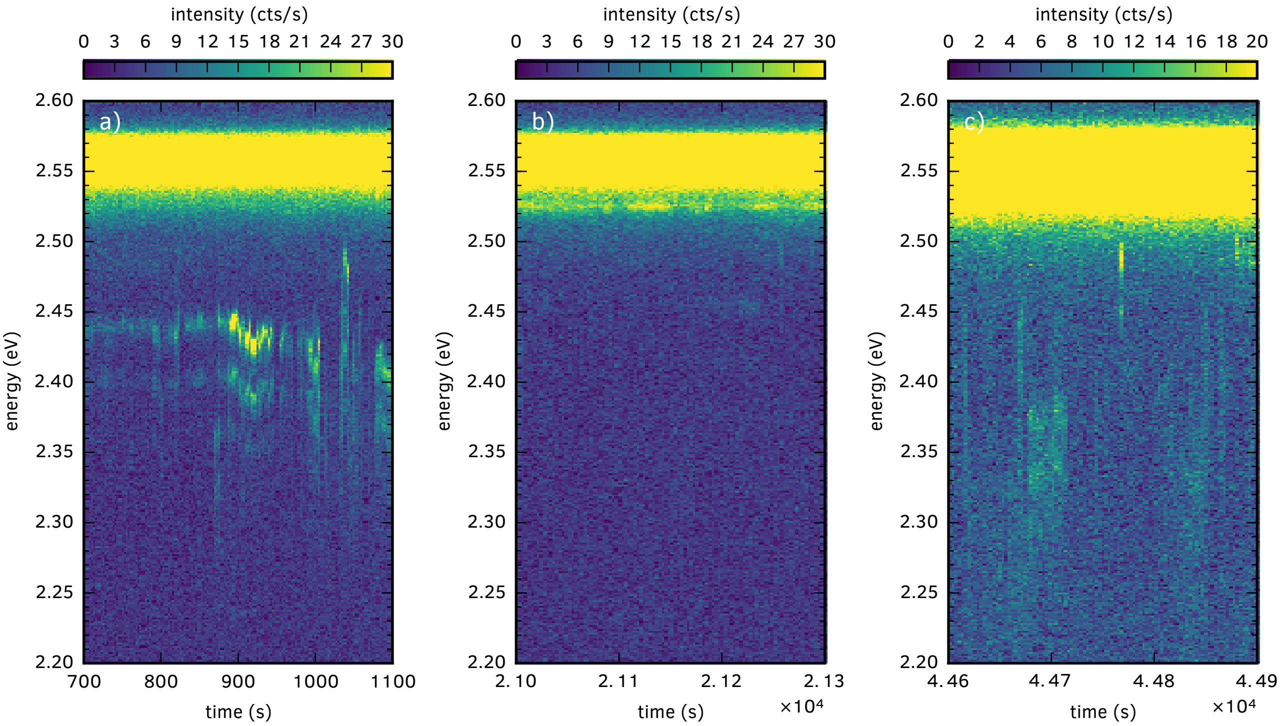

Figure 6.19: The luminescence dynamics of the green emission band of a single CdS bulk nanowire. Three different excerpts of a 47 000 s trace are shown. a) The trace segment from 700 s to 1100 s. b) The trace segment from 21 000 21300s. c) The trace segment from 44 600 44900s.

shown in chronological order from bottom to top. The first spectrum shown was recorded at 303 s measurement time, while the topmost spectrum was recorded at 44 855 s. The spectra were plotted and scaled in a way to best show the green emission.

The first observation that can be made is that the spectra that show the green emission change less from the early phase of the measurement to after more than 12.5 hours. This implies that a certain stability of the related defects and local potential landscape can be assumed. That said during the recording of the series strong changes in this emission can be observed, both in intensity – down to the complete quenching of the emission, as shown in the orange spectrum, fourth from the bottom – as well as in terms of emission energy. The observed zero phonon emission lines shown in the spectra are located from 2.469 eV to 2.341 eV, or at distances from the A exciton of 86 to 214 This energy range encompasses the reported range of the green emission (113 eV to 159 eV) but, as the *I* emission before, exceeds that range both in the blue and red. Here again similar mechanisms as in CdSe quantum nanowires can be assumed for these shifts and jumps, due to the strong similarity in appearance.

As the defect related emission in CdS bulk nanowires is relatively low in comparison the HE emission, especially when compared to the emission of CdSe quantum nanowire spectra, it is even harder to isolate and analyse the emission dynamics of these lines. The attempt of at least qualitative analysis of those dynamics related to changes in luminescence decay time is shown in figure 6.21a to c. The intensity trajectories show the first 900 s of the *I* band dynamics also shown in figure 6.18 with a bin time of 50 ms.

In figure 6.21a the intensity represents the sum of all lifetime channels, while in figure 6.21b only the first 20 channels after the lifetime curve maximum are shown and in figure 6.21c the last 500 channels of the curve.

As the spectral traces show that the excitonic HE emission in CdS bulk nanowires is exceptionally stable in terms of its emission intensity

Figure 6.21: Lifetime gating of the intensity trajectory recorded simultaneously to the spectral trace in figure 6.17. The blinking is visible in the entire intensity trace in a). In b) the short lifetime component of the luminescence does not show any intensity variations, while in the long lifetime component c) the blinking is well visible, but a constant background of the luminescence is also preserved.

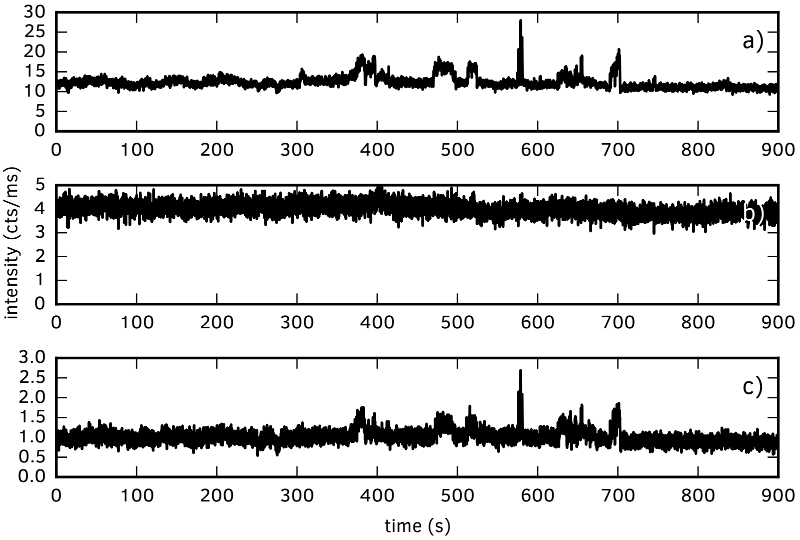

the fluctuation in the trace is likely due to the defect related *I* emission blinking. The *On* states can be made made out as clearly defined states, but the difference in intensity is small and for the majority of the time this emission pathway is not available.

Lifetime gating of the emission shows that the emission intensity related to short decay times is exceptionally constant, as can be seen in figure 6.21b. This part of the luminescence follows a very constant average value which is only affected over the long time minuscule changes in excitation laser emission intensity.

In comparison the long decay time component of the CdS bulk nanowire emission contains the intensity fluctuations that can be observed in the sum of all lifetime channels, but also, different to the CdSe luminescence, contains a baseline emission intensity. This baseline means that a significant part of the static luminescence is emitted through the decay of long-lived channels. Going by the emission spectra of the nanowires this means that the excitons of the CdS bulk nanowires are much more long-lived than those of CdSe quantum nanowires – and that not as many quick non-radiative recombination paths, for example through surface states are available.

The emission fluctuation or blinking of emitters has until usually been considered a property of nanoscale systems, such as molecule or nanocrystals experiencing quantum confinement. The above data shows that also defect-related recombinations in bulk systems can exhibit these properties.

Figure 6.22: The luminescence dynamics in a single CdSe bulk nanowire. One τ band can be seen to exhibit intensity fluctuations.

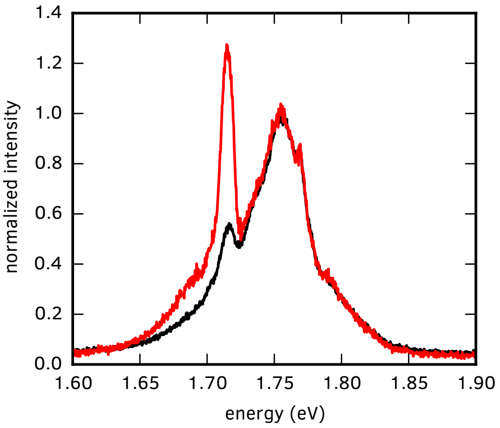

As a further contribution to these observation of nano-effects in bulk systems, the spectra in figure 6.22 were recorded from a single CdSe bulk nanowire, which had a diameter of 80 nm. These nanowires did typically not show very defined spectra, their luminescence intensity was so low that they often required spectra integration time of 30 s, even at low sample temperatures, and luminescence dynamics could usually not be observed. That said for the wire observed in figure 6.22 luminescence dynamics could be observed for the T band zero phonon line at 1.716 eV or 85 meV from the exciton emission and its phonon replica. This emission can be seen to change increase tremendously in intensity from the black to the red spectrum, reminiscent of the emission dynamics of the quantum nanowire T emission. This confirms that the emission in bulk systems that stems from localized charge carrier complexes act as their own nanoscale systems that will be strongly influenced by their surroundings.

7

Summary and conclusions

The CdSe quantum nanowire and CdS bulk nanowire low temperature (~5 K to 7 K) luminescence could be observed in static and time resolved measurements, on time scales from the hour to the nanosecond. For either system the nanoscale dimensions were found to influence the luminescence properties, even in the absence of quantum confinement for the CdS bulk nanowires. In the following the observations will be summarised for both types of nanowires and the observation that could be made for both system – the single band luminescence blinking will be discussed in light of the studies and discussions that have been published regarding the blinking of nanocrystals.

The luminescence of CdSe quantum nanowires summarised For the CdSe quantum nanowire luminescence this study was able to expand on our findings in previous studies.[19, 20, 75] The characteristic spectral shape and the luminescence dynamics that occurred independent for different parts of the emission spectrum could be observed again and for multiple samples from different synthesis batches. Most importantly, the two emission group assignment was found to be incomplete and a third, independent group could be identified. This expanded the description of the CdSe QNW spectra by differentiating the high energy and NBE emission for the narrow, higher energy side of the spectrum. This is illustrated by the marked areas in figure 7.1.

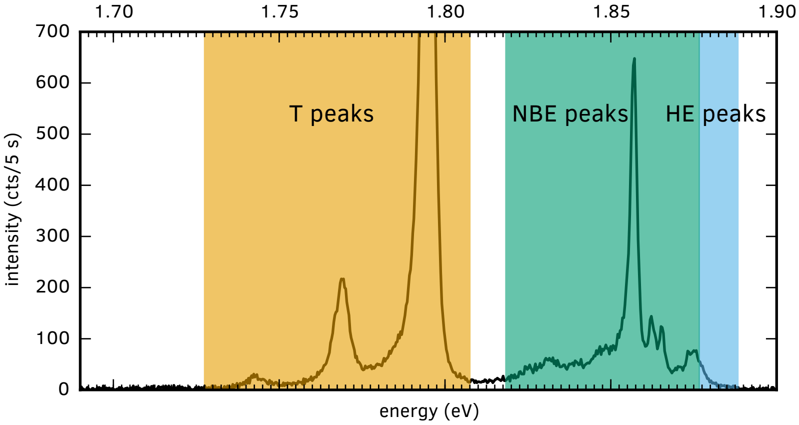

Figure 7.1: The new emission band group assignment that could be deduced from the time-resolved spectral measurements in this work. The T band (marked yellow) assignment is unchanged while the NBE emission group has to be divided into the NBE (marked green) and HE (marked blue) emission.

The very weak HE emission (marked in blue in the example spectrum in figure 7.1) are now a better match for the relative energy values of the free exciton and weakly bound exciton lines as reported in the literature.[105] The remaining NBE emission was found to to occur in an energy range of 10 meV to 90 meV from the exciton energy and overlap significantly with the observed range of T emission zero phonon lines.

While the NBE emission was observed in all measured spectra, the T emission was not always present. All three signals groups, HE, NBE and T were found to exhibit luminescence dynamics. While the HE emission was much too weak for comprehensive studies, the NBE and T emission could be studied through long spectral and TTTR traces. Spectral traces dominated by either emission group are shown in figure 7.2. In figure 7.2a a spectral trace showing only NBE luminescence is plotted in false colour. The spectrum does not show any T bands, but does show blinking of the NBE luminescence. In comparison, figure 7.2b shows nanowire luminescence with a strong T band just at about 1.79 eV with three characteristic phonon replicas. There is some NBE luminescence present, but the T emission is dominant. The T band shows clear luminescence blinking and shifting. The shifts in luminescence energy were accompanied by changes in luminescence lifetime with lower energies resulting in longer lifetimes as well as stronger phonon coupling. That said, this relationship was always only true for each individual T band, as the absolute luminescence lifetime and phonon coupling would differ between bands, with no direct relationship to the band spectral position. This strong differences in position in the spectra and in magnitude of phonon coupling between individual T bands confirms that these bands are linked to individual defect sites with very specific, individual surrounding potential landscape.

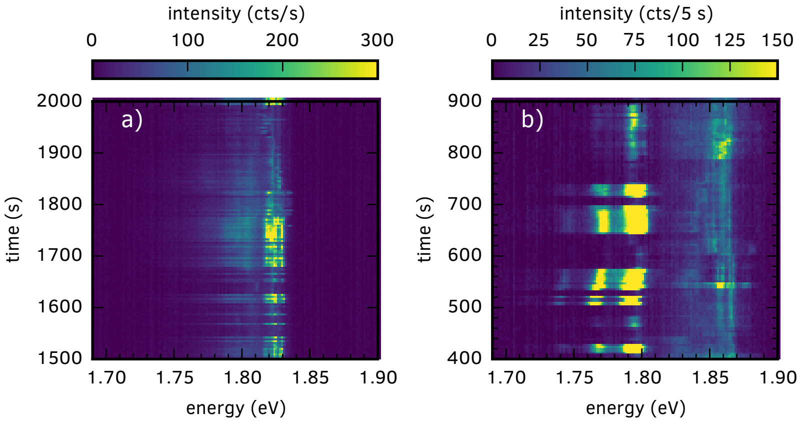

Figure 7.2: The two main types of CdSe QNW emission blinking: a) NBE blinking, T band blinking.

In comparison the NBE emission could be found to consists of plenty of overlapping narrow signals that would show two types of intensity fluctuation. The first was the fluctuation of single bands within this dense group of emission lines. Single lines would suddenly increase and decrease in emission intensity, with no clear dependence on the luminescence lifetime shown. Also, the entire group of signals would show blinking and flickering, more or less identical in appearance to the blinking of the T emission. Phonon replicas could not be observed for this group of signals. The observed behaviour implies that the origin of this signal group is related to multiple, but energetically similar charge carrier–defect complexes whose radiative and non-radiative transitions rates can be influenced by one shared factor.

While the fluctuations of theseT and NBE emission line groups would usually appear to be completely independent of each other, in some cases clear interdependence could be observed, implying mechanisms that involve the same defect sites.

Based on the new observations new assertions about the mechanism behind these charge carrier pair recombinations could be made. The charge carrier–defect complexes for the HE, NBE, and T emission are shown in figure 7.3a, b, and c. The before identified signal groups of the HE and T emission[75] could be confirmed to arise from weakly bound excitons

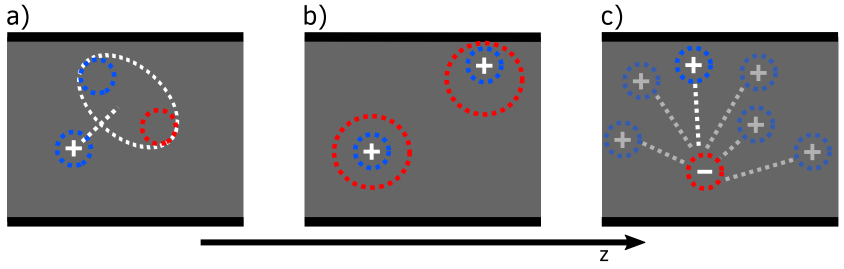

Figure 7.3: The proposed charge carrier–defect complexes whose radiative recombinations are responsible for the CdSe QNW luminescence pattern. a) An exciton, weakly bound to a neutral defect, likely responsible for the HE emission. b) The likely origin of the NBE emission, a charge carrier pair bound to a single ionised defect site. c) A donor–acceptor pair between one minority and several majority defect sites as the origin for the broad T emission.

(figure 7.3a) and donor–acceptor pair, complexes, respectively. The T band emission mechanism specifically was expanded to explain the broad line with, while retaining the dependence on a single defect and the possibility of a plausible blinking mechanism. This is illustrated in figure 7.3c. In this mechanism one minority defect site (in this case an acceptor) is surrounded by several majority defect sites. A DAP will have the hole always localise at the acceptor, while the electron can localise at several sites, slightly varying the DAP energy and broadening the emission band. A blinking mechanism of the band would be related to the minority defect site.

For the NBE emission a completely new mechanism had to be proposed, as these bands had not been described before. As the weakly bound excitons and strongly localised DAPs were well reported for the bulk the one complex type that could most easily explain all observed emission behaviours was that of the an electron–hole pair bound to a single ionised defect. This is illustrated in figure 7.3b. While the exact nature of the bond – either a localisation of the exciton or a free–to–bound complex are possible – could not be determined within the scope of this study, the appearance of signal group (many, distinguishable bands that fluctuate individually but can interact with the T emission, fit into the image of the NBE emission being caused by complexes of charge carrier pairs with the majority defect type.

The luminescence of CdS bulk wires summarised CdS bulk nanowire synthesised via solvothermal synthesis were the chosen system to compare the luminescence of confined charge carrier complexes to those in a system significantly larger than the exciton Bohr radius. This choice was made due to the ability to synthesise high quality nanowires via a chemical method from a material with very similar electronic properties to the standard CdSe.

The spectra of these wires at low temperature ($T = 5\,\mathrm{K}$) showed mostly the expected blue shift of the exciton band but no large difference in the broad, deep trap related luminescence. Like at room temperature the low temperature luminescence could be modulated through the injection of charge carriers, with the modulation experiment already implying that the CdS bulk nanowire shallow dopant concentration was very low. This was further confirmed by comprehensive spectral analysis of single nanowires which showed strong changes in deep trap luminescence, but the appearance of the shallow trap luminescence only in very few spots.

As this shallow trap luminescence was the one that could be most easily compared to the CdSe quantum nanowire NBE and T emission it was specifically sought through hyperspectral imaging. This method could reveal a strong spatial heterogeneity in the I line and green band spectral regions. From both of these groups signals could be identified, but an exact determination of the defect identity using the emission energy was not possible, as the signals were in fact shifted both to the red and blue of the values reported in the bulk literature, while the quite steady exciton recombination bands showed very good agreement with the bulk literature. Also, low excitation power HSI measurements showed that the relative emission intensity of the defect related emissions increased with lower excitation photon fluences. This is in agreement with the assertion that the ionisation state of the defect sites approaches a steady state depending on excitation intensity and number of available trap sites. As the number and concentration of trap sites in the CdS bulk nanowires was already expected to be much lower than that in the CdSe quantum nanowires the stronger dependence on the illumination power can be explained.

The low number of trap states also explains the quite uniform luminescence decay time along the nanowires, as the luminescence is usually dominated by the free exciton decay. This could be observed through fluorescence lifetime imaging. As the exceptional case of photo-induced spot defect luminescence shows, defect complexes, as expected exhibit a longer lifetime than the free exciton, but their low concentration within the wire limit their influence on the luminescence properties of the wire segment in the confocal spot.

The above described broad range of emission energies of the charge carrier pairs localised at defect sites in a broad system is a luminescence property that is not usually expected for a system with bulk electronic properties. The nanoscale nature of the charge carrier pair–defect complexes is further underlined by one property that is only associated with nanostructures and single molecules – the *I* and green emission in CdS bulk nanowires exhibits luminescence blinking and energy fluctuations, just as the T and NBE bands in CdSe quantum nanowires.

Blinking in CdSe and CdS nanowires – similarities, differences and the meaning of the observations made in this study. As described above, both the entire range of NBE and single T bands in the CdSe quantum nanowire luminescence exhibit intensity fluctuation which is very similar to the intensity fluctuations of single nanocrystals and molecules. That said, instead of a completely dark *Off* state, the nanowire dark periods still clearly show a baseline emission. This emission can be ascribed to very quick radiative decay routes and usually show an on average very constant luminescence. Intensity histograms show that usually the dark state events dominate and the bright states compromise a broad distribution of intensities. No part of the spectrum is truly constant, rather, the constant emission short lifetime emission can be observed throughout the whole HE and NBE spectral range.

In comparison the *I* and green bands in CdS bulk nanowires show emission blinking that can best be compared to the T emission blinking in CdSe quantum nanowires. In the analysed systems the *On* events of these defect–bound charge carrier pairs are even more rare than in the CdSe quantum nanowires. They are in fact so rare and often low in intensity that statistic analysis of the blinking is not possible using the recorded data.

The spectral observations of the defect related emission in CdS bulk nanowires imply a strong dependence on the potential landscape on the nanoscale which influences the defects and the charge carrier pairs bound to them. As with the CdSe quantum nanowires the emissions look on first sight like the emission lines reported for the bulk luminescence, but their energetic positions fall into a much broader range. In the spectral traces of the CdS bulk nanowire luminescence these lines can in addition be seen to fluctuate strongly in luminescence energy, which also implies a changing potential landscape. This leads to a point at which the lowest energy *I* emission bands overlap with the highest energy green bands and the otherwise clear assignment of these bands is again ambivalent.

On the other hand the HE emission of the CdS nanowires are completely constant in energy and emission intensity, as would be expected from a bulk system and which means that the free exciton can easily move within the nanowire volume.

The defects that contribute to the blinking and fluctuating luminescence bands can therefore be expected to be closely located to the nanowire surface. This is illustrated in figure 7.4.

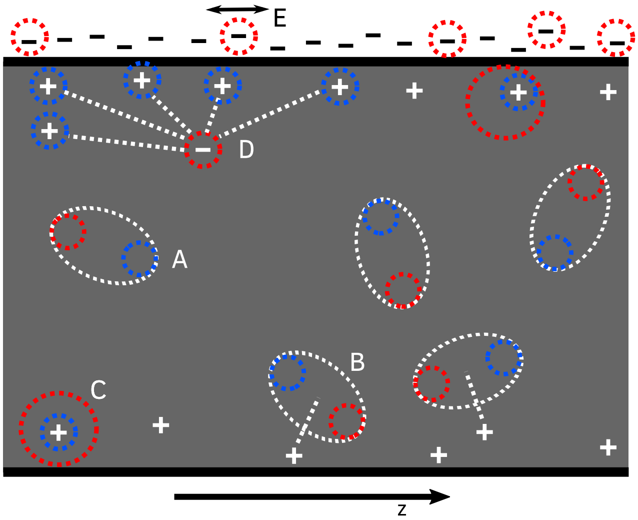

Figure 7.4: Proposed processes in bulk nanowires. A shows a free exciton, B bound excitons, C a free–to–bound complex and D a DAP. If the involved defect sites are located close to the nanowire surface, the surface will influence the bound charge carrier potential energy, as will charges that are trapped on the surface, as shown in E.

As illustrated, an exciton (A) can easily move within the volume of the bulk nanowire without experiencing confinement. Excitons can bind to ionised defect sites (B), or be localised in a free–to–bound configuration (C). As in CdSe nanowires, DAP configurations are likely to occur if a minority defect site is present near several majority defect sites (D). If a charge is trapped close to the surface it can be easily confined through potential landscape changes in the bulk. Also, charged trap sites on the surface itself can easily influence the local potential energy and charge fluctuations in surface traps will lead to charge fluctuation for the localised charge carrier pairs.(E) The processes are now very similar to those happening in CdSe quantum nanowires.

These processes, as described above, are likely to occur at every bulk semiconductor surface. That said, what is observed is the average behaviour of the charge carriers and their complexes with defects in the bulk, which are much more numerous and therefore dominate the emission spectrum.

As the observed blinking in CdS bulk nanowires is so similar to that of the T bands of CdSe quantum nanowires – both only occur for bands that arise from the recombination of strongly localised charge carrier pairs – the same mechanism can be suspected to cause the phenomenon. The analysis of the blinking statistics of the CdSe quantum nanowire luminescence makes it possible to compare the blinking behaviour to that of the in the literature much more comprehensively analysed blinking of CdSe nanocrystals. While a spectral extraction of the blinking bands is not easily possible, the lifetime gating of the blinking of of nanowires showing isolated T band blinking as well as a spectrally independent NBE blinking can be used to extract those intensity fluctuations that go together with changes in luminescence lifetime. Both types of blinking show a clear power law behaviour with no observed cut-off time for both *On* and *Off* times. CdSe blinking better analysed, summary of statistical analysis: power law with no observed cut-off. The general blinking time frame spans 2 to 3 orders of magnitude, while the T emission blinking spans 3 to 4.

As the simple power law behaviour with average power law exponents well within the range reported for CdSe nanocrystals all mechanism and kinetics that have been discussed for those systems can be valid for the nanowire defect emission as well. This also implies a high likelihood that the mechanisms of the switching between *On* and *Off* state are likely very similar between the 0D crystals and the 1D nanowires. When looking at the emission mechanisms, as proposed in this work, all blinking emission in a non-confined system (the CdS bulk nanowires) arises from the recombination of localised charge carriers. This localisation takes the charge carrier pair and confines it in a potential space that is not so different from the confinement in nanocrystals.

At the same time, while all three types of emission in CdSe quantum nanowires – HE, NBE, and T emission – are seen to show emission blinking, observations of bulk nanowires show that in less globally confined system the blinking is mostly observed in the bands arising from the more localised charge carrier pairs in the T emission.

The CdSe quantum nanowire T emission blinking, the CdS *I* and green band emission blinking and the CdSe nanocrystal blinking are therefore more easily compared to each other than to the much less specific NBE blinking. For the nanocrystal blinking the bright and dark state definition involves a bright ground state, a bright excited state, as well as a dark ground state and a dark excited state. The nature of these states and the switching between them differ from model to model, but the definition of these states are still paramount for any further description.

For the CdSe nanowire luminescence it is far from easy to define those states. This is due to the already very complex mechanisms that have to be considered for the defect-related emission mechanisms. Possible processes that can lead to non-radiative recombination paths are described in chapter 5.3.1. As all emission mechanisms involve not only one but many defect sites and emission mechanisms for T and NBE emission are very likely related to each other the clear *On* and *Off* states of both the T bands and the entire NBE emission groups very likely involves a further unknown. This might be the involvement of surface trap sites involved in AUGER processes, or the role of the surface energy band and its relative position to the defect levels.

One option for a simple but again unsatisfyingly vague process that could be valid for both NBE and T emission blinking is the proposal of a type of charge carrier trap. If localisation to these traps competes with the localisation to those traps that can contribute to radiative recombinations. This would make it possible to describe the nanowire luminescence similar to what has been proposed byVIETMEYER *et al.*.[73] If the difference between a radiative and non-radiative trap could be explained this might be one option to explain the nanowire luminescence behaviour.

While this model was specifically proposed to describe nanowire luminescence it starts with the assumption that all nanowire radiative emission stems from the recombination of the free exciton, which could be shown in this study is not the case, at least at low temperature. This also shows that the MRC model as described by FRANTSUZOV *et al.*[61] cannot be assumed for nanowires, at least not without major modifications, as the localisation – trapping – of a charge carrier is an important step in the luminescent processes of the studied nanowires.

One model that is more easily translated to work with the emission mechanisms of nanowires is the model of VERBERK *et al.*.[48] It proposes the dependence of the dark state on the proximity of an additional charge to the nanocrystal core an allows grey states for charges that are close but not close enough to contribute to AUGER PROCESSES. These kind of processes were also proposed by ZHANG *et al.* to contribute to continuous distributions in FLIDS. In nanowires this might mean that a certain defect concentration might contribute to an increased number of radiative decays, while too many defect sites will lead to an increase in non-radiative recombinations. The blinking of a defect-related band will now depend on the surrounding of the individual involved defects. Suppose that most defects in the nanowire are in fact ionised during illumination and measurement of luminescence (which would mean a minimum of excess charge carrier in the nanowire volume that could contribute to AUGER processes) a certain fluctuation as to which defects would trap excess charges could be enough to lead to fluctuations between *On*, *Off* and *grey* states through influencing the charge carrier–defect complexes accordingly. In this case the excess charge carrier concentration in the nanowire and their diffusion from defect to defect would be the two relevant values, at least for the fluctuation of the T emission.

This still leaves the relatively global NBE blinking with no satisfactory explanation. The observed emission fluctuations have to be explained for a multitude of localised charge carrier pairs at the same time. As this is not easily explained by single localised charges more global factors, like the surface bands, have to play a role. One option would be to assume a fluctuation of the surface potential or that of the transition conditions to that band.

The above descriptions are still unsatisfyingly vague, especially when compared to the existing studies of the nanocrystal luminescence fluctuations. This is mostly due to the fact that nanocrystal studies across the decades usually consider the excited state of the crystal the (confined) exciton[45, 51, 68, 140, 158] which can in this way not be translated to the observed nanowire luminescence. That said, the actual nature of the defect-related luminescence can still not definitely be determined, due to the strong shift in energetic position. This is especially clear in the differentiation between *I* emission and green bands in the CdS bulk nanowires and for the actual identification of the CdSe quantum nanowire NBE emission. In past studies on bulk materials the natures of the charge carrier–defect interactions have been characterised with methods that are much more suitable to macroscopic crystals than to nanocrystals, such as the HALL effect.[93, 94] These kind of studies – the clear identification of the defect complexes behind the luminescence bands – would be a worthwhile effort and the best first step to identify the complex multitude of recombination processes in any kind of semiconductor nanostructure.

In the end, what can be said with certainty is, that the luminescence of both CdSe and CdS nanowires are much more complex than was previously assumed. The CdSe QNWs show a previously not reported group of luminescence signals, while the CdS bulk nanowires show emission behaviour in their defect-related emission bands that were previously only associated with strongly confined systems. Both observations could be comprehensively observed and described in this work and qualitative descriptions for possible underlying mechanisms could be found. Despite the overall complex behaviour, the defect-related luminescence can be isolated and it is clear that single luminescence bands are related to single minority defects. Especially for the CdSe quantum nanowires the defect luminescence is the main emission mechanism – an important aspect for any future synthesis of high photoluminescence quantum yield nanowires.

Bibliography

1. Harford, T. *Why the falling cost of light matters* Retrieved 2019-01-04. `<https://www.bbc.com/news/business-38650976>`.
2. Atkins, P. & de Paula, J. *Physical Chemistry* 8th (Oxford University Press, Oxford, 2006).
3. Spedding, F. H. Part II.–Luminescence in solids. Introductory paper. *Trans. Faraday Soc.* **35,** 65–69 (1939).
4. Broser, I., Kallmann, H. & Warminsky, R. Vorstellungen über den Leitungsmechanismus in Cadmiumsulfid-Kristallen. *Zeitschrift für Naturforschung A* **4,** 631–637 (1949).
5. Furlong, L. R. & Ravilious, C. F. Low-Temperature Luminescence and Absorption of CdS. *Physical Review* **98,** 954–955 (1955).
6. Collins, R. J. Mechanism and defect responsible for edge emission in CdS. *Journal of Applied Physics* **30,** 1135–1140 (1959).
7. Kulp, B. A. & Kelley, R. H. Displacement of the Sulfur Atom in CdS by Electron Bombardment. *Journal of Applied Physics* **31,** 1057 (1960).
8. Hopfield, J. J. & Thomas, D. G. Fine structure and magneto-optic effects in the exciton spectrum of cadmium sulfide. *Physical Review* **122,** 35–52 (Apr. 1961).
9. Thomas, D. G. & Hopfield, J. J. Optical properties of bound exciton complexes in cadmium sulfide. *Physical Review* **128,** 2135–2148 (1962).
10. Henry, C. H., Nassau, K. & Shiever, J. W. Double-Donor–Acceptor Pair Lines and the Chemical Identification of the I_1 Lines in CdS. *Physical Review Letters* **24,** 820–822 (1970).
11. Minami, F. & Era, K. Lifetimes of bound excitons in CdSe. *Solid State Communications* **53,** 187–189 (1985).
12. Yoffe, A. Low-dimensional systems: quantum size effects and electronic properties of semiconductor microcrystallites (zero-dimensional systems) and some quasi-two-dimensional systems. *Advances in Physics* **42,** 173–262 (1993).
13. Nirmal, M. *et al.* Fluorescence intermittency in single cadmium selenide nanocrystals. *Nature* **383,** 802–804 (1996).
14. Efros, A. L. & Rosen, M. Random Telegraph Signal in the Photoluminescence Intensity of a Single Quantum Dot. *Physical Review Letters* **78,** 1110–1113 (1997).
15. Kuno, M., Fromm, D. P., Hamann, H. F., Gallagher, A. & Nesbitt, D. J. "On"/"off" fluorescence intermittency of single semiconductor quantum dots. *The Journal of Chemical Physics* **115,** 1028–1040 (2001).
16. Heydari, N., Ghorashi, S. M. B., Han, W. & Park, H.-H. *Quantum-dot Based Light-emitting Diodes* (ed Ghamsari, M. S.) 64 (InTech, 2017).

17. Jiang, Y., Cho, S.-Y. & Shim, M. Light-emitting diodes of colloidal quantum dots and nanorod heterostructures for future emissive displays. *Journal of Materials Chemistry C* **6,** 2618–2634 (2018).
18. Littig, A., Lehmann, H., Klinke, C., Kipp, T. & Mews, A. Solution-Grown Nanowire Devices for Sensitive and Fast Photodetection. *ACS Applied Materials & Interfaces* **7,** 12184–12192 (2015).
19. Franz, D. *Zeitaufgelöste Fluoreszenzspektroskopie an CdSe-Nanodrähten bei tiefen Temperaturen* Ph.D. Thesis (Universität Hamburg, 2012).
20. Reich, A. *Low Temperature Photoluminescence Spectroscopy on Single CdSe Nanowires* Master's Thesis (Universität Hamburg, 2013).
21. Madelung, O., Rössler, U. & Schulz, M. *Landolt-Börnstein – Group III Condensed Matter* (Springer-Verlag Berlin Heidelberg, Berlin, Heidelberg, 1999).
22. Myalitsin, A. *et al.* Diameter scaling of the optical band gap in individual CdSe nanowires. *ACS Nano* **5,** 7920–7927 (2011).
23. Grätzel, M. Photoelectrochemical cells. *Nature* **414,** 338–344 (2001).
24. Birman, J. L. Simplified LCAO Method for Zincblende, Wurtzite, and Mixed Crystal Structures. *Physical Review* **115,** 1493–1505 (1959).
25. Imada, A., Ozaki, S. & Adachi, S. Photoreflectance spectroscopy of wurtzite CdS. *Journal of Applied Physics* **92,** 1793–1798 (2002).
26. Kaneta, A. & Adachi, S. Photoreflectance study of hexagonal CdSe. *Journal of Physics D: Applied Physics* **32,** 2337–2341 (1999).
27. Atkins, P. & Ronald, F. *Molecular Quantum Mechanics* 4th (Oxford University Press, Oxford, 2008).
28. Parak, W. J., Manna, L., Simmel, F. C., Gerion, D. & Alivisatos, P. *Nanoparticles* 1st. (ed Schmid, G.) (Wiley-VCH Verlag GmbH & Co. KGaA, Weinheim, 2004).
29. Cohen-Tannoudji, C. & Dalibard, J. Single-Atom Laser Spectroscopy. Looking for Dark Periods in Fluorescence Light. *Europhysics Letters* **1,** 441–448 (1986).
30. Stefani, F. D., Hoogenboom, J. P. & Barkai, E. Beyond quantum jumps: Blinking nanoscale light emitters. *Physics Today* **62,** 34–39 (2009).
31. Orrit, M. & Bernard, J. Single pentacene molecules detected by fluorescence excitation in a p-terphenyl crystal. *Physical Review Letters* **65,** 2716–2719 (1990).
32. Ambrose, W. P. & Moerner, W. E. Fluorescence spectroscopy and spectral diffusion of single impurity molecules in a crystal. *Nature* **349,** 225–227 (1991).
33. Lu, H. P. & Xie, X. S. Single-molecule spectral fluctuations at room temperature. *Nature* **385,** 143–146 (1997).
34. Dickson, R. M., Cubitt, A. B., Tsien, R. Y. & Moerner, W. E. On/off blinking and switching behaviour of single molecules of green fluorescent protein. *Nature* **388,** 355–358 (1997).
35. Koberling, F., Mews, A. & Basché, T. Single-dot spectroscopy of CdS nanocrystals and CdS/HgS heterostructures. *Physical Review B* **60,** 1921–1927 (1999).

36. Protasenko, V. V., Hull, K. L. & Kuno, M. Disorder-induced optical heterogeneity in single CdSe nanowires. *Advanced Materials* **17,** 2942–2949 (2005).

37. Protasenko, V., Gordeyev, S. & Kuno, M. Spatial and intensity modulation of nanowire emission induced by mobile charges. *Journal of the American Chemical Society* **129,** 13160–13171 (2007).

38. Rust, M. J., Bates, M. & Zhuang, X. Sub-diffraction-limit imaging by stochastic optical reconstruction microscopy (STORM). *Nature Methods* **3,** 793–796 (2006).

39. Hess, S. T., Girirajan, T. P. & Mason, M. D. Ultra-High Resolution Imaging by Fluorescence Photoactivation Localization Microscopy. *Biophysical Journal* **91,** 4258–4272 (2006).

40. Betzig, E. *et al.* Imaging Intracellular Fluorescent Proteins at Nanometer Resolution. *Science* **313,** 1642–1645 (2006).

41. Cook, R. J. & Kimble, H. J. Possibility of Direct Observation of Quantum Jumps. *Physical Review Letters* **54,** 1023–1026 (1985).

42. Haase, M. *et al.* Exponential and power-law kinetics in single-molecule fluorescence intermittency. *Journal of Physical Chemistry B* **108,** 10445–10450 (2004).

43. Hoogenboom, J. P., Hernando, J., van Dijk, E. M. H. P., van Hulst, N. F. & García-Parajó, M. F. Power-Law Blinking in the Fluorescence of Single Organic Molecules. *ChemPhysChem* **8,** 823–833 (2007).

44. Cichos, F., von Borczyskowski, C. & Orrit, M. Power-law intermittency of single emitters. *Current Opinion in Colloid & Interface Science* **12,** 272–284 (2007).

45. Shimizu, K. T. *et al.* Blinking statistics in single semiconductor nanocrystal quantum dots. *Physical Review B* **63,** 205316 (2001).

46. Kuno, M., Fromm, D. P., Hamann, H. F., Gallagher, A. & Nesbitt, D. J. Nonexponential "blinking" kinetics of single CdSe quantum dots: A universal power law behavior. *The Journal of Chemical Physics* **112,** 3117–3120 (2000).

47. Frantsuzov, P., Kuno, M., Jankó, B. & Marcus, R. a. Universal emission intermittency in quantum dots, nanorods and nanowires. *Nature Physics* **4,** 519–522 (2008).

48. Verberk, R., Oijen, A. M. V. & Orrit, M. Simple model for the power-law blinking of single semiconductor nanocrystals, 1–4 (2002).

49. Pelton, M., Grier, D. G. & Guyot-Sionnest, P. Characterizing quantum-dot blinking using noise power spectra. *Applied Physics Letters* **85,** 819–821 (2004).

50. Margolin, G., Protasenko, V., Kuno, M. & Barkai, E. in *Advances in Chemical Physics, Fractals, Diffusion and Relaxation in Disordered Complex Systems* 327–356 (2005).

51. Efros, A. L. & Nesbitt, D. J. Origin and control of blinking in quantum dots. *Nature Nanotechnology* **11,** 661–671 (2016).

52. Kuno, M., Fromm, D. P., Johnson, S. T., Gallagher, A. & Nesbitt, D. J. Modeling distributed kinetics in isolated semiconductor quantum dots. *Physical Review B* **67,** 125304 (2003).

53. Pelton, M., Smith, G., Scherer, N. F. & Marcus, R. A. Evidence for a diffusion-controlled mechanism for fluorescence blinking of colloidal quantum dots. *Proceedings of the National Academy of Sciences* **104,** 14249–14254 (2007).

54. Tang, J. & Marcus, R. A. Mechanisms of fluorescence blinking in semiconductor nanocrystal quantum dots. *The Journal of Chemical Physics* **123,** 054704 (2005).

55. Tang, J. & Marcus, R. A. Diffusion-controlled electron transfer processes and power-law statistics of fluorescence intermittency of nanoparticles. *Physical Review Letters* **95,** 107401 (2005).

56. Marcus, R. A. On the Theory of Oxidation-Reduction Reactions Involving Electron Transfer. I. *The Journal of Chemical Physics* **24,** 966–978 (1956).

57. Frantsuzov, P. A. & Marcus, R. A. Explanation of quantum dot blinking without the long-lived trap hypothesis. *Physical Review B* **72,** 155321 (2005).

58. Pokrant, S. & Whaley, K. Tight-binding studies of surface effects on electronic structure of CdSe nanocrystals: the role of organic ligands, surface reconstruction, and inorganic capping shells. *The European Physical Journal D - Atomic, Molecular and Optical Physics* **6,** 255–267 (1999).

59. Schlegel, G., Bohnenberger, J., Potapova, I. & Mews, A. Fluorescence Decay Time of Single Semiconductor Nanocrystals. *Physical Review Letters* **88,** 137401 (2002).

60. Frantsuzov, P. A., Volkán-Kacsó, S. & Jankó, B. Model of Fluorescence Intermittency of Single Colloidal Semiconductor Quantum Dots Using Multiple Recombination Centers. *Physical Review Letters* **103,** 207402 (2009).

61. Frantsuzov, P. A., Volkán-Kacsó, S. & Jankó, B. Universality of the Fluorescence Intermittency in Nanoscale Systems: Experiment and Theory. *Nano Letters* **13,** 402–408 (2013).

62. Peterson, J. J. & Nesbitt, D. J. Modified Power Law Behavior in Quantum Dot Blinking: A Novel Role for Biexcitons and Auger Ionization. *Nano Letters* **9,** 338–345 (2009).

63. Knappenberger, K. L., Wong, D. B., Romanyuk, Y. E. & Leone, S. R. Excitation Wavelength Dependence of Fluorescence Intermittency in CdSe/ZnS Core/Shell Quantum Dots. *Nano Letters* **7,** 3869–3874 (2007).

64. Zhang, K., Chang, H., Fu, A., Alivisatos, A. P. & Yang, H. Continuous Distribution of Emission States from Single CdSe/ZnS Quantum Dots. *Nano Letters* **6,** 843–847 (2006).

65. Margolin, G., Protasenko, V., Kuno, M. & Barkai, E. Photon Counting Statistics for Blinking CdSe–ZnS Quantum Dots: A Lévy Walk Process. *The Journal of Physical Chemistry B* **110,** 19053–19060 (2006).

66. Malko, A. V. *et al.* Pump-Intensity- and Shell-Thickness-Dependent Evolution of Photoluminescence Blinking in Individual Core/Shell CdSe/CdS Nanocrystals. *Nano Letters* **11,** 5213–5218 (2011).

67. Galland, C. *et al.* Lifetime blinking in nonblinking nanocrystal quantum dots. *Nature Communications* **3,** 908 (2012).

68. Galland, C. *et al.* Two types of luminescence blinking revealed by spectroelectrochemistry of single quantum dots. *Nature* **479,** 203–207 (2011).

69. Glennon, J. J., Tang, R., Buhro, W. E. & Loomis, R. a. Synchronous photoluminescence intermittency (blinking) along whole semiconductor quantum wires. *Nano Letters* **7,** 3290–3295 (2007).

70. Vietmeyer, F., Tchelidze, T., Tsou, V., Janko, B. & Kuno, M. Electric field-induced emission enhancement and modulation in individual cdse nanowires. *ACS Nano* **6,** 9133–9140 (2012).

71. Schäfer, S., Wang, Z., Kipp, T. & Mews, A. Fluorescence modulation of single CdSe nanowires by charge injection through the tip of an atomic-force microscope. *Physical Review Letters* **107,** 137403(1–5) (2011).

72. Wayman, V. L. *et al.* Bound 1D excitons in single CdSe quantum wires. *Journal of Physical Chemistry Letters* **3,** 2627–2632 (2012).

73. Vietmeyer, F., Frantsuzov, P. a., Janko, B. & Kuno, M. Carrier recombination dynamics in individual CdSe nanowires. *Physical Review B* **83,** 115319 (2011).

74. Vietmeyer, F., McDonald, M. P. & Kuno, M. Single nanowire microscopy and spectroscopy. *Journal of Physical Chemistry C* **116,** 12379–12396 (2012).

75. Franz, D. *et al.* Quantum-Confined Emission and Fluorescence Blinking of Individual Exciton Complexes in CdSe Nanowires. *Nano Letters* **14,** 6655–6659 (2014).

76. Pankove, J. I. *Optical Processes in Semiconductors* isbn: 0-486-60275-3 (Dover Publications Inc., New York, 1975).

77. Wang, Z. *et al.* Solution-Liquid-Solid Synthesis of Semiconductor Nanowires Using Clusters as Single-Source Precursors. *Small* **7.** doi:`10.1002/smll.201100343` (2011).

78. Michelssen, F. Luminescent Screen. *US Patent № 1988605* (1935).

79. Ruska, E. & Ruska, H. Electron microscope. *US Patent № 2267137 A* (1941).

80. Kröger, F. Luminescence and absorption of zincsulfide, cadmiumsulfide and their solid solutions. *Physica* **7,** 1–12 (1940).

81. Gudden, B. & Pohl, R. Lichtelektrische Beobachtungen an isolierenden Metallsulfiden. *Zeitschrift für Physik* **2,** 361–372 (1920).

82. Thomas, D. G. & Hopfield, J. J. Exciton Spectrum of Cadmium Sulfide. *Physical Review* **116,** 573–582 (1959).

83. Pässler, R. Basic Model Relations for Temperature Dependencies of Fundamental Energy Gaps in Semiconductors. *physica status solidi (b)* **200,** 155–172 (1997).

84. Henry, C. H. & Nassau, K. Lifetimes of bound excitons in CdS. *Physical Review B* **1,** 1628–1634 (1970).

85. Henry, C. H., Nassau, K. & Shiever, J. W. Optical Studies of Shallow Acceptors in CdS and CdSe. *Physical Review B* **4,** 2453–2463 (1971).

86. Lovergine, N., Cingolani, R., Mancini, A. M. & Ferrara, M. Photoluminescence of CVD grown CdS epilayers on CdTe substrates. **118,** 304–308 (1992).

87. Handelman, E. & Thomas, D. The effects of low temperature heat treatments on the conductivity and photoluminescence of CdS. *Journal of Physics and Chemistry of Solids* **26,** 1261–1267 (1965).

88. Randolph, L. P., Oswald, R. B. & Thorpe, A. N. Radiation-Induced Changes in the Photoluminescence Spectra of Cadmium Sulfide. *IEEE Transactions on Nuclear Science* **18,** 31–39 (1971).

89. Reynolds, D. C. & Litton, C. W. Edge Emission and Zeeman Effects in CdS. *Physical Review* **132,** 1023–1029 (1963).

90. Gutowski, J. & Hoffmann, A. Magneto-Optics of Excitons Bound to Dislocations in CdS. *Materials Science Forum* **38-41,** 1391–1396. issn: 1662-9752 (1989).

91. Hoffmann, A., Christen, J. & Gutowski, J. Cathodoluminescence Wavelength Imaging for Spatial Mapping of Excitons Bound to Dislocations and Structural Defects in CdS. **1,** 25–28 (1992).

92. Smeaton, M. D. Long Wavelength Bound Exciton Emission in CdS. *Canadian Journal of Physics* **52,** 803–812 (1974).

93. Maeda, K. Nature of the edge emission in cadmium sulfide. *Journal of Physics and Chemistry of Solids* **26,** 1419–1430 (1965).

94. Colbow, K. Free-to-bound and bound-to-bound transitions in CdS. *Physical Review* **141,** 742–749 (1966).

95. Henry, C. H., Faulkner, R. A. & Nassau, K. Donor-Acceptor Pair Lines in Cadmium Sulfide. *Physical Review* **183,** 798–806 (1969).

96. Broser, I., Gutowski, J. & Riedel, R. Excitation spectroscopy of the donor-acceptor-pair luminescence in CdS. *Solid State Communications* **49,** 445–449 (1984).

97. Broser, I., Päthe, D. & Rosenzweig, M. Excitation spectroscopy of the green edge luminescence in CdS II. Low excitation intensity. *Solid State Communications* **54,** 849–853 (1985).

98. Shiraki, Y., Shimada, T. & Komatsubara, K. F. Edge emissions of ion-implanted CdS. *Journal of Physics and Chemistry of Solids* **38,** 937–941 (1977).

99. Frerichs, R. On the Conductivity Produced in CdS Crystals by Irradiation with Gamma-Rays. *Physical Review* **76,** 1869–1875 (Dec. 1949).

100. Bryant, F. J. & Cox, A. F. J. Heat treatment effects in cadmium sulphide. *British Journal of Applied Physics* **16,** 1065–1074 (1965).

101. Kulp, B. A. Displacement of the Cadmium Atom in Single Crystal CdS by Electron Bombardment. *Physical Review* **125,** 1865–1869 (1962).

102. Halsted, R. E., Aven, M. & Coghill, H. D. Fluorescent Emission Spectra in II–VI Compounds. *Journal of The Electrochemical Society* **112,** 177 (1965).

103. Ermolovich, I. B., Matvievskaja, G. I. & Sheinkman, M. K. Electron-phonon interactions at radiative carrier capture on deep centers in cadmium sulfide single crystals. *Journal of Luminescence* **10,** 58–68 (1975).

104. Ramsden, J. J. & Grätzel, M. Photoluminescence of small cadmium sulphide particles. *Journal of the Chemical Society, Faraday Transactions 1: Physical Chemistry in Condensed Phases* **80,** 919 (1984).

105. Fasoli, A. *et al.* Photoluminescence of CdSe Nanowires Grown With and Without Metal Catalyst. *Nano Research* **4,** 343–359 (2011).

106. Arora, A. K. & Ramdas, A. K. Resonance Raman scattering from defects in CdSe. *Physical Review B* **35,** 4345–4350. issn: 0163-1829 (1987).

107. Abbe, E. Beiträge zur Theorie des Mikroskops und der mikroskopischen Wahrnehmung. *Archiv für Mikroskopische Anatomie* **9,** 440–456 (1873).

108. *Lehrbuch der Experimentalphysik - 3 : Optik: Wellen- und Teilchenoptik* (ed Niedrig, H.) (De Gruyter, Berlin, 2004).

109. Minsky, M. Memoir on inventing the confocal scanning microscope. *Scanning* **10,** 128–138 (1988).

110. Minsky, M. *Microscopy Apparatus* 1961.

111. *Handbook of biological confocal microscopy* 3rd ed. (ed Pawley, J. B.) (Springer Science+Business Media, LLC, New York, 2006).

112. *The Nobel Prize in Chemistry 2014* `https://www.nobelprize.org/prizes/chemistry/2014/summary/`. Retrieved 2018-12-17.

113. Knoll, M. & Ruska, E. Das Elektronenmikroskop. *Zeitschrift für Physik* **78,** 318–339 (1932).

114. Von Ardenne, M. Das Elektronen-Rastermikroskop. *Zeitschrift für Physik* **109,** 553–572 (1938).

115. Binnig, G. & Rohrer, H. Scanning tunneling microscopy. *Surface Science* **126,** 236–244 (1983).

116. Binnig, G., Quate, C. F. & Gerber, C. Atomic Force Microscope. *Physical Review Letters* **56,** 930–933 (1986).

117. Karraï, K. & Grober, R. D. Piezoelectric tip-sample distance control for near field optical microscopes. *Applied Physics Letters* **66,** 1842–1844 (1995).

118. Wagner, R. S. & Ellis, W. C. VAPOR-LIQUID-SOLID MECHANISM OF SINGLE CRYSTAL GROWTH. *Applied Physics Letters* **4,** 89–90 (1964).

119. Trentler, T. J. *et al.* Solution–Liquid–Solid Growth of Crystalline III–V Semiconductors: An Analogy to Vapor-Liquid-Solid Growth. *Science* **270,** 1791–1794 (1995).

120. Böttcher, H. J. *Synthesis and properties of II-VI semiconductor nanowires* Ph.D. Thesis (École polytechnique fédérale de Lausanne, 2009).

121. Braun, K. *Synthese und optische Charakterisierung von Cadmiumselenid-Nanodrähten auf Silizium-Substraten* Bachelor's Thesis (Universität Hamburg, 2015).

122. Hagelmann, H. *Fluoreszenzmikroskopie an Cadmiumselenid-Quantendrähten bei tiefen Temperaturen* Bachelor's Thesis (Universität Hamburg, 2014).

123. Jannsen, N. *Modulation der Fluoreszenz einzelner CdS-Nanodrähte* Bachelor's Thesis (Universität Hamburg, 2016).

124. Gross, E. F., Razbein, B. S., Fedorov, V. P. & Naumov, Y. P. Bound Exciton Complexes in CdSe Crystals. *Physica Status Solidi (B)* **30,** 485–494 (1968).

125. Van Sark, W. G. J. H. M. *et al.* Photooxidation and Photobleaching of Single CdSe/ZnS Quantum Dots Probed by Room-Temperature Time-Resolved Spectroscopy. *The Journal of Physical Chemistry B* **105,** 8281–8284 (2001).

126. Hässelbarth, A., Eychmüller, A. & Weller, H. Detection of shallow electron traps in quantum sized CdS by fluorescence quenching experiments. *Chemical Physics Letters* **203,** 271–276 (1993).

127. Landes, C. F., Braun, M. & El-Sayed, M. A. On the Nanoparticle to Molecular Size Transition: Fluorescence Quenching Studies. *The Journal of Physical Chemistry B* **105,** 10554–10558 (2001).

128. Vela, J. *et al.* Effect of shell thickness and composition on blinking suppression and the blinking mechanism in 'giant' CdSe/CdS nanocrystal quantum dots. *Journal of Biophotonics* **3,** 706–717 (2010).

129. Smyder, J. a. *et al.* The influence of continuous vs. pulsed laser excitation on single quantum dot photophysics. *Phys. Chem. Chem. Phys.* **16,** 25723–25728 (2014).

130. Sasaki, F., Mishina, T. & Masumoto, Y. Ultrafast pump-and-probe spectroscopy in CdSe: Hot-carrier and exciton dynamics. *Physical Review B* (1992).

131. Braun, D., Rühle, W. W., Trallero-Giner, C. & Collet, J. Spectroscopic determination of the optical deformation-potential constant in semiconductors. *Physical Review Letters.* doi:`10.1103/PhysRevLett.67.2335` (1991).

132. Henry, C. H., Nassau, K. & Shiever, J. W. Study of Two-Electron Transitions of a Donor in CdSe. *Physical Review B* **5,** 458–462 (1972).

133. Reynolds, D. C., Litton, C. W. & Collins, T. C. Edge Emission and Magneto-Optical Effects in CdSe. *Physical Review* **156,** 881–889 (1967).

134. Filinski, I. & Wojtowicz-Natanson, B. Low temperature 'edge emission' of CdSe. *Journal of Physics and Chemistry of Solids* **32,** 2409–2413 (1971).

135. Arora, B. M. & Compton, W. D. Luminescence from impurities and radiation defects in CdSe and CdS. *Journal of Applied Physics* **43,** 4499–4507 (1972).

136. Kokubun, Y., Watanabe, H. & Wada, M. Photoluminescence of CdSe Single Crystals. *Japanese Journal of Applied Physics* **13,** 1393–1398 (1974).

137. Silberstein, R. P. & Tomkiewicz, M. Characterization of polycrystalline electrodeposited CdSe photoelectrodes using photoluminescence spectroscopy. *Journal of Applied Physics* **54,** 5428 (1983).

138. Perna, G., Capozzi, V. & Ambrico, M. Structural properties and photoluminescence study of CdSe/Si epilayers deposited by laser ablation. *Journal of Applied Physics* **83,** 3337 (1998).

139. Gnatenko, Y. P., Bukivskij, P. M., Faryna, I. O., Opanasyuk, A. S. & Ivashchenko, M. M. Photoluminescence of high optical quality CdSe thin films deposited by close-spaced vacuum sublimation. *Journal of Luminescence* **146,** 174–177 (2014).

140. Park, Y. S., Bae, W. K., Pietryga, J. M. & Klimov, V. I. Auger recombination of biexcitons and negative and positive trions in individual quantum dots. *ACS Nano* (2014).

141. Granados del Águila, A. *et al.* Observation of the Full Exciton and Phonon Fine Structure in CdSe/CdS Dot-in-Rod Heteronanocrystals. *ACS Nano* **8,** 5921–5931 (2014).

142. Zhang, X. B., Taliercio, T., Kolliakos, S. & Lefebvre, P. Influence of electron-phonon interaction on the optical properties of III nitride semiconductors. *Journal of Physics: Condensed Matter* **13,** 7053–7074 (2001).

143. Zeng, Y. & Kelley, D. F. Surface Charging in CdSe Quantum Dots: Infrared and Transient Absorption Spectroscopy. *The Journal of Physical Chemistry C* **121,** 16657–16664 (2017).

144. Jasieniak, J. & Mulvaney, P. From Cd-Rich to Se-Rich - the Manipulation of CdSe Nanocrystal Surface Stoichiometry, 2841–2848 (2007).

145. Zeng, Y. & Kelley, D. F. Two-Photon Photochemistry of CdSe Quantum Dots. *ACS Nano* (2015).

146. Tarbaev, N. I. Low-temperature photoluminescence determination of dislocation slip systems in CdSe single crystals. *Physics of the Solid State* **40,** 1672–1675 (1998).

147. Gnatenko, Y. P., Opanasyuk, A. S., Ivashchenko, M. M., Bukivskij, P. M. & Faryna, I. O. Study of the correlation between structural and photoluminescence properties of CdSe thin films deposited by close-spaced vacuum sublimation. *Materials Science in Semiconductor Processing* **26,** 663–668 (2014).

148. Jäger-Waldau, R. *et al.* Thin-film CdSe: Photoluminescence and electronic measurements. *Journal of Applied Physics* **64,** 2601–2606. issn: 0021-8979 (Sept. 1988).

149. Reynolds, D. C., Litton, C. W. & Collins, T. C. Some Optical Properties of Group II–VI Semiconductors (II). *physica status solidi (b)* **12,** 3–55 (1965).

150. Hayes, W. & Stoneham, A. M. *Defects and Defect Processes in Nonmetallic Solids* isbn: 0-486-43483-4 (Dover Publications Inc., New York, 1985).

151. Kulp, B. A. Effects of Electron Bombardment on Single-Crystal CdSe at 77°K. *Journal of Applied Physics* **37,** 4936–4938 (1966).

152. Lott, K., Nirk, T. & Volobujeva, O. Chemical self-diffusion in undoped ZnS and in undoped CdSe. *Crystal Engineering* **5,** 147–153 (2002).

153. Schäfer, S., Reich, A., Wang, Z., Kipp, T. & Mews, A. Charge separation in CdSe/CdTe hetero-nanowires measured by electrostatic force microscopy. *Applied Physics Letters* **100,** 2012–2015 (2012).

154. Schäfer, S. *Optical and electrical properties of individual semiconductor nanowires* Ph.D. Thesis (Universität Hamburg, 2011).

155. Erland, J., Razbirin, B. S., Pantke, K.-H., Lyssenko, V. G. & Hvam, J. M. Exciton diffusion in CdSe. *Physical Review B* **47,** 3582–3587 (1993).

156. Li, Z. *et al.* Controlled Synthesis of CdSe Nanowires by Solution–Liquid–Solid Method. *Advanced Functional Materials* **19,** 3650–3661 (2009).

157. Behn, D. *Kombinierte optische, elektrische und rasterkraftmikroskopische Untersuchungen an CdS-Nanowires* Ph.D. Thesis (Universität Hamburg, 2017).

158. Efros, A. L. *et al.* Band-edge exciton in quantum dots of semiconductors with a degenerate valence band: Dark and bright exciton states. *Physical Review B* **54,** 4843–4856 (1996).

159. *GESTIS-Stoffdatenbank* `http://www.dguv.de/ifa/de/gestis/stoffdb/index.jsp`. Retrieved 2019-02-07.

160. *Sigma-Aldrich Safety Data Sheet for trioctylphosphine* `https://www.sigmaaldrich.com/MSDS/MSDS/DisplayMSDSPage.do?country=DE&language=EN-generic&productNumber=718165&brand=ALDRICH`. Retrieved 2019-02-07.

161. *Merck KGaA Safety Data Sheet for trioctylphosphine oxide* `http://www.merckmillipore.com/Web-DE-Site/de_DE/-/EUR/ProcessMSDS-Start?PlainSKU=MDA_CHEM-814868&Origin=PDP`. Retrieved 2019-02-07.
162. KGaA, M. *Safety Data Sheet for AZ 826 MIF Developer* 2019-01-31.
163. KGaA, M. *Safety Data Sheet for AZ ECI 3012 Photoresist* 2017-04-22.

Danksagung

Zu dieser Arbeit haben viele Leute durch ihre Hilfe und Unterstützung beigetragen. Dafür möchte ich bedanken bei:

- Prof. Dr. Alf Mews, für die Möglichkeit diese Arbeit in seiner Gruppe anfertigen zu dürfen.
- PD Dr. Tobias Kipp und Dr. Christian Strelow, die mit ihrem enormen Fachwissen und mit ihren Rechnungen zur Interpretation meiner Daten beigetragen haben.
- Cornelius Fendler und Charlotte Ruhmlieb für die Messungen am Rasterelektronenmikroskop, Jan Siebels und Andreas Kolditz für die Unterstützung bei der Elektronenstrahllithographie, Dino Behn für die CdS-Nanodrahtproben, sowie Tobias Redder und Zhe Wang für die CdSe-Nanodrahtproben.
- Jan Flügge für das Beheben technischen Probleme aller Art, die Konstruktion und Umsetzung des kontaktierten Probenhalters für den Kryostaten und natürlich die vielen netten Gespräche.
- Meine Praktikanten und Bachelorstudenten, die mit ihrer Arbeit auch zu meiner Forschung beigetragen haben: Dennis Brückner, Felix Thiel, Henri Hagelmann, Jack Graneek, Katharina Braun, Nora Jannsen, Timo Jung, Yen Nguyen und Zineb Sayah.
- Martina Krasa für die Hilfe mit allem was mit Bürokratie und Organisation zu tun hat.
- Alle Mitglieder im Arbeitskreis Mews für die freundliche Atmosphäre.
- Dem ProExzellenzia-Programm, sowohl für die finanzielle Unterstützung, als auch die Möglichkeit mich persönlich weiterzuentwickeln.

Außerdem bedanken möchte ich mich bei allen, die mich in den letzten Jahren von der Seitenlinie aus angefeuert haben. Vielen lieben Dank an:

- Meine Freunde. Für die lieben Worte, und die entspannte und entspannende Zeit, mit und ohne Strickzeug.
- Kristina und Lasse, für das Korrekturlesen.
- Meine Familie. Insbesondere meine Mutter, zu der ich immer kommen konnte, wenn ich ein aufmunterndes Wort oder einen Platz zum Schreiben brauchte.
- Christoph.

Eidesstattliche Erklärung

Hiermit erkläre ich an Eides statt, die vorliegende Dissertation selbst verfasst und keine anderen als die angegebenen Hilfsmittel benutzt zu haben.

Ort, Datum, (Aina Reich)

Appendices

A

Additional data

Figure A.1: 5.50a.

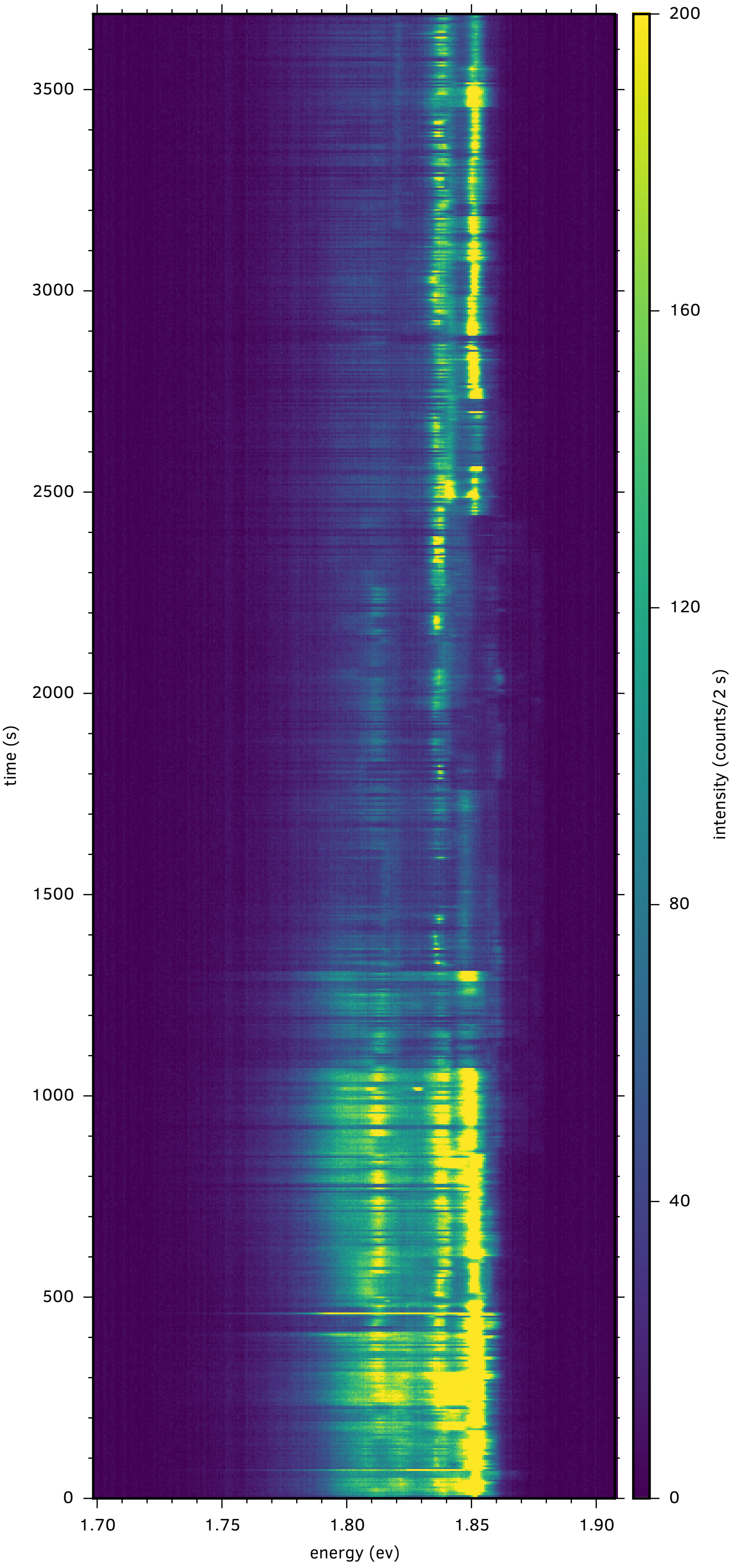

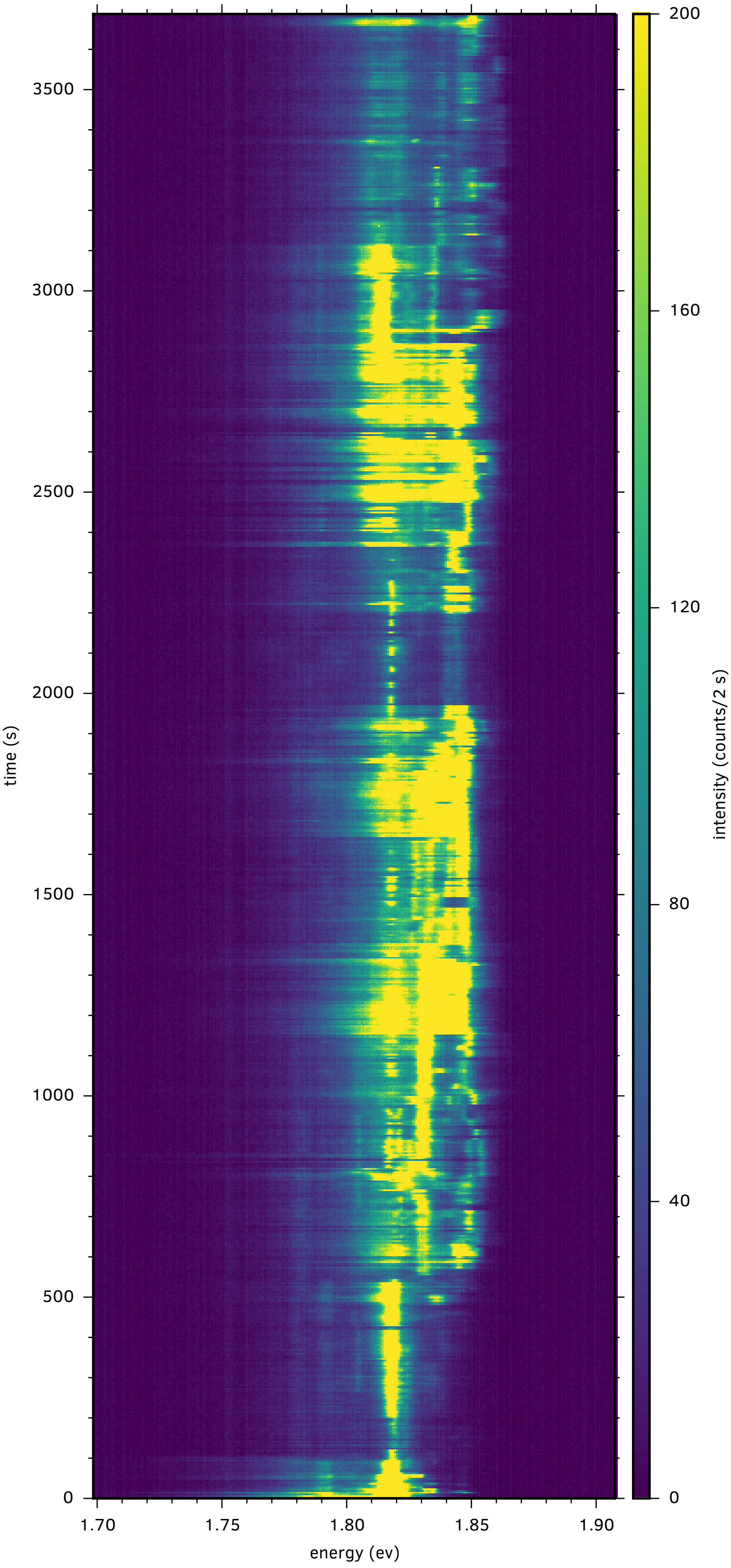

Figure A.2: 5.50b.

Figure A.3: 5.50c.

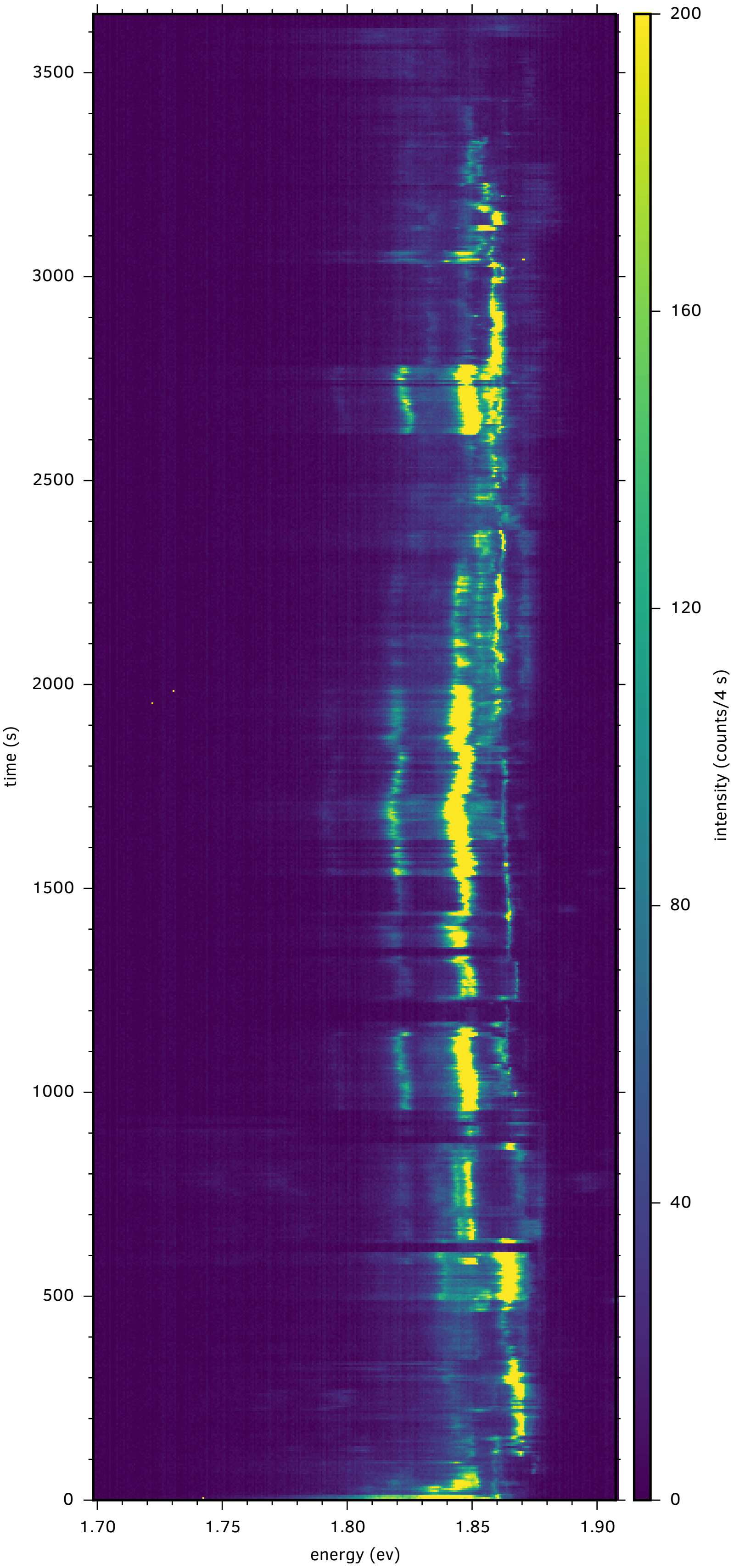

B

Safety

The chemicals used in this work are listed in table B.3, together with their respective hazard and precaution statement numbers, as well as any 1a and 1b classifications of carcinogenicity, mutagenicity and reproductive toxicity (CMR classifications). The hazard and precaution statements are listed in tables B.1 and B.2.

Table B.1: H-statements that apply to the used chemicals.

H225: Highly flammable liquid and vapour.
H226: Flammable liquid and vapour.
H290: May be corrosive to metals.
H301: Toxic if swallowed.
H302: Harmful if swallowed.
H304: May be fatal if swallowed and enters airways.
H311: Toxic in contact with skin.
H312: Harmful in contact with skin.
H314: Causes severe skin burns and eye damage.
H315: Causes skin irritation.
H318: Causes serious eye damage.
H319: Causes serious eye irritation.
H330: Fatal if inhaled.
H331: Toxic if inhaled.
H335: May cause respiratory irritation.
H336: May cause drowsiness or dizziness.
H341: Suspected of causing genetic defects.
H350: May cause cancer.
H361: Suspected of damaging fertility or the unborn child.
H361d: Suspected of damaging the unborn child.
H361fd: Suspected of damaging fertility. Suspected of damaging the unborn child.
H371: May cause damage to organs.
H372: Causes damage to organs through prolonged or repeated exposure.
H373: May cause damage to organs through prolonged or repeated exposure.
H410: Very toxic to aquatic life with long lasting effects.
H411: Toxic to aquatic life with long lasting effects.
H412: Harmful to aquatic life with long lasting effects.
H413: May cause long lasting harmful effects to aquatic life.

Table B.2: P-statements that apply to the used chemicals.

P201: Obtain special instructions before use.
P210: Keep away from heat/sparks/open flames/hot surfaces. — No smoking.
P233: Keep container tightly closed.
P235: Keep cool.
P240: Ground/bond container and receiving equipment.
P243: Take precautionary measures against static discharge.
P261: Avoid breathing dust/fume/gas/mist/vapours/spray.
P262: Do not get in eyes, on skin, or on clothing.
P273: Avoid release to the environment.
P280: Wear protective gloves/protective clothing/eye protection/face protection.
P284: Wear respiratory protection.
P301: IF SWALLOWED:
P302: IF ON SKIN:
P303: IF ON SKIN (or hair):
P304: IF INHALED:
P305: IF IN EYES:
P308: IF exposed or concerned:
P310: Immediately call a POISON CENTER or doctor/physician.
P312: Call a POISON CENTER or doctor/physician if you feel unwell.
P313: Get medical advice/attention.
P314: Get medical advice/attention if you feel unwell.
P330: Rinse mouth.
P331: Do NOT induce vomitting.
P332: If skin irritation occurs:
P337: If eye irritation persists:
P338: Remove contact lenses, if present and easy to do. Continue rinsing.
P340: Remove victim to fresh air and keep at rest in a position comfortable for breathing.
P351: Rinse cautiously with water for several minutes.
P352: Wash with plenty of soap and water.
P353: Rinse skin with water/shower.
P361: Remove/Take off immediately all contaminated clothing.
P370: In case of fire:
P378: Use … for extinction.
P403: Store in a well-ventilated place.
P404: Store in a closed container.
P501: Dispose of contents/container to …

Table B.3: Used chemicals and their respective safety statements.[159–163]

Substance	Symbols	H-Statements	P-Statements	CMR 1a+b
acetone		225-319-336	210-240-305+351+338-403+233	—
AZ 826 MIF developer		290-302-311-314-371-373	280-302+352-305+351+338-308+310	—
AZ ECI 3012 resist	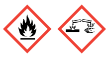	226-315-318-335	210-233-243-361-280-284-303+361+353-304+340-312-305+351+338-332+313-337+313-370+378-340+235-404-501	—
bismuth (bulk solid)	—	—	—	—
cadmium oxide		330-341-350-361fd-372-410	201-273-304+340-308+310	c1b
cadmium selenide		301+331-312-350-373-410	201-261-273-301+310+330-308+313-403+233	c1a
cadmium sulphide		302-341-350-361-372-410	201-273-301+312+330-308+313-501	c1b
ethanol		225-319	210-240-305+351+338-403+233	—
ethyl lactate		226-335-318	261-280-305-351-338	—
gold (bulk solid)	—	—	—	—
isopropyl alcohol		225-319-336	210-233-240-305+351+338-403+235	—
octanoic acid		314-412	305+351+338-310-280-301+330+331-303+361+353	—
poly(methyl methacrylate)	—	—	—	—
selenium (powder)		301-331-373-413	273-304+340-308+310	—
titanium (bulk solid)	—	—	—	—
toluene		225-304-315-336-361d-373	210-240-301+310+330-302+352-314-403+233	—
trioctylphosphine		314-318	280-305+351+338-310	
trioctylphosphine oxide		319-411	262-273-305+351+338	—